Search for heavy neutrinos in the T2K experiment and upgrade of the near detector ND280

Sergey Suvorov

▶ **To cite this version:**

Sergey Suvorov. Search for heavy neutrinos in the T2K experiment and upgrade of the near detector ND280. High Energy Physics - Experiment [hep-ex]. Université Paris-Saclay; Académie des sciences de Russie (1992-..), 2020. English. NNT : 2020UPASP031 . tel-03297119

HAL Id: tel-03297119

https://theses.hal.science/tel-03297119

Submitted on 23 Jul 2021

HAL is a multi-disciplinary open access archive for the deposit and dissemination of scientific research documents, whether they are published or not. The documents may come from teaching and research institutions in France or abroad, or from public or private research centers.

L'archive ouverte pluridisciplinaire **HAL**, est destinée au dépôt et à la diffusion de documents scientifiques de niveau recherche, publiés ou non, émanant des établissements d'enseignement et de recherche français ou étrangers, des laboratoires publics ou privés.

Thèse de doctorat

NNT: 2020UPASP031

université PARIS-SACLAY

RUSSIAN ACADEMY OF SCIENCES
INSTITUTE FOR NUCLEAR RESEARCH

Search for heavy neutrinos in the T2K experiment and upgrade of the near detector ND280

Thèse de doctorat de l'université Paris-Saclay et de l'Institute for Nuclear Research

École doctorale n° 576, Particules, Hadrons, Énergie et Noyau: Instrumentation, Imagerie, Cosmos et Simulation (PHENIICS)
Spécialités: Physique des particules
Unité de recherche: Université Paris-Saclay, CEA, Département de Physique des Particules, 91191, Gif-sur-Yvette, France

Thèse présentée et soutenue à Paris-Saclay, le 25 Septembre 2020, par

Sergey SUVOROV

Composition du jury:

Alessandra TONAZZO Professeur, Université Paris Diderot	Présidente
Boris POPOV Directeur de recherche, LPNHE, Sorbonne Université	Rapporteur et Examinateur
Anselmo MEREGARDIA Chargé de recherche, HDR, Université de Bordeaux	Rapporteur et Examinateur
Dmitry GORBUNOV Professeur, INR RAS, Russie	Examinateur
Boris TUCHMING Ingénieur/Chercheur, CEA SACLAY-IRFU	Examinateur
Marco ZITO Directeur de recherche, Université Paris-Saclay	Directeur de thèse
Yury KUDENKO Professeur, INR RAS, Russie	Codirecteur de thèse

Contents

I Introduction

II Heavy neutrino study

RÉSUMÉ

La physique des neutrinos est un domaine très prometteur de la physique des particules. La découverte des oscillations des neutrinos a été une étape importante, car elle a permis de prouver que les neutrinos ont une masse non nulle. Actuellement, les expériences sur les neutrinos effectuent des mesures précises des paramètres d'oscillation. En particulier, la phase δ_{CP} est intéressante car elle permet la violation de la parité de charge dans le processus d'oscillation des neutrinos. Il y a deux façons d'étudier les oscillations des neutrinos : en observant la réduction du neutrino de la saveur initiale (disparition) ou en observant le neutrino d'une autre saveur par rapport à celle produite initialement (apparition). Seul le canal de l'apparition est sensible à la violation de CP. Les expériences sur l'accélérateur offrent une possibilité unique d'étudier à la fois le canal neutrino/anti-neutrino et le canal d'apparition/disparition. Ainsi, ce type d'expériences est adapté pour les mesures de δ_{CP}.

Tokai-to-Kamioka (T2K) est une expérience d'oscillation à longue base située au Japon. Elle utilise un faisceau provenant d'un accélérateur de protons de 30 GeV (J–PARC) pour produire un intense faisceau pur de neutrinos muoniques. Le faisceau oscillé est étudié avec le détecteur lointain Super–Kamiokande situé à ~ 300 km. Il s'agit d'un détecteur Cherenkov composé de 50 kt d'eau. Avant les oscillations, le flux est mesuré par le détecteur proche (ND280). Le ND280 permet une réduction suffisante de l'incertitude systématique dans l'analyse des oscillations. La prise de données T2K a réalisé la première mesure de l'angle de mélange θ_{13} et la mesure la plus précise de l'angle de mélange θ_{23}. Récemment, la collaboration T2K a indiqué avoir limité la valeur du δ_{CP} avec un intervalle de confiance de 3σ. Les mesures actuelles du δ_{CP} sont limitées par les statistiques. L'exécution de T2K a été étendue avec pour objectif final de collecter 20×10^{21} de protons sur la cible. Dans ces statistiques, les incertitudes systématiques des mesures de la violation du CP domineront. Les incertitudes du modèle d'interaction des neutrinos sont dominantes dans les mesures de δ_{CP}. La réduction des incertitudes peut être réalisée soit par une mise à niveau de la configuration du détecteur, soit par une nouvelle technique d'analyse. Les deux approches sont présentées dans la présente thèse.

1 Mise à niveau du détecteur proche

Le détecteur proche de l'expérience T2K ND280 permet une réduction remarquable des incertitudes de 14% à 7% avec des mesures de la section efficace des neutrinos en fonction du temps de flux. Mais ses performances peuvent encore être améliorées. La configuration actuelle n'est pas adaptée aux traces émises avec un angle élevé par rapport à la direction du faisceau. Le seuil d'énergie de la détection des hadrons est élevé, ce qui fait que toutes les particules secondaires provenant des interactions des neutrinos ne sont pas détectées et que l'énergie reconstruite des neutrinos est étalée. Les sections efficaces d'interaction de neutrinos et les modèles nucléaires ne peuvent pas être sondés avec précision. Afin d'améliorer la précision des mesures d'interaction des neutrinos, une mise à niveau de ND280 est en cours de réalisation [1]. Il a été démontré qu'une

combinaison du détecteur à scintillateur à grain fin (FGD) et des chambres de projection temporelle verticale (TPC) offre de bonnes performances dans le suivi des particules, l'identification de la charge et des particules l'impulsion.

Un nouveau détecteur à scintillateur à grain fin SuperFGD [2] entièrement actif sera installé comme cible supplémentaire de neutrinos. Il est constitué de cubes de 1 cm^3 et permet de reconstruire les traces en 3D. Les dimensions du nouveau détecteur sont de $192\times184\times56$ cm^3 et la masse de référence est de 2 tonnes. La granularité fine réduit le seuil de détection des hadrons et des muons. Presque toutes les particules secondaires chargées provenant des interactions avec les neutrinos vont être détectées. Le détecteur sera capable d'identifier le type de particules pour les particules isolées. Avec le nouveau détecteur, la précision des mesures d'interaction des neutrinos sera accrue.

La production et le montage du nouveau détecteur sont compliqués. Une méthode pour l'assemblage du SuperFGD a été développée et testée. Il a été démontré que l'ensemble du détecteur peut être assemblé de cette manière. La structure libre des cubes permettra leur auto-alignement lors de l'insertion de la ligne de pêche en trois dimensions. Les fibres fragiles ne sont insérées qu'à la dernière étape de la contraction du détecteur. J'ai participé aux tests de la technologie d'assemblage du SuperFGD et à la construction du détecteur.

Un test de faisceau a été effectué pour tester les nouvelles caractéristiques du détecteur. J'ai participé à la construction du prototype et aux tests. Nous avons observé un rendement lumineux élevé au niveau de 40 photoélectrons par canal avec un faisceau de particules faiblement ionisantes. La résolution temporelle a été estimée au niveau de 1 ns. Les tests ont confirmé le grand potentiel de cette nouvelle configuration. Le rendement lumineux élevé et la précision des mesures temporelles permettent une mesure précise des interactions des neutrinos.

Une boîte à outils de simulation pour le détecteur SuperFGD a été mise au point. J'ai calibré la simulation de la réponse du détecteur avec les données prises lors du test du faisceau. J'ai estimé le rendement lumineux pour différentes topologies d'événements. La simulation de l'interférence optique entre les cubes a été réalisée. Avec une telle simulation, j'ai démontré que le détecteur peut séparer différentes particules avec les mesures de l'énergie déposée. La gamme dynamique des MPPC est suffisamment large (2668 pixels) pour mesurer les protons s'arrêtant dans le détecteur, qui fourniront au maximum 600 photoélectrons. J'ai estimé un seuil pour la détection des protons de faible énergie au niveau de 300 MeV/c qui est beaucoup plus bas que la valeur actuelle de 600 MeV/c. Le proton provenant des interactions des neutrinos dans le ND280 devrait avoir une impulsion à partir de 200 MeV/c. Ainsi, la majorité des protons peuvent être détectés dans le SuperFGD et leur énergie peut être reconstruite.

Deux nouvelles TPC seront installeés au-dessus et au-dessous du SuperFGD. Ils permettront un suivi précis, l'identification de la charge et du type de particule, des mesures précises de l'impulsion. L'acceptation angulaire totale de 4π des particules secondaires provenant des interactions avec les neutrinos sera atteinte. Des Micromegas résistifs seront utilisés comme détecteur sensible. Une feuille résistive placée au-dessus du détecteur de Micromegas habituel epermet le partage de la charge entre les cellules sensibles et de l'amélioration de la résolution spatiale, tout en conservant la même taille de cellule. La résolution de l'impulsion devient donc meilleure.

Les prototypes des nouveaux détecteurs ont été construits et testés avec des faisceaux de particules chargées. Les performances de la TPC ont été jugées supérieures aux attentes. La résolution spatiale pour les traces parallèles aux bords de la plaquette a été mesurée au niveau de 200 μm. La résolution spatiale des TPC actuelles dans des conditions similaires est de 600 μm. Une telle amélioration permettra des mesures très précises de l'impulsion des particules secondaires, ce qui permettra de sonder avec précision les modèles d'interaction des neutrinos. La résolution énergétique a été estimée au même niveau que celui observé dans le TPC actuel (10% par module) [3].

Grâce à la combinaison des nouveaux détecteurs SuperFGD et des TPC horizontaux, nous allons réduire l'incertitude systématique dans l'analyse des oscillations de 7% à 4%. Les nouveaux détecteurs fourniront des informations plus détaillées sur les interactions des neutrinos, ce qui nécessitera la mise au point de nouvelles méthodes d'analyse. Une nouvelle méthode de reconstruction de l'énergie des anti-neutrinos utilisant les mesures de l'énergie du temps de vol des neutrons dans le SuperFGD a été proposée. Avec la boîte à outils de simulation du SuperFGD, j'ai démontré qu'avec ces informations supplémentaires, l'interaction sur l'hydrogène peut être séparée des interactions sur le carbone. Nous pouvons donc sélectionner un échantillon d'interactions de neutrinos sur l'hydrogène qui est exempt d'effets nucléaires et reconstruire l'énergie des neutrinos de manière très précise. Il a été prouvé que la dépendance de la précision de la reconstruction de l'énergie des neutrinos par rapport aux effets nucléaires mal étudiés a été éliminée grâce aux mesures de la cinématique des neutrons [4]. Cette méthode nous permettra de contraindre à la fois la normalisation du flux et sa forme, ce qui est essentiel pour des mesures précises de la phase δ_{CP}.

2 Recherche de neutrinos lourds

Les expériences de neutrinos d'accélérateur sont capables non seulement de mesurer les paramètres d'oscillation, mais aussi d'effectuer une recherche de physique au-delà du modèle standard (SM). Un phénomène d'oscillation de neutrino indique explicitement que le neutrino est massif. Cependant, dans le modèle standard, les neutrinos sont sans masse. L'explication de la nature de la masse des neutrinos nécessite l'existence de nouvelles particules. Une hypothèse proposant les leptons neutres lourds (HNL) est une extension du SM qui peut expliquer la nature de la masse des neutrinos, l'existence de la matière noire et l'asymétrie de baryon-antibaryon dans l'Univers. Il n'y a pas d'indications sur la masse des HNL. Elle peut prendre n'importe quelle valeur de l'échelle eV à l'échelle GUT. Les neutrinos lourds de l'échelle GeV peuvent être cherchés dans les expériences existantes.

Une recherche sur les désintégrations du HNL a été effectuée avec le détecteur proche de l'expérience T2K. On s'attend à ce que des neutrinos lourds soient produits dans la désintégration de méson. Avec la ligne de faisceau de T2K, un faisceau intense de kaons est produit. Ainsi, la recherche du HNL avec des masses $M_N < 500$ MeV/c^2 est possible. Je me suis concentré sur la recherche de sa désintégration en deux corps $N \to \mu\pi$, $N \to e\pi$ ainsi que le mode dimuon $N \to \mu\mu\nu$. Je m'attends à ce que le bruit de fond principal provienne des interactions de neutrinos actifs. Pour minimiser un tel bruit de fond, le volume actif du TPC a été choisi pour la recherche des désintégrations HNL. Le TPC à pression atmosphérique contiendra 10^3 fois moins d'interactions de neutrinos que le détecteur à scintillateur. Ainsi, le bruit de fond est naturellement supprimé. Le tracker ND280 a déjà démontré de bonnes performances et la capacité à identifier la charge et le type de particules. Cela est très utile dans la recherche de la désintégration de particules neutres.

Les signaux attendus ont été simulés dans le détecteur. Les simulations précises de la désintégration du kaon en neutrino actif ($K \to \mu\nu$) ont déjà été réalisées en T2K. J'ai utilisé les informations de la désintégration du kaon de cette simulation. Toutes les désintégrations ont été resimulées pour la production de HNL, en tenant compte de la modification de la cinématique de désintégration et des rapports d'embranchement. Avec une telle procédure, j'ai obtenu les spectres HNL sur le site de ND280. Ensuite, j'ai simulé les désintégrations des neutrinos lourds dans les TPC du ND280 et j'ai estimé la réponse des détecteurs pour les événements de signal.

Les spectres cinématiques des particules filles ont été étudiés afin de les séparer des interactions des neutrinos dans le gaz. Une séquence de coupures a été développée pour supprimer le bruit de fond. Les coupures cinématiques sont les plus efficaces dans l'élimination du bruit de

fond. La direction du HNL est extrêmement colinéaire au faisceau. Lorsque les deux particules de la désintégration HNL sont détectées, je peux reconstruire la direction du candidat HNL. Au contraire, les interactions des neutrinos standards produisent des particules dans un grand angle qui est différent de la cinématique de la désintégration à deux corps. En outre, la masse invariante du HNL reconstruite devrait être supérieure à la masse du produit et inférieure à la masse du kaon qui met en uvre une autre contrainte.

L'efficacité finale de la détection du signal a été observée au niveau de 20% et on ne s'attendait à pratiquement aucun bruit de fond. L'efficacité du signal est limitée par la conception du détecteur. La désintégration du HNL produit deux particules colinéaires qui ne sont pas faciles à séparer dans les TPC du ND280. Néanmoins, une efficacité relativement élevée nous permet d'effectuer une recherche sensible des désintégrations du HNL dans le ND280.

Les incertitudes systématiques dans la recherche de HNL ont été estimées. Les limites finales de l'existence du HNL sont fixées en fonction du nombre d'événements attendus. Ce nombre est estimé sur la base du flux HNL et de l'efficacité du détecteur. Ces deux éléments font l'objet d'incertitudes systématiques. Les incertitudes du flux HNL sont dominées par les multiplicités de production de kaon. Ces processus ont été mesurés par l'expérience NA61. J'ai estimé la systématique basée sur leurs mesures à un niveau de 20%. L'autre source d'incertitudes est la systématique des détecteurs. La systématique du détecteur a été estimée sur la base de la comparaison des échantillons de Monte-Carlo et de données pour chaque source particulière d'incertitude. La valeur totale de la systématique du détecteur a été estimée à 4%.

Après le dévoilement des données, un seul événement en mode $N \to \mu\mu\nu$ a été observé. Aucun événement n'a été observé dans les modes de décomposition à deux corps $N \to \mu\pi$ et $N \to e\pi$. Une forte limite supérieure de l'existence du neutrino lourd avec $M_N < 500$ MeV/c^2 a été fixée en utilisant la méthode Highland et Cousins. Le meilleur résultat est obtenu pour les masses élevées. Les angles de mélange ont été contraints avec $|U_e|^2 < 2 \times 10^{-9}$ pour $M_N > 420$ MeV/c^2 et $|U_e|^2 < 3 \times 10^{-9}$ pour $M_N > 350$ MeV/c^2. Ce résultat améliore l'analyse précédente effectuée par l'expérience PS191 [5].

ACKNOWLEDGMENTS

I would like to thank members of both INR and CEA Saclay/IRFU groups I have been working with. The friendly atmosphere and a mentorship from more experienced colleagues helped me a lot on my way during the Ph.D. work. I would like to express my great gratitude to both supervisors Yuri and Marco, who patiently taught me to do science and helped both with scientific and everyday problems.

In particular I would like to thank colleagues: Mathieu, Sasha, Artur with whom we were working on the search of heavy neutrinos in T2K; and Paul, Samira, Sara, Laura, Davide, Stephen, Cesar, Ko with whom we worked on the ND280 upgrade project. All the T2K collaboration members were very friendly and helpful during the researches.

I would like to thank funding support that helped me during the research: French government program “Vernadski scholarship ”, CEA and INR funds, RFBR and RSCF funds.

Part I

Introduction

CHAPTER 1

NEUTRINO PHYSICS

Exploration of the neutrinos is a very promising direction of research in particle physics. Over the last 60 years since its first experimental observation, several breakthroughs were made. Many of them have been awarded notable prizes. All this speaks of the great interest of the community on this topic. Many puzzles are still unsolved, several challenging experiments are ongoing.

Neutrino was always a kind of "mysterious" particle. It was proposed as an almost undetectable particle to explain the unexpected behavior of the beta decay (section 1). It remained a hypothesis for 36 years until it was finally observed in the breakthrough experiment. After the first detection, a new puzzle was found. The neutrino flux from the Sun was much lower than expected. Both Solar and neutrino models remained in doubt for 40 years until the phenomenon of the missing neutrinos was solved. It led to the discovery of an extremely interesting effect — neutrino oscillations (section 3). It was found that neutrinos are changing flavor while propagating in the vacuum. This fact indicates that neutrino has non-zero masses, as only massive particles can change their state in time.

The non-zero neutrino mass triggered several hypotheses about its origin (chapter 2). It can't be explained within the Standard Model — the main framework in particle physics. Hence this fact can indicate a new unexplored region of fundamental physics. One of the most probable explanation is the existence of the new particle(s). Such a hypothesis can have many applications, such as the explanation of the Dark Matter phenomenon. Thus the explorations in the neutrino physics can lead to very interesting discoveries.

Another interesting subject is a charge–parity violation in the neutrino oscillations (subsubsection 3.1.c). Some hints were found that the neutrino oscillation process is not symmetric under the change of particle charge and the space inversion. This effect together with the existence of the new particles can explain the phenomenon of the matter-dominance in the Universe (subsubsection 1.4.b).

To sum up, neutrino physics is a very promising field of research with several open challenges and interesting results awaiting.

1 Historical overview

The prerequisites of the neutrino existence were found at the beginning of the XXth century. The spectrum of the electrons from the β-decay was measured to be continuous [6]. The β-decay

corresponds to a neutron transformation into electron and proton. Following the laws of both momentum and energy conservation, the electron produced in the 2-body decay should have fixed energy defined by the mass difference between the neutron and the proton. Non-discrete spectrum provoked several theories such as energy non-conservation (by N. Bohr) or existence of the new hypothetical particle (by W. Pauli [7]). Later Enrico Fermi developed a complete theory of beta decay [8]. In the modern notation, the decay process was presented as $n \rightarrow p^+ + e^- + \overline{\nu}_e$, where neutrino is noted as ν.

1.1 Discovery of the neutrino

The experimental discovery of the neutrino was quite challenging. Neutrinos are not taking part in the electromagnetic or strong interactions. The only way to detect them is through the weak interaction. Based on Fermi's theory, along with the beta decay $n \rightarrow p + e^- + \overline{\nu}_e$ the inverse beta decay $\overline{\nu} + p \rightarrow n + e^+$ should exist. Such a process can be used for the direct detection of the neutrino. But the expected cross-section for such a process was estimated to be at the level of 10^{-44} cm^2. That was about a couple of dozen orders of magnitude less than cross-sections of other known processes. That's why the neutrino discovery happened only 26 years after the idea of the neutrino existence had been proposed.

After the proposal of the new particle few indirect measurements were performed, but the direct observation remained a challenge. The first successful neutrino detection was done by the group led by Frederick Reines and Clyde Cowan [9]. They performed a series of experiments trying to detect neutrino from the most powerful source at that time - nuclear power plant. Relatively new material a liquid scintillator was used as a target and detector. The inverse beta decay was used as a detection reaction:

$$\bar{\nu} + p \rightarrow n + e^+ \tag{1.1}$$

The positron shortly annihilates emitting two photons that can be detected with photomultipliers (PMTs). But not only neutrino interactions can cause such a signal. To suppress the background, a Cadmium isotope was added to the detector. Thus the neutrons would also be detected with reaction

$$n + {}^{108}Cd \rightarrow {}^{109m}Cd \rightarrow {}^{109}Cd + \gamma \tag{1.2}$$

As the ${}^{109m}Cd$ lifetime is few tens of microseconds the signal will have a unique signature: positron annihilation, followed by the gamma-ray emission with a known delay time. Thus rare signal events can be separated from a variety of backgrounds.

Such a strategy lead to the successful discovery of the particle that was supposed to be "undetectable" before.

1.2 Neutrino flavors

The first neutrino detection was made using a nuclear reactor as a particle source. Such a source is extremely powerful but isotropic. For the precise measurements, it will be extremely useful to gain the statistics with the focused particle beam. For this, accelerators can be used. The general idea is to use a proton beam hitting a target to produce mesons. The charged meson can be focused with a magnetic field and further decay, producing the focused neutrino beam with high intensity. The description of such a scheme in the modern experiment can be found in section 1. This approach was used the first time to determine if the neutrino has flavors [10]. At that time it was known that there are two generations of the charged leptons: electron and muon. The question was if the electron neutrino was different from the muon neutrino. The main idea of the

experiment is to use the neutrino flux produced from the pion decay. Because of the mass difference between electron and muon charged pion decays mainly to the muon, e.g. $\pi^+ \to \mu^+ + \nu_\mu$. The experiment showed clearly that the reaction Equation 1.4 is severely suppressed comparing the reaction Equation 1.3.

$$\nu_\mu + p \to n + \mu \tag{1.3}$$
$$\nu_\mu + p \nrightarrow n + e \tag{1.4}$$

That means that neutrino has flavors. It can be either produced or detected with the lepton of the same flavor. The existence of the different types of neutrino confirmed the doublet structure of the leptons. This fact will play an important role in the theory of neutrino oscillations (section 3).

1.3 Neutrino in the Standard Model

Physicists have used gauge ("scale") symmetries to build the field theories. It is a powerful and elegant tool. The group theory appeared to be a natural mathematical framework for the description of gauge fields. After the development of quantum mechanics, the scale was turned to a complex value. Thus the quantum electrodynamic theory was created using $U(1)$ abelian gauge group.

The first step towards the general model of particle physics was done by Yang and Mills by extending the concept of the gauge theory to the non-abelian groups $SU(2)$. This made possible to describe the phenomenon of strong interactions [11]. Later Glashow found a way to unify the electromagnetic and weak interactions [12]. Salam and Weinberg finished the theory with the implementation of the Higgs mechanism into the Glashow theory [13].

Many experiments brilliantly confirmed the proposed model and demonstrated its predictive power. For example, in the sector of the electroweak interactions, the most important observations were: neutral current discovery [14], the Z and W boson discovery [15], the $\gamma - Z$ interference, neutrino generation number [15], Higgs boson discovery [16], and many others.

In general, the SM is based on the Yang–Mills theory with local $SU(3) \times SU(2) \times U(1)$ gauge symmetry. It can be divided into several sections:

- Quantum chromodynamics sector
- Electroweak sector
- Higgs sector
- Yukawa sector

In the context of the current thesis, we will discuss in detail the electroweak sector. It is based on group $U(1) \times SU(2)_L$. It means that we will have two sets of generators: the weak hypercharge Y_W for $U(1)$ and Pauli matrices for $SU(2)_L$. Index L means that it affects only left-chiral fermions.

Helicity, polarity, chirality

Helicity is a projection of the spin onto the direction of the momentum.

$$h = \frac{\vec{s} \cdot \vec{p}}{|\vec{s}|\,|\vec{p}|} \tag{1.5}$$

The helicity can be "left" or "right" that corresponds to the spin direction opposite or co-directed with momentum. For the massless particles, helicity is Lorentz invariant. The polarization of the particle beam is the fraction of the particles with a given helicity. For example, 50% polarization means that half of the particles are "left" and half are "right".

The chirality is a more fundamental characteristic compared to helicity. It is determined by whether the particle wave function transforms with a right- or left-handed representation of the Poincare group.

Chirality is a conserved quantum number for massless fermions. It means that independent rotation of the left- and right- handed components doesn't affect the theory. For them, the helicity is always the same as chirality.

The massive particles break the chiral symmetry explicitly. Also for the massive fermions, the helicity is not equivalent to the chirality as one can choose the reference frame moving faster than the particle and inverse the helicity.

In the SM fermions are described as doublets (subsection 1.2). For each charged lepton there is a corresponding neutrino. While charged lepton can be either right-handed or left-handed, the neutrino can be only left-handed. This part of the theory is based on the empirical observations [17] and this is strictly fixed in the model. A neutrino can interact via the charge current (CC) or neutral current (NC). The corresponding interaction terms are written as:

$$\begin{aligned} -\mathcal{L}_{CC} &= \frac{g}{2}\sum_{\alpha} \bar{\nu}_{L\alpha}\gamma^{\mu}\ell_{L\alpha}W^{+}_{\mu} + h.c. \\ -\mathcal{L}_{NC} &= \frac{g}{\sqrt{2\cos\theta_W}}\sum_{\alpha} \bar{\nu}_{L\alpha}\gamma^{\mu}\nu_{L\alpha}Z^{0}_{\mu} \end{aligned} \tag{1.6}$$

Thus there is no possibility for the production or detection of the right-handed neutrino (left-handed anti-neutrino). The existence of such "exotic" particles is proposed in the various theories (subsection 1.4).

a Number of neutrino flavors

After the magnificent confirmation of the Standard Model with the discovery of the neutral current and W and Z bosons, it became possible to measure precisely the number of the neutrino generations. This analysis became possible with the massive production of the Z-bosons at Large Electron-Positron Collider (LEP) at CERN.

The general idea of the study is to look at the different modes of the Z decays. These decays can be classified into several groups:

$$\begin{aligned} Z &\to q\bar{q} \\ Z &\to \ell^{+}\ell^{-} \\ Z &\to \nu\bar{\nu} \end{aligned} \tag{1.7}$$

The total width of the boson decay is a sum of these three channels. As the width of $Z \to \ell^+\ell^-$ is the same of all charged leptons and $Z \to \nu\bar{\nu}$ is the same for all neutrino types because of the lepton universality. The total Z^0 width can be written with:

$$\Gamma_Z = \Gamma(Z \to hadrons) + N_\ell \times \Gamma(Z \to \ell^+\ell^-) + N_\nu \times \Gamma(Z \to \nu\bar{\nu}) \tag{1.8}$$

In the experiment, Γ_Z, $\Gamma(Z \to q\overline{q})$ and $\Gamma(Z \to \ell^+\ell^-)$ were measured. The equality of the $\Gamma(Z \to e^+e^-)$ and $\Gamma(Z \to \mu^+\mu^-)$ was checked. The width of the decay into neutrinos came from the theory. The number of neutrino generations remained the only unknown variable in the Equation 1.8. The results of the precise measurements of the Z-boson resonance and predictions for 2, 3 and 4 neutrino generations are shown in Figure 1.1. At LEP, the number of neutrino generations was measured to be $N_\nu = 2.9840 \pm 0.0082$ [18]. So we can conclude that in Standard Model there are only three types of the left-handed neutrino with masses less than half of the Z-boson mass.

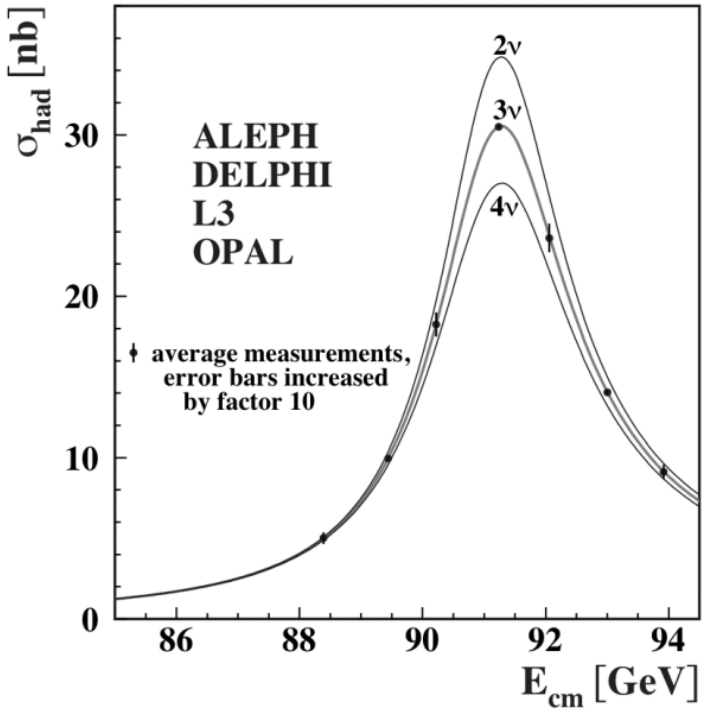

Figure 1.1: Measurement of the hadron production cross-section as a function of the LEP center-of-mass energy around the Z-boson resonance.

2 Neutrino interactions

The precise measurements in neutrino physics such as neutrino oscillation and search for CP–violation require accurate knowledge about the neutrino interactions' rates. This is still one of the dominating uncertainties in the experiments. Roughly we can divide the neutrino interactions with the matter on the interactions with electron and nucleus. The neutrino interactions with the single fermion are described very accurately with the Standard Model. So far no deviations are found in the experiment.

2.1 Interactions with electron

Neutrino interactions with the single electron are the simplest ones. They can be described with the tree-level Feynman diagrams presented in Figure 1.2. Electron neutrino can interact with the electron both through the scattering through the charged current (Figure 1.2 (a)) and neutral current (Figure 1.2 (c)), while muon and tau neutrino can scatter[1] only via neutral current.

The muon neutrino can also interact with the electron through the charged current (Figure 1.2 (b)), but this is a threshold process. The minimal neutrino energy can be estimated by $E_\nu^{th} = \left(m_\mu^2 - m_e^2\right) / (2m_e) = 10.9GeV$ neglecting the neutrino mass. Thus the muon can not be produced by the neutrinos from the Sun or other low-energy neutrinos.

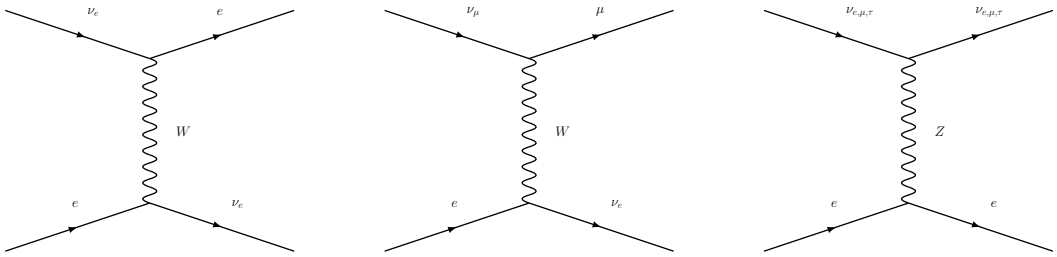

(a) (b) (c)

Figure 1.2: Tree-level Feynman diagrams of the neutrino interactions with electron: (a) and (b) electron and muon neutrino scattering through the charged current, (c) all-type neutrino scattering through the neutral current.

The anti-neutrino interaction with the electron can be described with the Feynman diagrams presented in Figure 1.3. Comparing with the neutrino case, a muon anti-neutrino can not interact with the electron through the charged current $\overline{\nu}_\mu + e^- \nrightarrow \mu^- + \overline{\nu}_e$.

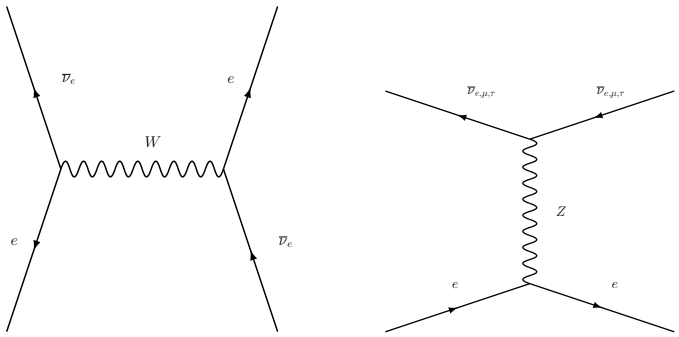

(a) (b)

Figure 1.3: Tree-level Feynman diagrams of the anti-neutrino interactions with electron: (a) electron anti-neutrino scattering through the charged current, (c) all-type anti-neutrino scattering through the neutral current.

The cross-sections for the processes mentioned above are presented on the Figure 1.4.

[1] Here "scattering" means that the initial electron is not changing the flavor, e.g. does not transform into muon

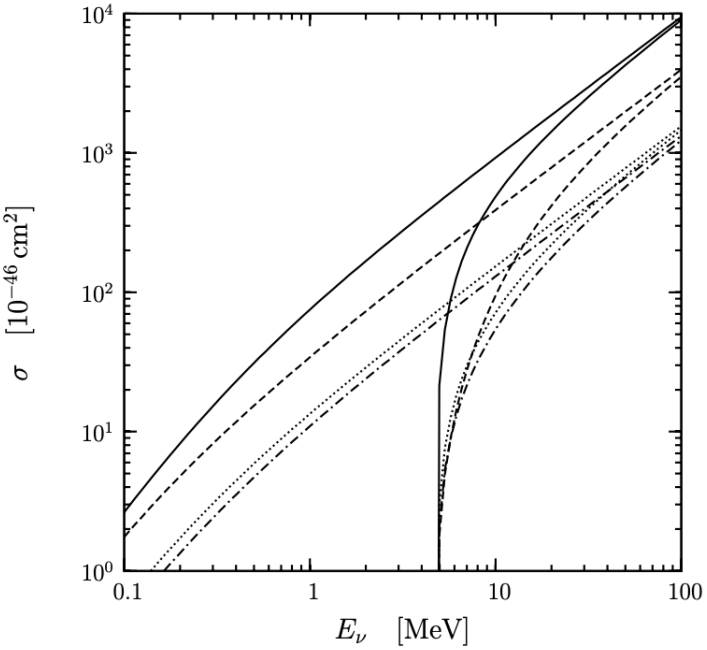

Figure 1.4: Electron neutrino cross-sections as a functions of the neutrino energy E. Solid line: $\nu_e + e^- \rightarrow \nu_e + e^-$. Dashed line: $\overline{\nu}_e + e^- \rightarrow \overline{\nu}_e + e^-$. Dotted line: $\nu_{\mu,\tau} + e^- \rightarrow \nu_{\mu,\tau} + e^-$. Dash-dotted line: $\overline{\nu}_{\mu.\tau} + e^- \rightarrow \overline{\nu}_{\mu.\tau} + e^-$. For each scattering process the upper curve is the cross-section without a threshold for the kinetic energy of the recoil electron, whereas the lower curve is obtained with $T_e^{th} = 4.50 MeV$, which corresponds to $E_\nu^{th} = 4.74 MeV$. From [19]

2.2 Interactions with nuclei

Neutrino interactions with a single fermion (e.g. quark) are very well known. But the atomic nuclei are complicated structures consisting of several particles that make the neutrino interaction description much more complicated. The reaction topology severely depends on the neutrino energy. The following energy scales can be set:

- $E_\nu < 0.1$ GeV: the neutrino interacts with the whole nucleus,
- $E_\nu \sim 0.1 - 2$ GeV: the neutrino interacts with one or few nucleons inside the nucleus,
- $E >$ few GeV: the neutrino interacts with the individual quarks

The energy scales above can be easily understood with De Broglie's wave approach. The incoming neutrino wavelength should be compared with the target's size.

From the experimental point of view, we can classify the neutrino interactions based on the outgoing particles. Thus we can divide all the reactions in the charged current and neutral current exchange. In the case of a charged current exchange, one will observe an outgoing charged lepton, while in case of neutral current exchange only hadrons and photons can be seen. Now we will define several topologies for the interactions via charged current. At the energies ≤ 1 GeV neutrino mostly interacts in a quasi-elastic way (CCQE — charge current quasi–elastic), transforming neutron into a proton. For the neutrinos with energies of 1 GeV the most probable reaction is a Δ^{++} production with its further decay into proton and pion. Also at this energy scale, we can see the coherent pion production, when a neutrino interacts with the whole nucleon or interactions with two nucleons simultaneously (2p2h interactions). With the energy growth, one will observe

the dominance of the deep inelastic scattering with the various hadron production as a result of the broken nucleon. The Feynman diagrams for the processes mentioned above are shown in Figure 1.5.

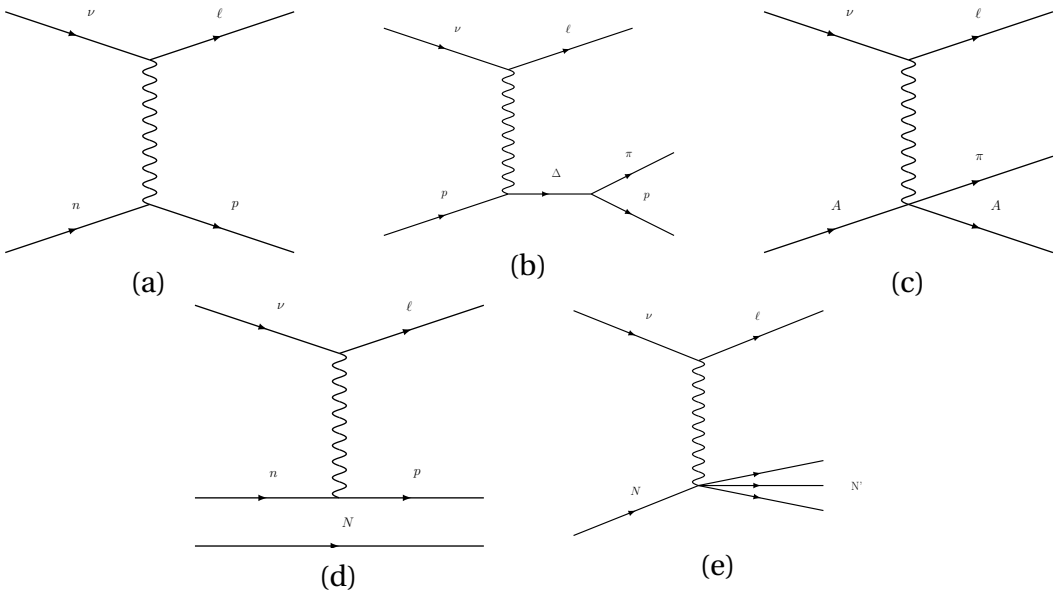

Figure 1.5: Feynman diagrams for the neutrino interactions with nucleus. The following reactions are shown: (a) quasi elastic scattering, (b) resonance pion production, (c) coherent pion production, (d) 2p2h, (e) deep inelastic scattering.

The evaluation of the neutrino and anti-neutrino cross-sections with the energy is shown in Figure 1.6.

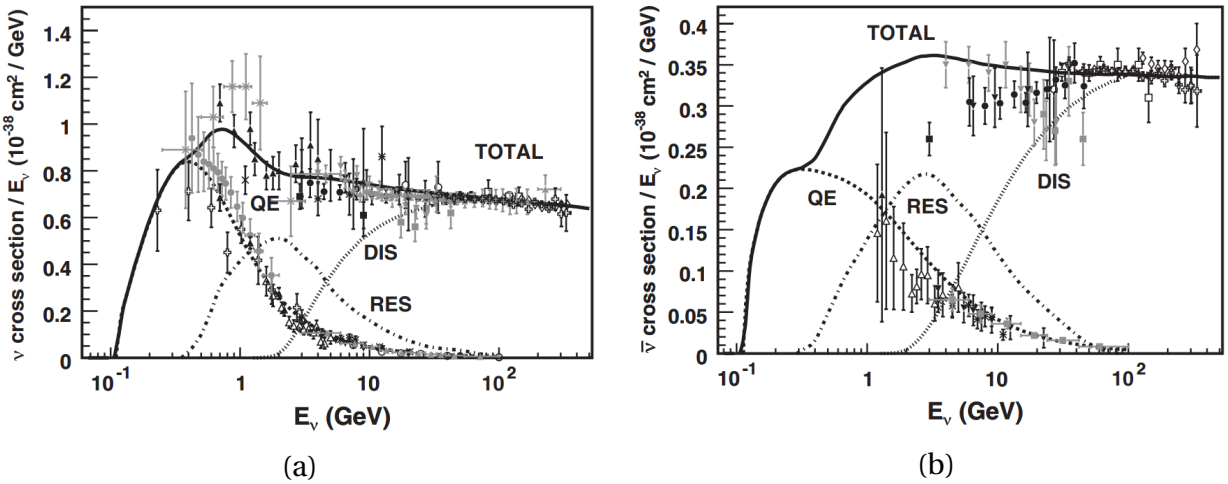

Figure 1.6: (a) neutrino and (b) anti-neutrino per nucleon CC cross sections from [20].

Discussing the neutrino interaction with the nucleus it is worth mentioning the main experimental challenges. Above we discussed mostly the interactions on the single nucleon. While in fact, it happens only for targets made from Hydrogen. In most of the experiments, heavier targets are used. As a result, the neutrino interactions are affected by the following nuclear effects:

- Fermi motion. The nucleons are not at rest inside the nucleus. This effect is called Fermi motion. Several models can be used to parametrize this phenomenon, e.g. Relativistic Fermi Gas (RFG) with the typical momentum depending on the nucleus. For example for Carbon $p_F \approx 220 MeV/c^2$,

- ➢ Final State Interactions (FSI). After the initial neutrino reaction, final state particles such as pions or nucleon can interact while propagating inside the nucleus. For example, the pion can be absorbed, or additional hadrons can be produced.
- ➢ collective effects. The neutrino can interact with several nucleons at the same time. The most common case is the interaction with 2 particles – 2p2h (2 particles, 2 holes). As the models of nucleons interactions are not precise enough this effect introduces relatively large uncertainty in the analysis.

The detailed description of the neutrino-nucleus interactions can be found in [20].

3 Neutrino oscillations

The neutrino oscillation phenomenon research started with the phenomenological prediction, followed by the puzzle of the small neutrino flux from the Sun. A milestone was reached recently with the robust confirmation of the effect. Many interesting discoveries were made during the oscillation analysis, e.g. non-zero neutrino mass, large mixing angles, hints for the CP–violation; many different ways to produced and study neutrinos were found. But many results are still awaiting. In this section, the modern understanding of the phenomenon will be presented as well as the latest experimental results.

3.1 Theory

The experimental confirmation that neutrino and anti-neutrino interact differently came soon after neutrino discovery. Inspired by the observed oscillations of neutral kaons $K^0 \rightarrow \overline{K^0}$ Bruno Pontecorvo proposed the oscillations $\nu \rightarrow \bar{\nu}$ [21]. For such process neutrino should have small but non-zero mass. At that time the experimental confirmation of such a hypothesis was very challenging as the effect can not be measured in the laboratory but with cosmological observations only.

After the discovery of the muon neutrino, a different hypothesis of the neutrino flavor oscillations $\nu_e \rightarrow \nu_\mu$ was proposed. Maki, Nagava and Sakata developed a theory of the 2-flavor neutrino oscillations [22].

a Phenomenology

The phenomenology of the neutrino oscillation will be described below with the quantum mechanics approach for 3 neutrino flavors. The state of the neutrino can be described either with a flavor basis $|\nu_\alpha\rangle$ or with a mass basis $|\nu_k\rangle$. The relation between them is defined by the mixing matrix $U_{\alpha k}$.

$$|\nu_\alpha\rangle = \sum_k U^*_{\alpha k} |\nu_k\rangle \tag{1.9}$$

where $\alpha = e, \mu, \tau$ and $k = 1,2,3$. Thus the mixing between the flavor and mass states of the leptons are allowed. We measure the flavor of both produced and interacted neutrino with the flavor of the accompanying charged lepton. But the propagation of the particle is defined by its mass. Within the quantum mechanics approach the Schroedinger equation will describe the changes of the system with time.

$$i\frac{d}{dt}|\nu_k(t)\rangle = \mathcal{H}|\nu_k\rangle \tag{1.10}$$

where the Hamiltonian of the system is such that

$$\mathcal{H}|\nu_k\rangle = E_k|\nu_k\rangle \tag{1.11}$$

The changes with time will be described by the evolution of the operator

$$|\nu_k(t)\rangle = e^{-iE_k t}|\nu_k\rangle \tag{1.12}$$

As was mentioned above the production and detection of the neutrino should be described by the flavor states. Modifying Equation 1.12 with Equation 1.9 we will get

$$|\nu_\alpha(t)\rangle = \sum_{\beta=e,\mu,\tau}\left(\sum_k U^*_{\alpha k}e^{-iE_k t}U_{\beta k}\right)|\nu_\beta\rangle \tag{1.13}$$

The oscillation probability is the square of the matrix element

$$\begin{aligned} P_{\nu_\alpha\to\nu_\beta} &= \left|A_{\nu_\alpha\to\nu_\beta}(t)\right|^2 = \left|\langle\nu_\beta|\nu_\alpha(t)\rangle\right|^2 \\ &= \sum_{k,j} U^*_{\alpha k}U_{\beta k}U_{\alpha j}U^*_{\beta j}e^{-i(E_k-E_j)t} \end{aligned} \tag{1.14}$$

Neutrino masses are expected to be extremely small $\leqslant 1eV$ while we want to describe the energy scale above a few keV. In this case, an ultra-relativistic approximation is applicable.

$$\begin{aligned} E_k - E_j &\simeq \frac{\Delta m^2_{kj}}{2E} \\ \Delta m^2_{kj} &\equiv m^2_k - m^2_j \end{aligned} \tag{1.15}$$

Thus the oscillation probability versus the travel distance and neutrino energy will be defined as

$$P_{\nu_\alpha\to\nu_\beta}(L,E) = \sum_{k,j} U^*_{\alpha k}U_{\beta k}U_{\alpha j}U^*_{\beta j}\exp\left(-i\frac{\Delta m^2_{kj}L}{2E}\right) \tag{1.16}$$

The neutrino oscillations can be classified into two major types:

- ➢ "disappearance" — the phenomenon of observation of less neutrino with a given flavor comparing to the produced amount
- ➢ "appearance" — the phenomenon of the observation of neutrino flavor which was not initially produced, e.g. ν_e, while only ν_μ was produced

There is a common practice to split the real and imaginary part of the oscillation probability as they will demonstrate different behavior. For example, the real part is CP conservative, while the imaginary part violates CP symmetry. The "appearance" probability will be calculated with

$$\begin{aligned} P_{\nu_\alpha\to\nu_\beta}(L,E) = \delta_{\alpha\beta} &- 4\sum_{k>j}\mathfrak{Re}\left[U^*_{\alpha k}U_{\beta k}U_{\alpha j}U^*_{\beta j}\right]\sin^2\left(\frac{\Delta m^2_{kj}L}{4E}\right) \\ &+ 2\sum_{k>j}\mathfrak{Im}\left[U^*_{\alpha k}U_{\beta k}U_{\alpha j}U^*_{\beta j}\right]\sin\left(\frac{\Delta m^2_{kj}L}{2E}\right) \end{aligned} \tag{1.17}$$

In its turn, the "disappearance" phenomenon will be described by

$$P_{\nu_\alpha\to\nu_\alpha}(L,E) = 1 - 4\sum_{k>j}|U_{\alpha k}|^2\left|U_{\alpha j}\right|^2\sin^2\left(\frac{\Delta m^2_{kj}L}{4E}\right) \tag{1.18}$$

Mixing matrix unitarity

In this section we assumed the unitarity of the mixing matrix

$$U^{\dagger}U = 1 \Longleftrightarrow \sum_{\alpha} U^{*}_{\alpha k} U_{\alpha j} = \delta_{jk} \tag{1.19}$$

This assumption came from the fundamental laws of QFT. And it indeed should be true for mixing matrix of any dimension. As will be described in chapter 2 the model with 3x3 mixing matrix is not essential for the explanation of the neutrino mass. In this case, due to the existence of other neutrino states the mixing matrix of 3 left-handed neutrino is not unitary.

$$\sum_{\alpha=e,\mu,\tau} U^{*}_{\alpha k} U_{\alpha j} \neq \delta_{jk} \tag{1.20}$$

At the moment there is no experimental confirmation of this effect.

b Mixing matrix parametrization

In this subsection, we will describe the most common parametrization of the 3-flavor neutrino mixing matrix. This matrix was named Pontecorvo-Maki-Nagava-Sakata in memory of the pioneers of the oscillation theory. In the common representation, the matrix consists of 9 elements

$$\begin{pmatrix} \nu_e \\ \nu_\mu \\ \nu_\tau \end{pmatrix} = \begin{pmatrix} U_{e1} & U_{e2} & U_{e3} \\ U_{\mu 1} & U_{\mu 2} & U_{\mu 3} \\ U_{\tau 1} & U_{\tau 2} & U_{\tau 3} \end{pmatrix} \begin{pmatrix} \nu_1 \\ \nu_2 \\ \nu_3 \end{pmatrix} \tag{1.21}$$

for easier parametrization, it is usually written as a multiplication of four matrices

$$\begin{aligned} U = &\begin{pmatrix} 1 & 0 & 0 \\ 0 & \cos\theta_{23} & \sin\theta_{23} \\ 0 & -\sin\theta_{23} & \cos\theta_{23} \end{pmatrix} \times \begin{pmatrix} \cos\theta_{13} & 0 & \sin\theta_{13} e^{-i\delta} \\ 0 & 1 & 0 \\ -\sin\theta_{13} e^{+i\delta} & 0 & \cos\theta_{13} \end{pmatrix} \times \\ &\times \begin{pmatrix} \cos\theta_{12} & \sin\theta_{12} & 0 \\ -\sin\theta_{12} & \cos\theta_{12} & 0 \\ 0 & 0 & 1 \end{pmatrix} \times \begin{pmatrix} \exp\frac{i\alpha_1}{2} & 0 & 0 \\ 0 & \exp\frac{i\alpha_2}{2} & 0 \\ 0 & & 1 \end{pmatrix} \end{aligned} \tag{1.22}$$

Such parametrization is done with three mixing angles: $\theta_{12}, \theta_{13}, \theta_{12}$ and three CP-violating phases: δ and α_1, α_2. The mixing angles define the transition from the mass state basis to the flavor state basis. The schema of these rotations is shown in Figure 1.7.

Before rewriting the equations 1.17 and 1.18 with the new parametrization, let me specify the following notations

$$c_{ij} = \cos\theta_{ij} \qquad\qquad s_{ij} = \sin\theta_{ij} \tag{1.23}$$

$$\begin{aligned} \Delta_{reactor} \equiv \Delta_{13} &= \frac{\Delta m^2_{13} L}{4E_\nu} \\ \Delta_{solar} \equiv \Delta_{21} &= \frac{\Delta m^2_{21} L}{4E_\nu} \\ \Delta_{atm} \equiv \Delta_{32} &= \frac{\Delta m^2_{32} L}{4E_\nu} \end{aligned} \tag{1.24}$$

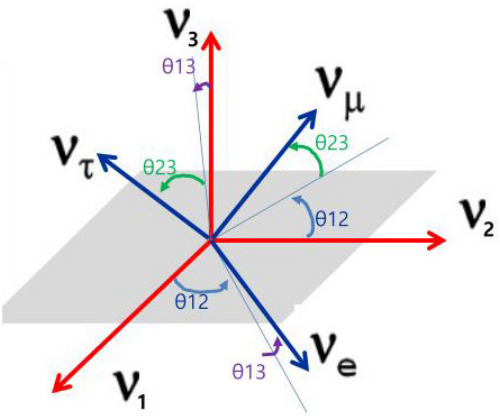

Figure 1.7: Reference rotation of the flavor basis versus the mass basis. The corresponding mixing angles are shown.

The Δ_{13}, Δ_{21} and Δ_{32} terms are referred as reactor, solar and atmospheric oscillation phases. The impact of these phases is dominating at the neutrino energies and ranges typical for the mentioned sources. The mixing angles and mass differences can be also referred based on the experiments where they are dominating. For example, θ_{13} and Δm^2_{13} are called reactor oscillation parameters. The accelerator neutrino experiments are sensitive to both reactor and atmospheric parameters.

With the defined notation the ν_μ disappearance probability can be written:

$$\begin{aligned}
P_{\nu_\mu\to\nu_\mu} =& 1-\left(c_{13}^4\sin^2 2\theta_{23}+s_{23}^2\sin^2 2\theta_{13}\right)\sin^2\Delta_{13}\\
&+\left\{c_{13}^2\left(c_{12}^2-s_{13}^2s_{23}^2\right)\sin^2 2\theta_{23}+s_{12}^2s_{23}^2\sin^2 2\theta_{13}-c_{13}\sin 2\theta_{13}\sin 2\theta_{23}\sin 2\theta_{12}\cos\delta\right\}\\
&\times\left\{\frac{1}{2}\sin 2\Delta_{21}\sin 2\Delta_{13}+2\sin^2\frac{\Delta m^2_{21}L}{4E_\nu}+2\sin\Delta_{21}\sin^2\Delta_{13}\right\}\\
&-\left\{\sin^2 2\theta_{12}\left(c_{23}^2-s_{13}^2s_{23}^2\right)^2+s_{13}^2\sin^2 2\theta_{23}\left(1-\cos\delta^2\sin^2 2\theta_{12}\right)\right.\\
&+2s_{13}\sin 2\theta_{12}\cos 2\theta_{12}s_{23}\cos 2\theta_{23}\cos\delta\\
&-\frac{1}{2}c_{13}\sin 2\theta_{13}\sin 2\theta_{23}\sin 2\theta_{12}\cos\delta s_{23}^2s_{12}^2\\
&\left.+\sin^2 2\theta_{23}c_{13}^2\left(c_{12}^2-s_{13}^2s_{12}^2\right)+s_{13}^2s_{23}^2\sin^2 2\theta_{13}\right\}\times\sin^2\Delta_{21}
\end{aligned}\tag{1.25}$$

The formula above is quite complicated but it can be simplified for each particular experiment. For example, for an accelerator experiment with a neutrino beam with energies around 1 GeV (e.g. T2K experiment) and with latest results of the parameters measurements (Table 1.1) the phases $\sin^2\Delta_{21}\approx 0$ and $\sin 2\Delta_{32}\approx 0$. As a result the probability can be rewritten as:

$$P\left(\nu_\mu\to\nu_\mu\right)\approx 1-\left(cos^4\theta_{13}\sin^2 2\theta_{23}+\sin^2 2\theta_{13}\sin^2\theta_{23}\right)\sin^2\frac{\Delta m^2_{31}L}{4E_\nu}\tag{1.26}$$

The first term in the brackets is the leading one and the following is next-to-leading. It is important to highlight that the probability will not change for the anti-neutrino disappearance ($\overline{\nu}_\mu\to\overline{\nu}_\mu$). Also, the phase δ_{CP} is severely suppressed in Equation 1.25.

The full probability for the ν_e appearance will be given by

$$
\begin{aligned}
P_{\nu_\mu \to \nu_e} =& 4c_{13}^2 s_{13}^2 s_{23}^2 \sin\Delta_{13} \\
&+8c_{13}^2 s_{12} s_{13} 2_{23} \left(c_{12} c_{23} \cos\delta - s_{12} s_{13} s_{23}\right) \cos\Delta_{32} \sin\Delta_{13} \sin\Delta_{21} \\
&-8c_{13}^2 c_{12} c_{23} s_{12} S_{13} S_{23} \sin\delta \sin\Delta_{32} \sin\Delta_{31} \sin\Delta_{21} \\
&+4s_{12}^2 c_{13}^2 \left(c_{12}^2 c_{23}^2 + s_{122}^2 s_{23}^2 s_{13}^2 - 2c_{12} c_{23} s_{12} s_{23} s_{13} \cos\delta\right) \sin^2\Delta_{21}
\end{aligned}
\tag{1.27}
$$

The probability for the anti-neutrino oscillation will be obtained with the change $\delta \to -\delta$. The second line is invariant under this transformation while the third one will be the opposite. It means that neutrino and anti–neutrino oscillate differently. This effect can be observed only in the appearance channel. The importance of such a phenomenon is described in the next subsection.

As for the muon disappearance, the appearance formula can be quite simplified. The first term is the leading one. For the accelerator experiment with 1 GeV neutrino beam the probability around the 1st oscillation maximum can be estimated with the leading and CP–odd term.

$$
P\left(\nu_\mu \to \nu_e\right) \approx \sin^2\theta_{23} \sin^2 2\theta_{13} \sin^2 \frac{\Delta m_{32}^2 L}{4E_\nu} \tag{1.28}
$$

$$
- \sin 2\theta_{12} \sin 2\theta_{13} \cos\theta_{13} \sin\delta \sin^2 \frac{\Delta m_{32}^2 L}{4E_\nu} \sin \frac{\Delta m_{21}^2 L}{4E_\nu} \tag{1.29}
$$

The visualization of the formulas above is provided in Figure 1.9 (Figure 1.8 and Figure 1.10 for initial electron and tau neutrino beam respectively). The oscillation curves for each initial state (e, μ, τ) and two E/L are shown. From such a plot, it is much easier to understand the meaning of the oscillation parameters. The mixing angles define oscillation amplitude and the mass difference defines frequency.

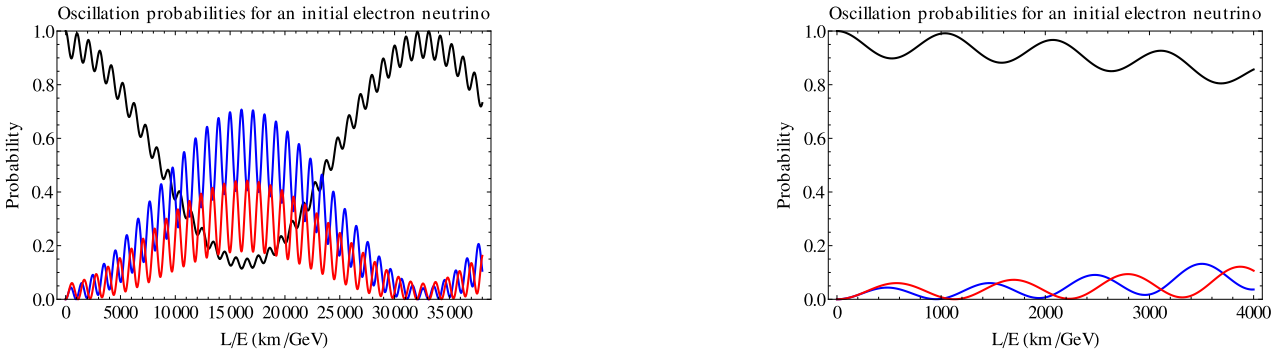

Figure 1.8: Oscillation probabilities for the initial electron neutrino state for two different L/E scales. The black line corresponds to the electron neutrino component, blue line for muon neutrino and red line for tau neutrino.

c CP violation in the neutrino oscillations

The phenomenon of the CP–violation in the neutrino oscillation is worth emphasizing. The dominance of matter over the anti-matter was observed in the Universe. Modern cosmology faces the problem of explaining such a phenomenon. The fundamental conditions for the matter-dominance generation were developed by Sakharov [23]. One of the key conditions is CP–violation. This phenomenon was observed in the quark sector [24]. But the precise measurements show that the amplitude of the CP–violation is not sufficient to generate the observed asymmetry in the Universe.

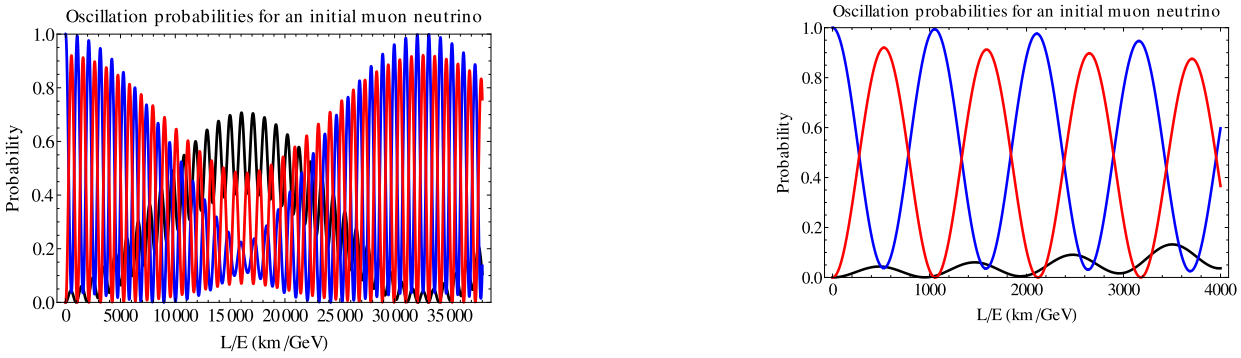

Figure 1.9: Oscillation probabilities for the initial muon neutrino state for two different L/E scales. The black line corresponds to the electron neutrino component, blue line for muon neutrino and red line for tau neutrino.

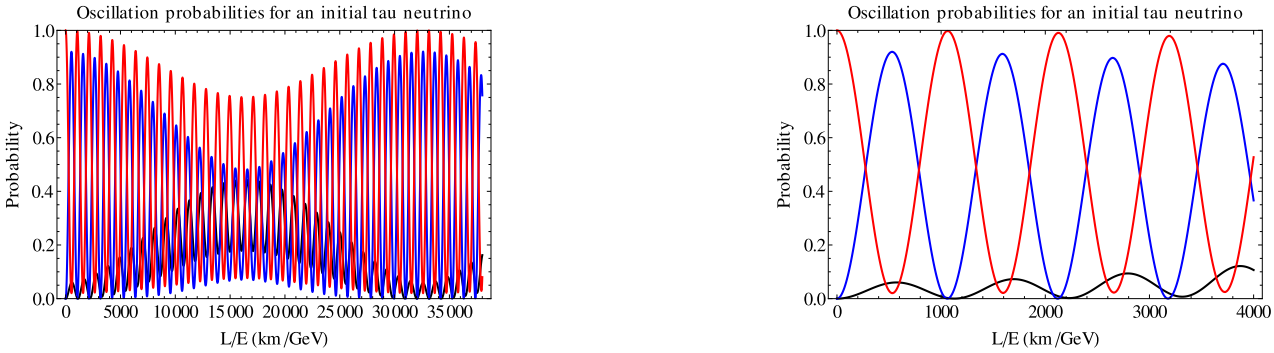

Figure 1.10: Oscillation probabilities for the initial tau neutrino state for two different L/E scales. The black line corresponds to the electron neutrino component, blue line for muon neutrino and red line for tau neutrino.

Several models propose the generation of the matter dominance through the lepton sector [25]. The non-zero CP-violation phase (Equation 1.22) is required for such an effect. From the Equation 1.25 and Equation 1.27 we can clearly see that the CP-violating phase can be measured only in the appearance channel and the total effect is scaled by the value of the mixing angle θ_{13}. According to the latest measurements, the value of the θ_{13} mixing angle is not zero that allows the direct search for the leptonic CP-violation in the experiment.

The latest results of the CP–violation measurements in the neutrino oscillations will be presented in subsection 3.2. It is important to note that the CP–violation in the mixing of three known neutrino generations is not the only essential condition to generate the matter-dominance in the early Universe. The existence of heavy neutrinos (subsection 1.4) is also necessary.

Transformations: C, P, T

In particle physics there are three important transformations: charge (C), parity (P) and time (T).

Parity inversion (P) flips the sign of the spatial coordinate $\mathcal{P}\vec{r} = -\vec{r}$. In the QFT it is described as $\mathcal{P}|\psi\rangle = c|\psi\rangle$ where c is the eigenvalue of $\mathcal{P}$. The parity violation means a process that changes the eigenvalue of the parity transformation for some system. The theoretical possibility of such a process was found by Lee and Yang [26] and proved in the Wu's experiment [27]. The asymmetry of the outgoing electrons from the Cobalt with respect to the nucleus polarization was the nice and clear proof for the effect.

Charge transformation (C) changes a particle to its anti-particle. $\mathcal{C}|\psi\rangle = \eta_C|\bar{\psi}\rangle$, where η_C is the eigenvalue of the transformation. The example of the eigenvalue non-conservation experimental observation can be found in [28].

Time transformation (T) inverses the time direction. After the discovery of the separate P and C violations, the combined symmetry breaking was looked for. As it will be a hint towards T-symmetry breaking. CP–violation was observed in the neutral kaons oscillations process [29]. Later such a process was confirmed with the direct measurements of kaon decays [30] and [31], B-meson decays [32] and [33], D-mesons [34].

It has been demonstrated that any Lorentz invariant local quantum field theory with a hermitian Hamiltonian must be invariant under CPT.

d 2–flavor oscillations

In the previous section, the modern framework of the neutrino oscillations was described. Historically the neutrino mixing theory was developed for 2 flavors. While 3-flavor oscillation probability equations are quite complicated, a 2–flavor approximation often provides sufficient accuracy and suitable for the many experiments. In this approach, the mixing matrix becomes a usual 2×2 rotation matrix

$$U = \begin{pmatrix} \cos\theta & \sin\theta \\ -\sin\theta & \cos\theta \end{pmatrix} \tag{1.30}$$

and the oscillation probabilities will be written as

$$P_{\nu_\alpha \to \nu_\alpha} = 1 - \sin^2 2\theta \sin^2 \frac{1.27\Delta m^2 L}{E_\nu} \tag{1.31}$$

$$P_{\nu_\alpha \to \nu_\beta} = \sin^2 2\theta \sin^2 \frac{1.27\Delta m^2 L}{E_\nu} \tag{1.32}$$

In this notation the neutrino energy unit is supposed to be GeV, the distance unit is km and the mass difference unit is $\mathrm{eV}^2/\mathrm{c}^4$.

e Oscillation in matter

The framework presented above, describes the oscillations in vacuum. In the case of neutrino propagation in matter, the effect will be different. Going through a medium neutrino suffers from the forward elastic scattering with electrons and nucleons. This effect is similar to the phenomenon of light propagation in the matter. A new potential which is equivalent to the refraction index needs to be taken into account. But the interaction types are slightly different for different

neutrinos. All neutrino types may scatter on electrons, protons and neutrons through the neutral current exchange. Also, electron neutrino scatters on the electrons with the charge current. The framework of the neutrino oscillations in matter was developed by Wolfenstein [35]. The mixing angle and the mass difference should be replaced by the effective ones, depending on the matter density.

Describing the neutrino propagation in matter one needs to modify the Hamiltonian function from Equation 1.11. In addition to the neutrino energy, the potential of the neutrino interactions with electron should be added.

$$H_{i,j} = \left(E_\nu + \frac{m_i^2}{2E_\nu} \right) \delta_{i,j} + U_{ei}^* U_{ej} \sqrt{2} G_F n_e \tag{1.33}$$

where U is the neutrino mixing matrix, G_F is the Fermi constant and n_e is the electron density in matter. For the simplification, I will estimate the changing of the oscillation parameters in the 2–flavor framework in matter with a constant density. In vacuum, the mixing angle and the mass difference are defined with θ and Δm^2 parameters. The new effective values in matter can be written as:

$$\sin^2 2\theta_M = \frac{\sin^2 2\theta}{\cos^2 2\theta (1-\lambda)^2 + \sin^2 2\theta} \tag{1.34}$$

$$\Delta m^2_M = \Delta m^2 \frac{\sin 2\theta}{\sin 2\theta_M} \tag{1.35}$$

$$\lambda = \frac{2\sqrt{2} G_F E_\nu n_e}{\Delta m^2 \cos 2\theta} \tag{1.36}$$

In the case of a slightly changing density of matter, there is a region where the mixing angle reaches its maximum possible value $\pi/4$ [36]. This phenomenon is called Mikheyev-Smirnov-Wolfenstein (MSW) effect.

The effect of the oscillations in matter is quite small in the reactor experiments but not negligible in accelerator experiments. The beam is traveling hundreds of kilometers through the matter. The effect is more dramatic with the longer baseline. The disappearance channel ($\nu_\mu \to \nu_\mu$) is nearly unaffected by the presence of matter, but the appearance probability ($\nu_\mu \to \nu_e$) will change. For the accelerator experiment with 1 GeV neutrino beam, the Equation 1.28 will be updated with

$$P(\nu_\mu \to \nu_e) \approx \sin^2\theta_{23} \sin^2 \theta_{13} \sin^2 \frac{\Delta m^2_{32} L}{4E_\nu} \left(1 + \frac{2a}{\Delta^2_{31}} \left(1 - 2\sin^2\theta_{13} \right) \right) \tag{1.37}$$

$$- \sin 2\theta_{12} \sin 2\theta_{13} \cos\theta_{13} \sin\delta \sin^2 \frac{\Delta m^2_{32} L}{4E_\nu} \sin \frac{\Delta^2_{21} L}{4E_\nu} \tag{1.38}$$

where $a \equiv 2\sqrt{(2)} G_F n_e E = 7.56 \times 10^{-5} eV^2 \frac{\rho}{g cm^2} \frac{E}{GeV}$. The effect for the anti–neutrino is opposite, so a will be replaced with $-a$.

3.2 Experiment overview

The experimental story of the neutrino oscillation starts from the Raymond Davis experiment in the Homestake mine (USA) [37]. The idea of the experiment was to measure the neutrino flux from the Sun core using the 400 m^3 barrel with C_2Cl_4. The inverse beta-decay reaction was used to detect neutrinos $\nu_e + {}^{37}Cl \to {}^{37}Ar + e^+$. After every 70 days of the exposition the radioactive ^{37}Ar isotopes were extracted from the reservoir, and their decays were counted. The total neutrino flux was measured as one third of the expectations from the Sun model. The observation was

confirmed later with gallium experiments GALLEX [38] and SAGE [39], and the water Cherenkov detector Kamiokande [40]. There were four possible interpretations of these results:

- ➢ The model of the Sun is incorrect and the number of the produced neutrinos is different from the predicted value
- ➢ Neutrinos are oscillating (changing flavor) on the way from the production to detection. Since only electron neutrino was used for the observations the possible transformation of the electron neutrino to muon and tau neutrino can explain the anomaly
- ➢ Neutrinos are unstable and can decay
- ➢ All the experiments had the same systematic error that was not taken into account

The last option is discarded as different targets and different analysis methods were used. The second hypothesis can be tested by detecting all kinds of neutrinos from the Sun. Such an experiment, called SNO, was performed in the Sudbury mine. Heavy water D_2O was used as a neutrino target. The benefits of usage of the deuterium are the possibility to measure both the electron neutrino flux through the charge current (CC) interactions and the total neutrino flux through the neutral current (NC) interactions. Also, the electron neutrino flux estimations can be cross-checked with the measurements of the electron neutrino elastic scattering on electrons through both CC and NC.

$$\nu_e + d \rightarrow p + p + e^+ \tag{1.39}$$
$$\nu_\alpha + d \rightarrow p + n + \nu_\alpha \qquad \alpha = e, \mu, \tau \tag{1.40}$$
$$\nu_\alpha + e^- \rightarrow \nu_\alpha + e^+ \qquad \text{though } \nu_e \text{ int. is dominating with } \sigma_{\nu_e} \approx 6\sigma_{\nu_\alpha} \tag{1.41}$$

Thus it can be determined whether there is a deficit of all kinds of neutrinos or only of electron neutrinos. It was proved that the total neutrino flux is in a perfect agreement with model of the Sun, but the electron neutrino flux is lower than expected [41]. Super-Kamiokande measured both solar and atmospheric neutrinos oscillations [42]. The discovery of the atmospheric neutrino oscillations was a breakthrough since the solar neutrino oscillation points only to the non-zero mixing angles, while the atmospheric ones point to the non-zero mass-difference between neutrino eigenstates (subsubsection 3.1.e). Thus the neutrino mass was discovered.

But even after such brilliant confirmations of the phenomena the proof of the effect with the well-known source was essential. Such confirmation came with the measurements of the reactor antineutrinos with the KamLAND experiment [43]. It was the final confirmation of the neutrino oscillation phenomena.

a Modern experimental results

After the discovery of the neutrino oscillations, many experiments study the phenomenon with different techniques.

- ➢ Solar neutrinos: experiments Borexino, Super-Kamiokande. These experiments are powerful in θ_{12} angle constraints and can also measure Δm^2_{21} and θ_{13}
- ➢ Reactor experiments: KamLAND [43], RENO [44], Double Chooz [45], Daya Bay [46]. These experiments study the electron anti-neutrino disappearance and are sensitive to the θ_{12}, Δm^2_{21} (KamLAND) and θ_{13}, Δm^2_{32} (RENO, Double Chooz, Daya Bay).

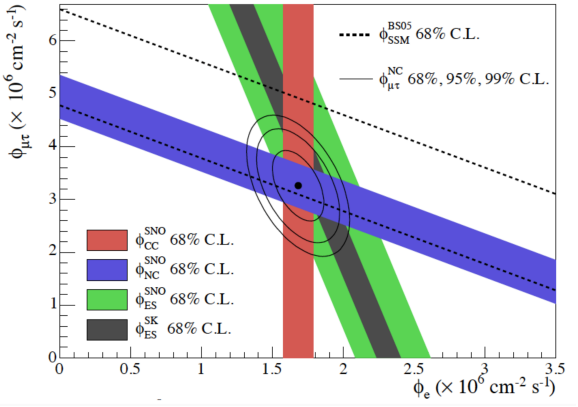

Figure 1.11: The comparison of the fluxes ν_e and $\nu_{\mu,\tau}$ based on the measurements by SNO and Super-Kamiokande.

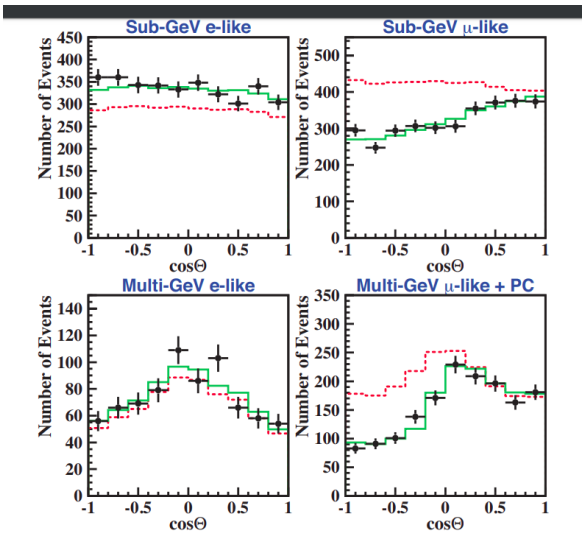

Figure 1.12: The angular distribution of the muon and electron events in the Super-Kamiokande. The dotted histograms represented the simulation results w/o the neutrino oscillations and solid histograms corresponds to the best fit with oscillation hypothesis.

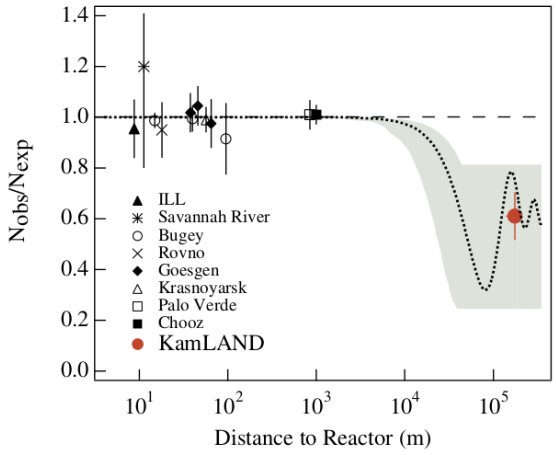

Figure 1.13: The ratio of the observed and expected neutrino flux from reactors. Figure from [43].

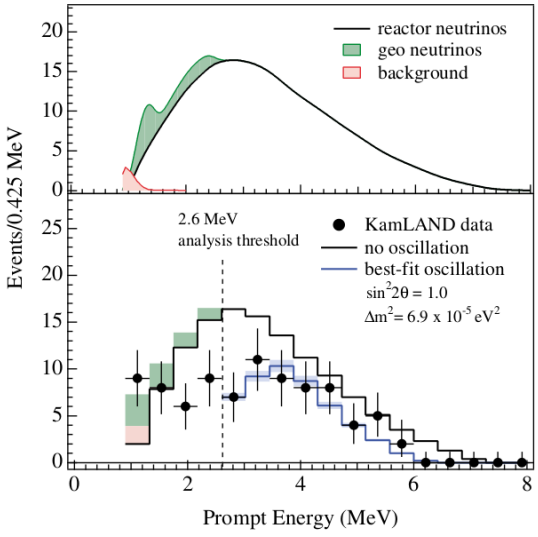

Figure 1.14: The energy spectrum of the neutrinos observed in the KamLAND experiment comparing to the expectations w/o neutrino oscillations. Figure from [43].

- Accelerator experiments: K2K [47], MINOS [48], T2K [49], NOvA [50]. These experiments started with studying muon (anti-)neutrino disappearance and MINOS, T2K and NOvA managed to observe the electron neutrino appearance, OPERA observed the tau neutrino appearance [51]. Thus these experiments are very precise in measurements of the θ_{23} angle and sensitive to the CP–violation. They can also measure θ_{13} and Δm^2_{32} parameters
- Atmospheric and cosmology neutrinos: Super-Kamiokande [52], IceCube [53]. They can probe interesting processes in cosmology and also measure θ_{23}, θ_{13}, Δm^2_{32} and δ_{CP} parameters, but less precisely comparing to the experiments mentioned above

So far the neutrino oscillation parameters are measured very precisely (Table 1.1), but there is still room for the improvements.

	Normal Order		Inverse Order	
param	best fit value	3σrange	best fit value	3σrange
$\frac{\sin^2\theta_{12}}{10^{-1}}$	3.20	2.73→3.79	3.20	2.73→3.79
$\theta_{12}/^\circ$	34.5	31.5→38.0	34.5	31.5→38.0
$\frac{\sin^2\theta_{23}}{10^{-1}}$	5.47	4.45→5.99	5.51	4.53→5.98
$\theta_{23}/^\circ$	47.7	41.8→50.7	47.9	42.3→50.7
$\frac{\sin^2\theta_{13}}{10^{-2}}$	2.160	1.96→2.41	2.220	1.99→2.44
$\theta_{13}/^\circ$	8.45	8.0→8.9	8.53	8.1→9.0
$\delta_{CP}/^\circ$	218	157→349	281	202→349
$\frac{\delta m^2_{21}}{10^{-5}eV^2}$	7.55	7.05→8.24	7.55	7.05→8.24
$\frac{\delta m^2_{32}}{10^{-3}eV^2}$	2.42	2.334→8.24	-2.50	-2.59→-2.39

Table 1.1: Summary of the neutrino oscillation parameters measurements from [24] for both normal and inverse neutrino mass order.

The visual representation of the neutrino oscillation parameters constrains is presented in Figure 1.15.

The effect of the CP–violation is a subject of research nowadays. The accelerator experiments are more sensitive to this phenomenon. Both T2K and NOvA put their limits on the possible δ_{CP} values. The constraints are presented in Figure 1.16. The most recent T2K results providing 3σ confidence interval on the δ_{CP} value are published in [55].

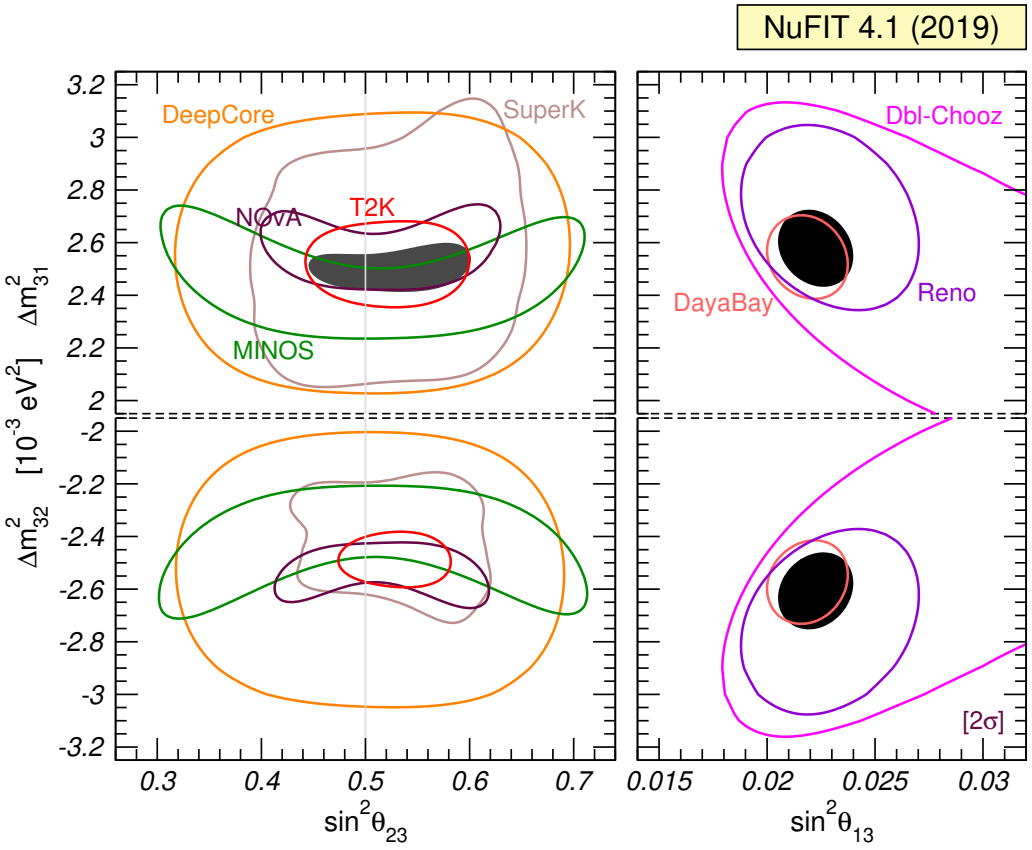

Figure 1.15: The global fit of the neutrino oscillation parameters and results from the particular experiments used in the fit. The upper figures corresponds to the normal mass order and lower figures for inverted mass order. The figure from [54].

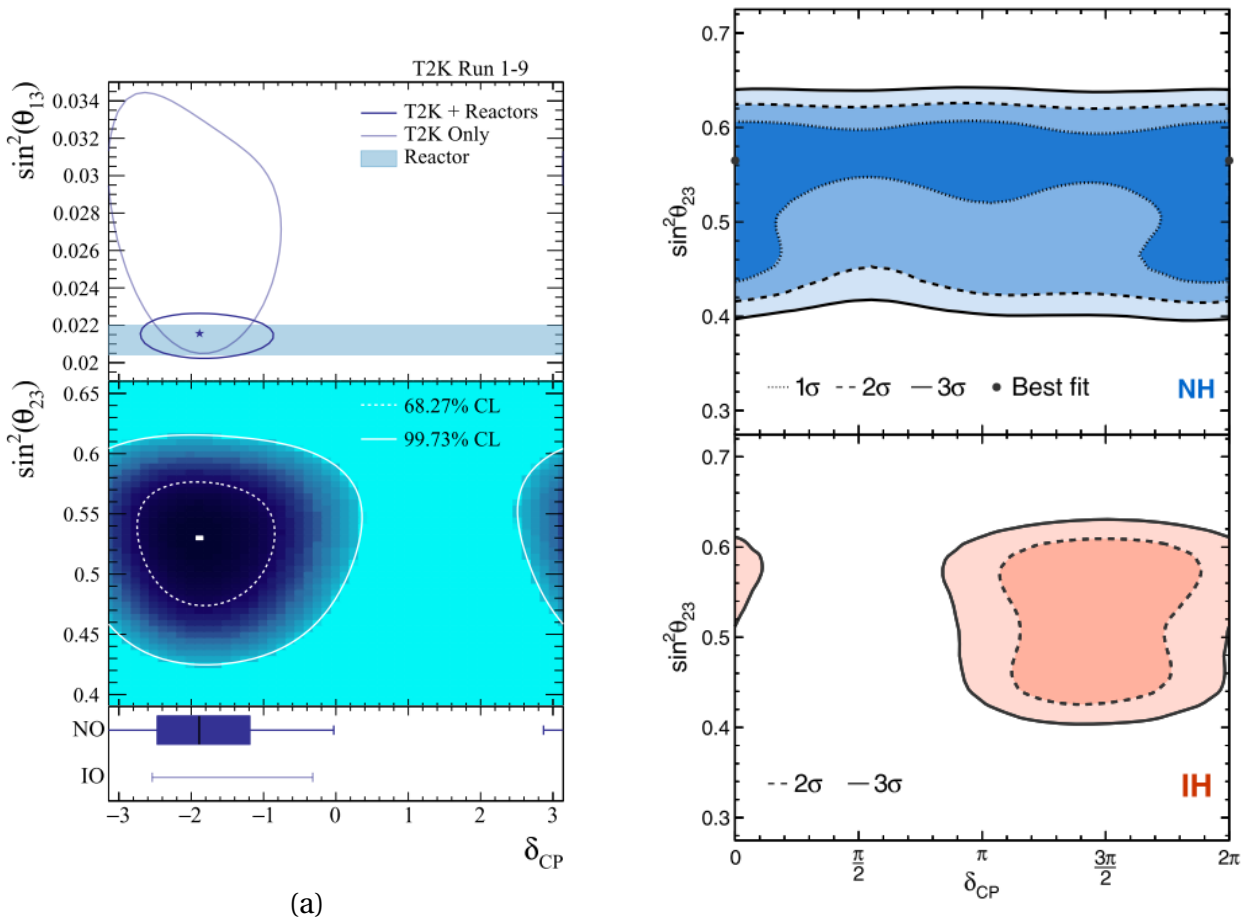

(a) (b)

Figure 1.16: Recent results of the CP–violation phase constraints in the T2K experiment (a)[55] and NOvA experiment (b)[50].

CHAPTER 2

NEUTRINO MASS

As presented in the section 3 of chapter 1 the existence of the neutrino oscillation phenomenon explicitly indicates a non-zero mass difference between neutrino eigenstates. Thus at least two of three eigenstates should be massive. In the Standard Model of particle physics neutrinos are massless (subsection 1.3 of chapter 1). A theory explaining the mass origin of the neutrino is required.

The easiest solution is to try to implement the same process which gives mass to all other particles in the SM — Higgs mechanism [56] (also called Englert-Brout-Higgs-Guralnik-Hagen-Kibble mechanism for all contributed scientists). There are several problems in this approach:

- the scale of the neutrino mass is very different from the other particles in the SM. The neutrino masses are less than 1 eV [57], while the other particles masses are $m \gtrsim 0.5$ MeV, which gives a difference of at least 6 orders of magnitude. It can be even larger up to 8 orders in the case of minimum possible neutrino mass. It is hard to believe that the same mechanism is responsible for the generation of mass at so different scales.
- as described in the subsection 1.3 only left-handed neutrinos and right-handed anti-neutrinos were observed. However for the Higgs mechanism both left and right-handed particles are required.

That leads to the fact that we need to implement some new mechanisms or/and new fundamental particles to explain the origin of the neutrino masses.

1 Theory

In this section, the main models of neutrino mass generation will be overviewed. The first idea is to describe the neutrino mass in the same way as masses of other fermions — with Higgs mechanism. All the other fermions are described as a solution of the Dirac equation, thus referred to as a Dirac fermions. In the general solution of this equation a particle is different from its anti-particle. But in this assumption for the neutrino, the problem of the neutrino helicity rises. Since only left-handed neutrinos have been observed, but the theoretical framework requires both left and right-handed particles.

Another approach is to use a specific solution of the Dirac equation. Majorana proposed the fermion that is invariant under particle/anti–particle symmetry. Neutrino is the only candidate to

be such a particle as it is the only neutral fundamental fermion. This theory gives an interesting opportunity to describe the neutrino mass and also open the door for the new physics beyond the Standard Model.

However, the most interesting hypothesis is mixing Dirac and Majorana theories. An example of such a hypothesis is a "see–saw" mechanism. It provides a natural explanation of the tiny neutrino mass through the mixing with the heavier partner. The Higgs mechanism is used at the same scale as in the SM (GeV) and new physics beyond the SM is implemented. Nevertheless, the new exotics particles appear only at the extremely large energy scale. That explains why they have not been observed.

1.1 Dirac mass term

In the Standard Model of particle physics, the masses of all the particles are generated with the Higgs mechanism. The Higgs-lepton Yukawa Lagrangian provides an explanation for the masses for the charged leptons

$$\mathcal{L}_{H,L} = -\sum_{\alpha,\beta=e,\mu,\tau} Y'^{\ell}_{\alpha\beta}\overline{L'_{\alpha L}}\Phi\ell'_{\beta R} + h.c \tag{2.1}$$

Applying the same approach for the neutrino mass generation we will get the Lagrangian

$$\begin{aligned}\mathcal{L} &= -\sum_{\alpha\beta=e,\mu,\tau} \bar{\nu}_{L,\alpha}(m_D)_{\alpha\beta}\nu_{R,\beta} + h.c. = \\ &= -\overline{\nu_L} m_D \nu_R + h.c.\end{aligned} \tag{2.2}$$

where m_D is a 3x3 complex matrix, corresponding to 3 neutrino generations, ν_L and ν_R are a left–handed and right–handed neutrino. It can be diagonalized $m_D = U^{\dagger} m V$, where U and V are unitary and $m_i\delta_{ik}$, $m_i > 0$. After diagonalization, we can separate

$$\begin{aligned}\nu_{\alpha L} &= \sum_i U_{\alpha i}\nu_{iL} \\ \nu_{\alpha R} &= \sum_i V_{\alpha i}\nu_{iR}\end{aligned} \tag{2.3}$$

and define $\nu \equiv \nu_L + \nu_R$. Thus the Dirac mass term will be expressed as

$$\mathcal{L}^D_{mass} = -\sum_i m_i \overline{\nu_i}\nu_i \tag{2.4}$$

where ν_i, $i = 1,2,3$ are neutrino mass eigenstates and $\nu_{\alpha L}$ are left-handed neutrino flavor eigenstate. Their mixing is defined with PMNS matrix (Equation 1.9). The equations above implement the right-handed neutrino ν_R that is essential for the Higgs mechanism, but has not been observed in the experiments. It happens because the weak interaction allows only left-handed neutrino to interact with matter.

1.2 Majorana mass term

The Dirac fermion is the most general solution of the Dirac equation. But there is an interesting particular solution. A Majorana fermion satisfies Dirac equation under the assumption that this particle is the same as its anti–particle ($\psi = \psi^C$). Neutrino is the only candidate to be a Majorana fermion as it is the only neutral fundamental fermion. The charged fermion obviously can not satisfy such a condition because particle and anti–particle carry an opposite electric charge.

Whether neutrino is a Majorana fermion is still an open question, but such a hypothesis provides interesting consequences. To generate the mass for such a particle we need only one chiral fermion field. As neutrino is left-handed let us denote is as ν_L. To write the mass term for this specific case we need to use ν_L alone. Modifying Equation 2.4

$$\mathcal{L}^D_{mass} = -m\overline{\nu}\nu = -m\left(\overline{\nu_R}\nu_L + \overline{\nu_L}\nu_R\right) = -m\overline{\nu_R}\nu_L + h.c. \tag{2.5}$$

Here ν_R should be replaced with the right-handed function of the ν_L. It is the charge conjugated field

$$\nu^C_L = C\overline{\nu_L}^T \tag{2.6}$$

Thus the Majorana mass term can be expressed as

$$\mathcal{L}^M_{mass} = -\frac{1}{2}m\overline{\nu^C_L}\nu_L + h.c. \tag{2.7}$$

The Majorana mass term provides an interesting mechanism for the generation of the neutrino mass. But it implements also physics beyond the SM. The lepton number is invariant in the SM because of a global U(1) symmetry. With the Majorana model, there is no such symmetry anymore. This leads to the processes where the lepton number is violated, e.g. neutrino-less double beta decay.

1.3 Mixing Dirac and Majorana terms

The most interesting approach is a combination of both Dirac and Majorana terms. In this case, the model is very flexible and can provide an explanation of the neutrino masses with minimum extension of the Standard Model. The mass term will be written with

$$\mathcal{L}^{D+M}_{mass} = \mathcal{L}^D_{mass} + \mathcal{L}^R_{mass} + \mathcal{L}^L_{mass} \tag{2.8}$$

where

$$\mathcal{L}^L_{mass} = \frac{1}{2}\sum_{\alpha,\beta}\nu'^T_{\alpha L}C^\dagger M^L_{\alpha\beta}\nu'_{\beta L} + h.c. \tag{2.9}$$

$$\mathcal{L}^R_{mass} = \frac{1}{2}\sum_{s,s'}\nu^T_{sR}C^\dagger M^R_{ss'}\nu'_{s'R} + h.c. \tag{2.10}$$

$$\mathcal{L}^D_{mass} = -\sum_{s=s_1,\ldots,s_{N_s}}\sum\alpha\overline{\nu}_{sR}M^D_{ss'}\nu'_{\alpha L} + h.c. \tag{2.11}$$

In the equations above the Greek indexes, as usual, corresponds to the flavor states, L and R illustrate the chirality and s_i describes the sterile neutrino types. Thus the matrix M^L will be symmetric 3x3, M^R — symmetric $N_s \times N_s$ and M^D — $N_s \times 3$. The mass matrix for combination of these three components will be written with

$$M^{D+M} \equiv \begin{pmatrix} M^L & M^{D\,T} \\ M^D & M^R \end{pmatrix} \tag{2.12}$$

The mass states will be given by

$$\nu^C_R \equiv \begin{pmatrix} \nu^C_{s_1R} \\ \vdots \\ \nu^C_{s_{N_S}R} \end{pmatrix} \qquad N'_L \equiv \begin{pmatrix} \nu'_L \\ \nu^C_R \end{pmatrix} \tag{2.13}$$

And the mass term Equation 2.8 with new notations will be rewritten as

$$\mathcal{L}_{mass}^{D+M} = \frac{1}{2} N'^{T} C^{\dagger} M^{D+M} N'_{L} + h.c. \tag{2.14}$$

There are different ways to combine Dirac and Majorana terms. With different initial assumptions, the theory result can be quite different. Here there are the main hypotheses. The notation m_D describes the Dirac mass, m_L, m_R describe Majorana mass and the $m_{1,2}$ describes the mass eigenstates observable in the experiment.

- ➢ Maximal mixing. $m_L = m_R$, $m_{2,1} = m_L \pm m_D$, $\Delta m^2 = m_2^2 - m_1^2 = 4 m_L m_D$
- ➢ Dirac limit. $m_L = m_R = 0$, $m_{2,1} = \pm m_D$
- ➢ Pseudo-Dirac neutrinos. $|m_L|, m_R \ll m_D$, $m_{2,1} \approx \frac{m_L + m_R}{2} \pm m_D$
- ➢ See–saw mechanism. $m_D \ll m_R$, $m_L = 0$

a See–saw mechanism

Among all of the theories with Dirac and Majorana mixing the see–saw mechanism seems to be the most promising. Here are the main advantages of this hypothesis:

- ➢ The gauge symmetry is not broken as $m_L = 0$
- ➢ The only "exotic" part (SM extension) is the implementation of m_R
- ➢ The Dirac mass can be easily explained with the Higgs method as m_D is close to the mass of the SM particles
- ➢ Tiny mass of the observed neutrino eigenstates is understood as m_D is scaled with m_R

So, how can we explain the fact that observed neutrino mass is so small? m_D is generated with a Higgs mechanism and can be at the GeV scale. m_R is an exotic part of the theory. As it is a Majorana term it will violate the lepton number. But it will take place only at extremely high energies, much higher than the electroweak scale. The observed neutrino mass at first order will be given by the mixing:

$$m_1 \approx \frac{m_D^2}{m_R} \ll m_D \qquad\qquad m_2 \approx m_R \gg m_D \tag{2.15}$$

and the mixing angle will be given by

$$\theta \approx \frac{m_D}{m_R} \ll 1 \tag{2.16}$$

For example, imagine the Dirac mass is fixed at $m_D = 170 GeV$ and observed neutrino mass $m_1 = 5 \times 10^{-2} eV$, then the Majorana mass will be at an extremely high energy scale $M_R \approx 10^{15} GeV$.

1.4 Heavy Neutral Lepton

In the previous section, it was proven that an extension of the SM is necessary to explain the neutrino mass. The see–saw mechanism is a minimal extension that can provide such an explanation. But there is no hint for the mass scale of the proposed new particles.

a Light sterile neutrino

The special case is the light sterile neutrino with $m \approx 1eV$. To meet the agreement with the LEP results of the Z boson decay measurements (subsubsection 1.3.a) the 4th neutrino should not couple with the Z boson. That's why such a particle is notated as a "sterile" neutrino. Also, their mixing with the other three active neutrinos should be quite small $|U_{e4},|, \left|U_{\mu 4},\right|, |U_{\tau 4},| \ll |U_{s4},|$. In most of the neutrino oscillation experiments 3-flavor neutrino model describes the observation quite well. However, in some experiments, an anomaly that can be explained with the 4th neutrino with $\Delta m^2_{41} \approx 1eV$ was found. The first such an experiment was LSND [58], followed by MiniBooNE [59], that inspired the short-baseline neutrino oscillation research program. Some anomalies have also been found in the experiments with neutrinos from reactors and with solar neutrinos in the gallium experiments. However, there is no final conclusion if it is a significant observation or the result of the unaccounted systematic error. Many experiments are running now in order to figure out the nature of the phenomenon. We can generally divide them in the short-baseline accelerator experiments: MicroBooNE, Short Baseline Program in Fermilab, and others, and reactor experiments: NEOS [60], DANSS [61], STEREO [62], PROSPECT [63], NEUTRINO-4 [64], SoLid, and others.

More information about the light sterile neutrino can be found in [65].

b Neutrino Minimal Standard Model (νMSM)

A minimal extension of the SM introducing the neutrino mass explanation was developed by Asaka and Shaposhnikov [66]. The existence of three heavy neutrinos N_1, N_2, N_3 was proposed. It is worth mentioning that there are several extensions of the SM with different numbers of additional particles. νMSM is highlighted because of its minimalism, which has always been an advantage of the physics theory.

Long living (comparing to the Universe's age) N_1 with a mass around keV can be responsible for the phenomenon of the Dark Matter. It can be produced in the early Universe and can still exist. N_1 can explain the gravitational anomalies such as galaxies mass and galaxy rotation speed.

N_2 and N_3 are two nearly degenerated fermions with masses in the range $140MeV < M < 80GeV$. The model contains 6 CP-violating phases that allow the violation of the lepton number L. Such an asymmetry can be transferred to the active leptons through the mixing with the active neutrino. With the help of the sphaleron mechanism, the violation of the lepton number can cause the violation of the baryon number B, but conserving the $B-L$. Hence the model can explain the observed baryon asymmetry of the Universe [67].

2 Experiments

Despite the Standard Model assumption about the massless neutrino nature, there were several attempts to measure its mass. After the confirmation of the fact that neutrino has mass from the neutrino oscillation phenomenon (section 3), these measurements became essential.

2.1 Neutrino mass measurements

In this section, both direct and indirect methods of the neutrino mass measurements will be overviewed. The latest experimental results will be presented.

a Beta decay

The straightforward approach for the neutrino mass measurements is a search for the effect of the nonzero neutrino mass in the beta decay spectrum. One needs to measure the energy of outgoing electrons and look at the far end of the distribution. The variation of the neutrino mass changes dramatically the energy spectrum in this particular region. For the electron source, a deuterium or a tritium isotope is usually chosen. The main technological issues are to perform extremely precise measurements of the electron energy. The most accurate limits obtained with this method for a long time belonged to Mainz [68] and Troitsk [69] experiments. Recently KATRIN experiment announced more precise neutrino mass limits $m_\nu < 1.1eV$ with 90%C.L. [57].

It is important to notice what is the "neutrino mass" m_ν that is measured in the beta decay. Because of the lepton mixing the mass eigenstates can not be measured independently, but only in the superposition.

$$m_\nu \equiv m_\beta \equiv \sqrt{\sum_i |U_{ei}|^2 m_i^2} \tag{2.17}$$

More details about the neutrino mixing were presented in section 3.

b Neutrinoless double beta decay

If the neutrino has a Majorana nature, it is possible to measure the $m_{\beta\beta}$ in the process of the neutrinoless double beta decay. The Feynman diagram of the process is shown in Figure 2.1.

$$m_{\beta\beta} = \sum_i U_{ei}^2 m_i \tag{2.18}$$

All the $0\nu\beta\beta$ experiments are putting the limits on the $m_{\beta\beta}$ value. The most precise result was obtained by KamLAND-Zen experiment $m_{\beta\beta} < (61-165)meV$ 90% C.L. [70]. Relatively large uncertainties come from the poor knowledge about nuclear matrix elements. The summary of all the constraints from different experiments is shown in Figure 2.2. One should keep in mind that successful measurement is possible only in the case of Majorana neutrino nature.

c Cosmology

Cosmology provides different possibilities for neutrino mass measurements. One of the earliest attempts was done based on the timing measurements of the neutrinos from SN1987 — the earliest and so far the only observation of the neutrino from the supernova collapse.

The other method is a precise observation of the evolution of the early Universe. The combination of the cosmic microwave background (CMB) and baryon acoustic oscillation provides the limit on the neutrino mass $m_\nu = \sum_i m_{\nu_i} < 0.12eV$ 90% C.L. [71].

The main problem of such analyses is a dependence on the theoretical models such as supernova collapse or early Universe evolution.

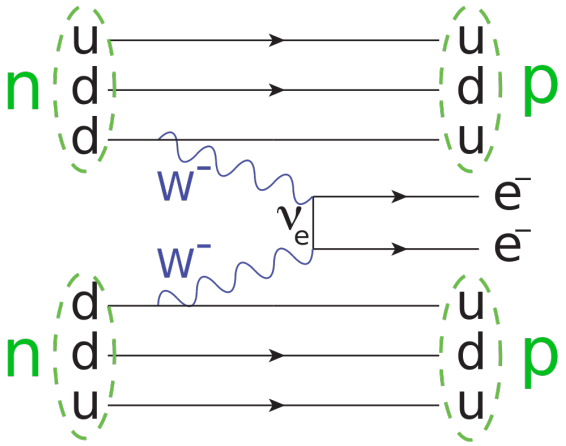

Figure 2.1: Feynman diagram for the neutrinoless double beta decay

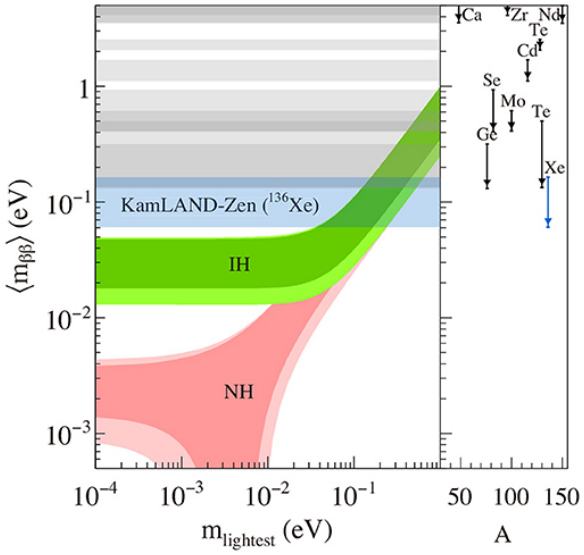

Figure 2.2: The current limits on the $m_{\beta\beta}$ and the allowed regions for both normal and inverse mass ordering.

2.2 Search for Heavy Neutral Lepton

As mentioned in the subsection 1.4, there are several models proposing the existence of the Heavy Neutral Lepton (HNL). Various analyses in different experiments were performed to find the HNL. In this section, we will describe the search for the HNL in the context of the νMSM framework, but the results can be applied for other models introducing the heavy neutrino via mixing with the active one.

a HNL at keV scale

The lightest HNL at the keV scale can be detected through its decays $N_1 \to \nu\nu\overline{\nu}$ and $N_1 \to \gamma\nu$. While the first reaction is undetectable from the practical point of view, the latter will produce the observable X-rays. There are several analyses searching for the X-ray signal from the cosmological object (e.g. Galaxy core, other galaxies, etc.) [72, 73]. The latest results are presented in Figure 2.3.

So far the region is almost excluded but there is still a possibility to find N_1 from νMSM [74].

b HNL at GeV scale

This is a scale where we expect to find the heavy neutrinos N_2 and N_3 from the νMSM. Its mass allowed the direct search through the decay into SM particles. The work [75] provides a detailed overview of the HNL production and the decay modes. The main production mode is a meson two-body decay.

$$H \to \ell + N \tag{2.19}$$

Thus we can expect the HNL production in the decays of π, K, D, B and heavier mesons. The HNL is unstable hence the decay channel into the active lepton is open. The decay modes to the lighter

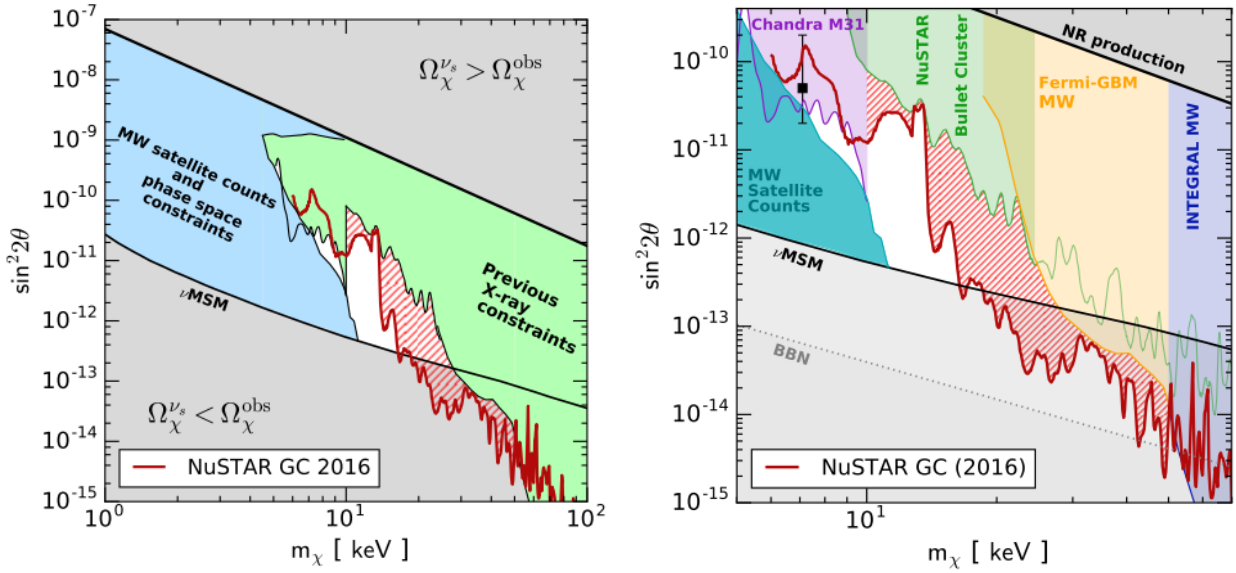

(a) (b)

Figure 2.3: The constrains on the mixing angle of the N_1 with respect to its mass: (a) the general figure and (b) the detailed view at the region of interest. Figure provided by [73].

HNL $N_{1,2} \to N_1 + ...$ are strongly suppressed. Thus the most probable modes are

$$N \to \overline{\nu}\nu\nu,\ \mu e\nu,\ \pi^0\nu,\ \pi e,\ \mu\mu\nu,\ \pi\mu,\ Ke,\ K\mu,\ \eta\nu,\ \rho\nu, ... \tag{2.20}$$

The two-body decay modes are more probable over the three-body decay modes, hence they are preferable for the direct search in the experiment. Also, the channels with at least two charged particles in the final state are much easier for the observation. Thus 3ν and $\pi^0\nu$ modes are often not considered in the analysis due to an extremely hard detection.

In general, the HNL search can be separated into several categories:

- analysis of the meson decay. The effect is proportional to $|U|^2$. For example, E949 and NA62 explored the decay $K^+ \to \mu^+ N$. Thus the region of the HNL mass $M_{HNL} < m_K - m_\mu = 388 MeV/c^2$ can be explored.
- direct search for the HNL decay. For example, PS191 experiment searched for the HNL produced with $\pi/K \to eN$ and $\pi/K \to \mu N$ and further decayed into $e\pi$, $\mu\pi$, $\mu e\nu$.
- a direct search can be performed in the collider experiments. DELPHI and LHCb looked for the HNL decays, produced in the Z boson decay.
- joint search for HNL production and decay. For example, ATLAS and CMS performed the search for the two leptons with the same charge: one lepton along with HNL production the other comes from its decay. Such a process is possible only in the case of the Majorana nature of the HNL.

So far, no evidence of the HNL existence was found and upper limits on the mixing angles were set. The latest results from all the experiments can be found in Figure 2.4, Figure 2.5 and Figure 2.6.

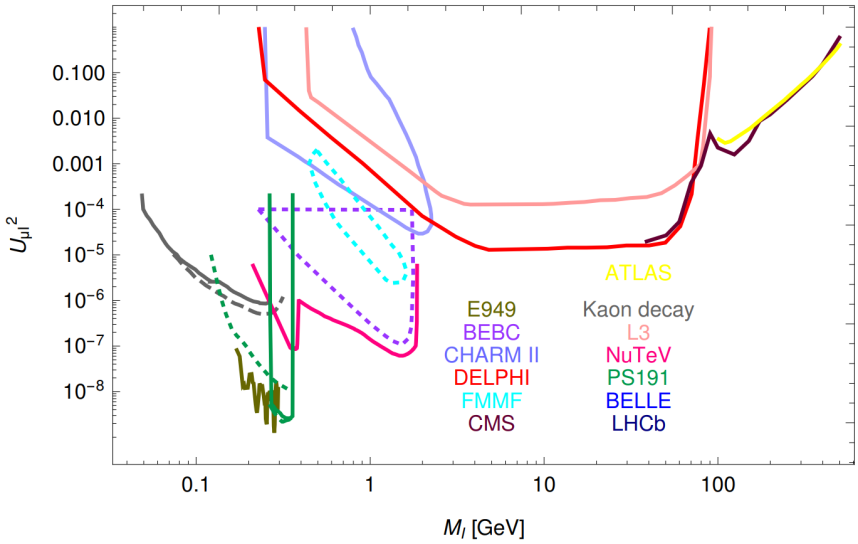

Figure 2.4: Constraints on the mixing matrix element $|U_\mu|^2$ from the experiments CMS [76], DELPHI [77], L3 [78], LHCb [79], BELLE [80], BEBC [81], FMMF [82], E949 [83], PIENU [84], TRIUMF/TINA [85], PS191 [86], CHARMII [87], NuTeV [88], NA3 [89] and kaon decays in [90]. The plot is similar to Ref. [91], some comments on the interpretation can be found in that article and references therein.

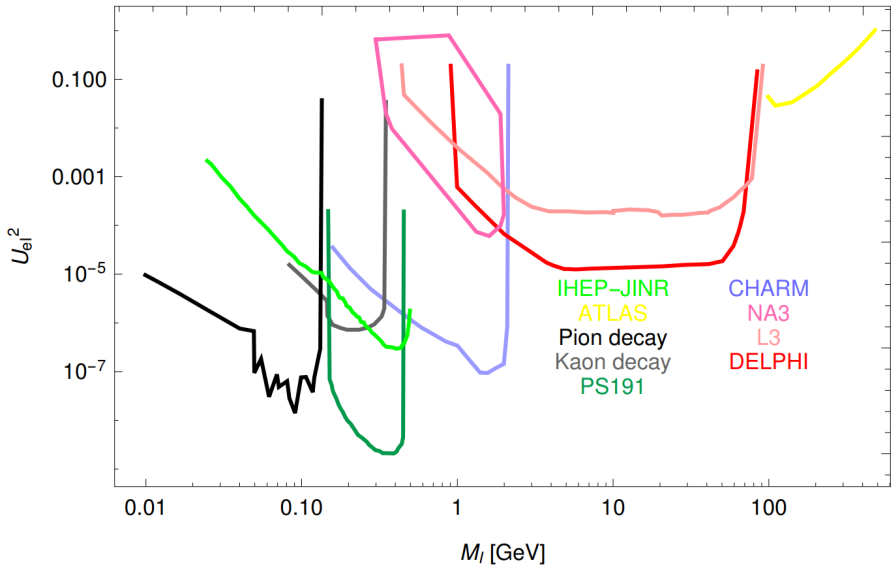

Figure 2.5: Constraints on the mixing matrix element $|U_e|^2$ from the experiments DELPHI [77], L3 [78], PIENU [84], TRIUMF/TINA [85], PS191 [86], CHARM [92], NA3 [89], IHEP-JINR [93] and kaon decays. The plot is similar to Ref. [91], some comments on the interpretation can be found in that article and references therein.

3 Prospects of the neutrino physics

In the introduction part, it was highlighted several times that we still have several open questions in the neutrino physics. The most important among them are:

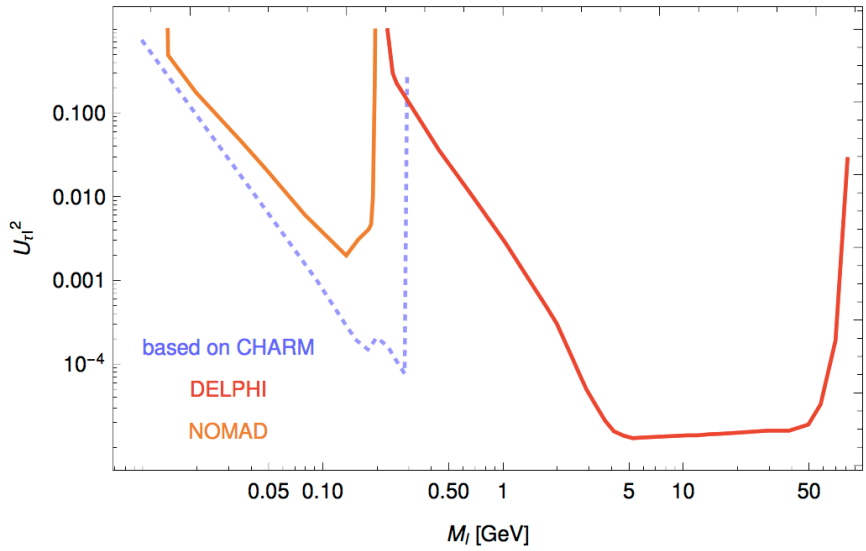

Figure 2.6: Constraints on the mixing matrix element $|U_\tau|^2$ from the experiments CHARM [94], NOMAD [95], DELPHI [77] and L3 [78], some comments on the interpretation can be found in that article and references therein.

- CP-violation in the lepton sector. Does it exist?
- Is neutrino a Dirac or a Majorana fermion?
- What is the neutrino mass order? $m_1 < m_2 < m_3$ or $m_3 < m_1 < m_2$?
- What are the absolute values of the neutrino mass?
- What is the nature of the neutrino masses?
- What are the other neutrinos except known 3 generations?
- Can neutrino (or heavy neutrino) solve the problems of modern cosmology: Dark Matter existence and the matter-dominance in the Universe?

Answer for any of them will be a remarkable step forward in our understanding of fundamental physics.

4 Future neutrino experiments

Several experiments are working on solving the problems above. Many proposals were made about future experiments.

The ongoing long-baseline accelerator experiments T2K and NOvA already observed a hint for the maximal CP-violation in the neutrino oscillations. The T2K experiment will be able to reach 3σ sensitivity for some values of the δ_{CP} [96]. The future experiments Hyper-Kamiokande [97] and DUNE [98] are proposed to reach 5σ sensitivity for almost all the values of the δ_{CP}.

The JUNO experiment [99] is going to perform the extremely precise measurements of the reactor anti–neutrino oscillations. With the help of these observations the neutrino mass order can be determined.

Several experiments are looking for the neutrino-less double-beta decay. They are looking for small signal in the low background environment. Different isotopes are used as a supposed source

of the $0\nu\beta\beta$ decay. KamLAND-ZEN uses the ^{136}Xe isotope, GERDA [100] uses ^{76}Ge, CUORE [101] ^{82}Se and SNO+ ^{130}Te. Any of the positive results will indicate the Majorana nature of the neutrino.

Astrophysics experiments are studying neutrino from the sources outside of the Solar System. Usually, they are using Cherenkov light from the lepton or other particles produced in the neutrino interactions. The probability of such events is relatively low, so the fiducial volume is extended as much as possible. But the energy of such events is quite high. The examples of such experiments are IceCube [102] using 1 km^3 of ice at the South Pole; Antares — the first sea neutrino telescope; proposed experiment KM3NeT [103] is a one cubic kilometer neutrino telescope in the Meridian sea. These experiments can detect the neutrinos from the supernova core or active galaxy core that makes them very powerful for testing the cosmological models.

The very important class of the experiments are searching for sterile neutrino in the reactor experiments. Some anomalies, e.g. lack of the neutrino events in the short-baseline reactor experiments or Gallium experiments can be explained with the implementation of the 4th neutrino flavor. The extremely short-baseline reactor experiments are very sensitive to its existence. Some of them are able to change the baseline with the movable detector. The oscillations are modulated by the ratio of the energy to distance E/L. With the unmovable detector, the effect is measured only varying the energy, hence the very precise knowledge of the reactor anti–neutrino energy spectrum is essential. With the movable detector, this source of uncertainty is severely suppressed. The examples of the experiments are: NEOS [60], DANSS [61], STEREO [62], PROSPECT [63], NEUTRINO-4 [64], SoLid. These experiments will give a clear answer about the existence of the sterile neutrino in the near future.

In the context of current thesis the future experiments dedicated to the search of the heavy neutrino are worth mentioning. Any experiment with the intense meson production can be used for this purpose. Thus DUNE [98], Hyper-Kamiokande [97], FCC [104] projects will be able to perform HNL search. But there is a proposal of the standalone experiment aimed only for the heavy neutrino search. SHiP (Search for Hidden Particles) [105] will study exclusively decays of the HNL in the vacuum vessel. The experiment will use 400 GeV/c proton beam for the production of the D and B mesons. The wide range of the heavy neutrino masses will be explored with this setup.

CHAPTER 3

THE T2K EXPERIMENT

The T2K (Tokai to Kamioka) is a long-baseline accelerator neutrino experiment. Its main purpose is precise measurements of the neutrino oscillation parameters. T2K is a continuation of the successful history of the previous accelerator experiments: KEK, MINOS, etc. At the beginning of the T2K era, the main challenge was the measurements of the θ_{13} mixing angle. Only the upper limit on its value was set at that moment and $\theta_{13} = 0$ was possible. The value of this angle is important as the amplitude of the CP–violation (subsubsection 3.1.c of chapter 1) is scaled with θ_{13} angle. If θ_{13} is equal to zero no CP–violation effect can be observed. Thus θ_{13} angle measurements became the main goal at the beginning of the T2K era.

The θ_{13} angle can be measured in both appearance ($\nu_\alpha \to \nu_\beta$) and disappearance ($\nu_\alpha \to \nu_\alpha$) channels. The reactor experiments are very powerful in the analysis of the $\overline{\nu}_e \to \overline{\nu}_e$ disappearance process and thus can measure θ_{13} angle precisely. But the CP–violation effect can take place only in the appearance channel (subsubsection 3.1.c of chapter 1). The $\nu_e \to \nu_\mu$ channel is extremely challenging from the experimental point of view. There is no easy way to create an intense pure beam of high energetic electron neutrinos. On the contrary, the $\nu_\mu \to \nu_e$ channel is very promising. The charged mesons (e.g. pions, kaons) decay mainly into the muon neutrino. And the intense and focused beam of charged mesons can be easily created with a particle accelerator. Thus the accelerator experiments are the only way to probe the CP–violation. Also, they are very powerful in the measurements of the θ_{13}, θ_{23} and Δm^2_{32} parameters.

The approach of the accelerator oscillation experiment is to measure the energy spectrum of the neutrino beam at the far detector and compare it to the expectations without the oscillations. The reconstruction of the energy is critical as neutrino oscillates along L/E_ν. While the baseline L is fixed neutrino with different energies will arrive at the far detector in the different phase of the oscillation. The expected neutrino flux can be constrained with the measurements of the unoscillated neutrinos with the near detector. In the T2K the neutrino energy is reconstructed with the water Cherenkov detector Super–Kamiokande (section 3) and the magnetized near detector ND280 (subsection 2.2). The water detector measures the energy of the particle with the opening angle of Cherenkov radiation and the ND280 measures the momentum with the track curvature in the magnetic field. The easiest way to measure neutrino energy is to work in the energy region where the most probable neutrino interaction is quasi-elastic $\nu_\ell + n \to \ell^- + p$ ($\overline{\nu}_\ell + p \to \ell^+ + n$). As this is a two-body process and the incoming neutrino direction is known the neutrino energy can be calculated with the outgoing lepton kinematics only. This reaction dominates at energies below 1 GeV. But if the neutrino has higher energy then several particles can be produced. Some of

them can be low energetic or neutral hence will not be detected. That makes the neutrino energy reconstruction extremely difficult. The problem is that the mesons with the wide energy range are produced in the proton beam interactions in the target. That results in a very wide neutrino spectrum. To deal with this T2K uses the "off-axis" beam to produce quasi-monoenergetic neutrino flux (subsection 1.1).

T2K was designed to measure the appearance process $\overset{(-)}{\nu}_\mu \to \overset{(-)}{\nu}_e$ which was expected to be rather rare. First of all the signal rate should be enhanced as much as possible. The J-PARC accelerator provides a very intense muon neutrino beam. Further improvement is considered (section 1 of chapter 6). Secondly, all the processes that can mimic the $\nu_\mu \to \nu_e$ signal should be suppressed or precisely controlled. One of the main concerns is the electron neutrinos initially produced in the beamline. The meson's decay mostly leads to the muon and muon neutrino production. But the muon decay will result in the electron anti-neutrino $\mu^- \to e^- \overline{\nu}_e \nu_\mu$. To suppress such a process, the length of the meson decay volume is limited. The produced muons are stopped in the beam dump just after the decay pipe and emit the electron neutrinos isotropically, not pointed towards the far detector. The second process of concern is the neutral pion production in the neutrino interactions through the neutral current. The π^0 will further decay into two photons. At our energies, photons will convert into the electron-positron pair. In the case of asymmetric π^0 decay, one of the components of the pair can be lost resulting in the detection of a single electromagnetic shower. The SK doesn't distinguish electrons and positrons thus $NC\pi^0$ event can mimic the electron production from the neutrino interaction. To estimate the rate of the neutral pion production the special π^0 subdetector was built in the near detector complex (subsubsection 2.2.a).

When studying the CP–violation it is critical to distinguish neutrino and anti-neutrino oscillations since the effect is the opposite for them. The Super—Kamiokande can not separate μ^+ from μ^- (positrons from electron) as Cherenkov rings will be similar for them. Thus the neutrino can not be distinguished from the anti-neutrino. The near detector ND280 is magnetized. Charged current neutrino and anti-neutrino interactions will produce leptons of the opposite charge. Their tracks will curve in opposite directions and can be easily separated. Therefore the contamination of the anti-neutrino in the neutrino beam and vice-versa can be measured. The effect of the wrongly reconstructed neutrino type can be taken into account in the oscillation analysis. Hence the CP–violation is measured much more precisely with this additional information.

The sketch of the T2K setup is shown in Figure 3.1. In brief, the overall scheme of the T2K experiment is the following:

1. The proton beam hits the carbon target producing mesons.

2. The mesons are focused with horns into the decay volume. The horn polarity defines whether positively or negatively charged mesons will be focused.

3. In the decay volume, the mesons decay mostly into the muon neutrino or anti-neutrino. Thus the horn polarity defines the neutrino mode: ($H^+ \to \mu^+ \nu_\mu$ or $H^- \to \mu^- \overline{\nu}_\mu$). The energy spectrum of the off-axis neutrino beam is quasi-monoenergetic peaking around 0.6 GeV.

4. The muons from the meson decays are mostly stopped in the beam dump, preventing the large electron neutrino contribution in the flux.

5. The neutrino beam intensity and direction are constantly monitored by the muon monitor and the on-axis detector INGRID.

6. The neutrino and anti-neutrino fraction, the neutrino flavor and energy spectrum of the non-oscillated beam is measured with the off-axis ND280 detector (section 2)

7. After traveling 295 km the neutrino beam reaches the far detector complex Super-Kamiokande (section 3). The baseline and neutrino energy are fixed at the first oscillation maximum ($\Delta m^2_{32} L/E \approx 1$).

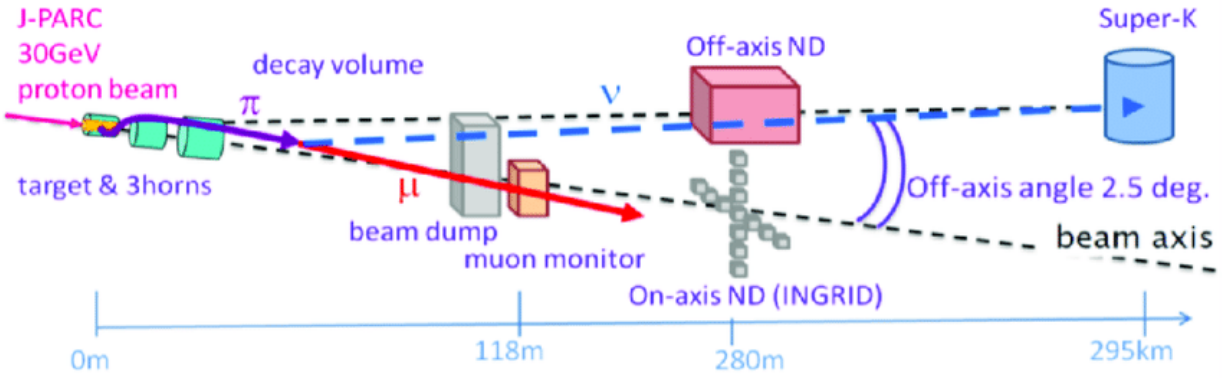

Figure 3.1: The sketch of the T2K setup shows all the key elements of the experiment.

The main goals of the T2K experiment are:

- precise measurements of the oscillation parameters Δm^2_{23} and θ_{23} with the muon (anti–) neutrino disappearance $\nu_\mu \to \nu_\mu$ ($\overline{\nu}_\mu \to \overline{\nu}_\mu$)
- measurements of the θ_{13} angle with the electron appearance $\nu_\mu \to \nu_e$ and $\overline{\nu}_\mu \to \overline{\nu}_e$
- search for the CP violation $\sin\delta_{CP} \neq 0$ by studying the difference between $\nu_\mu \to \nu_e$ and $\overline{\nu}_\mu \to \overline{\nu}_e$
- along with the oscillation measurements, the neutrino interactions are studied carefully to reduce the systematic uncertainty. Thus the neutrino cross-sections on carbon, water and iron are measured.

T2K successfully measured the non-zero value of the θ_{13} [106, 107] and made a discovery detecting $\nu_\mu \to \nu_e$ appearance thus opening the way for the CP–violation search. At the moment it is a major goal of the experiment together with more precise measurements of other oscillation parameters. In this chapter, the details about the T2K setup as well as an analysis technique will be overviewed.

1 Neutrino beam

The proton accelerator is used for the production of the T2K neutrino beam. The 30 GeV kinetic energy protons from the J-PARC accelerator hit the target producing mesons. At these energies mainly pions are produced. There is still some minor contribution of kaons in the meson flux. Mesons with the proper charge are focused in the decay volume while the wrong-charged mesons are defocused and neutral particles remain unfocused. In the decay volume, the mesons decay mainly into the muon and muon neutrino. The decay to the electron and electron neutrino is suppressed by 4 orders by the V-A structure of the weak interaction. The mesons of the same charge always produce neutrino or anti-neutrino. Thus the wrong-sign component of the neutrino beam is severely suppressed with the meson focusing system. The polarity of the focusing system may be changed resulting in an almost pure neutrino or anti-neutrino beam.

The accelerator neutrino experiment has several benefits as it uses a man-made neutrino beam. It is focused, thus extremely intense, high energetic and precisely controlled. It mostly consists

of muon neutrino. The possibility to switch between neutrinos or anti-neutrinos beam is critical for the CP–violation search. To constrain the δ_{CP} phase the difference between neutrino and anti-neutrino oscillations should be studied. The beam monitoring reduces the systematic uncertainties related to the flux. The intense pure beam of the muon neutrino is essential for the precise studies of the $\nu_\mu \rightarrow \nu_e$ oscillations. The purity of the beam will minimize the electron neutrino contamination in the neutrino beam that is a background for the ν_e appearance process. The lower background will make easier the signal observation. In this section, the details about the beam production and monitoring within the T2K experiment will be presented.

1.1 Off-axis flux

Mesons produced in the proton collisions have a wide energy spectrum. That leads to a wide range of neutrino energies. It makes the oscillation analysis difficult. Neutrino oscillation depends on L/E_ν. Thus for the given baseline, only neutrinos with the given energy will demonstrate the maximum appearance or disappearance. All the neutrinos with other energies will be less affected by the oscillations and can mask the process of interest. As mentioned in the introduction, to gain energy reconstruction precision only quasi-elastic interactions are used. It means that we are looking for events with one lepton and nothing more. The incoming neutrino energy is estimated assuming the quasi-elastic interaction as well. This is a dominant topology of the neutrino interactions at the energies below 1 GeV. With energy growth, the cross-section of the neutrino interactions dramatically increases. The main reaction becomes deep inelastic processes with a production of several different particles. If the particle energy is lower then the threshold of Cherenkov radiation emission it is completely invisible in the Super–Kamiokande. Thus high energy neutrinos are a very nuisance for the T2K. They interact more often and produce many particles that can be low energetic. Hence we can wrongly classify such an event as quasi-elastic and reconstruct the neutrino energy with the wrong assumption.

To handle this the T2K experiment uses a so-called “off-axis” concept to obtain a quasi-monoenergetic neutrino beam. The key idea is to use not the neutrinos pointed along the beam axis, but directed at a slight angle. Such neutrinos will have a relatively narrow energy spectrum. The dominating neutrino production mode in the T2K is a pion decay $\pi \rightarrow \mu\nu$. The neutrino energy in the two-body decay in the laboratory frame will be given by

$$E_\nu \approx \left(1 - \frac{m_\mu^2}{m_\pi^2}\right) \frac{E_\pi}{1 + \gamma^2\theta^2} \tag{3.1}$$

where γ is the pion kinematic parameter and θ is a neutrino direction angle w.r.t. pion momentum. The equality of the derivative of the neutrino energy over the pion energy to zero means full independence of the first from the latter. In case $\theta = \gamma^{-1}$, the derivative of the neutrino energy becomes zero $dE_\nu/dE_\pi = 0$ that means that the energy depends weakly on the parent pion momentum. Finally, we will get

$$E_\nu \approx \left(1 - \frac{m_\mu^2}{m_\pi^2}\right) \frac{m_\pi}{2\theta} \approx \frac{29.8 MeV}{\theta\,[rad]} \tag{3.2}$$

The T2K beamline was set to the 2.5° off-axis angle. It was tuned to set the neutrino energy peak to the oscillation maximum. With the fixed mixing angle and mass difference the energy spectra for different angles are shown in Figure 3.2. The figure provides also the oscillation probability of the muon neutrino at a distance of 295 km versus the energy. Thus with the off-axis angle tuning the maximum oscillation effect can be measured. Though the high energy neutrinos are harmful to the oscillation analysis nevertheless high energy mesons can be useful for other studies. For example,

they can be helpful for the Heavy Neutral Lepton (HNL subsection 1.4) search. High energy mesons decay will result in the focused HNL beam while low energy mesons will produce HNL over a very wide angle. The heavy neutrino study is one of the main topics of the current thesis (section 1).

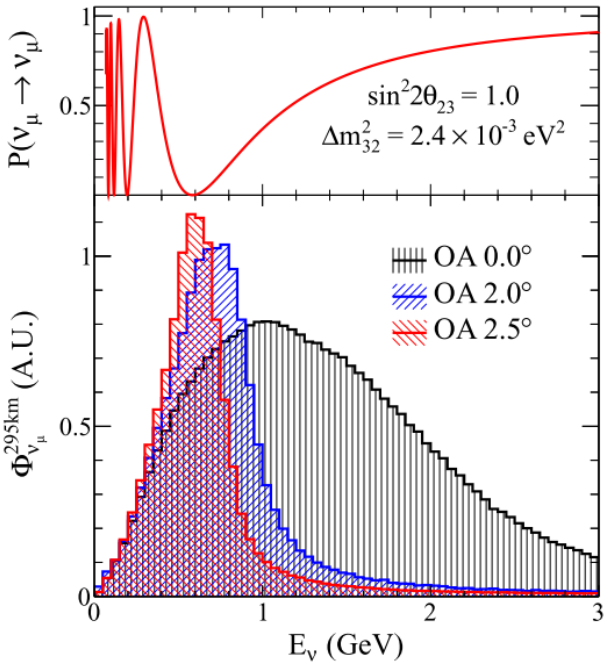

Figure 3.2: Muon neutrino survival probability at 295 km and neutrino fluxes for different off-axis angles. Figure from [108].

1.2 Neutrino beamline

The T2K neutrino beamline can be generally divided into two stages: primary beamline and secondary beamline. The first takes the protons from the J-PARC accelerator main ring, performs measurements of the beam parameters and focuses it on a carbon target. The secondary beamline focuses the produced mesons with the horns into the decay volume and monitors its decay. The general scheme of the beamline is shown in Figure 3.3. A detailed description can be found in [108].

a Primary beamline

The primary beamline takes the proton from the J-PARC main ring. The beam is structured into the spills coming with 0.5 Hz rate. Each spill is 5 μs wide and consists of 8 bunches with $\sigma \approx 18$ ns and 58 ns separation. Per each spill, 3×10^{14} protons can be delivered. Thus the total maximum power of the beamline can be estimated as 750 kW. The total number of protons hitting the target (POT - Protons On Target) is used as the main measure of the statistics collected in the T2K experiment. The evolution of the accumulated statistics, as well as the beam power, is shown in Figure 3.4.

The initial beam is steered with the arc section made with superconducting magnets and horizontally aligned with the direction to the detectors. At this stage, the measurements of the beam parameters are performed. The beam intensity is measured with current transformers that use toroidal coils around a cylindrical ferromagnetic core. The uncertainties of the measurements are

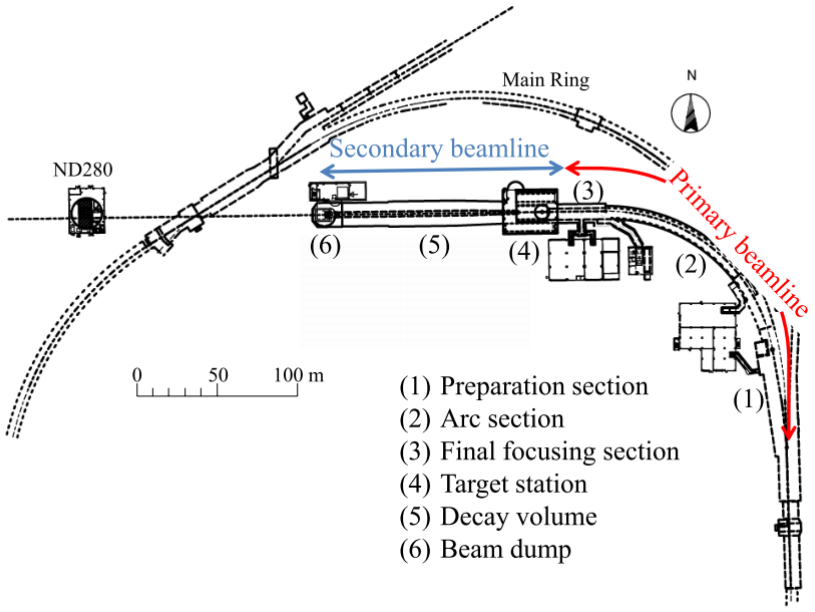

Figure 3.3: The scheme of the T2K neutrino beam line. Primary beamline (proton line) is shown in red and secondary beamline is shown in blue.

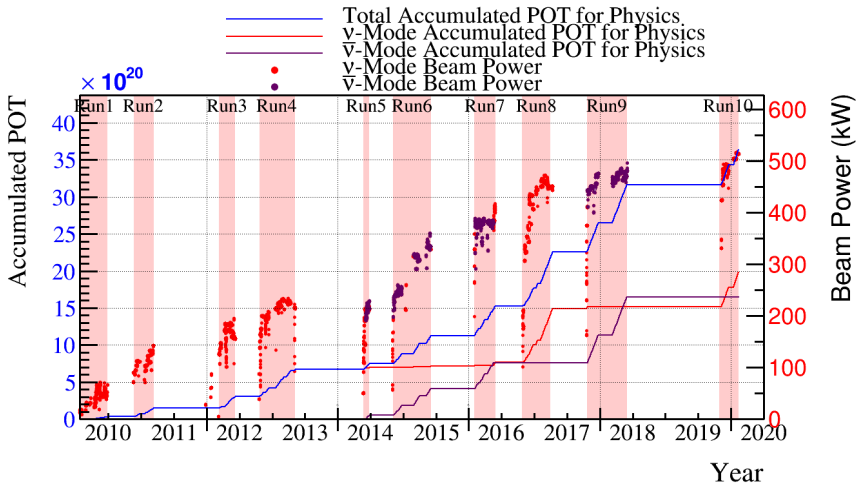

Figure 3.4: The collected statistics in the T2K experiment in POT (Proton On Target) together with the beam intensity along the data accumulation until April 2020.

estimated at the level of 2%. The beam position is measured with electrostatic monitors and secondary emission monitors. The first measures the beam position with the accuracy of 450 μm, while the latter measures the beam width with the precision of 200 μm. After the measurements, the beam is directed downward and focused on the carbon target.

b Secondary beamline

The secondary beamline is responsible for neutrino production. The target for protons is made of a Carbon cylinder of 2.6 cm width and 91.4 cm length (1.9 interaction length). The target core heats up to 700°C during the operation. The target is held in a titanium case for fast heat transfer

to the water cooling system. The target is inserted into the first magnetic horn, so the mesons are affected by the focusing magnetic field from the moment of production.

The meson focusing system consists of three magnetic horns. The first one contains the target where the mesons are produced. The horns are operated with the pulsed current at the level of 250-320 kA. The polarity can be changed to focus negatively or positively charged mesons resulting in neutrino or anti-neutrino production. The dramatic gain of the horn usage for the neutrino beam intensity is shown in Figure 3.5.

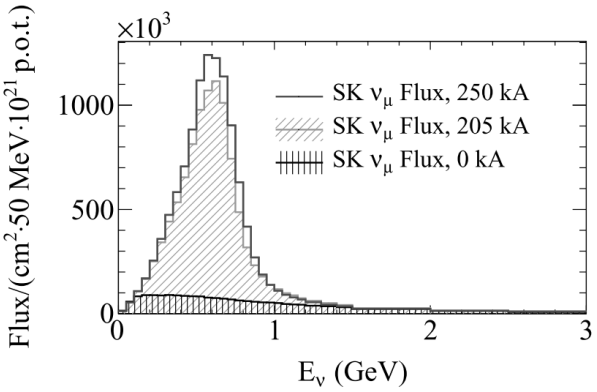

Figure 3.5: The effect of horn usage on the beam intensity at the far detector

The hadrons are focused into the decay volume. It is a 96 m tunnel widening from 1.4×1.7 m^2 at the beginning up to the 3.0×5.0 m^2 at the end. The volume is filled with Helium gas and is cooled with water. The particles possibly producing neutrinos are $\pi^{\pm}$, $K^{\pm}$, K^0_L and $\mu^{\pm}$. The most probable neutrino production reactions are:

$$\pi^{\mp} \to \mu^{\mp} \overset{(-)}{\nu}_{\mu} \qquad K^{\mp} \to \mu^{\mp} \overset{(-)}{\nu}_{\mu} \tag{3.3}$$

$$K^{\mp} \to \pi^0 e^{\mp} \overset{(-)}{\nu}_{e} \qquad \mu^{\mp} \to e^{\mp} \overset{(-)}{\nu}_{\mu} \overset{(-)}{\nu}_{e} \tag{3.4}$$

The energy spectra divided into neutrino flavor and parent particle are provided in Figure 3.6.

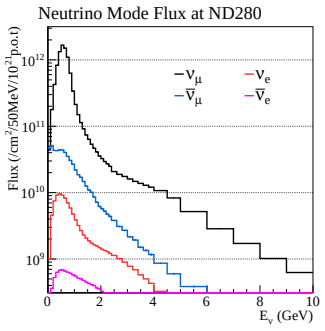

(a)

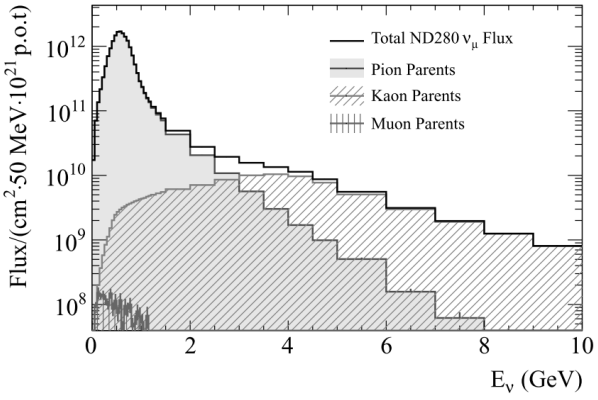

(b)

Figure 3.6: The neutrino beam at the near detector side divided into (a) neutrino flavor and (b) parent particle.

The beam dump is placed just after the decay pipe. It is made of 75 tons of graphite and suppresses all the charged particles except the high energy muons (E>5 GeV). Thus a majority of low

energy muons will not decay in flight, producing electron neutrinos pointed to the far detector. It is critical for successful oscillation analysis. High energy muons can be used for the neutrino beam stability monitoring. They are mostly produced along with neutrinos in the 2-body meson decays. Thus the muon direction will explicitly indicate the direction of the neutrino beam. The muon monitor is made with an array of ionization chambers and another array of silicon PIN photodiodes. The center of the muon profile is reconstructed with 3 cm precision resulting in 0.25 mrad angular accuracy.

The overview of the T2K secondary beamline together with the near detector complex is presented in Figure 3.7.

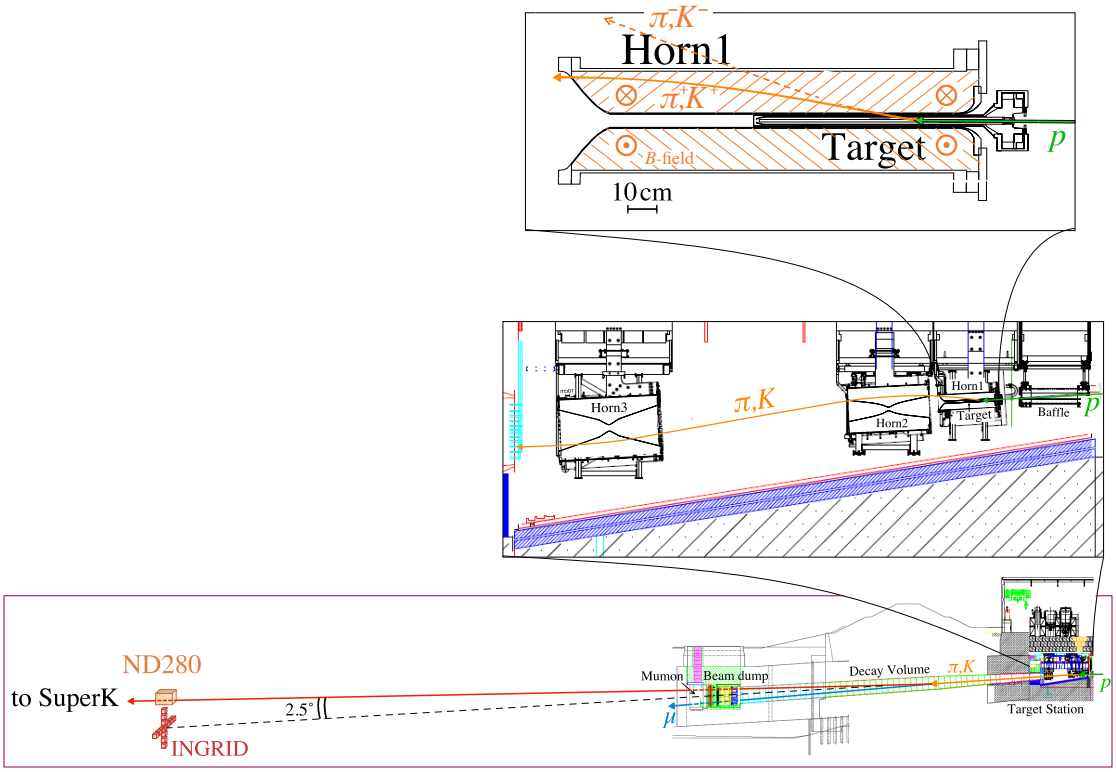

Figure 3.7: The overview of the T2K secondary beamline and the near detectors.

2 Near detector

Precise knowledge about the initial neutrino beam is essential for the accurate oscillation measurements. The T2K near detector complex is placed at 280 meters from the proton target and its main goal is the monitoring of the unoscillated beam. Two detectors are used for this purpose: on-axis INGRID and off-axis ND280. The schematic views of both detectors are presented in Figure 3.8.

2.1 INGRID

The main goal of the INGRID detector is controlling the position and intensity of the neutrino beam. It consists of 14 modules arranged in a cross with two additional modules placed outside

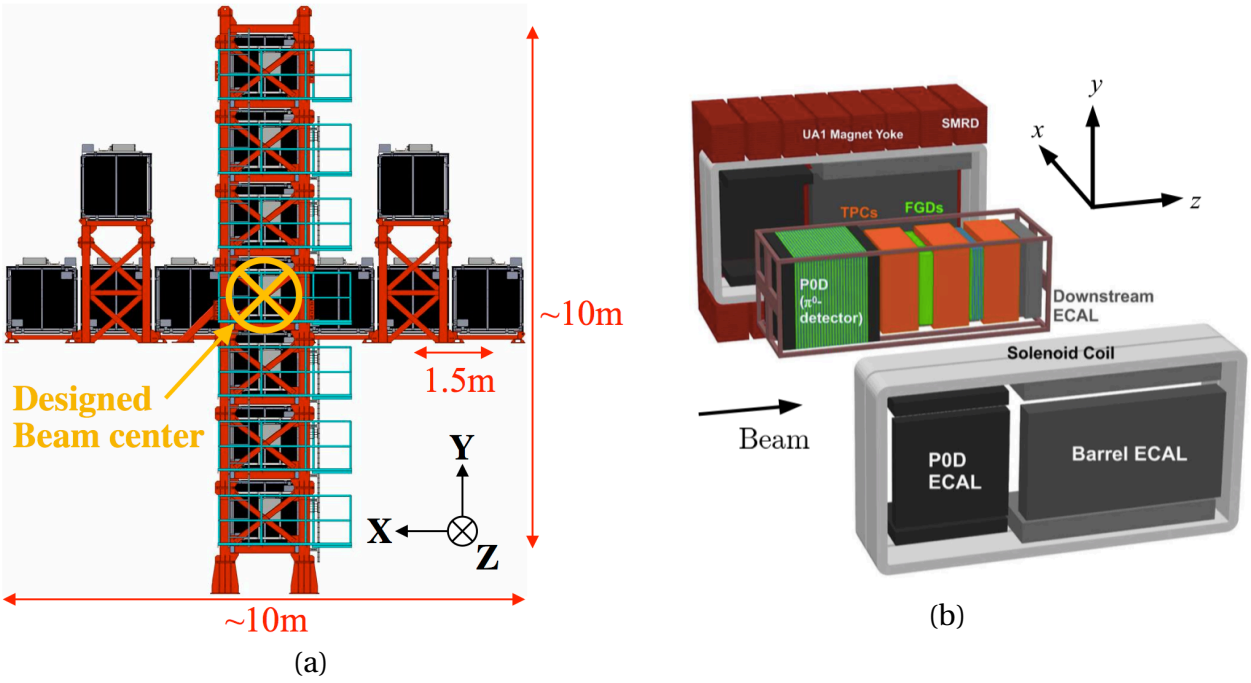

Figure 3.8: An exploded view of the near detector complex: (a) on-axis INGRID detector, (b) off-axis ND280 detector.

the main cross (Figure 3.8 (a)). The center of the cross is placed at 0° angle w.r.t. proton beam direction. Each detector module consists of a sandwich of iron and tracking planes. We expect enough neutrino interactions in the iron targets every day for the day-to-day monitoring of the neutrino beam parameters: intensity and direction. Figure 3.9 represents the results of such measurements. Both intensity and direction variations are small and the related uncertainties in the oscillation analysis are negligible. The initial requirement for the beam direction accuracy was set to 1 mrad.

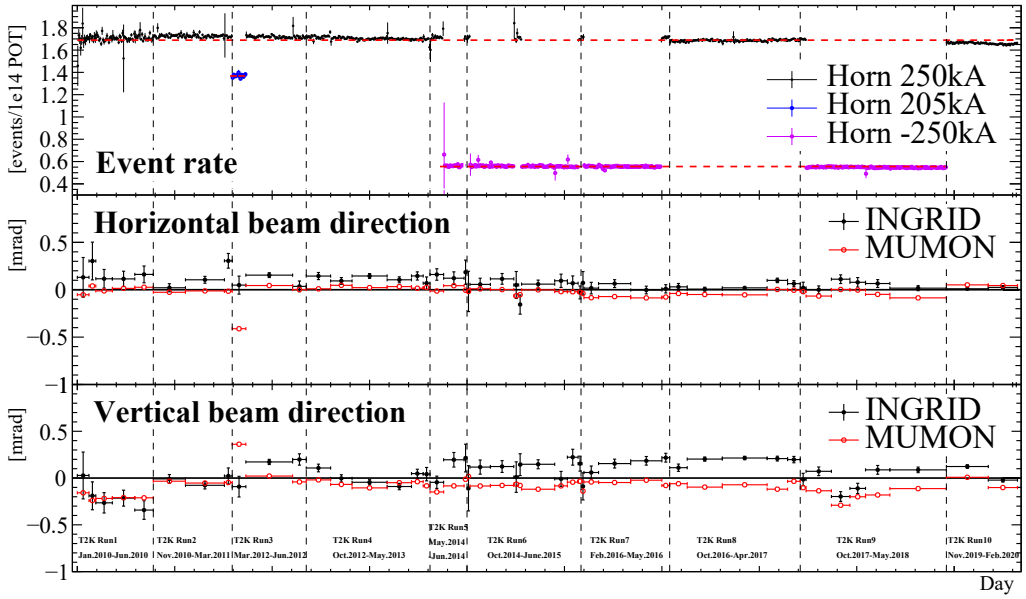

Figure 3.9: The INGRID measurements of the neutrino beam intensity and position.

2.2 Near detector ND280

The ND280 is an off-axis detector centered at the line from the target towards the far detector Super-Kamiokande. Its goal is measurements of the neutrino interaction dividing them into neutrino/anti–neutrino, flavor and reaction topology. The incoming neutrino energy is reconstructed from measurements of the lepton kinematics from quasi–elastic interactions. For this purpose, the detector is composed of different sub-detectors. The Fine Grained Detectors (FGD) are used as a target for neutrino interaction and the tracking of the outgoing particles. The gaseous Time Projection Chambers (TPC) are used for the charged particle tracking. The particle charge and momentum are measured with the track curvature in gas. The type of the particle is also reconstructed with the ionization energy losses. Thus the incoming neutrino type (neutrino/anti-neutrino), flavor and energy can be determined. The electromagnetic calorimeter (ECAL) detects the gamma conversion and improves electron and muon separation. The SMRD detector works as a trigger for the cosmic rays and may help with the muon identification. The P0D detector is used for the measurements of the π^0 production in the neutrino interactions.

The ND280 measurements are used to constrain the parameters of the flux and the theoretical models of the neutrino interactions. The fact that we know the neutrino type, flavor, energy and the reaction type allows us to probe several models' parameters independently. This will result in the smaller uncertainty of the global oscillation analysis. The subdetectors structure and features will be overviewed in the following subsections.

a π^0 detector (P0D)

The primary goal of the P0D detector is to measure the cross-section of the π^0 production in the neutrino interactions through the neutral current (NC). As was mentioned in the introduction it was believed to be the main background for the ν_e appearance measurements in the far detector. The asymmetrically converted photons from the π^0 decay can be misreconstructed as $\nu_\mu \rightarrow \nu_e$ signal and bias the oscillation analysis. The same flux and the same target material should be used for accurate background treatment. As the detector is aimed to detect the NCπ^0 production it should be good in the charged particle tracking to distinguish CC and NC interactions. Also, it should be effective for photon detection. The sensitive volume of the P0D is made from scintillator bars aligned along X and Y axis (perpendicular to the beam axis). The readout is done with wavelength shifting fibers (WLS). The XY scintillator layers are alternated with brass sheets and water bags. Such a structure allows efficient reconstruction of a charged particle track as well as an electromagnetic shower. The latter is used for photon detection. The scintillator layers are alternated with the lead sheets instead of water bags in the upstream and downstream parts of the detector. This improves the containment of the EM showers. The measurements of the $NC\pi^0$ production can be done with and without water in the target, thus the cross-section on water can be extracted.

b Fine grained detectors (FGD)

Two FGD modules [109] are used as a target for the neutrino interactions. The size of the module is $2 \times 2 \times 0.3$ m^3. They consist of a sandwich structure of bars made with plastic scintillators and oriented along X and Y axis, while the beam is coming along Z axis. The bars are pierced with WLS for the light collection and transportation to the photosensors. The light readout is done with

multi-pixel photo counters (MPPC) that provide high detection efficiency and sufficient dynamic range.

In the second FGD the plastic layers are alternated with the water modules. Thus the measurements of the neutrino interaction with the water can be done. Such a measurement is important in the context of T2K as far detector uses water target only. The difference between neutrino interaction cross-section with Carbon and Oxygen can be a source of systematic uncertainty.

c Time projection chambers (TPC)

The TPCs [110] are gaseous detectors that perform the 3D reconstruction of the charged particle's track. The scheme of the detector is presented in Figure 3.10.

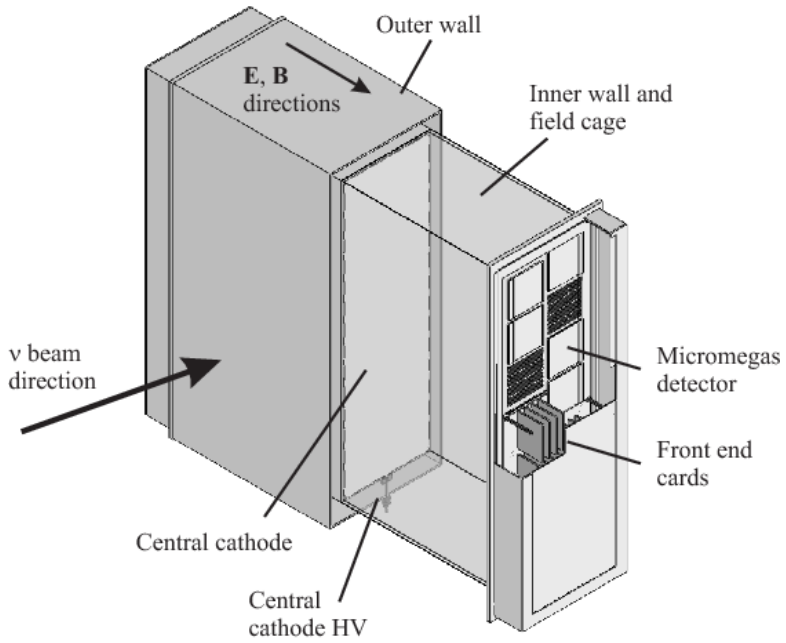

Figure 3.10: The scheme of the TPC module

The general principle of the TPC operation and the key characteristics of the T2K TPCs are presented in Figure 3.11. The active volume of the detector is filled with the gas mixture of Argon, CF_4 (tetrafluoromethane) and iC_4H_{10} (isobutane) in the volume proportions 95:3:2. A charged particle going through the gas volume loses energy through ionization. The electrons from the ionization drift against the direction of the electric field — from the cathode towards the micromegas. The positive ions are drifting towards the cathode. The Argon was chosen as a main component of the gas mixture because it is a noble gas. It is very easy to ionize thus we will have a lot of initial electrons. Also, it will not subject to a chemical reaction. It is especially important in the amplification region, where chemical reactions are most probable. Isobutane provides quenching of the avalanche in the amplification region by absorbing UV photons. CF_4 is responsible for the speed-up of the electron drift. Such a mixture is very powerful resulting in high speed, low diffusion, and good performance with micromegas detectors.

The electric field strength is constant in the drift region. The voltage between the cathode and micro mesh is 25 kV at a distance of 1 meter. The signal is dramatically amplified between the micro mesh and pads as a voltage of 350 V is applied to the 128 μm gap. The produced avalanches

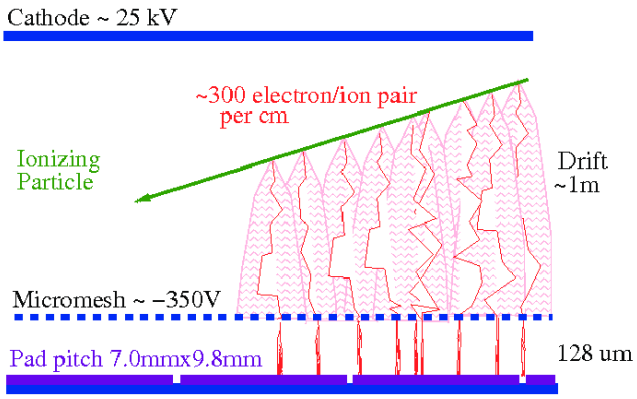

Figure 3.11: The general concept of the TPC operation.

are detected with the 6.9×9.7 mm^2 pads. Here the electrons avalanche produce the analog electric signal that will be later digitized with the electronics.

In total, the readout surface of one TPC module consists of 12 micromegas 48×36 pads each. The 2D projection (YZ) of the track is reconstructed with the hit pads. The drift time is measured to reconstruct the track curvature in XY plane. The external detector (FGD) is used for the reconstruction of the absolute position along X axis.

The core of the ND280 — the tracker, consists of 3 TPCs alternated with 2 FGDs. Such a structure is aimed at the effective detection of the lepton produced in the neutrino interactions inside FGDs. The particle type, sign and momentum can be precisely measured with such a setup.

The particle type is estimated based on its ionization loss. The mean deposited energy for the particular particle with given momentum is described with Bethe–Bloch formula [111]. But the fluctuations follow Landau distribution [112] and are rather large. The distributions of the energy loss per unit length for the particles from neutrino interactions in ND280 are shown in Figure 3.12. Four hypotheses for the particle type are considered: electron, muon, pion, and proton. For each hypothesis, the expected energy loss is compared with the measured values. The cut on the likelihood value is set to find out if the given track satisfies the hypothesis of the particular particle type.

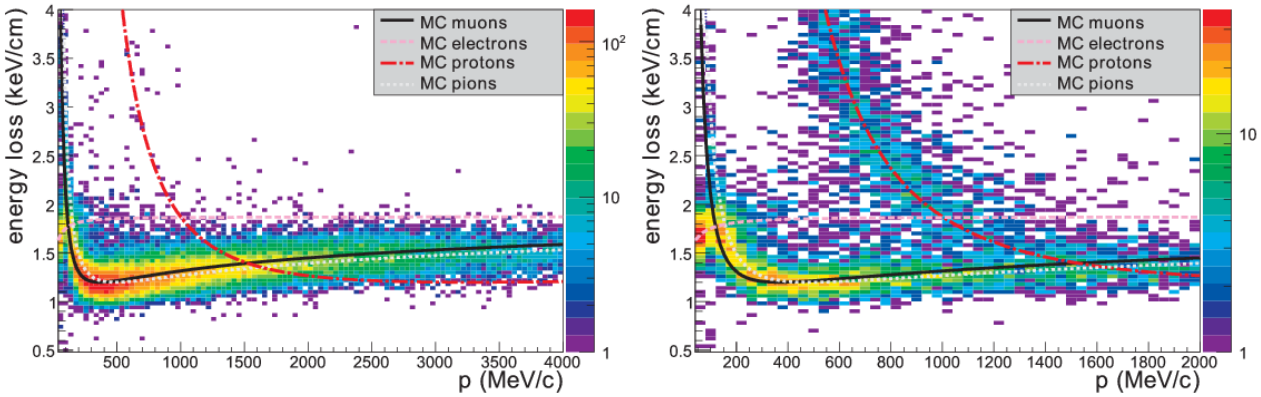

Figure 3.12: The distribution of the energy loss per unit length for the (a) negatively and (b) positively charged particles produced in neutrino interactions in ND280 TPCs

d Electromagnetic calorimeter (ECaL)

The calorimeters are used for the detection of the gammas from the π^0, produced in the neutrino interactions. They also can help with particle identification. Electrons and hadrons will produce showers while muons will have a clear clean track. The calorimeters are surrounding the inner detectors of the ND280. They consist of the sandwich structure of plastic bars 4×1 cm^2 in cross-section, alternating with 1.75 mm thick absorber layers made with lead. The downstream ECaL consists of 34 layers and provides the most precise results, while P0D and barrel ECaL consists of 31 layers.

e Side muon range detector (SMRD)

The SMRD is surrounding the whole ND280 and is a multifunction detector. It allows rejecting the events triggered by the cosmic rays or the neutrino interactions in the outer detectors or concrete of the pit. SMRD is useful for the detection of the muons that exit the detector with high angles. Since there is no TPC in this direction the momentum measurement can be done only with SMRD. The detector itself consists of 440 1.7 cm thick plastic scintillator modules that are inserted in the gaps between 4.8 cm thick steel plates of the magnet yoke.

3 Super–Kamiokande

The far detector of the T2K experiment is Super–Kamiokande (SK) [113] located 295 km away from the proton target in the Kamioka mine. 50 tons of water is used as a target for neutrino interactions. The water tank is viewed by 13 thousand photomultipliers (PMT) aimed at the detection of Cherenkov light from the charged lepton produced in the neutrino interactions. The schematic view of the detector is presented in Figure 3.13.

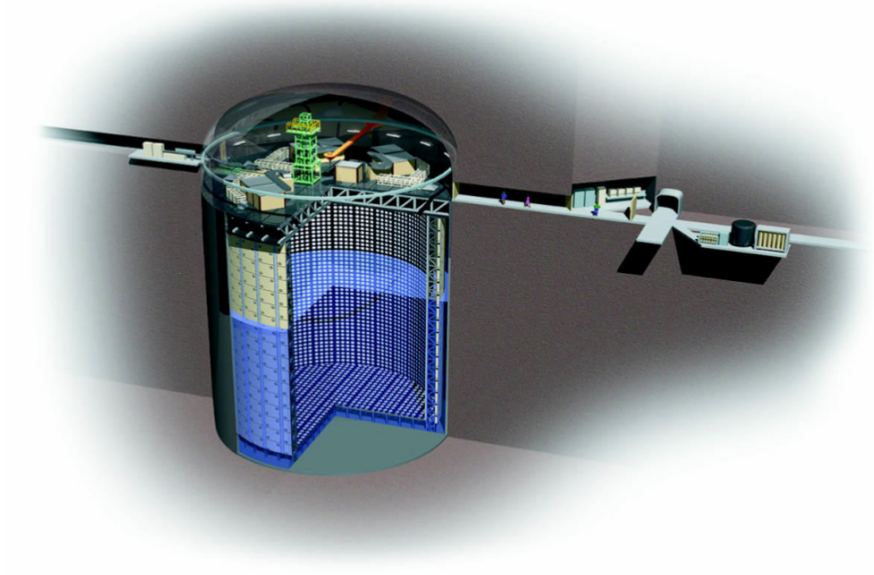

Figure 3.13: The scheme of the Super-Kamiokande detector.

The working principle of the detector is based on the effect of Cherenkov radiation. When a charged particle passes through a dielectric medium at a speed greater than the phase velocity of light in that medium a conic wavefront is formed. The opening angle of the cone is defined by the particle speed and the refraction index of the medium $\cos\theta = 1/n\beta$, where $\beta = v/c$. The emission of the radiation is a threshold effect. As could be seen from the equation above, the wavefront can be formed only if the particle is fast enough $\beta > 1/n$. For the water detector, the thresholds are 1.4 GeV for protons, 160 MeV for muons and 775 keV for electrons. The maximum angle is also limited by $\theta_{max} = \arccos(1/n) \approx 42°$.

Super-Kamiokande continues the successful history of the neutrino detectors in the Kamioka mine. The first experiment KamiokaNDE (Kamioka Nucleon Decay experiment) started looking for the nucleon decays in 1983. The atmospheric neutrino interactions were the main background. During the detector operation, a nice performance of the neutrino detection was observed and the experiment was refocused on the neutrino analysis. Since then the detector was massively improved and new setups were built: Kamiokande II, Super-Kamiokande. The latter is operating now as a far detector of the T2K experiment. The experience collected during the studies in Kamioka allows excellent physics performance.

There are many challenges in neutrino studies with water Cherenkov detectors. First of all, the statistics is limited due to the small cross-section. To increase the number of events the detector was enlarged several times from 3 kt (KamiokaNDE) to 50 kt (Super-Kamiokande). But the detection of Cherenkov light becomes an issue with a larger tank. The intensity of such a light is quite low. Thanks to the hard work of the SK collaboration the water purity is extremely high. The transparency is very stable at the level of 100 meters. The other issue is the photon detection itself. The photo coverage of the active area surface is 40% aiming at the collection as many photons as possible. Large 20-inch PMTs with high detection efficiency are used for it. The wavelength of Cherenkov light extends to the ultraviolet region, while the efficiency of the PMTs is quite low there. The light intensity decreases as λ^3 with the increasing of the wavelength, that's why the excellent performance of the PMT is essential for the successful detector operation.

The other challenge is background suppression. The detector is placed in a mine to reduce the flux of the cosmic rays. However, extremely high energy muons can reach the water tank. Also, muons can be produced by the neutrino interactions in the rock close to the detector. The Super–Kamiokande is divided into two volumes: inner and outer detectors. They are optically isolated, so a signal detection in the outer volume will explicitly indicate an out-of-tank particle production. Only leptons produced in the inner detector are considered for the neutrino analysis.

The detector allows separating Cherenkov ring produced by muon and electron. Due to their lighter mass electrons are more subject to bremsstrahlung. Since the critical energy for the electrons in water is tens of MeV and the typical energy of the electrons produced by the T2K neutrinos is hundreds of MeV, we expect to see electromagnetic showers that will distort Cherenkov ring. The examples of the events are presented in Figure 3.14. The left image demonstrated a much less distorted ring from the muon while the right image demonstrates the result of the electron showering. Up to now, the Super–Kamiokande separates these two topologies with excellent purity. The probability to identify a single electron (muon) as muon (electron) is 0.7% (0.8%). That's extremely important for the oscillation experiment. The neutrino will produce the charged lepton of the same flavor and we are studying a very rare process of the electron neutrino appearance. That's why any confusion between muon and electron is extremely dangerous.

The Super–Kamiokande provides powerful shielding from the cosmic rays, but the atmospheric neutrino can easily go through the rock and interact inside the inner detector. That's how the atmospheric studies are done, but for the T2K we need to distinguish neutrinos from the atmosphere and J-PARC accelerator. For this purpose, the timing information is the most useful one. As mentioned in section 1 the beam is grouped in 8 bunches 19 ns width coming every 2 seconds. The time

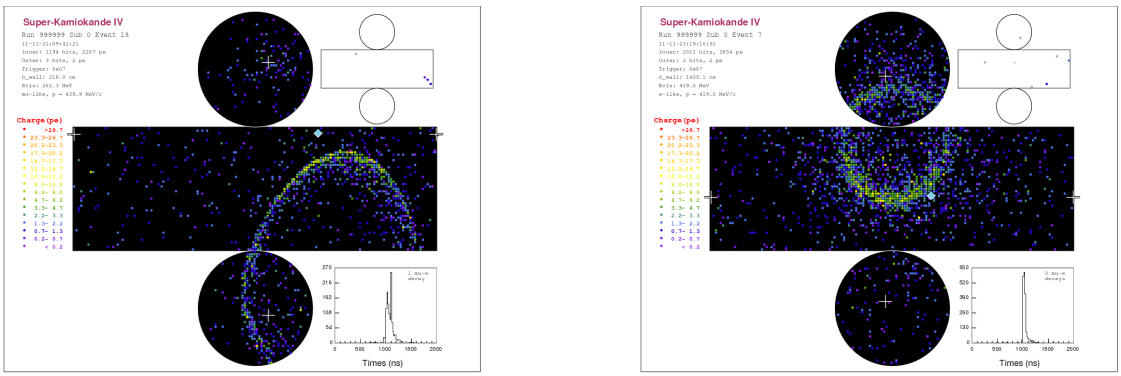

(a) (b)

Figure 3.14: The event display of Cherenkov ring inside Super-Kamiokande detector: (a) ring from muon, (b) ring from electron.

synchronization between J-PARC and Super-Kamiokande allows us to select accurately neutrinos that fall into bunches and suppress the atmospheric background that is uniform in time. Thus the background is suppressed by 8 orders of magnitude.

4 Analysis overview

4.1 Oscillation analysis

a General overview

As mentioned in the introduction the main goal of the T2K experiment is precise measurements of the neutrino oscillation parameters and search for the CP–violation in the lepton sector. This is done by measuring the neutrino energy spectrum at the far detector and comparing it with the expectation without the oscillations. Spectra are divided into the neutrino flavor (muon and electron) and type (neutrino/anti–neutrino), thus 4 spectra are the basic input for the oscillation analysis. Super–Kamiokande measures neutrino energy with the assumption of the quasi–elastic interaction (Equation 3.5).

$$E_\nu^{rec} = \frac{m_f^2 - (m_i')^2 - m_\ell^2 + 2m_i E_\ell}{2\left(m_i' - E_\ell + p_\ell \cos\theta_\ell\right)} \tag{3.5}$$

where $E_b = 27$ MeV is called "liberation[1] energy" and it is mean energy that is required to eject a nucleon from the Oxygen nucleus, $m_i' = m_i - E_b$, m_i and m_f are initial and final nuclei mass

[1] Sometimes notated as a "binding"

respectively, m_ℓ, E_ℓ, p_ℓ, θ_ℓ are outgoing lepton mass, energy, momentum and angle w.r.t neutrino beam respectively.

Four neutrino energy spectra are essential for the minimal oscillation analysis, but the precision can be dramatically improved with the near detector. ND280 is used for the constraints of the flux and cross-section models.

Despite neutrino production is well controlled the resulting flux can be slightly different from the expectations. The possible reasons are wrong assumptions about the hadron production model, proton beam profile, off-axis angle, horn current, horn alignment, and other factors. The hadron production model is responsible for the total number and spectra of the produced mesons. The horn configuration affects the meson focusing, thus can affect the intensity, symmetry and direction of the beam. Different beam off-axis angle can change the neutrino energy spectrum in our detectors. The ND280 can constrain exactly the same off-axis flux that will pass through Super–Kamiokande but before the oscillations. For each source of error mentioned above, the underlying parameters in the model are varied to evaluate the effect on the flux prediction in bins of neutrino energy for each neutrino flavor. The example of the prior and ND280 constrains on the ν_μ flux are presented in Figure 3.15 (a).

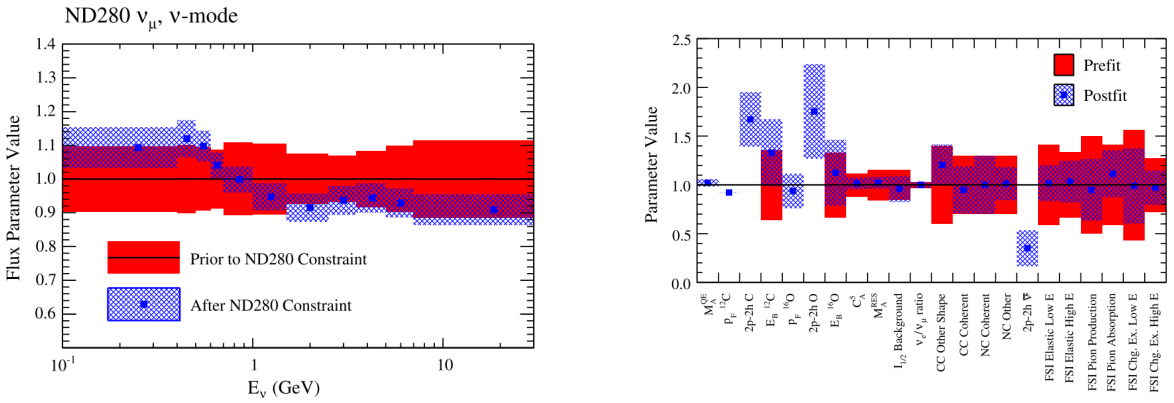

Figure 3.15: The priors (red) and the results of the ND280 fit (blue) for ν_μ (a) flux and (b) cross-section parameters. The T2K is operating in neutrino mode. Figure from [114].

The neutrino interaction models are also tuned with the ND280 data. The models depend on many parameters. The advantage of the ND280 is the sampling of the measurements in the neutrino type, flavor and topology. "Topology" can be described as a multiplicity of the neutrino interaction. In ND280 we select the following topologies: CC interactions with no pions ($CC0\pi$), interactions with 1 pion ($CC1\pi$) and other CC ($CCOther$). The "topology" can be different from the initial reaction type because of nuclear effects (subsection 2.2 of chapter 1). For example, after the interaction with pion production $\nu_\mu + p \rightarrow \mu^- + p + \pi^+$ the latter can be absorbed by the nucleus and the event will look exactly like quasi-elastic scattering. That is why the events are classified with the particles in the final state, but not with the type of the initial neutrino interaction. The nuclear effects add additional uncertainty in the oscillation analysis. The different model parameters are affecting different topologies. Therefore measurements with three samples will allow to precisely constrain different neutrino interaction types.

Only quasi–elastic (QE) interactions are used in the far detector for the oscillation analysis. But as was overviewed some nonQE reactions can mimic the signal. The ND280 measures both QE and nonQE interactions precisely (e.g. Figure 3.16) and constrain the models parameters that affect particular reactions (Figure 3.15 (b)). Thus this type of background is constrained.

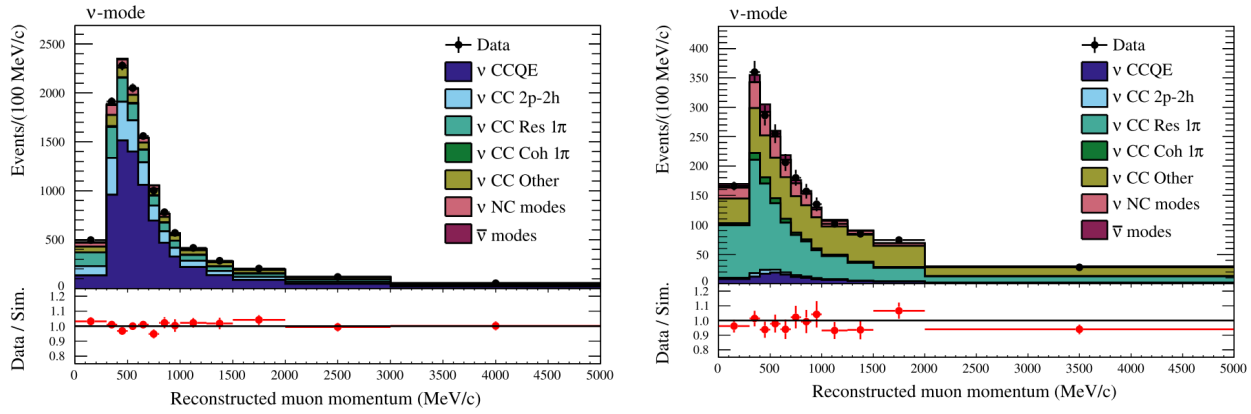

(a) (b)

Figure 3.16: Data MC comparison for the (a) $CC0\pi$ and (b) $CC1\pi$ samples measured with the ND280 in the neutrino mode. Figure from [114].

b Analysis machinery

The scheme of the analysis workflow is presented in Figure 3.17. Different colors at the block-scheme represent the measurements (green), models (violet) and fit algorithms (blue).

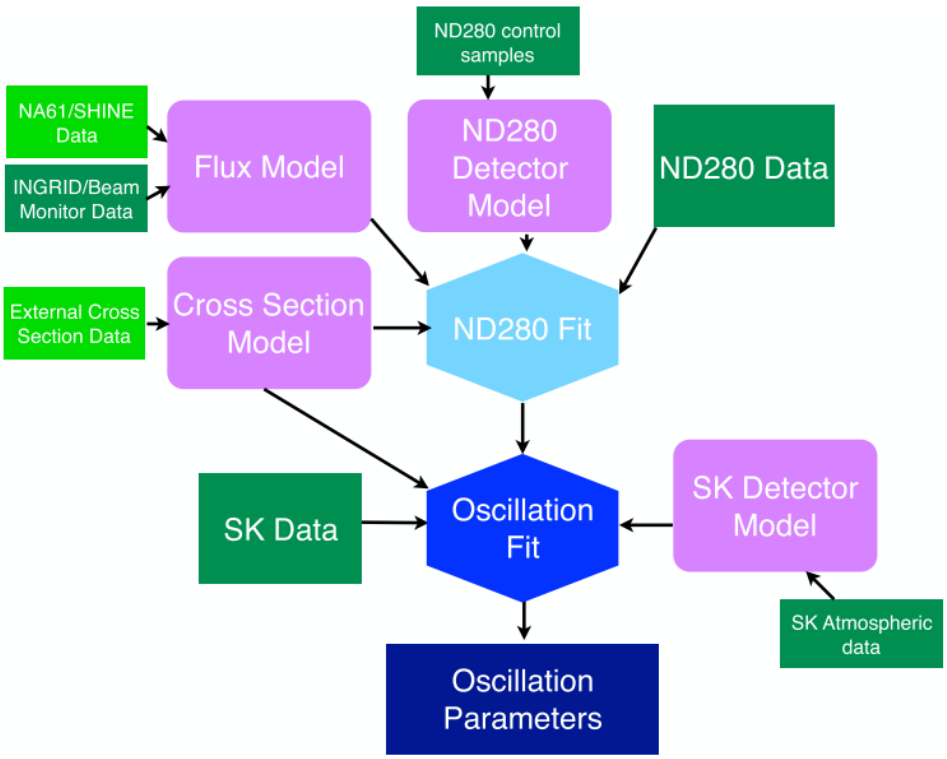

Figure 3.17: The scheme of the T2K oscillation analysis workflow. The measurements are presented in green (light — external, dark — T2K), the models are presented in violet and the fitter tools are presented in blue.

The measurements start with the beamline monitors where the parameters of the proton beam are estimated. Then the data from the NA61 experiment is used to estimate the meson production in the target. The neutrino beam intensity and direction are monitored with the on-axis near detector INGRID. All these results allow us to build the neutrino flux model.

The near detector ND280 performs the measurements of the neutrino interaction rate. The observations are sampled in the neutrino/anti–neutrino interactions and the reaction topology: quasi-elastic, pion production, deep inelastic. We use the results of other experiments as a prior estimation for the cross-section of neutrino interactions. But there are several parameters in the model that can be tuned precisely using all the samples collected in the ND280. Thus flux and the cross-section model are tuned together with the ND280 control samples.

The long history of the atmospheric neutrino measurements in Super-Kamiokande provides accurate knowledge of the detector operation. This detector response model is used together with the T2K events in the SK for the final oscillation measurements. The spectrum of the observed electron neutrinos in the far detector are compared to the expectations without the oscillations is presented in Figure 3.18.

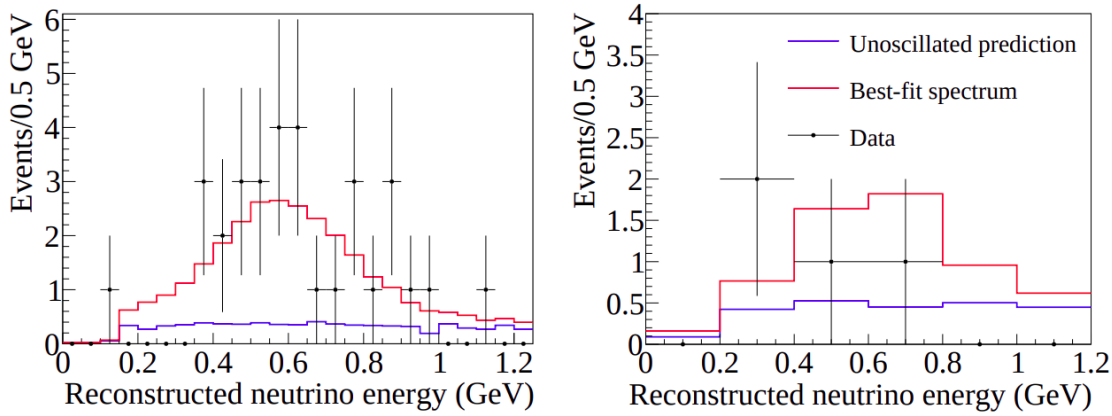

Figure 3.18: The spectrum of the electron neutrinos observed in the far detector comparing to the expectations without oscillation (blue) and the best oscillation fit (red).

As one could see the oscillation fit is the heart of the analysis. Its goal is to extract the neutrino oscillation parameters from the data sets and to estimate the impact of all the uncertainties on the final result. The likelihood minimization method is used for this purpose. The expected number of events in the far detector is assumed to follow Poisson distribution. The data is sampled in the energy bins. Therefore the likelihood function is defined with:

$$-2\ln\mathcal{L}\left(\vec{o},\vec{f}\right)=2\sum_{i=0}^{N-1}\left[n_i^{obs}\cdot\ln\left(n_i^{obs}/n_i^{exp}\right)+\left(n_i^{exp}-n_i^{obs}\right)\right] \tag{3.6}$$

The vectors $\vec{o}$ and $\vec{f}$ are neutrino oscillation parameters (the goal of the fit) and nuisance parameters respectively; n_i^{obs} and n_i^{exp} are observed and expected events in the i-th energy bin. The likelihood function defined above is high dimensional. The nuisance parameters can be marginalized with integration over the product of the likelihood function and priors:

$$\mathcal{L}_{marg}\left(\vec{o};x\right)=\int_F\mathcal{L}\left(\vec{o},\vec{f};x\right)\pi(\vec{f})d\vec{f}=\frac{1}{n}\sum_{i=1}^{n}\mathcal{L}\left(\vec{o};\vec{f}_i,x\right) \tag{3.7}$$

This defines a function that depends only on the oscillation parameters and given data. The model parameters such as cross-section, flux, detector performance are embedded in the function

as priors following Gaussian distribution. After the likelihood minimization, limits in the oscillation parameters space are set [115].

T2K performs three different analyses with slightly different techniques. The main strategy of likelihood minimization is the same for all of them. Two of the methods are doing it with the frequentist framework. The Equation 3.7 converges to the χ^2 distribution. The confidence region can be set with $-2\Delta\mathcal{L}(\vec{o}) \leqslant X_{crit}(\vec{o})$. And the critical values of X are taken based on the desired confidence, e.g. 90%. The only difference between the two frequentist methods is data sampling. One of them uses outgoing charged lepton momentum with the lepton direction w.r.t. neutrino beam. The other uses neutrino energy instead of lepton momentum. Both methods are expected to give the same results and are used for the cross-check. The third analysis is using Markov chain Monte Carlo method for the likelihood minimization.

The result is considered as robust only if all the methods are in a good agreement about the confidence/credible intervals. The oscillation results are presented in Figure 3.19.

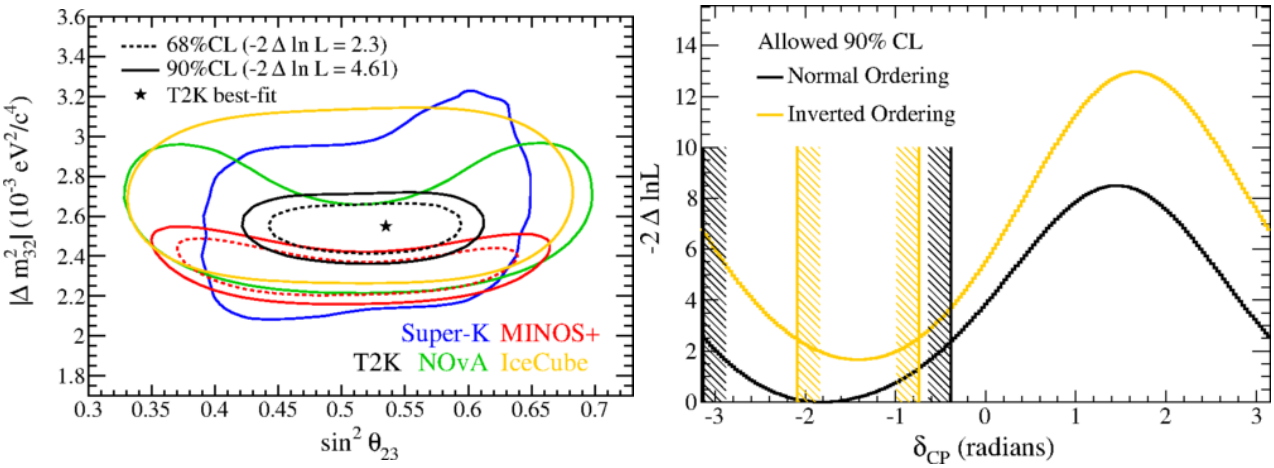

(a) (b)

Figure 3.19: The oscillation results from the T2K experiment obtained with frequentist approach: (a) θ_{23} and Δm^2_{32} constraints and (b) δ_{CP} constraints with statistics $3.12 \times 10^2 1$ POT

4.2 Neutrino cross-section measurements

Alongside the oscillation analysis, T2K performs very precise measurements of the neutrino cross-sections. The knowledge of the neutrino interactions' rates is essential for the oscillation analysis as the most realistic theoretical model can be chosen. The ND280 provides an opportunity to study neutrino interaction with carbon, oxygen and iron with both neutrino and anti-neutrino and with both flavors: muon and electron. The dominating reaction final state in the ND280 is a muon with no pions. It is the main process for the T2K energies that's why it is studied quite well [49]. It is more difficult to study the interaction of the electron neutrinos. The result of the comparison of the ν_e and $\overline{\nu}_e$ cross-section is presented in Figure 3.20 [116].

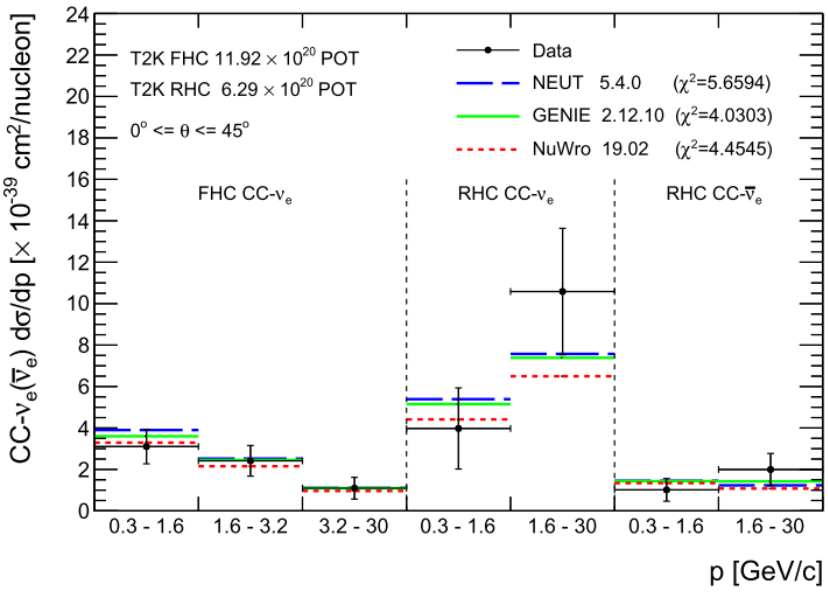

Figure 3.20: The result of the cross-section measurements in the ND280. Results for ν_e (Forward Horn Current, FHC) and $\overline{\nu}_e$ (Reverse Horn Current, RHC) are compared against various theoretical models.

Part II

Heavy neutrino study

CHAPTER 4

HNL IN T2K EXPERIMENT

1 HNL search prospects in T2K

As mentioned in the chapter 2 the discovery of the neutrino oscillation phenomena explicitly indicates non-zero neutrino mass. Several theoretical frameworks were developed trying to describe its nature. Most of them predict the existence of the Heavy Neutral Lepton (HNL) — an electrically neutral particle, that interacts only through the weak interaction. It's sometimes refereed to as a "heavy neutrino". Neutrino Minimal Standard Model (νMSM, subsubsection 1.4.b) is a minimal extension to the Standard Model. It postulates the existence of 3 HNLs. One of them N_1 is pretty light ($M_{N_1} \propto 1keV$) and is responsible for the phenomenon of the Dark Matter. It interacts with SM particles extremely weakly. Two other heavy neutrinos (N_2, N_3) should interact stronger to explain the observed behavior of neutrino oscillations. Their mass can be in a pretty wide range from 100 MeV/c^2 up to 80 GeV/c^2. To be able to generate the baryon asymmetry in the early Universe they should be nearly degenerated $\Delta M_{2,3} \ll M_{2,3}$.

N_2 and N_3 interact with the SM particles through the mixing with the active neutrino. Thus they can be produced in the meson decays $H \to \ell + N$. The mixing is expected to be quite weak hence large statistics is essential for the search for such a process. Only experiments with very intense meson beams are sensitive enough for the HNL production detection. For example, kaon experiments (E949 in BHL, NA62 in CERN) are using stopped kaons to study their decay. They measure precisely the kaon decay position, all the daughter particles, and their kinematics. These experiments performed a search for the rare kaon decay into the massive neutrino $K \to \ell + N$ among the dominating decay into an active light neutrino $K \to \ell + \nu$. The signal signature is slightly different kinematics of the HNL production comparing to the decay into a light neutrino.

The other class of setups with an extremely intense meson beam are neutrino accelerator experiments. The neutrino beam is produced with the proton accelerator. Protons hit the target, producing mesons. These mesons are focused with the magnetic field to obtain the intense neutrino beam. Some of the mesons can decay into the exotic particle — heavy neutrino. There are few neutrino beamline facilities in the world: J-PARC in Japan (T2K experiment) and NuMI in the USA (NOvA, MINOS, MINERvA experiments). The meson beam in such experiments is not precisely monitored, so it's not possible to find a rare meson decay with slightly different kinematics, like in

the kaon experiments. But there is room for a direct search for the HNL decay. The benefit of the decay search is increased sensitivity for the HNL with high mass. In the kaon experiments, higher mass causes low momentum lepton that is hard to detect. On the contrary, high HNL mass causes more energetic daughter particles and increases the detection efficiency in the decay search experiments.

The most probable HNL decays are $N \to \mu\pi$ and $N \to e\pi$. In the neutrino experiments, we expect a huge amount of similar events from neutrino interactions. Neutrino can interact with the nucleus, producing lepton and pion $\nu_\mu + N \to \mu + \pi + N'$ and $\nu_e + N \to e + \pi + N'$. The huge advantage of the T2K experiment in the search for the HNL is a near detector configuration. As it was widely described in the chapter 3 the ND280 detector uses two scintillator targets alternated with three atmospheric pressure TPCs. The gaseous detectors are extremely interesting in the search for the heavy neutrino. The rate of neutrino interactions in gas is extremely low. Even more so the main reaction mode at T2K energies is quasi-elastic interaction, but not the pion production. ND280 is magnetized, so it can separate the oppositely charged lepton and pion from HNL decay. The TPCs provide particle identification with energy loss and also have a good spatial resolution. The latter is essential to select the interactions inside the TPCs only, as we expect many neutrino interactions in the material around the gas volume and the other detectors.

1.1 Analysis overview

In the current work, I study a possibility of the improvement of the constraints on the HNL mixing elements in the T2K experiment. As mentioned above, T2K is expected to have remarkable sensitivity because of the very intense meson beam and the configuration of the near detector. The 30 GeV proton beam from J–PARC accelerator produces mostly pions and kaons. The neutrino and anti-neutrino spectra divided into the parent particle type are presented in Figure 4.1.

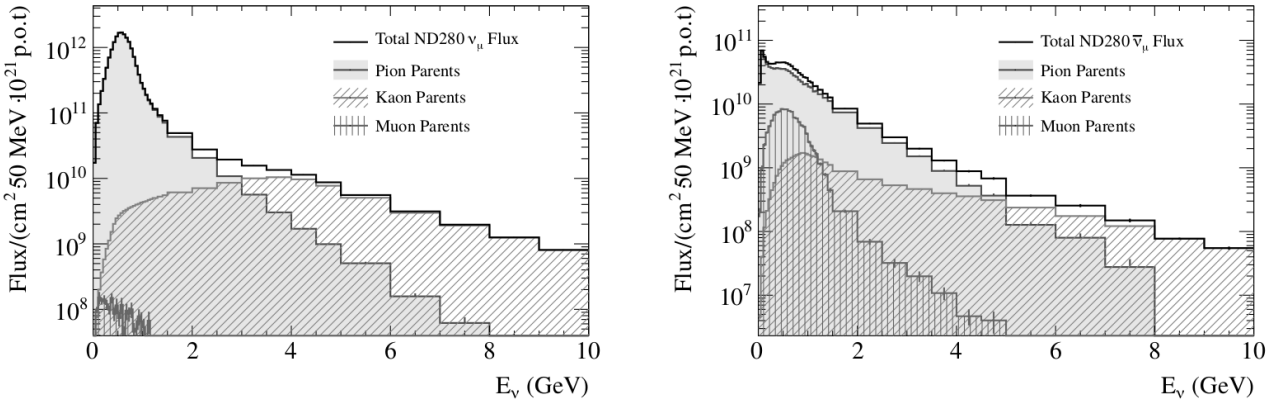

Figure 4.1: The muon neutrino and anti-neutrino flux prediction at the ND280 broken down by the neutrino parent particle type.

Neutrino from pions are dominating but there is still a notable contribution from the kaon decay. Kaons are much more preferable for heavy neutrino studies as they allow us to study a wider mass range. The various HNL production and decay modes are overviewed in [75]. I will use the two-body kaon decay $K \to \ell + N$ as the main source of the potential heavy neutrinos. Three-body reactions are much rarer. Also, they provide less focused HNL beam, thus fewer particles will reach near detector. Among the heavy neutrino decay modes, I will choose the "visible" ones that produce charged particles (e.g. $N \to \nu\nu\nu$ mode is omitted). The most probable among them are two-body decays into lepton and pion. Three-body reactions with the neutrino in the final state are less probable, but also considered in the current analysis. The chosen heavy neutrino production

and decay modes are presented in Figure 4.2. The HNL mass ranges allowed by the kinematics for each particular mode are shown.

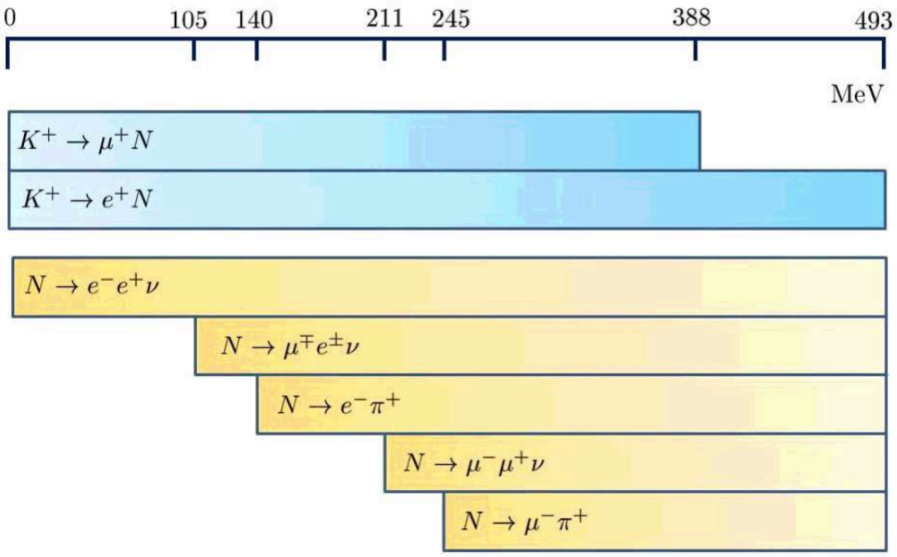

Figure 4.2: Summary of the production and detection processes of the heavy neutrino available for the analysis with the ND280. The horizontal axis corresponds to the HNL mass

The three ND280 TPCs will be used as a fiducial volume to search for the HNL decay. The density of the atmospheric pressure gaseous detectors is nearly 3 orders of magnitude smaller comparing to scintillator targets. Thus superior suppression of the active neutrino interactions is reached. The expected event signature is a production of the oppositely charged lepton and pion in the gas. The TPC allows to reconstruct accurately decay vertex position. The ND280 detector will provide the separation of the charged particles in the magnetic field. No activity is expected upstream to the vertex as we are looking for the neutral particle decay. The simulation of the signal events and the detector response as well as detector efficiency will be presented in subsection 1.2 of chapter 5.

The most probable background for the process of interest is the active neutrino interactions. Though their rate is quite low in the gas, with the large statistics we will still see some of them. The most dangerous process is pion production as it will mimic the signal. But such a background can be separated from the signal based on the different kinematics. The direction of the heavy neutrino can be reconstructed based on daughter particles tracks and it's expected to be strictly collinear to the neutrino beam. During the active neutrino scattering over the nucleus (e.g. $\nu + n \to \mu + \pi + p$) the direction of the $\mu\pi$ pair can be distributed over a wide angle.

We are going to search for the low-rate process in the low background environment. The usual method to compute the upper limit on the process of interest in such a case is Feldman & Cousins approach [117]. In my analysis proper treatment of the uncertainty is essential. Thus I will use the different algorithm that was developed by Highland & Cousins [115]. The details about the statistical interpretations of the results will be overviewed in section 3 of chapter 5.

The prediction of the possible improvements on the upper limits of the HNL mixing elements in the T2K experiment was done by Asaka [118]. One of the main goals of my study is to check the phenomenological prediction and to proceed to the final results.

2 HNL signal simulations

The first step of the analysis is the simulation of the HNL flux at the ND280. The simulation of neutrino flux at the near detector has already been developed for the oscillation analysis. I decided to use the obtained results and adapt them to the HNL analysis. With this simulation, we have all the information about the neutrinos entering the ND280 and their parent particles. Because of the kinematics, the phase space of the meson decay into HNL is more limited than the decay into a nearly massless neutrino. E.g. the maximum angle of the HNL direction with respect to the parent meson direction is lower comparing to the massless neutrino case. Thus if we consider only mesons that can produce neutrino entering ND280 and omit all the others, we will definitely take all the possible HNL parent particles.

For the heavy neutrino simulation, we consider the particular meson decay and reweight it taking into account new kinematic and the branching ratios. Thus we will obtain the heavy neutrino spectrum in our detector. The next step is the simulation of the HNL decay in the sensitive detector. I considered two- and tree-body decays of the heavy neutrino. A random direction of the daughter particle was generated and the appropriate decay width was taken into account. Thus I obtained the Monte–Carlo signal samples that can be used for the selection optimization and the detector systematic studies.

2.1 T2K flux simulation

The accurate prediction of the neutrino flux is extremely important for precise oscillation analysis. That's why the T2K collaboration has spent great effort into tuning the flux simulation most accurately [108]. All the elements of the neutrino beamline are taken into account. The most tricky part is the evaluation of meson production through the proton interactions in the carbon target. As this step is critical for the HNL study, I will overview the simulation process in detail.

The overview of the T2K beamline is presented in section 1 of chapter 3. The proton beam spatial distribution and divergence are measured with the beamline monitors. The FLUKA generator is used to perform the simulation of the hadron interaction with the target and a baffle. The position and direction of an incident proton is well–defined with beamline monitors measurements. Proton energy is set to 30 GeV. The information of the generated particles that exited the target volume is stored. The cross–section and the multiplicity of the meson production is a subject of uncertainty. The NA61/SHINE experiment has performed the series of measurements with the T2K-replica target to measure precisely the process of interest.

NA61/SHINE experiment

The NA61/SHINE (SPS Heavy Ion and Neutrino Experiment) [119] is a multi-purpose facility at CERN that operates with a secondary beam from the Super Proton Synchrotron (SPS) in the North Area of CERN. A 450 GeV proton beam is focused on the primary target. The secondary particles with given momentum are selected by the horn system and focused on the secondary target. The main physics goals are:

- ➢ study the properties of the onset of QCD deconfinement and search for the quark–gluon plasma critical point with investigating p+p, p+Pb and nucleus-nucleus collisions,
- ➢ precise hadron production measurements for improving calculations of the initial neutrino beam flux in the long-baseline neutrino oscillation experiments as well as for more reliable simulations of cosmic-ray air showers.

The detector operates at the fixed-target mode at a secondary SPS beam. The detector scheme is presented in Figure 4.3. The setup consists of the trigger system, TPC tracking system with superconducting magnets, time of flight detectors and Projectile Spectator Detector (PSD).

For the T2K purpose the experiment performed the measurements of the hadron interaction multiplicities in a proton-target collisions. Both thin carbon target and a T2K-replica target were used in the analysis. This data allows to constrain the neutrino production at the T2K much more precisely.

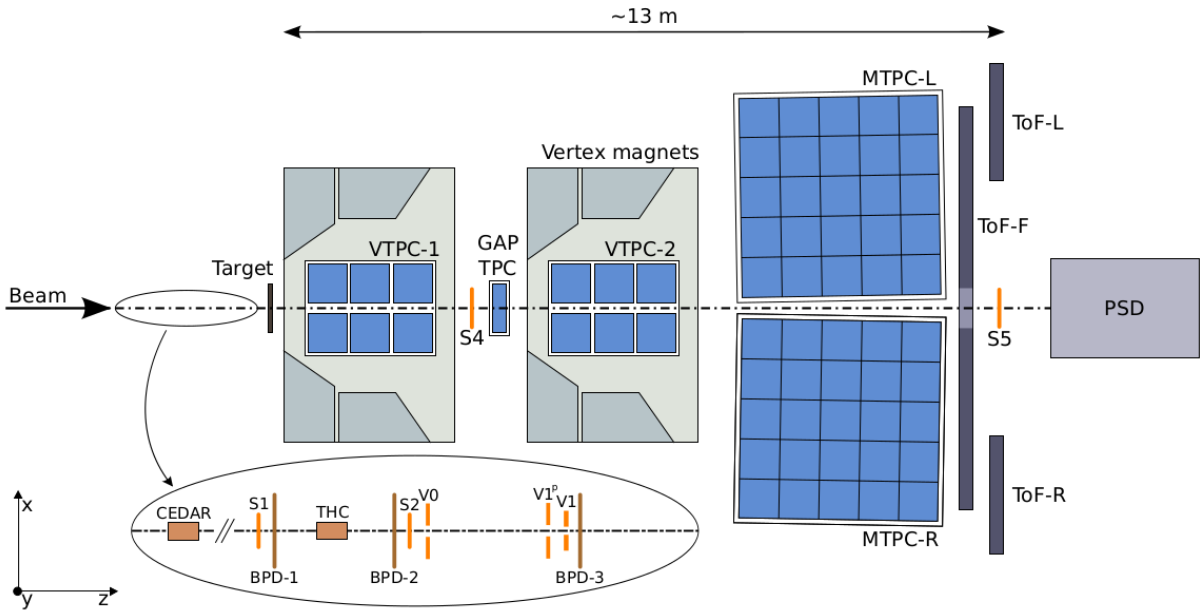

Figure 4.3: The scheme of the NA61/SHINE experiment.

The flow diagram of the neutrino flux simulation is shown in Figure 4.4. After the meson production simulation, we track them through the horns, helium vessel, decay volume, and surrounding concrete until the decay or the kinetic energy drop down below the threshold (10 MeV). The GEANT3 simulation toolkit is used for this purpose. At this step $\pi^{\pm}$, $K^{\pm}$, K^0_L, and $\mu^{\pm}$ decays are considered as neutrino sources. To save computing time, the daughter neutrino is pointing towards the Super–Kamiokande and the appropriate kinematic weight is assigned to the event.

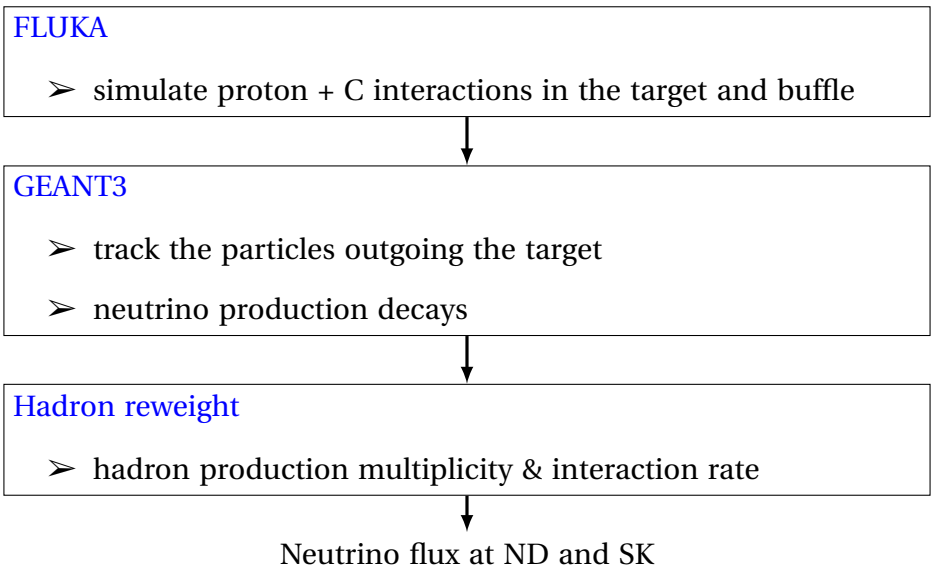

Figure 4.4: The neutrino flux prediction flow

After such a simulation chain is performed and the outgoing neutrino is registered the hadronic chain in each event is re-weighted based on the hadron interaction measurements. In our studies, we are particularly interested in kaon production. The generated kaon phase space and the coverage of the NA61 measurements are presented in Figure 4.5.

After the reweighting of the hadron chains, the total accuracy of the prediction is evaluated [108]. The main systematic errors come from the hadronic interactions, primary beam alignment, horn current, and magnetic field. The resulting uncertainty of the neutrino flux predictions is shown in Figure 4.6.

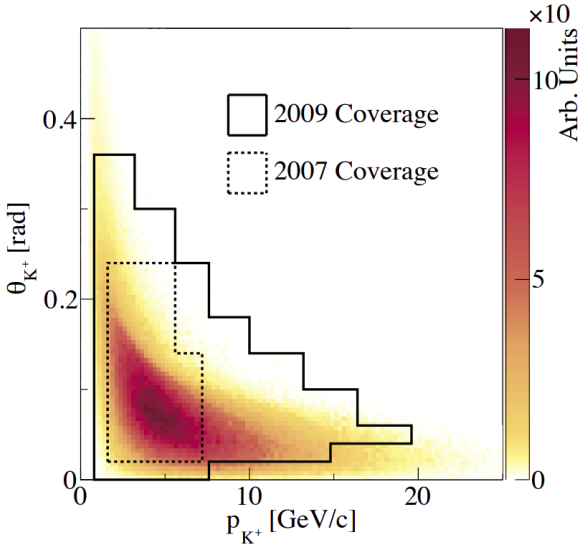

Figure 4.5: The phase space of positive kaons contributing to the predicted neutrino flux and the regions covered by the NA61/SHINE.

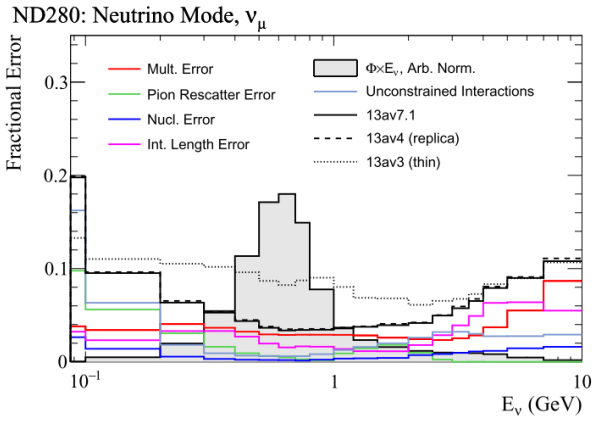

Figure 4.6: Fractional errors for the muon neutrino flux.

2.2 HNL production

For the purpose of our study, I would like to reweight the kaon decays for the case of HNL production. But I want to use all the fine-tuning described in the previous section to keep the uncertainties as small as possible. Looking at the Figure 4.4, I would like to apply a new weight at the second step "neutrino-producing decays", but to keep everything else at place. The HNL production will be different from the decay into active neutrino because of the different branching ratios and the kinematic weight.

The new branching ratio is calculated according to [75]:

$$Br(K \to \ell + N) = \frac{G_F^2 V_{us}^2 f_K^2 M_K M_{HNL}^2}{8\pi\hbar}\left(1 - \frac{M_{HNL}^2}{M_K^2} + \frac{2M_\ell^2}{M_K^2} + \frac{M_\ell^2}{M_{HNL}^2}\left(1 - \frac{M_\ell^2}{M_K^2}\right)\right) \sqrt{\left(1 + \frac{M_{HNL}^2}{M_K^2} - \frac{M_\ell^2}{M_K^2}\right)^2 - \frac{4M_{HNL}^2}{M_K^2}} \cdot \tau_K, \tag{4.1}$$

where

- G_F — Fermi constant,
- V_{us} — the CKM matrix element,
- M_ℓ and M_{HNL} — the lepton and the HNL masses,
- M_K, f_K, τ_K — kaon mass, form-factor, lifetime respectively.

The usual approach for the decay simulation is to throw the daughter particle direction uniformly in 4π angle. But in this case, most of the particles are lost because they will not reach the detector. To gain the simulation statistics I pointed all the produced heavy neutrinos into ND280. But to keep the total number of events consistent I assigned a weight to each heavy neutrino. The geometry weight is calculated as a probability of a daughter particle to have a momentum with a certain angle θ w.r.t. the parent momentum. As kaons mostly decay in flight I also need to apply the Lorentz boost from the center of mass frame to the laboratory frame.

$$\begin{aligned} weight_{geom,lab} &= \frac{p_{lab}E_{cm}}{p_{cm}^2} \cdot weight_{geom,cm} \\ weight_{geom,cm} &= \frac{1}{4\pi}\delta\left(p - p_{cm}\right) \end{aligned} \tag{4.2}$$

The final expression for the geometry weight will look like

$$weight_{geom,lab} = \frac{1}{4\pi}\frac{p_{lab}E_{cm}}{p_{cm}^2}\frac{cos\theta_{lab}\left(\beta/\beta_{lab} \pm \sqrt{1 + \gamma^2\left(1 - \left(\beta/\beta_{lab}\right)^2\right)tg^2\theta_{lab}}\right)}{\gamma\left(1 - \beta^2 cos^2\theta_{lab}\right)}. \tag{4.3}$$

Here I assume that the HNL's lifetime is large enough to reach the ND280. From the cosmology [75] we have an upper bound on the HNL lifetime $\tau < 0.1s$, which is mainly based on the baryogenesis models. So for the current analysis I have the HNL lifetime region $1\mu s \ll \tau < 0.1s$ which is wide enough. An estimation of the corresponding mean free path of the HNL gives $\Lambda_{HNL} = c\beta\gamma\tau \gg 280m$.

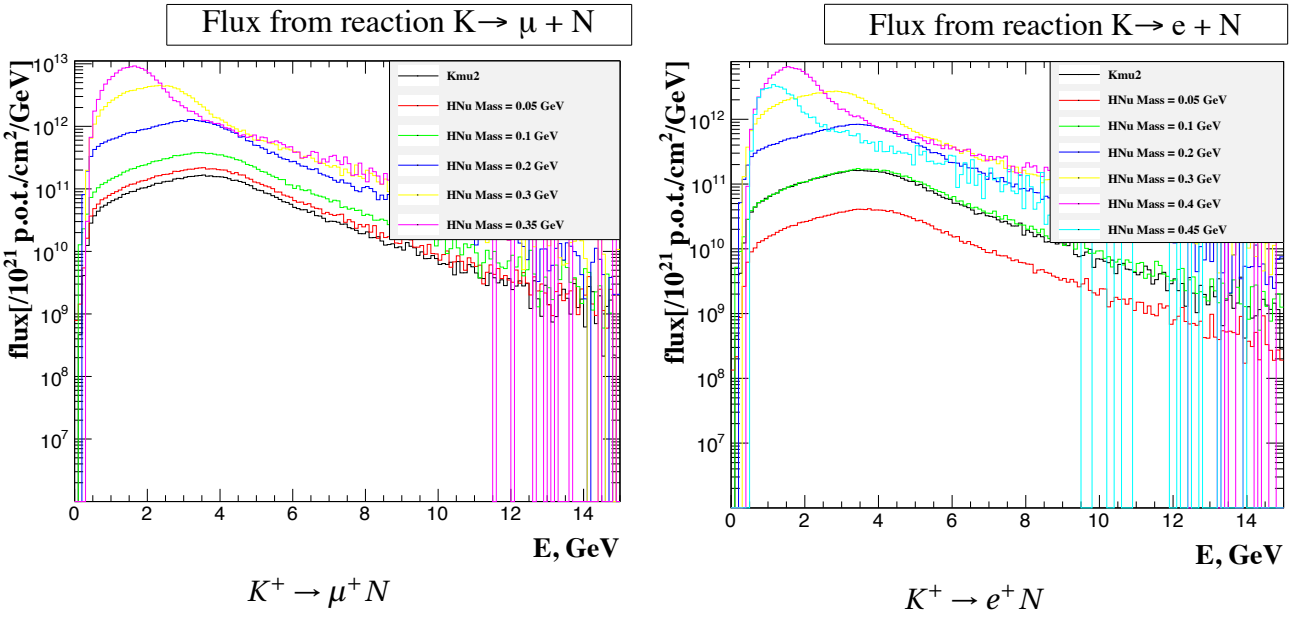

Figure 4.7: HNL energy spectra at the ND280 front plane for two production modes: $K^+ \to \mu^+ N$ and $K^+ \to e^+ N$ for the different HNL masses.

To cross-check my kinematic model I compared the HNL spectra for $M_{HNL} = 0$ with the active neutrino spectrum from $K\mu 2$ and made sure that they are identical. After performing modeling of all kaon decays I got the HNL spectra at the ND280 entrance plane (Figure 4.7).

There are two effects, that cause the flux difference comparing to the active neutrino flux. The first one is the "massive" kinematic of the parent meson decay. This correction is calculated according to Equation 4.3. This impact is shown in Figure 4.8. The branching ratio is assumed equal to 1. One can see that the higher mass increases the probability of the HNL to reach the detector. It's understandable as with the higher mass the maximum heavy neutrino angle w.r.t. kaon direction becomes lower. Most of the kaons decay in flight and the HNL is boosted towards the near detector.

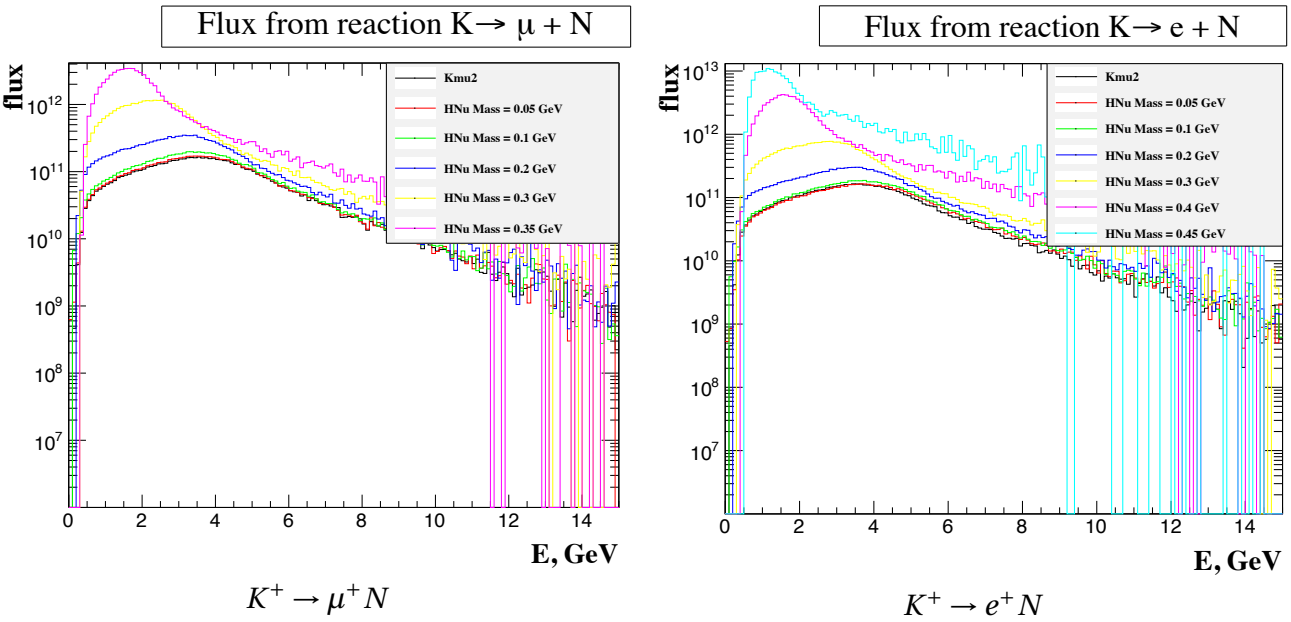

Figure 4.8: HNL spectra at the ND280 front plane for two modes and for the different HNL masses assuming the branching ratios equal to 1.

The second effect is the modification of the branching ratio of the kaon decay. It is calculated according to Equation 4.1. The branching ratio dependence is shown in Figure 4.9. Notice that it can be larger than 1 as the mixing element is considered 1, in reality, it will reduce the branching ratio below the level of one. The branching ration is decreasing dramatically for the low and high regions of the HNL mass. Sometimes low branching ratio can cancel the benefits from the kinematics. E.g. the light HNL flux from the $K \to e + N$ decay is lower than the active neutrino flux from $K\mu 2$.

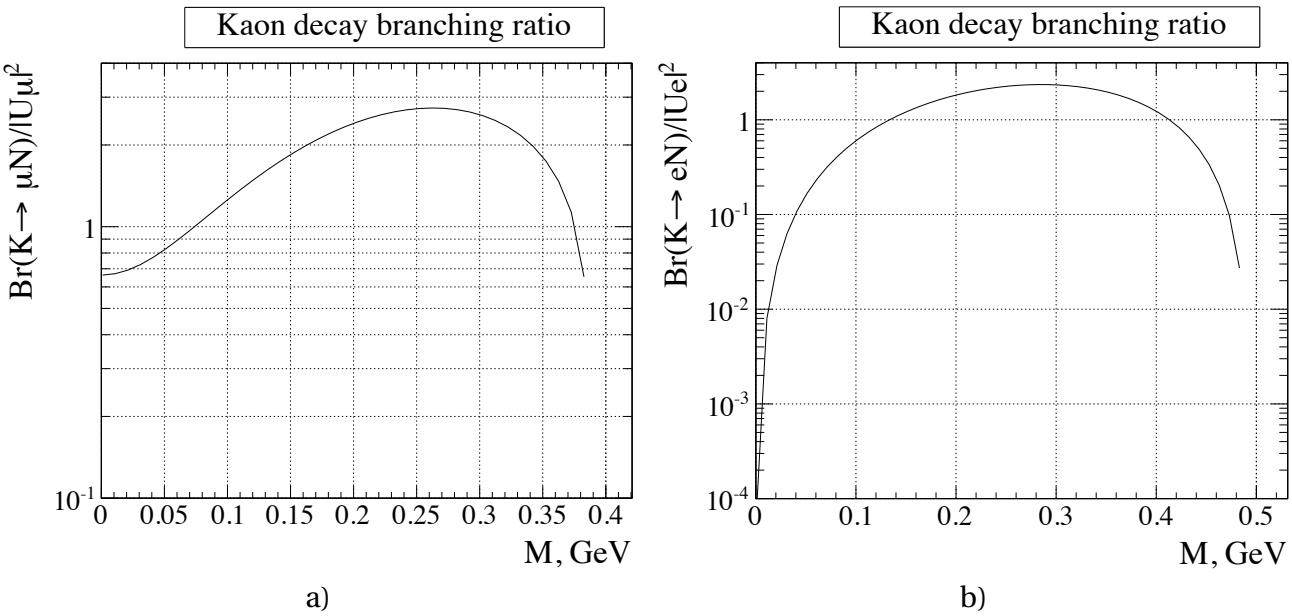

Figure 4.9: Kaon decay branching ratio divided into the mixing element for two modes: (a) $K \to \mu N$ and (b) $K \to eN$.

In our study, I assume the Majorana nature of the HNL. Hence the parent meson charge is irrelevant. In the analysis, I combine the heavy neutrinos from both K^+ and K^- decays. As one can see in Figure 4.1 the neutrino flux from the K^- is nearly 3 times smaller comparing to one from K^+. It is caused by the lower negative kaon production cross–section.

2.3 HNL decays

Now I have all the information about the HNLs that enter ND280. Thus I can generate the secondary particles that will be produced in the heavy neutrino decay. It will be the expected signal in my analysis. The decay itself is simulated in the HNL rest frame. Then the boost is applied towards the heavy neutrino initial direction. The decay points are randomly generated along the HNL tracks inside the TPC volume. So the decay positions are expected to be uniformly distributed in this volume (Figure 4.10). The small excess of HNL decays in the bottom left is related to the off-axis beam nature. This corner is closer to the beam axis.

The simulation of the 2-body decay is straightforward. The direction of the first particle is thrown isotropically. Then based on both momentum and energy conservation laws the whole decay is parametrized in the HNL rest frame. I will obtain the final kinematics of the daughters with the boost along with the heavy neutrino momentum. The kinematic evaluation is covered in [120], chapter 2.

The 3-body decay case is a bit more complicated. For this mode, I can't just throw all the directions as I have one degree of freedom in the decay. To deal with it I used the normalization with the

maximum width of the decay. For each event the direction of the daughter particles is still thrown randomly, but the following weight is assigned:

$$weight_{3-body} = weight_{K\to\ell N} \cdot \frac{\frac{d\Gamma(p_1,p_2)}{dp_1 dp_2}}{max\left(\frac{d\Gamma(p_1,p_2)}{dp_1 dp_2}\right)} \cdot P, \tag{4.4}$$

where P is a 3-body decay weight from the kinematics [121]. As $weight_{3-body} \leq 1$ the total number of 3–body decays is reduced. So this number can not be used for the proper estimation of the total number of events. It is crucial to evaluate the probability of the particular event. Because of the kinematics one event can be easier to reconstruct because of the hardware setup (e.g. larger opening angle), but it can be less probable. As I use these samples for the relative efficiency calculation only, the global normalization can be biased but the relative weight should be treated properly.

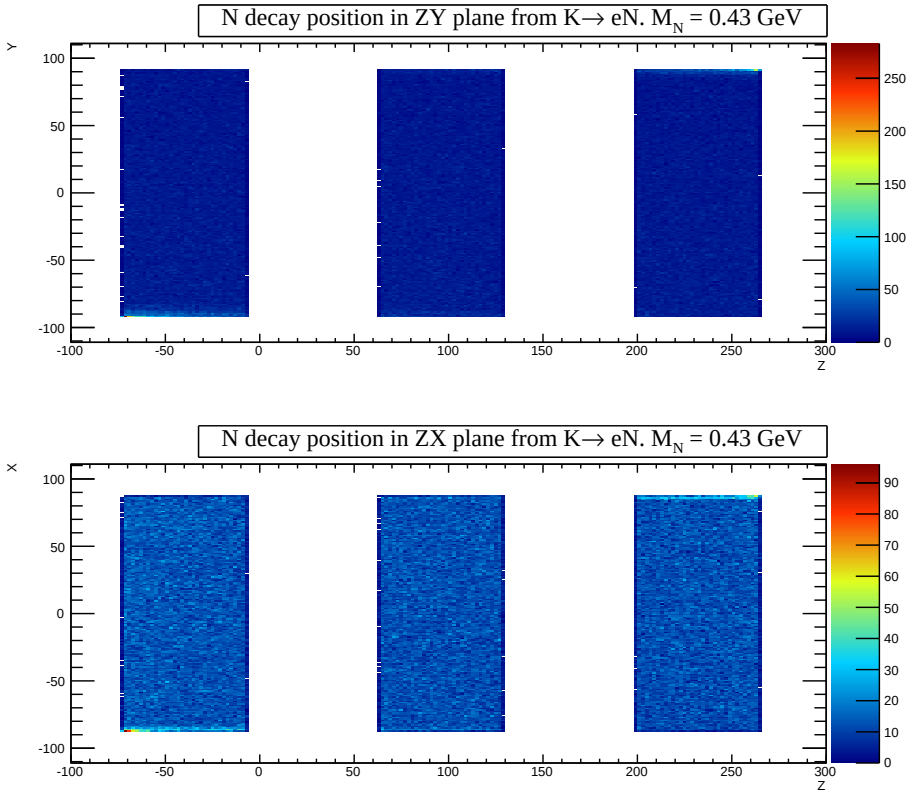

Figure 4.10: Distribution of HNL decay positions over 3 TPCs. The decay position is in the detector coordinate system in mm.

The polarization of the HNL is taken into account in the simulation according to the calculations from [122]. The HNL polarization is given by:

$$\overrightarrow{\prod} = \frac{(\delta_\ell - \delta_N)\,\lambda^{1/2}(1,\delta_\ell,\delta_N)}{\delta_\ell + \delta_N - (\delta_N - \delta_\ell)^2}\overrightarrow{n} \tag{4.5}$$

where

- $\delta_N = (M_N/m_K)^2$
- $\delta_\ell = (m_\ell/m_K)^2$
- $\lambda(x,y,z) = x^2 + y^2 + z^2 - (xy + yz + xz)$

➢ $\vec{n}$ is the kaon direction in the heavy neutrino rest frame

The polarization of the HNL as a function of its mass in the decay $K \to \mu + N$ is shown in Figure 4.11. One can see that in the limit $M_N \to 0$ the heavy neutrino behaves exactly as a massless neutrino and becomes left-handed. Also, it's interesting to see that the polarization vanishes when the HNL mass is equal to the muon one.

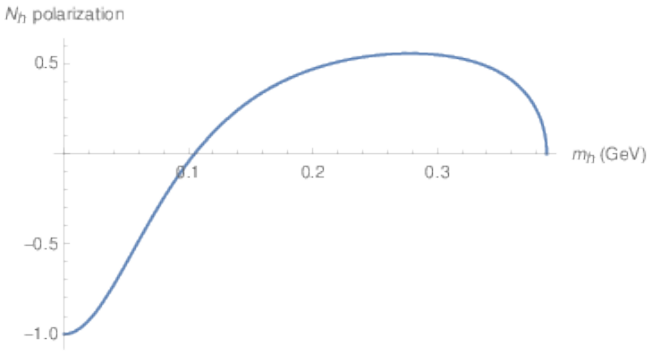

Figure 4.11: The polarization of the HNL as a function of its mass in the decay $K \to \mu + N$ [122].

The polarization of the beam ($\vec{\prod}$) is a statistical effect. As the HNL is a fermion it can take only discrete polarization: -1 or 1. In the simulation, the polarization value is computed for each decay and a random value is thrown in the range (-1; 1) to determine if the HNL is left-handed or right-handed. Then this characteristic is taken into account during the heavy neutrino decay simulation with:

$$\frac{dN}{d\cos\theta}(N \to \ell\pi) \propto \left(1-\delta'_\ell\right)^2 - \delta'_\pi\left(1+\delta'_\ell\right) - \frac{\sqrt{\lambda'}}{2}\left(1-\delta'_\ell\right)\vec{\prod}\cos\theta \tag{4.6}$$

where:

➢ $\delta'_\ell = (m_\ell / M_N)^2$

➢ $\delta_\pi = (m_\pi / M_N)^2$

➢ $\lambda' = \lambda\left(1, \delta'_\ell, \delta'_\pi\right)$

➢ θ is an angle between the outgoing lepton and the parent meson (kaon) in the HNL rest frame

After simulation of the HNL decays I have all information about the kinematics of the daughter particles, i.e. momentum, direction, opening angles. These characteristics are presented in Figure 4.12. It's important to note that most of the particles have momentum below 2 GeV/c. Our TPCs were designed to reconstruct the tracks with momentum below 10 GeV/c. So the charge and the momentum can be precisely measured.

The heavy neutrino daughter particles are propagated through the detector with the help of the Geant4 toolkit [123]. All the secondary interactions, decays, etc. are considered. An example of a "good" MC event with the HNL decay in the first TPC and further evolution of a daughter muon and a pion is shown in Figure 4.13. The detector response is fully simulated from the initial ionization until the readout signal from the electronics. Thus I can develop the event selection and estimate its efficiency with the MC generated signal sample.

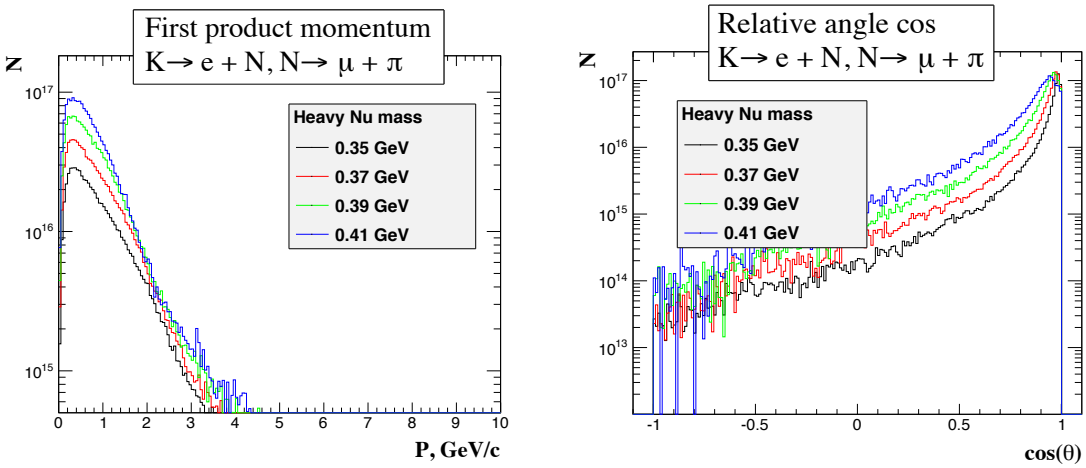

a (b)

Figure 4.12: Kinematics spectra of the HNL daughter particles: (a) momentum and (b) opening angle.

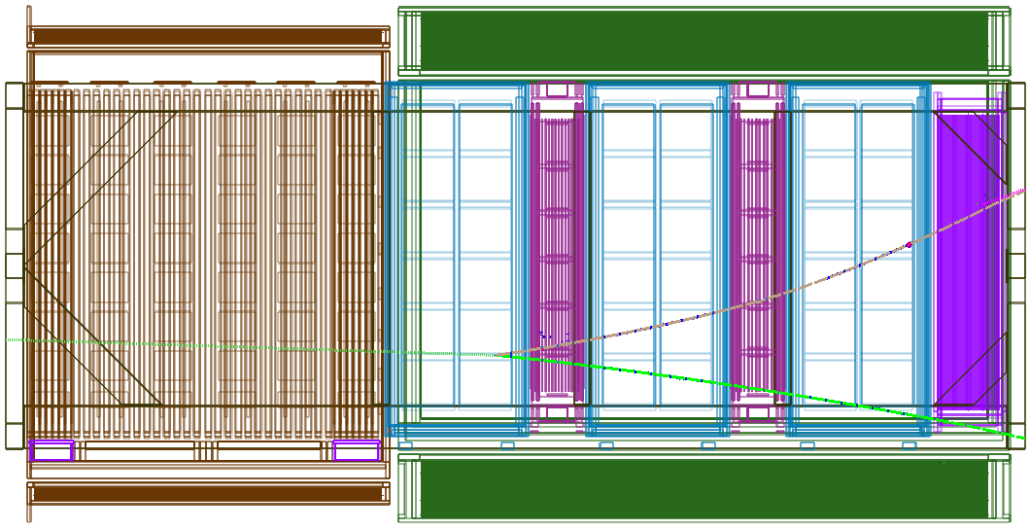

Figure 4.13: Example of simulated event from HNL decay in the first TPC. Dashed green line corresponds to HNL track, green line to the muon track, brown line to the pion track.

CHAPTER 5

HNL ANALYSIS

The search for heavy neutrinos consists of several steps. After the generation on the signal sample described in the previous chapter, the event selection can be developed. I don't expect too much background from the active neutrino interactions as we are using the fiducial volume of the atmospheric pressure TPC as the main detector. But because of the intense T2K neutrino beam some neutrinos will still interact there. The cut sequence to pick up the signal events and reject the background was developed to gain the sensitivity of the analysis.

An accurate systematic uncertainty evaluation is required to put robust upper limits on the HNL mixing elements. In our study, we use only HNL flux prediction simulation and detector efficiency to obtain the final results. Thus these two estimations are the only sources for the possible uncertainties. The systematics of kaon production have been studied in the other T2K analysis and can be applied in a straightforward way for the HNL analysis. The detector systematic needs to be studied more carefully. All the differences between the expected and observed detector behavior should be considered as an uncertainty. More details are provided in section 2.

1 Event selection

According to my analysis strategy, the background is severely suppressed by the fiducial detector choice. Very few active neutrino interactions are expected in the atmospheric pressure TPCs. But still, some of them are possible. The most dangerous are pion production as they are very similar to the expected signal. The vertex migration from the other detector is another possible reason for false HNL detection. The cut sequence is divided into two main parts: basic and advanced.

In the basic part, I select a pattern that is expected to be observed from the signal of interest. For example, for the $N \rightarrow \mu\pi$ decay, a vertex with two tracks should be reconstructed in the TPC fiducial volume. The particles should be oppositely charged and properly identified with the dE/dx in the gas. This part of the selection is referred to as "basic " as all the criteria came directly from the expected signal pattern. No cut changes are expected in this part.

The "advanced" part of the selection is dedicated to the separation between the signal and the background. First of all the veto cuts should be defined. As we are looking for the neutral particle decay the upstream activity may serve as good veto criteria. Then I am going to study the kinematics spectra for both signal and background samples and find the most optimum cut values to gain the analysis sensitivity. We expect the most powerful background reduction from the cut on the

reconstructed heavy neutrino direction. The decay of neutral particles is expected to be extremely collinear with the beam axis while the active neutrino interactions will produce particles in the wide angular range.

1.1 Cuts description

The "basic" selection searches for the signal-like pattern in the TPC fiducial volume. The following cut sequence is defined:

1. Vertex in the TPC fiducial volume.
2. Two oppositely charged tracks associated with this vertex;
3. Proper particle identification (PID) as $e\pi$ or $\mu\pi$ using dE/dx in the TPC;

With such a simple selection I would like to keep as many signal events as possible. Any signal event is expected to match the criteria above. The efficiency loss can be caused only by the wrong reconstruction.

The vertex requirement is a key point of the selection. The tracks matching into the vertex is performed with Kalman filter. It appeared that this requirement causes a dramatic efficiency reduction. Only 40% of signal events pass the first cut. It happens because T2K TPCs are not optimized for the reconstruction of close tracks. The HNL decay is usually very relativistic and the daughter particles have a very small opening angle (Figure 4.12). The length of the TPC is about 70 cm. Sometimes it is not enough for the robust track spiting despite the good spatial resolution of the detector. The HNL decay points are distributed uniformly over the TPC volume that makes the situation even worse. Quite often it is placed close to the downstream scintillator detector. The resolution of the latter is limited by the scintillator bar size. Quite often the outgoing pion can interact inside the scintillator detector that makes the vertex reconstruction completely impossible unless lepton and pion tracks were separated enough in the TPC volume.

Vertexing with Kalman filter

The Kalman filter is a recursive filter that estimates the internal state of a dynamic system from number of noisy measurements. Originally it was developed for the rocket science and is still actively used in this field. The flow of the method is shown in Figure 5.1. As one can see we start with the prior measurements, make a prediction about the next step based on the model, then correct the prediction with the actual measurement.

In the case of the vertex finding in the detector the model is the track propagation through the detector in magnetic field. For the prior we extrapolate the reconstructed tracks to the closest intersection point. Then we go through several iterations using the observed detector hits as a data. At the end we arrive to the precise reconstruction of the vertex position with the know uncertainty and the quality of the fit.

The second cut that rejects many signal events is particle identification. I use the energy loss in the TPC (dE/dx) to determine the particle type. In ND280 detector the particle identification is done with the likelihood function comparison. Four hypotheses are built with the comparison of the expected and observed energy loss for electron, muon, pion, and proton. The problem occurs in certain kinematics regions where the energy loss is similar for the different particles. E.g. proton and muon/pion can be confused at the momentum around 1.5 GeV/c. Also, positron and proton have very similar dE/dx at a momentum around 1 GeV/c. Though the particle identification works

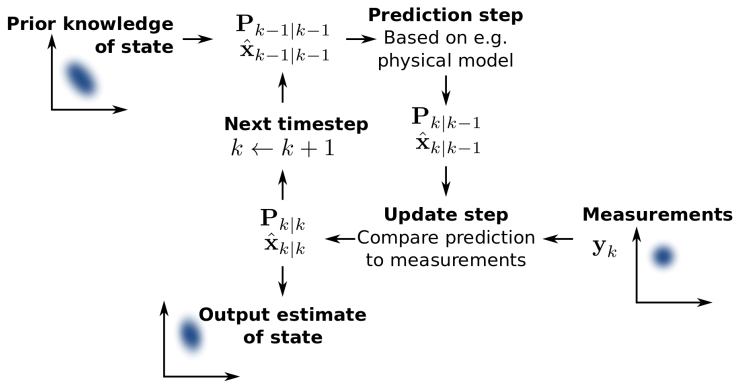

Figure 5.1: The flow of the Kalman filter usage.

quite well it is the second cut that most reduces the HNL selection efficiency (by 30% with respect to previous cut Figure 5.6).

The "advance" part of the selection is aimed at the background reduction. The following cuts are applied:

- ➢ No activity in the upstream detector;
- ➢ No other tracks start in the same TPC;
- ➢ Invariant mass cut: e.g. $140 MeV < M_{HNL} < 850 MeV$ for the $e\pi$ mode
- ➢ Polar angle for HNL candidate: e.g. $\theta < 8.0°$ for the $e\pi$ mode
- ➢ Opening angle between daughter particles $cos\theta > 0.00$;

These requirements affect very little the signal selection efficiency but are essential for the background reduction. The neutrino interaction can take place in the upstream detector but due to the reconstruction failure, the vertex can be placed in the TPC fiducial volume. To reject such an event any upstream activity is used as a veto and event is not considered as a signal. The other source of the backgrounds is the inefficient track matching into the vertex. For example, an active neutrino interacts in the TPC volume but more than two tracks are produced. Sometimes vertex matching algorithm can associate only two tracks with the vertex and leave the others unassigned. To reject this process I require no other activity in the TPC besides two tracks that are matched with the HNL candidate decay vertex.

The most powerful cuts for background rejection are the kinematic cuts. The reconstructed invariant mass should be in the kinematically allowed region. Since we are looking for the HNL from kaon decay it can not exceed 493 MeV/c^2. But ND280 can not measure the invariant mass of the HNL in a precise way. Some tolerance is needed to keep efficiency high enough. ND280 invariant mass resolution was found to be at level of 50 MeV/c^2 for $N \rightarrow \mu\pi$ mode and 70 MeV/c^2 for $N \rightarrow e\pi$ mode. Nevertheless, this cut is powerful for neutrino interaction rejection since this process can cause the "invariant mass" to be in a very wide range.

The reconstructed direction of the HNL candidate is expected to be parallel to the neutrino beam. The products of the neutrino interaction can be distributed in a wide angle. Neutrino interactions are affected by the nuclear effect thus the invariant direction is biased w.r.t. neutrino beam direction. I studied the distribution of the polar angle of the HNL candidate for events that passed all previous cuts, as it is the most strict kinematic cut. Then we looked at the opening angle of the HNL candidate daughters. The results are presented in Figure 5.2 and Figure 5.3.

The cut values are summarized in Table 5.1. The efficiency drop on each cut is shown in Figure 5.6 and compared to the background reduction in Table 5.2, Table 5.3.

Cut	$N \to e\pi$	$N \to \mu\pi$	$N \to \mu\mu\nu$
M^{inv}_{HNL}, MeV/c^2	140 - 850	250 - 750	-
θ^{polar}_{HNL}, degree	< 3.7	< 7.9	< 17
$\theta^{opening}$, degree	< 90		

Table 5.1: The cut values summary for different HNL decays modes.

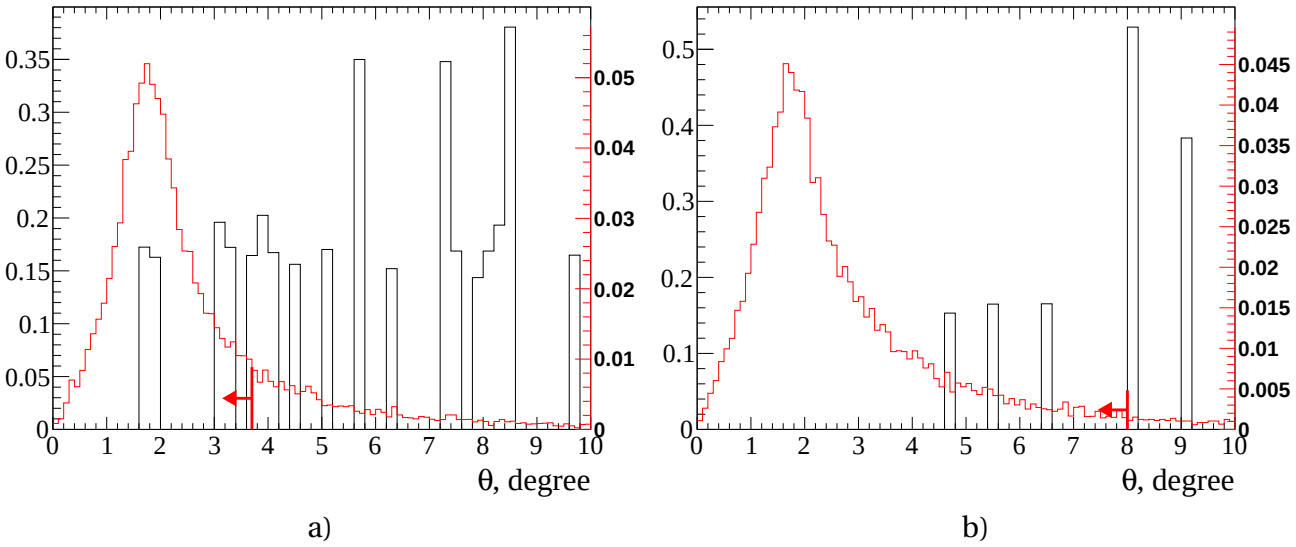

a) b)

Figure 5.2: Angular distribution of the HNL candidate events (a) for $\mu\pi$ mode and (b) for $e\pi$. Red is the MC signal samples, black is the MC background from the neutrino interactions and vertical line is a cut value. Background spectrum is normalized to $10^{21} POT$, signal is normalized to 1.

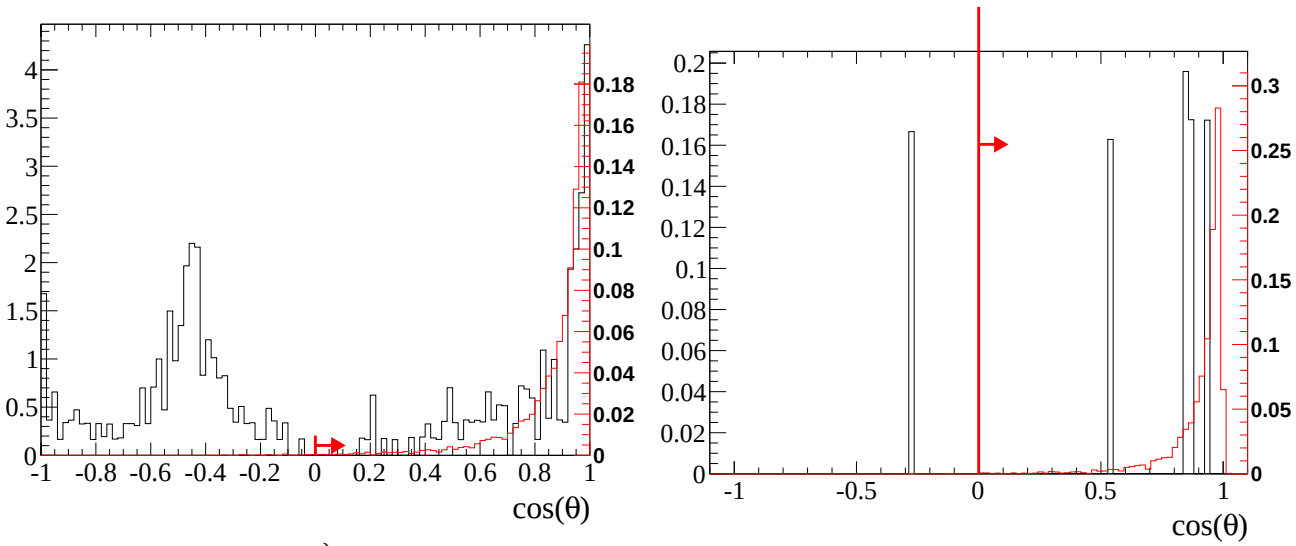

a) b)

Figure 5.3: Opening angle for the HNL daughter particles for the $\mu\pi$ mode (a) before the polar angle cut was applied and (b) after. Red is the MC signal samples, black is the MC background from the neutrino interactions and vertical line is a cut value. The background is normalized to $10^{21} POT$, the signal is normalized to 1.

a $N \to \mu\mu\nu$ mode cuts

The dimuon mode requires a special selection. Two muons can not be produced in the neutrino interactions and I want to use the benefits of that fact. But it is not possible to distinguish a

muon from a pion using the energy loss in the TPC. So I decided to use the ECal. Pions are expected to cause a shower in the calorimeter while a muon will leave a clean track. So an additional cut was applied. Each muon candidate should reach ECal and behave as a track there. The kinematics cuts were also reviewed. The three-body decay with a neutrino will not allow reconstructing the HNL direction as precisely as a two-body decay. So less strict cut on the polar angle was set.

1.2 Signal selection efficiency

Applying all these cuts to the signal samples give us the total selection efficiency (Figure 5.4, Figure 5.5). The efficiency of the HNL selection in my analysis is defined as a ratio of the number of the selected events to the number of the generated HNL events inside the TPCs fiducial volume. The main reason for the dependence of the efficiency on the HNL mass is track reconstruction. For the large HNL mass, we have more events with successfully reconstructed tracks associated with the decay vertex.

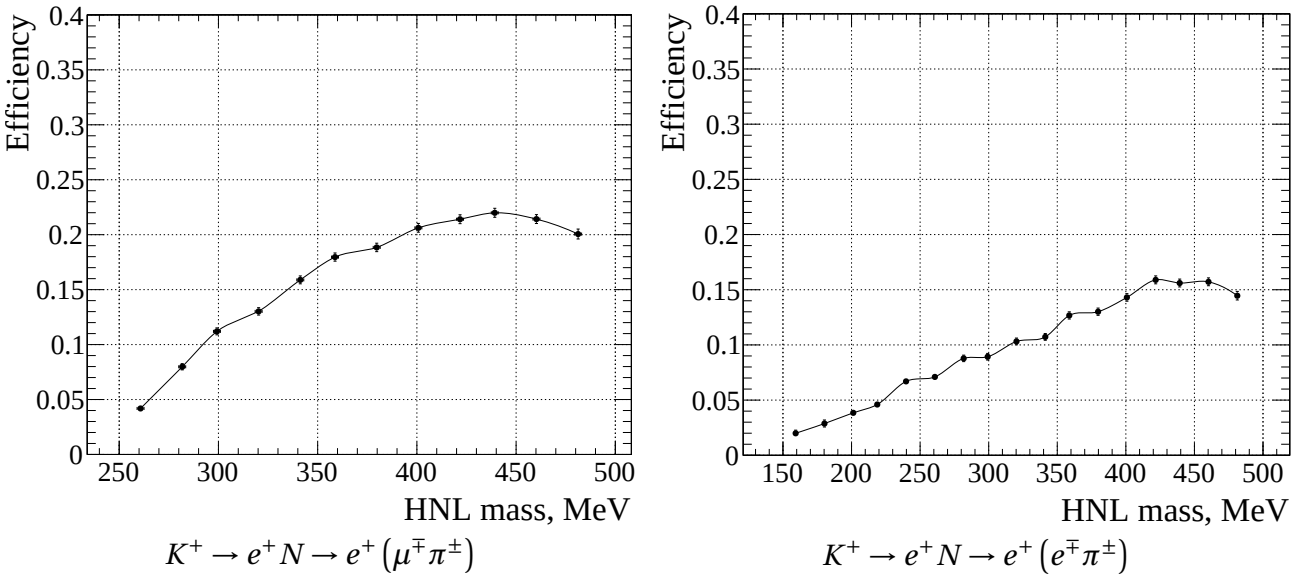

Figure 5.4: Selection efficiency for two body decays of HNL.

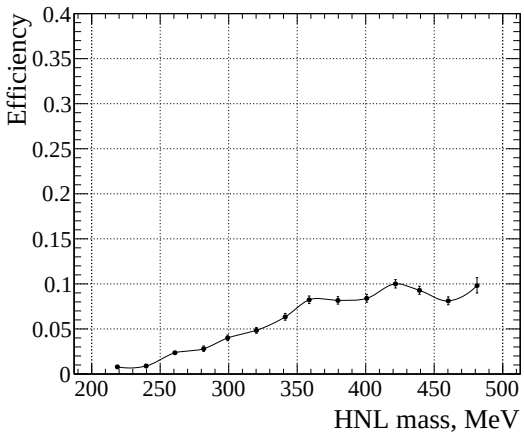

Figure 5.5: Selection efficiency for HNL decay mode $N \to \mu\mu\nu$.

The efficiency dependence on different cuts is shown in Figure 5.6. The main drop is caused by the inefficient track matching algorithm. As was mentioned above HNL decay cause two close tracks that are difficult to separate with ND280.

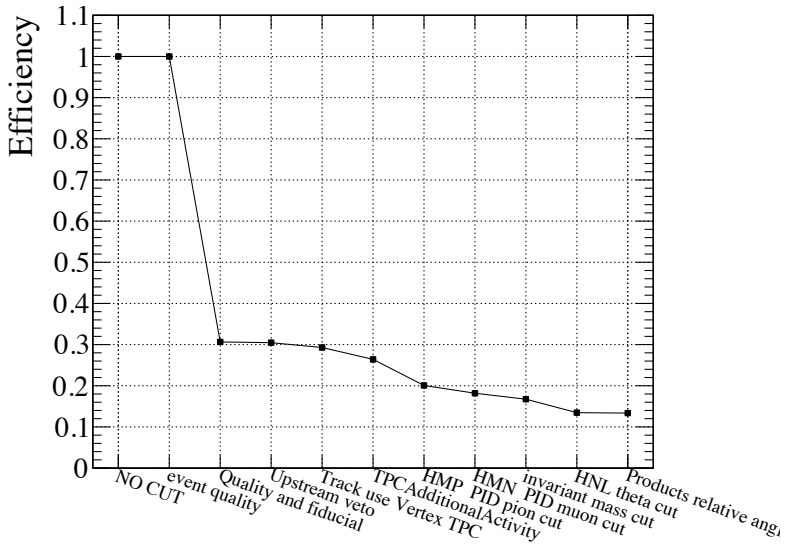

Figure 5.6: Efficiency dependence on the applied cuts for mode $N \to \mu^{\mp} + \pi^{\pm}$ for all HNL masses.

The dependence of the efficiency on the HNL momentum and opening angle of the daughter particles is shown in Figure 5.7. As expected the maximum efficiency is for HNL with momentum below 2 GeV/c. The TPCs were designed for the event reconstruction in this momentum region.

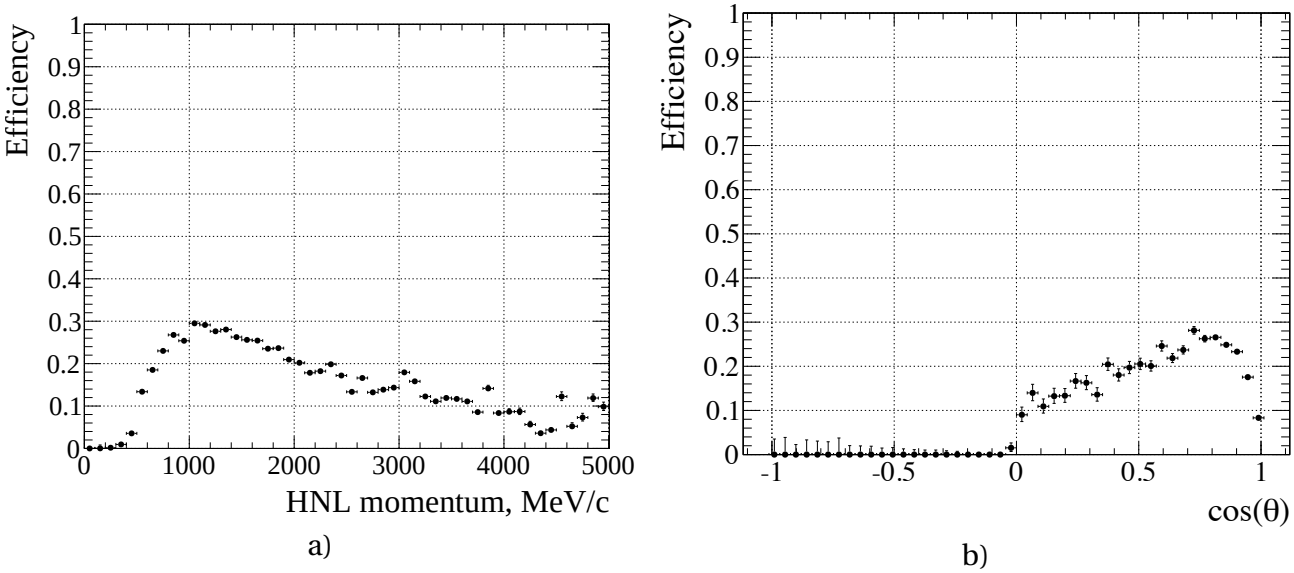

Figure 5.7: The dependence of efficiency for mode $N \to \mu\pi$: (a) on the HNL momentum and (b) opening angle of daughter particles.

Since we study the HNL production from K^+, K^- and their decays into $\ell^{\pm}h^{\mp}$, the efficiency should be evaluated for every mode. Such a result is presented in Figure 5.8. We can see the agreement of the efficiency study for the different channels.

1.3 Background suppression

In the T2K experiment neutrino interactions in the ND280 had been already simulated. Different neutrino generators had been used to consider several different models. In our study we are affected by the poorly studied processes of pion production in the gaseous Argon. Thus I used all the available generators and compared the results to minimize the model dependence. NEUT [124],

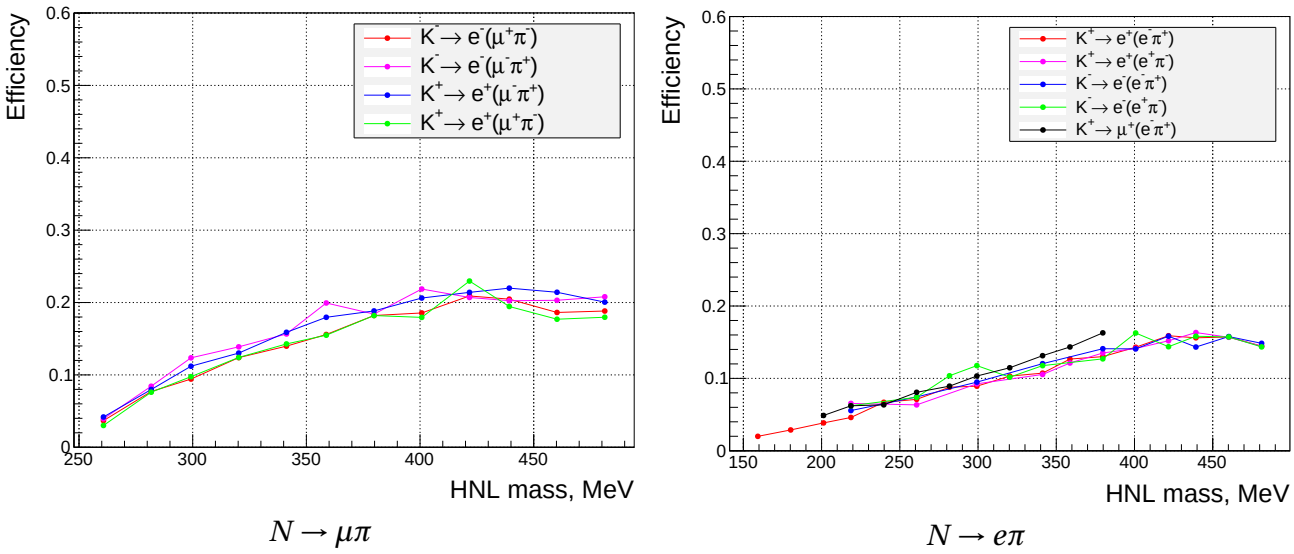

Figure 5.8: HNL selection efficiencies for several production and decay modes.

GENIE [125], and NuWro [126] toolkits were used for background estimation. For example, GENIE is believed to be more accurate in kaon production prediction, while I expected the neutral kaon decay $K_L^0 \to \ell\pi\nu_\ell$ to mimic the signal process. The statistics used for the Monte–Carlo simulation is nearly ten times bigger than the data collected in the experiment. Thus I am going to study the background with small statistical uncertainties. The background is divided into neutrino interaction types. Remaining backgrounds after each cut as well as a signal efficiency are summarized in Table 5.2 and Table 5.3.

N	Cut	CCQE	RES	DIS	COH	NC	2P2H	OOFV	$\bar{\nu}_\mu$	ν_e	Total	Eff
1	Vertex	140.11	30.88	20.34	4.57	8.48	1.65	647.31	2.39	3.63	859.34	44.0
2	Veto	122.44	21.24	10.75	3.89	6.55	0.82	281.47	1.80	2.43	451.39	39.1
3	PID	5.08	5.51	5.60	2.03	1.25	0.00	48.64	1.37	0.19	69.66	31.3
4	Inv mass	0.83	3.52	2.17	1.67	0.90	0.00	43.17	0.92	0.00	53.18	29.2
5	Kinematic	0.00	0.17	0.20	0.34	0.00	0.00	0.00	0.00	0.00	0.79	21.1

Table 5.2: The number of MC background events after every cut for 10^{21} POT from NEUT generator for $\mu\pi$ mode. The budget is split into quasi–elastic processes (CCQE), resonance π production (RES), coherent π production (COH), deep inelastic interaction (DIS), neutral current interactions (NC), multi–nucleons interaction (2P2H - 2 particles, 2 holes) out of fiducial volume interactions (OOFV), $\bar{\nu}_\mu$ and ν_e interactions.

The main background for the $N \to \mu\pi$ decay channel is pion production as was expected. Some contribution from deep inelastic processes was also observed. The veto cuts demonstrate it's high efficiency rejecting lots of active neutrinos but keeping the signal efficiency nearly the same.

For the $N \to e\pi$ mode, the main background process is expected to be different from the one for $N \to \mu\pi$ mode. Pion production is not so dangerous as in T2K the beam is almost pure. A pion production will always cause a muon production as well. Some contribution of the coherent pion production in the $N \to e\pi$ is caused by the wrong particle identification. But the main process is out of fiducial volume neutrino interactions. The neutral pion production is responsible for this contamination. π^0 decays almost immediately after the neutrino interaction and produce two gammas. One of the gammas can go downstream in the ND280 and convert in the next detectors. In case of the wrong particle identification of the e^+e^- pair we can reconstruct the process as $e\pi$ production. Photons can travel through several subdetectors in ND280. Because of the high

N	Cut	CCQE	RES	DIS	COH	NC	2P2H	OOFV	$\bar{\nu}_\mu$	ν_e	Total	Eff
1	Vertex	140.11	30.88	20.34	4.57	8.48	1.65	647.31	2.39	3.63	859.34	34.5
2	Veto	122.44	21.24	10.75	3.89	6.55	0.82	281.47	1.80	2.43	451.39	31.1
3	PID	5.74	0.17	0.92	0.17	0.20	0.00	13.91	0.00	0.00	21.11	17.8
4	Inv mass	0.66	0.17	0.37	0.17	0.20	0.00	13.32	0.00	0.00	14.87	17.1
5	Kinematic	0.00	0.00	0.00	0.17	0.00	0.00	0.32	0.00	0.00	0.69	14.8

Table 5.3: The number of MC background events after every cut for $10^{21} POT$ from NEUT for $e\pi$ mode. The budget is split into quasi–elastic processes (CCQE), resonance π production (RES), coherent π production (COH), deep inelastic interaction (DIS), neutral current interactions (NC), multi–nucleons interaction (2P2H - 2 particles, 2 holes) out of fiducial volume interactions (OOFV), $\overline{\nu}_\mu$ and ν_e interactions.

beam intensity I can not constrain all the activity in the ND280 as it will dramatically reduce the efficiency. Instead, I consider only the first upstream subdetector activity as a veto.

All the backgrounds from different neutrino interactions generators are put together in Table 5.4. All of them are providing similar estimations for every mode. The fact that NuWro underestimates the background for $e\pi$ mode is caused by the fact that out of fiducial volume (OOFV) processes are not simulated with this particular generator. As it's the main contributing process the result is very different.

	NEUT	GENIE	NuWro	NEUT $\bar{\nu}$
$\mu\pi$	0.79	0.69	0.85	0.91
$e\pi$	0.69	0.95	0.38	0.23
$\mu\mu\nu$	1.81	1.63	2.10	0.98

Table 5.4: The total number of MC background events for $10^{21} POT$.

The statistics accumulated in the T2K experiment is divided into 8 runs. The total good quality data available for analysis is $(10.23\nu + 6.29\bar{\nu}) \cdot 10^{20} POT$. The average background prediction across all the neutrino generators is scaled to the real data, collected at ND280, and gives us the expected number of the background events (Table 5.5).

	run 2-8
$\mu\pi$	1.44
$e\pi$	1.12
$\mu\mu\nu$	2.85

Table 5.5: The total number of MC background events scaled to real data statistics.

To conclude, the main background processes such as neutrino interactions with a pion production in gas or a π^0 production are poorly studied. The theoretical uncertainty on the rate of these processes are large. In the current analysis, I decided to put the conservative data-driven upper limits on the HNL mixing elements. It means that the background estimations will not be used for the final result. Instead, all the observed events will be interpreted as a signal (overestimated) and the conservative limit on the mixing elements will be set. The details about the statistical approach can be found in section 3.

2 Systematic uncertainties

In the general case, the systematic uncertainty will come from both the signal and background expectations. In the current analysis the background predictions are not affecting the final result. Thus only the systematic uncertainty of the signal prediction should be evaluated.

Assuming $|U|^2 = 1$ we calculated the events number according to:

$$N_{events} = \phi(HNL/10^{21}\, p.o.t./cm^2) \cdot \frac{V_{FV}}{c\beta\gamma} \cdot \Gamma_{mode} \cdot Eff, \tag{5.1}$$

where Eff is the selection efficiency. Possible uncertainties sources are:

- $\phi(HNL/10^{21}\, p.o.t./cm^2)$ — a HNL flux. As it is calculated based on the kaon flux, the uncertainties of the kaon flux modeling should be included here,
- Eff —- selection efficiency uncertainties, the detector systematics should be included here.

2.1 Detector systematics

The ND280 systematic uncertainties have been already studied for the T2K oscillation analysis. The uncertainties are estimated with a comparison of the data with the Monte–Carlo simulation. For each possible source of the model inaccuracy, a dedicated control sample is selected. Then the MC / data comparison will tell us how the model should be corrected. For example, we know that the track matching between TPC and FGD can be different in a model and data. Long straight tracks are selected to check this effect. The efficiency of the matching is different in MC and data. The simulated events will be re-weighted to predict the data more accurately. But these efficiencies are estimated with some uncertainty. This uncertainty will be taken into account in the analysis as systematics.

In the HNL analysis I considered the following list of possible uncertainties:

- magnetic field map
- TPC momentum scale,
- TPC momentum resolution,
- particle identification with dE/dx,
- TPC tracking efficiency,
- charge identification with track curvature,
- track matching between subdetectors,
- pion secondary interactions,
- Track association into the vertex (Kalman filter algorithm)

For the mode $N \to \mu\mu\nu$ we should consider additional ECal systematics as we use this detector in our cut sequence:

- TPC-ECal track clustering and matching efficiency,
- the separation between tracks and showers in ECal

Systematic evaluation in the ND280

The systematic uncertainties are estimated in the ND280 detector with two methods:

- Observable-variation systematic
- Efficiency-like systematic

The variation systematic is applied to all variables that are reconstructed quantities on which we have an uncertainty. The method of propagation includes varying the observable, applying all the selection cuts and study the selected event number variation. This variation will be the uncertainty estimation of the analysis result.

The efficiency-like (weight) systematic concerns all the variables that correspond to a reconstruction/detection probability. For example the probably to have or not to have the reconstructed track. The uncertainty estimation starts from choosing the appropriate control samples with lots of events with and without successful detection. Then we study the difference between MC and data samples. The mean of the difference will be used as the correction for the MC, while the variation will be used as the uncertainty of the value. This method is much faster from the computing point of view, as do not require to run the selection many times.

The systematic that was estimated by myself for this particular analysis is the uncertainty of the track association into the global vertex (GV). It's impossible to estimate track matching efficiency for neutrino interactions in the TPC FV because of the lack of statistics. So the interactions in the FGD volume were chosen for this study. I checked the efficiency of the successful association of the closed tracks from FGD into the vertex. Two samples are defined for the FGD1 and FGD2 respectively. Closed tracks are selected with the following cut sequence:

- both start in the FGD1/2 FV;
- oppositely charge;
- close start position;

The efficiency of the vertex merger is defined as the ratio of the number of the tracks' pairs associated in vertex to tracks' pairs that passed all the cuts. We should check if this efficiency depends on the parameters of the tracks i.e. momentum, opening angle. The results are presented in Figure 5.9

I concluded that there is neither angular nor momentum systematics dependence. The efficiency for MC and DATA are presented in Table 5.6. The systematics for the HNL study was estimated using these efficiencies differences with a weight-like method. One more check is the spa-

	FGD1	FGD2
DATA	$0.958^{+0.0023}_{-0.0024}$	$0.944^{+0.0027}_{-0.0026}$
MC	$0.962^{+0.0036}_{-0.0038}$	$0.952^{+0.004}_{-0.0042}$
Systematic uncertainty for $N \to \mu\pi$	0.58%	0.46%
Systematic uncertainty for $N \to e\pi$	0.51%	0.4%

Table 5.6: Global vertex association efficiency and systematics.

tial resolution comparison between the data and MC. We checked the difference between the track start position and the vertex position. The results are shown in Figure 5.10, the statistics is summarized in Table 5.7. As we can see the mean value for MC and data are rather close, the difference between them is close to the fit error and much less than the statistical uncertainty.

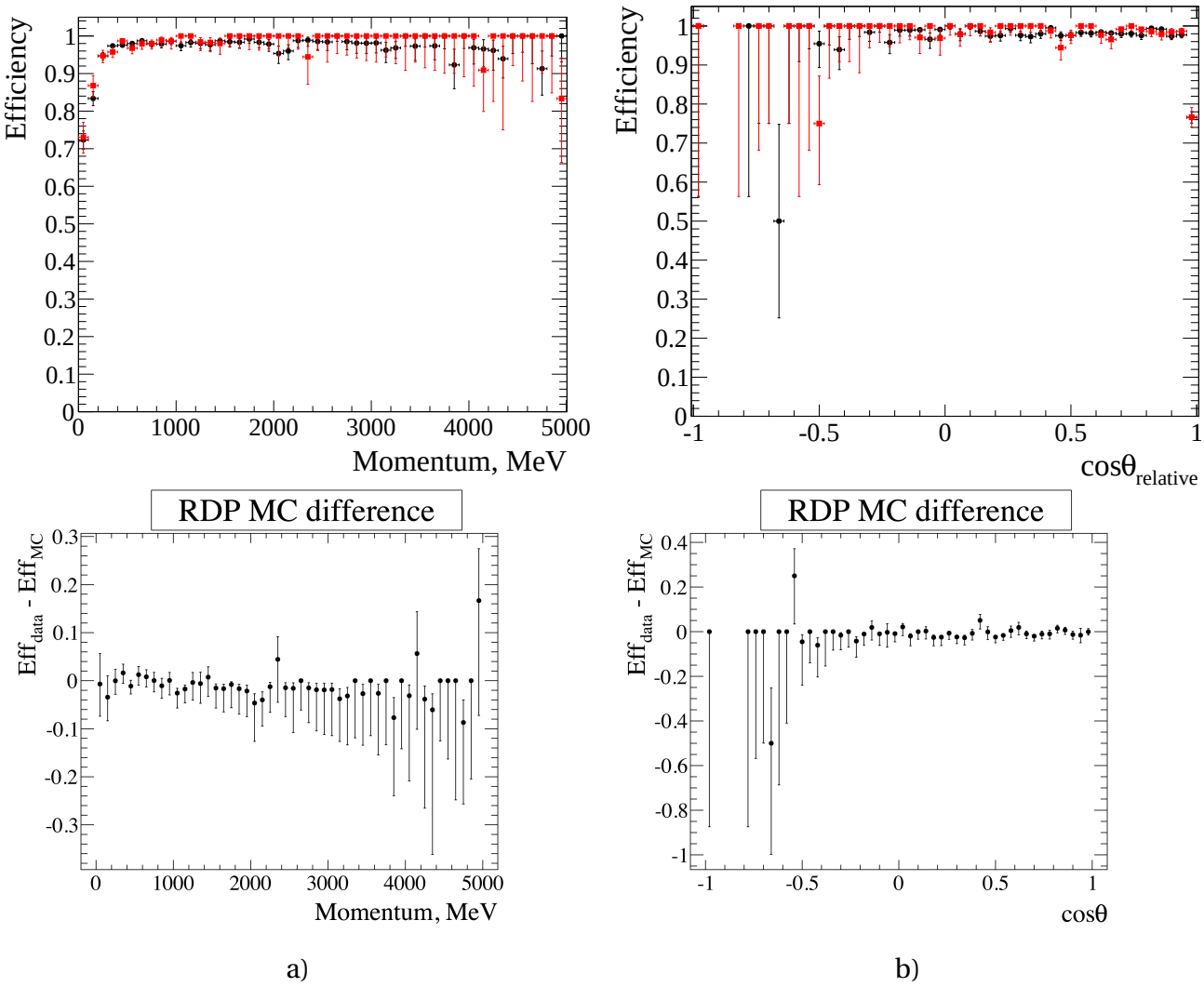

Figure 5.9: Dependence of the global vertex association systematics on the track momentum (a) and on the opening angle (b) for FGD1 sample in black for DATA and in red for MC.

Axis		Mean	RMS
X	MC	0.16 ± 0.09	7.20 ± 0.06
	DATA	0.1 ± 0.16	7.67 ± 0.11
Y	MC	0.09 ± 0.17	8.29 ± 0.12
	DATA	0.14 ± 0.09	7.5 ± 0.06
Z	MC	-5.76 ± 0.22	10.68 ± 0.15
	DATA	-5.38 ± 0.13	10.78 ± 0.09

Table 5.7: Summary of the statistics for spatial resolution for experimental and MC data presented in Figure 5.10.

The detector systematic dependence on HNL mass is shown in Figure 5.11 and Figure 5.12. As one can see the most critical uncertainty comes from the pion secondary interactions for the modes $e\pi$ and $\mu\pi$. As the dimuon mode $\mu\mu\nu$ doesn't produce pions in the final state it's free from that uncertainty and the total error is much smaller.

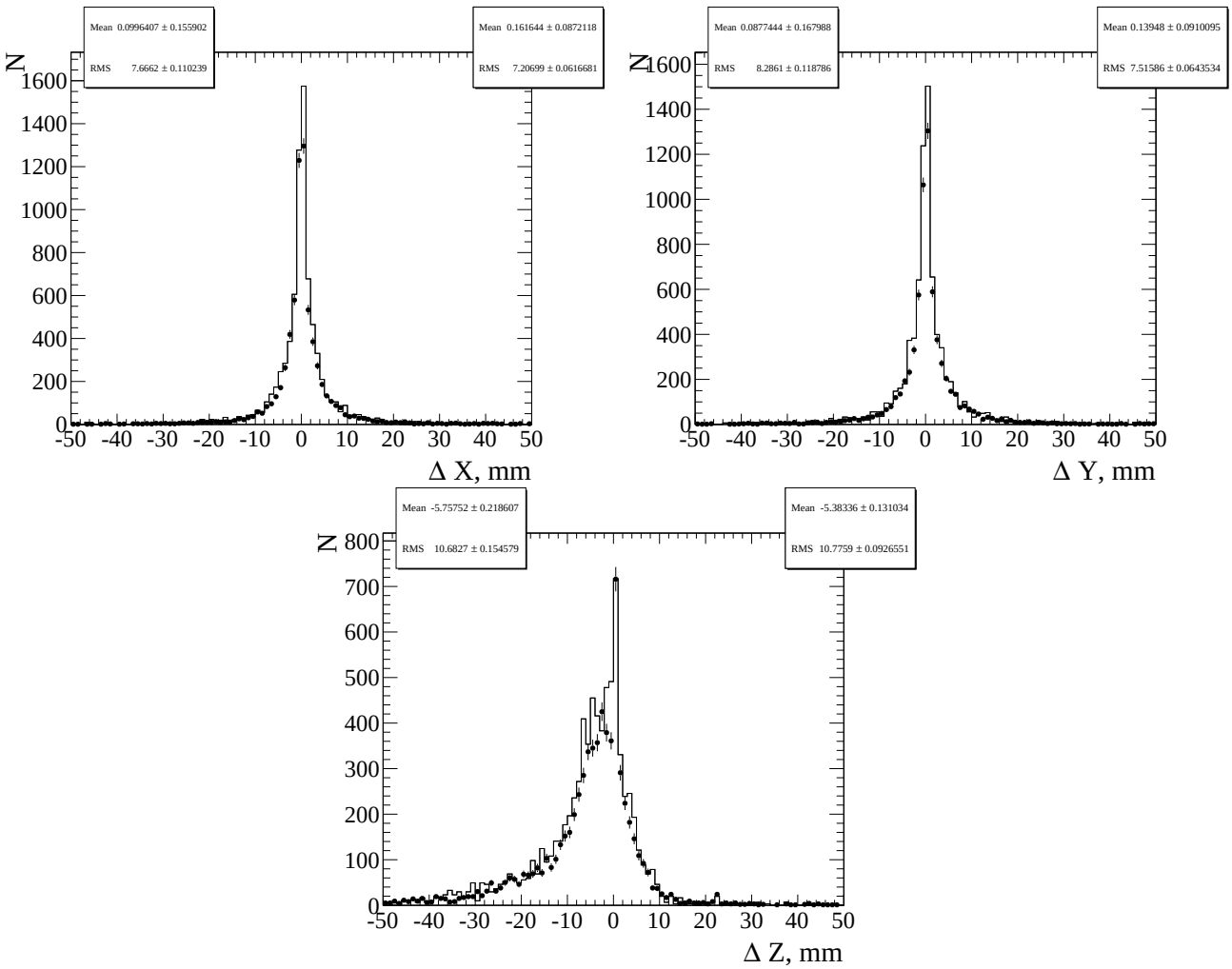

Figure 5.10: Global vertex spatial resolution for experimental and MC data. Dots and left statistic box corresponds to experimental data, histograms and right statistic represents the simulation result.

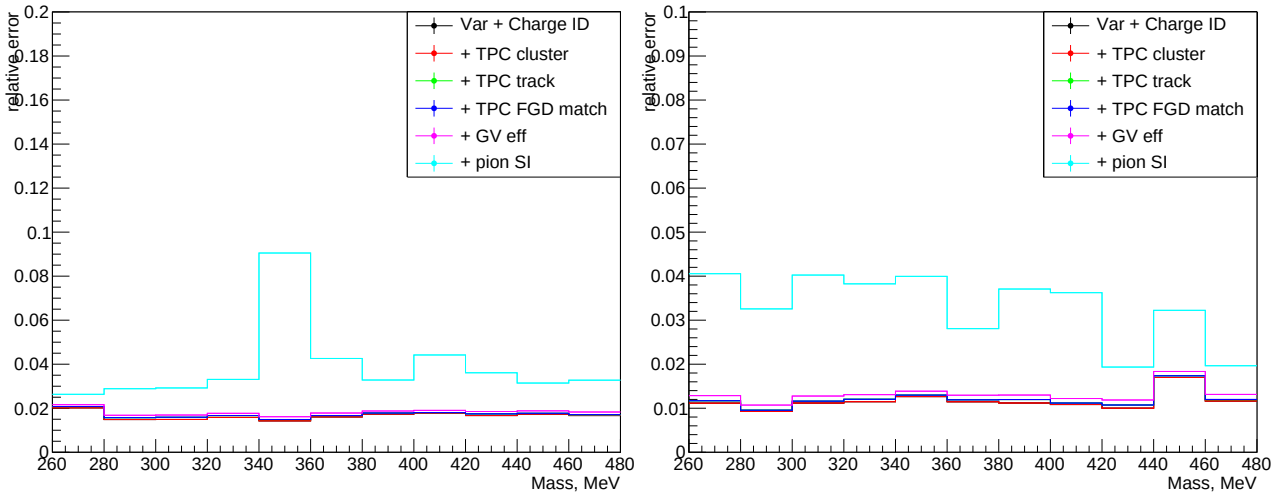

$K^+ \to e^+ N \to e^+ \left(\mu^- \pi^+\right)$ $K^+ \to e^+ N \to e^+ \left(e^- \pi^+\right)$

Figure 5.11: Detector systematics dependence on HNL mass

.

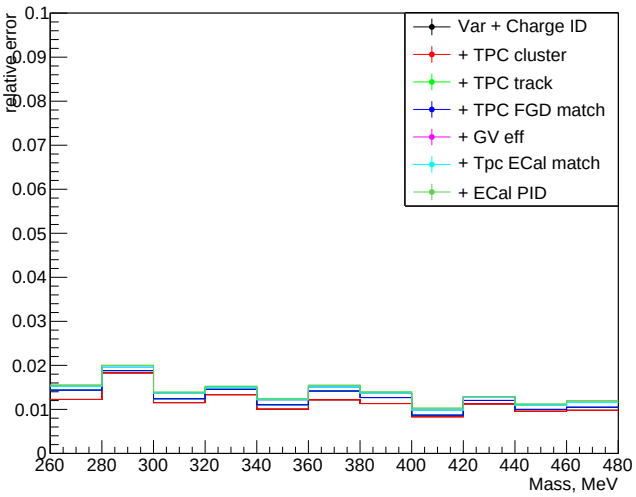

$$K^+ \to e^+ N \to e^+ \left(\mu^- \mu^+ \nu\right)$$

Figure 5.12: Detector systematics dependence on HNL mass

.

2.2 Flux systematics

Heavy neutrino flux in the ND280 is calculated based on the kaon flux produced in the proton collisions. Thus uncertainties of the kaon flux will affect the number of signal events. The total flux error consists of the uncertainties of the meson multiplicities, pion re-scatter, interaction length, focusing and other errors [108]. These fractional errors and the total flux uncertainty for the active neutrino beam are presented in the Figure 5.13. To estimate the kaon multiplicity errors we use data from NA61/SHINE. Relative uncertainties of the kaon multiplicities are shown in Figure 5.14. For HNL analysis we deal mainly with the kaons collinear to the beam axis. We consider a conservative estimation of the kaon multiplicity uncertainty as 20%. For all the other sources of the flux errors, we take the maximum value among all energy bins.

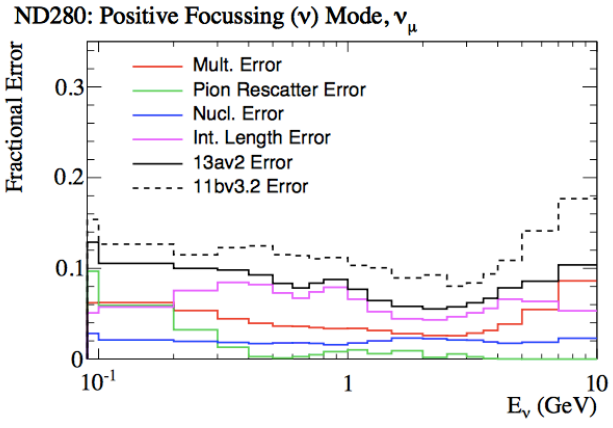

Figure 5.13: ν_μ Flux uncertainties.

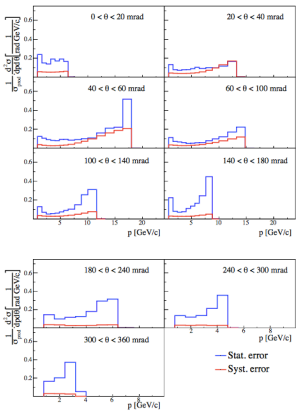

Figure 5.14: Kaon multiplicity uncertainties.

The results of the systematics study are presented in the Figure 5.15. The detector systematics is widely described in the previous subsection. As we analyze all charge conjugated modes together we take the highest systematics uncertainties among them.

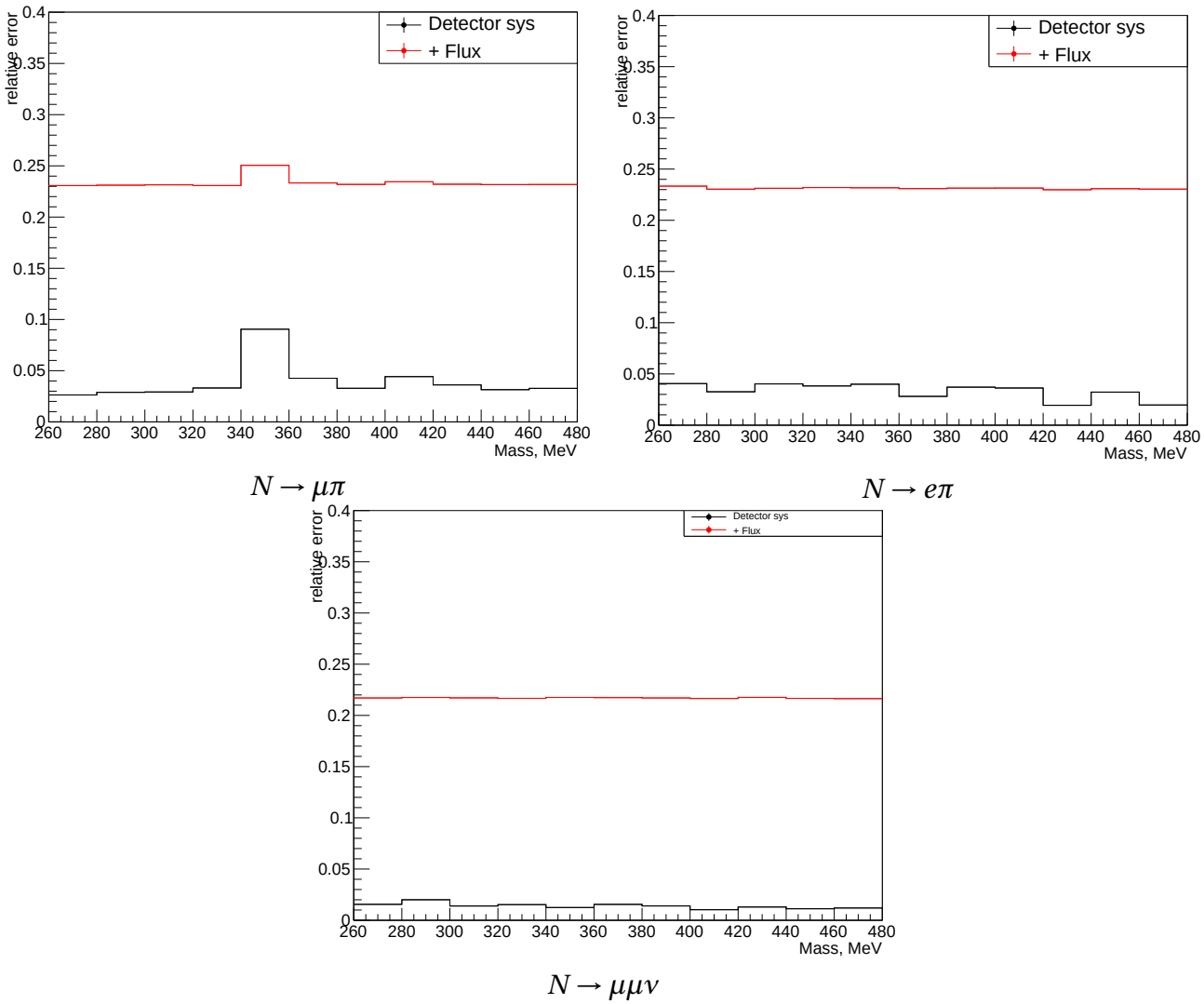

Figure 5.15: Detector and flux systematic errors for different modes.

3 Statistical methods

The statistical approach to the low-level signal analysis is described in the Highland and Cousins work [115]. As the number of the HNL decay events is proportional to the fourth power of the mixing element, constraints on $|U_i|^2$ without systematics looks like:

$$|U_i|^2_{limit} = \sqrt{\frac{U_n}{N_{events}}} \tag{5.2}$$

where

- $i = e, \mu$ is a lepton flavor,
- U_n is 90% C.L. Poisson limit for n observed events,
- N_{events} is an expected number of signal events assuming $|U|^2 = 1$.

If we take into account the detector acceptance uncertainty, the result can be calculated according to [115]:

$$U_n = U_{n0}\left\{1 + E_n\frac{\sigma^2_{Acc}}{2}\left(1 + \left(\frac{E_n\sigma_{Acc}}{2}\right)^2\right)\right\} \tag{5.3}$$

where

- U_{n0} is 90% C.L. Poisson limit for n observed events,
- σ_{Acc} is the acceptance error,
- $E_n = U_{n0} - n$ represents the excess of the upper limit of a Poisson parameter over the number n of observed events, for a specified confidence level.

This approach can be applied only while $\sigma_{Acc} < 1/E_n$. We already showed that in our study $\sigma_{Acc} \approx 0.3$ and $1/E_n > 0.5$ (section 2). So this method can be applied for the analysis.

One more important feature of the current analysis is that we don't consider the background and its uncertainty. We used the background estimations to tune our selection. For the final result we will treat all the observed events as a signal and then put a conservative limit on the mixing elements. The data–driven approach will be indeed conservative, but the advantage is that we are free from the background uncertainty at all. If during the unblinding several events were found we would put the worse limits on the mixing. Such a method can be improved in the future (see subsection 4.1).

4 Results

After studying the MC efficiency (subsection 1.2), background processes (subsection 1.3) and systematics (section 2), the real data can be unblinded and the final upper limit on mixing angles can be set. I will use the statistical method descried in Equation 5.3. Because of the small background the acceptance uncertainties have a small effect on the sensitivity.

The numbers of observed events in data after the unblinding are presented in the Table 5.8. All the results are presented for the full ND280 data set (run 2-8).

	Events in data
$\mu\pi$	0
$e\pi$	0
$\mu\mu\nu$	1

Table 5.8: The total number of events observed in data.

One event for the $N \to \mu\mu\nu$ mode was observed. It happened in the TPC3 and looks like a signal event: two muon-like tracks with the direction collinear to the beam axis. The event display for this event is presented in Figure 5.16.

A more accurate study shows that the invariant mass of this muon pair is too high for the heavy neutrino decay $M_{inv} \approx$ GeV. At this particular mode no cut on the HNL invariant mass was set. But based on the blind analysis method and our analysis strategy this event will be treated as a signal and an appropriate upper limit on the mixing element will be set.

The limits on the each particular mixing element is set under the assumption that the other mixing elements are negligible. For example, setting the limit on U_e^2 we assume $U_\mu^2, U_\tau^2 \ll U_e^2$.

The results are presented in Figure 5.17 and Figure 5.18. The data statistics $(10.23\nu + 6.29\bar{\nu}) \cdot 10^{20} POT$ was used.

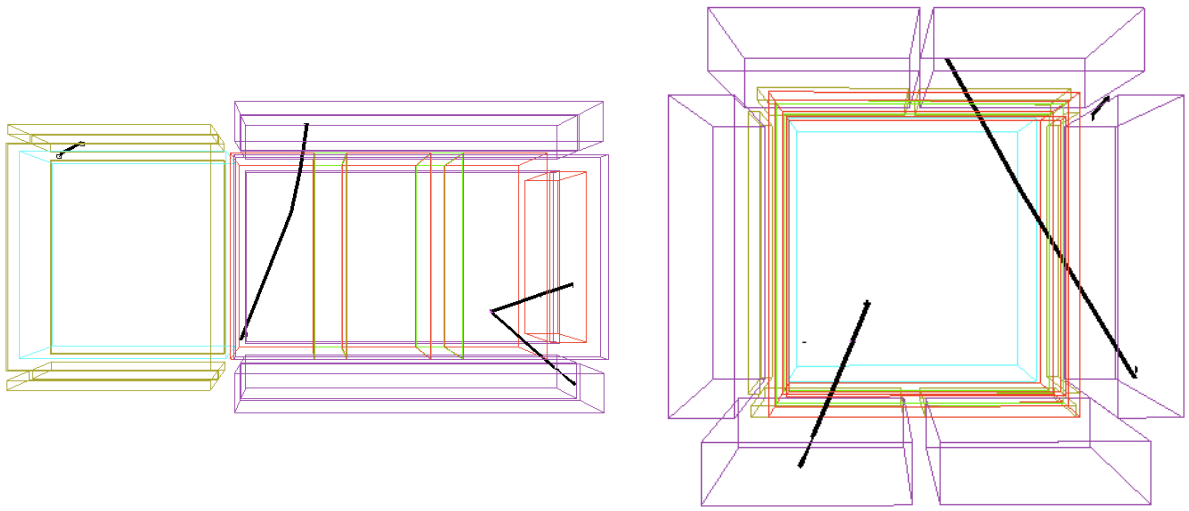

Figure 5.16: Event observed in the $N \to \mu\mu\nu$ mode in the data sample in the TPC3.

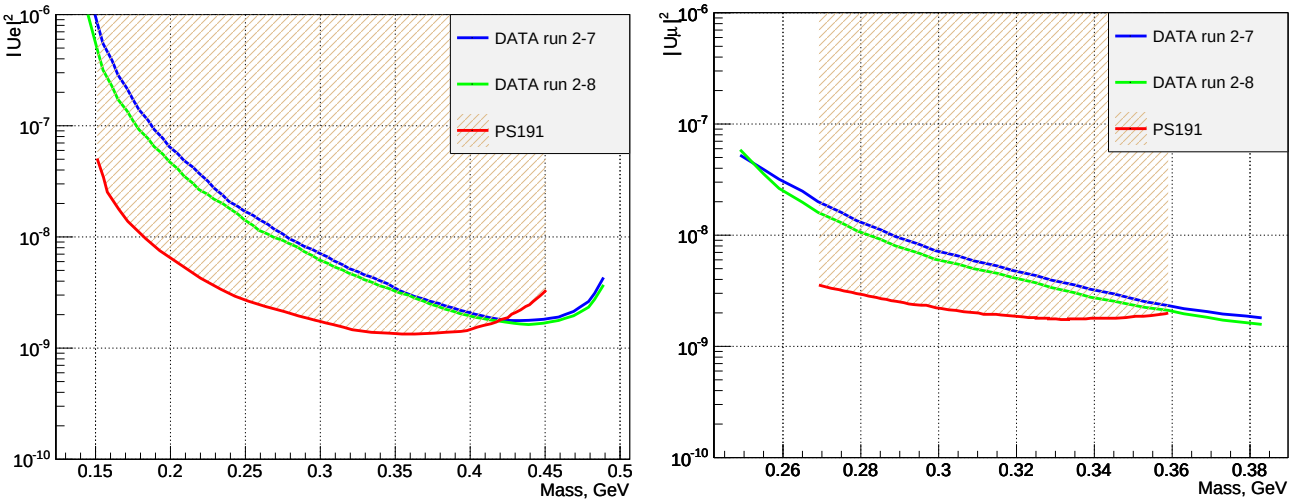

$K^+ \to e(e\pi)$ $K^+ \to \mu(\mu\pi)$

Figure 5.17: Limits on mixing elements $|Ue|^2$, $|U\mu|^2$ based on the data samples analysis.

4.1 Prospects

The current study puts a conservative limit on the mixing elements of the heavy neutrino. A more accurate result can be obtained with precise background estimations. This work was continued by other collaborators and other methods were used for the data treatment. The accurate background estimations were developed and a new Markov Chain Monte Carlo method was used for setting limits on the mixing elements. All the production and decay modes of the heavy neutrino are analyzed together and a robust final result is obtained. The joint analysis including all the methods was published [5].

The T2K experiment will continue taking data. The preliminary plan is to accumulate 20×10^{21} POT [96]. With larger statistics (x11 to current) we will be more sensitive to the HNL mixing

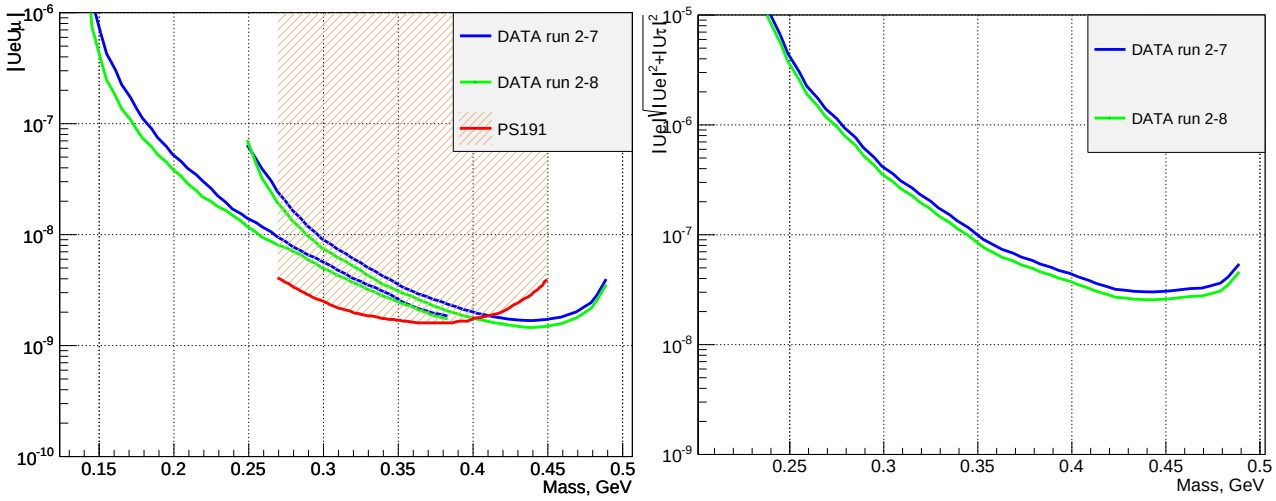

$K^+ \to \mu(e\pi)$ and $K^+ \to e(\mu\pi)$ $K^+ \to e(\mu\mu\nu)$

Figure 5.18: Limits on mixing elements $\left|UeU\mu\right|$ and $|U_e|\sqrt{|U_e|^2+|U_\tau|^2}$ based on the data samples analysis.

elements. Since the result is proportional to the square root from the expected events number the limits can be improved by the factor of 3.

The upgrade of the near detector complex is ongoing now [1] (also Part III). Two additional TPCs will be installed. For the current study, it means that the fiducial volume will be extended by ≈10%. That will also slightly improve the final result.

Part III

ND280 upgrade

CHAPTER 6

INTRODUCTION

As mentioned in chapter 3, the first goal of the T2K experiment was to measure the θ_{13} mixing angle. After the successful discovery of the θ_{13}, T2K entered a phase of the precise measurement of the neutrino oscillation parameters. The experiment provides the most precise estimations for the θ_{23} angle and also very accurate measurements of the Δm_{23} and θ_{13} parameters. Great progress was obtained in the search for the CP–violation with the determination of the 3σ confidence level on the possible values of the δ_{CP} [55]. The δ_{CP} measurement became the main goal of the experiment.

The next-generation experiments like DUNE [98] and Hyper-Kamiokande [97] will be able to achieve 3σ sensitivity to the CP–violation across the wide range of the δ_{CP} values but on the time scale 2026 and beyond. The T2K experiment can probe this effect with less sensitivity but much earlier. The sensitivity of the T2K experiment with the total statistics of 20×10^{21} POT is shown in Figure 6.1.

More statistics is necessary to determine the CP–violation more precisely and to justify if the effect takes place. The improvement of the sensitivity versus the collected data is shown in Figure 6.1 (b). Initially, T2K was supposed to collect the total statistics of 7.8×10^{21} POT. The extended run of the T2K experiment aiming at the total statistics 20×20^{21} POT was proposed [96]. This additional period of data collection was called T2K-II. The beamline will be upgraded to provide a more intense neutrino beam (section 1). Therefore the data statistics accumulation will go faster.

There is a room for further improvement of the sensitivity with the reduction of the systematic uncertainty. Figure 6.1 presents the sensitivity of the T2K experiment with different assumptions: current systematic uncertainties (in blue), improved systematics by factor 2/3 (in orange), only statistical uncertainty (in black). With the improved systematics, the desired sensitivity will be reached faster, and finally, a wider range of the δ_{CP} can be studied. The budget of the systematic uncertainties of the T2K experiment is described in [114]. The main sources in decreasing order are neutrino cross-sections, flux, secondary interactions in the SK, SK detector. The systematics related to the SK is very hard to reduce and it is going to be extremely expensive. Also, it gives a minor impact. The systematic uncertainty related to the neutrino cross-section and flux can be better constrained with the upgrade of the near detector.

T2K near detector provides good systematics reduction. It decreases the uncertainty of the oscillation analysis from 12% down to 6%. But for the T2K-II the further systematics reduction is required. To do this, several limitations of ND280 should be overcome. Originally ND280 was designed for the reconstruction of the forward-going particles, while the far detector Super-Kamiokande

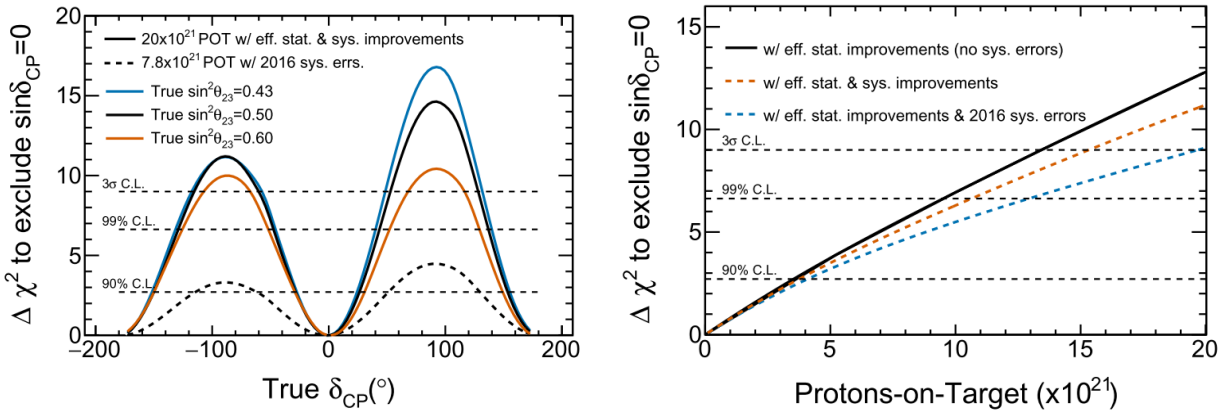

(a) (b)

Figure 6.1: An expected sensitivity of the T2K experiment to the CP–violation in the neutrino oscillations with respect to (a) true δ_{CP} value and (b) collected statistics. The known mass order is assumed. On the right plot three systematic uncertainties estimations are used: (blue) 2016 value, (orange) with improvements by factor 2/3 and (black) only stat. uncertainties. (a) shows the sensitivity over the δ_{CP} value and (b) shows the sensitivity evolution over the collected statistics for $\delta_{CP} = -\pi/2$.

detects the particles in the 4π phase space. Also, ND280 is not able to detect low energy nucleons produced in the neutrino interactions that make the neutrino energy reconstruction inaccurate. The upgrade of the near detector is proposed (section 2). The idea is to use a highly granular target to reduce the threshold of particle detection. Above and below this target two new TPCs will be placed. Thus the phase space acceptance will be enlarged to include particles pointing in the perpendicular direction with respect to the incoming neutrino. With the improvements mentioned above the systematic uncertainty of the oscillation analysis will go below 4%. The present value is about 6%. Hence the improvement of the sensitivity illustrated in Figure 6.1 is possible.

1 Beamline upgrade

Neutrino interactions are extremely rare processes. The natural way to gain statistics in the experiment is to use a very intense beam. The T2K experiment uses the beam produced by the J-PARC accelerator complex. After the few upgrades, the power of the beam in the main ring of the accelerator reached 500 kW. As a result, the J-PARC complex provides one of the most intense neutrino beams in the world. It was proved that T2K can obtain better physics results with the statistics extension to 20×10^{21} POT [96]. For this purpose, the J-PARC accelerator will be upgraded to provide an even more intense beam with the power of 1.3 MW.

The beamline power upgrade schedule is shown in Figure 6.2. The accelerator will be stopped for one year for the major hardware improvement. In the following years, the intensity will slightly grow alongside the data collection. The target power 1.3 MW is planned to be reached by 2028. This is beyond T2K. The Hyper-Kamiokande experiment is going to use the same beamline and use all the benefits from the power upgrade after the T2K. The details about the beamline upgrade are described in [127].

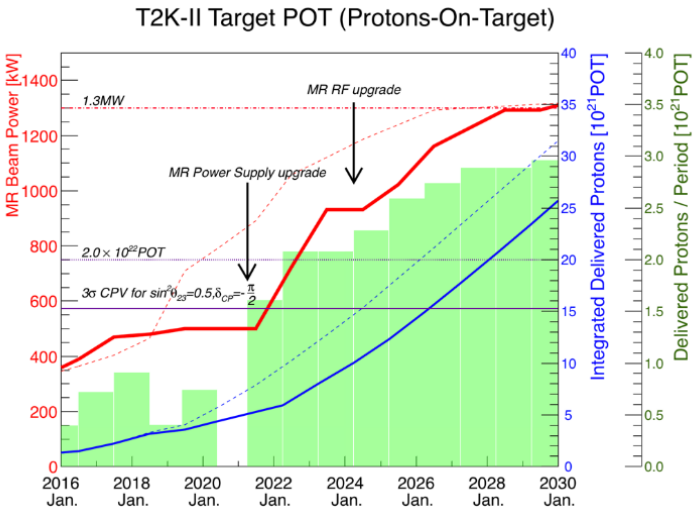

Figure 6.2: Target J-PARC beam power (red) and the expected total accumulated statistics (blue) as a function of the year. Two possible schedules are considered shown with solid and dashed lines.

2 Detector overview

2.1 Current detector limitations

The T2K off-axis near detector is described in subsection 2.2 of chapter 3. The schematic view of the setup is presented in Figure 3.8 (b). There are several known problems that limit the performance of the ND280. As a result, the total T2K systematics is dominated by the neutrino cross-section and flux uncertainty. These uncertainties can be reduced with better constraints with the upgraded ND280.

One of the main issues is limited phase-space coverage. An event display of a neutrino interaction in the ND280 as well as the detector layout is shown in Figure 6.3. The scintillator neutrino targets (Fine Grained Detectors) are shown in violet. They are alternated with 3 TPCs shown in blue. Such a setup is perfect for the reconstruction of the forward and backward going particles. But if the lepton from the neutrino interaction goes at a high angle w.r.t. the beam (up/down in Figure 6.3) we will not be able to perform accurate measurements. It will not leave a long enough track in the TPCs, hence we can not estimate the momentum with the curvature and the particle type with the energy loss. It is even possible that the particle goes along the single vertical bar in FGD. In this case, even tracking with the scintillator detector is impossible. The efficiency of the muon selection from the $\nu_\mu CC$ interactions in the FGD1 over the outgoing lepton angle is shown in Figure 6.4.

The far detector can detect the outgoing lepton with uniform efficiency over the 4π phase-space. But the near detector can effectively detect only forward–going leptons from neutrino interactions. The comparison of the detectors' acceptance and the expected lepton phase space are shown in Figure 6.5. To extend the constraints from the ND280 to the full phase-space various models of the neutrino interactions are used. But the uncertainties of such models are quite high. The direct measurements of the leptons in 4π angle in the near detector will reduce the systematic uncertainty.

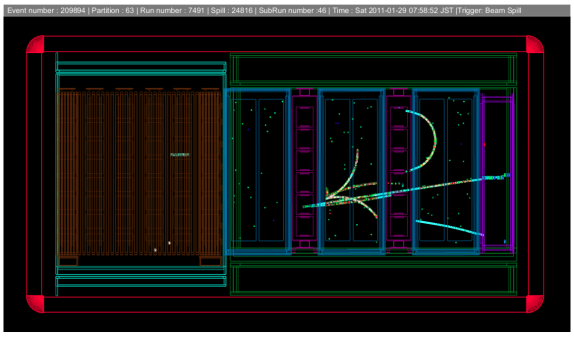

Figure 6.3: The event display of the neutrino interaction in the FGD1 in the ND280. The beam is coming from the left.

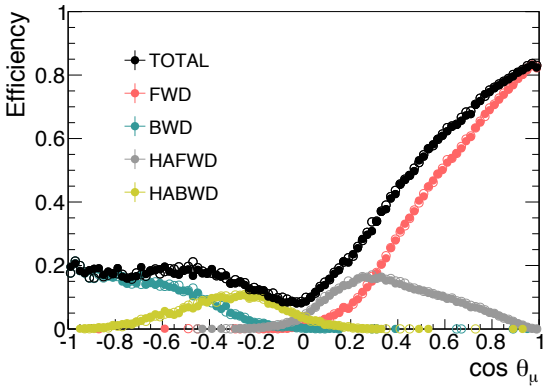

Figure 6.4: Muon selection efficiency for the $\nu_\mu CC$ interactions in the FGD1 as a function of the lepton angle w.r.t. Z axis.

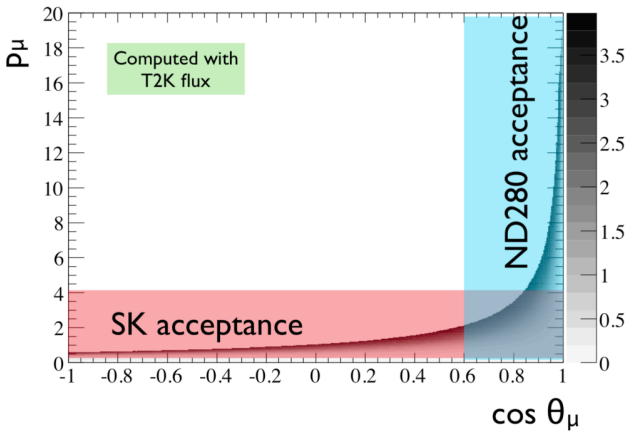

Figure 6.5: The acceptance of both near and far detectors of the T2K experiment over the expected lepton phase space.

The other subject of concern is the threshold of particle detection. Thanks to muon penetration ability, they are leaving a long track and can be easily detected. But protons from the neutrino interactions are mostly low energetic and travel a short distance. It's quite difficult to detect them with the sandwich scintillator detector like FGD. The proton should go through at least a few layers for robust detection. If it is produced at a high angle w.r.t. beam the situation is even worse. The current threshold of the proton detection in FGDs is around 500 MeV. Based on the current neutrino interaction models we expect the proton spectrum to start from 200 MeV. Nucleon detection from the neutrino interaction is extremely important in the T2K. As mentioned in chapter 3, Super–Kamiokande uses CCQE interaction assumption to reconstruct the neutrino energy. But in most of the cases, neutrino doesn't interact with the free nucleon but with Oxygen nuclei in SK and with Carbon and Oxygen nuclei in ND280. The nuclear effects (subsection 2.2 of chapter 1) are biasing the neutrino energy measurements. They can even change the event topology. For example, after neutrino interacts with pion production, the pion can be absorbed in the nuclei and the event will look like the CCQE interaction. That's why nuclear effects should be precisely constrained. It can be done with the precise measurement of both outgoing lepton and nucleon kinematics. The detection of short pion tracks will also help with the proper reconstruction of the interaction topology and will gain the neutrino energy estimation accuracy as well.

2.2 New proposed design

To improve the performance of the near detector its upgrade was proposed [1]. The ND280 tracker (2 FGDs and 3 TPCs) will be kept in place and will continue operation. Thus the data from both T2K-I and T2K-II can be analyzed together. The π^0 detector will be replaced with the new neutrino target and 2 horizontal TPCs. The upstream part will be surrounded by the time of flight (ToF) detectors. The various CAD models are presented in Figure 6.6 and Figure 6.7.

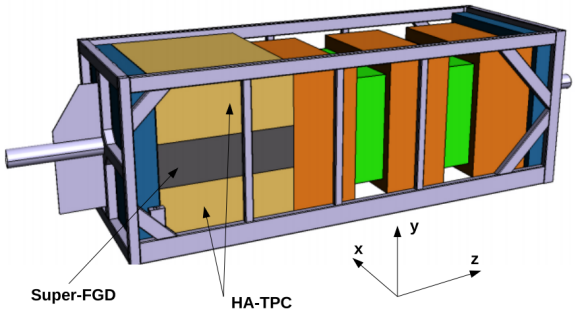

Figure 6.6: The scheme of the upgraded near detector. The downstream part is kept as it is. The new horizontal target (Super–FGD) and two high angle TPCs (HA–TPC) are put in the upstream part,

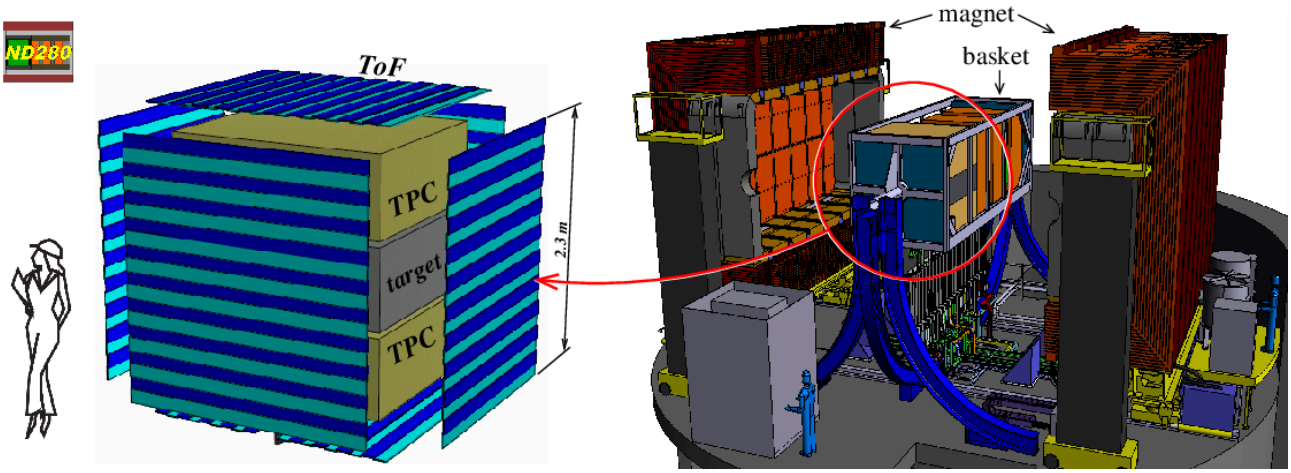

Figure 6.7: The CAD model of the whole upgraded detector setup and the inset of the mostly affected by the modifications upstream part.

The new neutrino target Super-FGD (SFGD) will be composed of small plastic scintillator cubes. The cube edge is set to 1 cm providing fine granularity. Three orthogonal holes are drilled in the cube for the light readout with the WLS fibers. Therefore the Super-FGD can reconstruct the tracks in 3D. High granularity significantly reduces the threshold of particle tracking. Also, such a structure will improve the separation between gamma conversion from $\nu NC\pi^0$ interactions and electron neutrino CC interaction resulting in more precise ν_e cross-section measurements. The dimensions of the new target are $182 \times 184 \times 56$ cm^3 giving a total mass close to 2 tonnes. The total fiducial mass of the ND280 will be nearly doubled. The large size of the target allows detecting the

secondary interactions of the neutrons from the anti-neutrino CCQE interactions $\overline{\nu} + p \rightarrow \ell^+ + n$. As mentioned in the Introduction measurement of the outgoing nucleons are critical for the precise neutrino energy reconstruction and probing neutrino interactions models. The details of the neutron detection proposal are presented in chapter 9. More details about SFGD detector will be provided in chapter 8.

Two atmospheric pressure High Angle TPCs (HATPC) will be put above and below the Super-FGD. They will enlarge the phase space to the full coverage. The readout will be organized by the Micromegas (MM) as for the current TPC, but new technology will be implemented. The Micromegas will be covered with the resistive foil resulting in charge spreading over the pads. Thus the spatial resolution can be improved with the same pad size. It will lead to better momentum reconstruction and finally more accurate neutrino energy estimations. The details about HATPC detector will be provided in chapter 7.

The Time of Flight (ToF) detectors will fully cover the upstream part of the ND280. It will be composed of scintillator bars and readout with the MPPC arrays. This detector will help with the reconstruction of the particle direction: to/from Super-FGD. Neutrino interacts quite often in the magnet coil and ECal and can produce a particle that will stop inside the SFGD. The relatively short track inside the scintillator target is not sufficient for the direction reconstruction, but the ToF detectors will give a clear answer. Also, this detector can help with particle identification. For example positrons and protons have very similar dE/dx around 1 GeV/c and can not be distinguished with the TPC but the time of flight is dramatically different.

To sum up, the upgraded ND280 will have several benefits comparing to the present setup:

- ➢ full phase space coverage for the particles produced in neutrino interactions
- ➢ low threshold of the particle detection
- ➢ doubled fiducial mass
- ➢ better separation of the particles going "in" and "out" the target
- ➢ electron/gamma separation, resulting in better ν_e measurements
- ➢ neutron detection from $\overline{\nu}CC$ interactions

3 Simulations

The bunch of simulations was made to estimate the upgraded detector performance. As was overviewed before, the limited acceptance in a main limitation of the current ND280. The goal of these studies is to prove that the new detector will gain the efficiency for the high angle tracks. Also, we studied the benefits of the new scintillator detector, such as lower threshold and particle identification.

3.1 Subdetectors simulation

To estimate the sensitivity of the new setup we have to parametrize the response of subdetectors. The performance of the existing detectors (TPC, ECal) are measured precisely. Thus we used their efficiencies and resolutions for the current analysis.

A track is considered to be reconstructed in the TPC if it is longer than 20 cm in the ZY plane (Micromegas plane). The TPCs are responsible for the charge and particle identification. The efficiency of proper charge reconstruction in the existing TPC binned in the momentum for each

particle type is used to determine the reconstructed charge of the particle. The ionization loss fluctuations are estimated based on the track length in the detector plane (ZY). After that, pulls and likelihoods for various particle hypotheses are computed. We consider electron, muon, pion, and proton as possible particle types. The PID is done with the cuts on the 4 likelihoods.

The Time Of Flight detector efficiency is assumed perfect. The measured time is smeared according to the known resolution of 150 ps. Each subdetector (SuperFGD, ToF, ECal, FGD) provides a time measurement. All the time stamps are smeared with the known time resolution of particular subdetector. The track direction is assigned with maximization of the time difference with respect to its uncertainty. Thus if, for example, a track was originated in SuperFGD and then passes TPC, ToF, and ECal, the information from the SuperFGD and ToF will be used as the most robust. For the long forward going track, time information from SuperFGD and downstream ECal will be considered. If as a result of smearing the track end point is earlier in time than the start point the track direction is flipped.

The ECal efficiency is binned in the particle type, momentum, and angle. The matching with the nearby detectors like TPC and FGD is also taken into account. If the track is recognized as "unmatched" the information from the ECal can not be used, and the ECal cluster is considered isolated.

The simulation of the SuperFGD is the most difficult part. For all the other detectors the performance is estimated precisely, but this one is a brand new detector. The SuperFGD materials are fully implemented in the GEANT4 framework. The readout simulation procedure is presented in section 3 of chapter 8. We take into account scintillator saturation, attenuation in the fibers, MPPC efficiency. Thus, the energy lost by particle for the ionization is transformed into the number of observed photoelectrons. With such a simulation we estimated the performance of the detector for the particle tracking and identification.

We want to compare the detector performance before and after the upgrade while the simulation framework for the upgraded setup is simplified and much less sophisticated comparing to existing ND280 software. To make the results comparable we used our simplified framework to simulate the current ND280 performance as well.

a Performance

After the procedure for the detector response simulation is established, we used a neutrino generator to simulate neutrino interactions in the upgraded ND280. Produced particles are further used as an input for the GEANT4 framework to estimate the particle behavior in the setup. As a next step, we estimated the response of different subdetectors with the procedures described in the previous section.

The final efficiency of the upgraded ND280 for the muon detection is shown in Figure 6.8. The detector becomes much more sensitive for high angle tracks. Furthermore SuperFGD gain the efficiency a lot with ability to track and identify self-contained particles. The phase space of the detected muons from ν_μCC interactions before and after the upgrade is shown in Figure 6.9. The increased statistics and acceptance of the high-angle tracks are clearly seen.

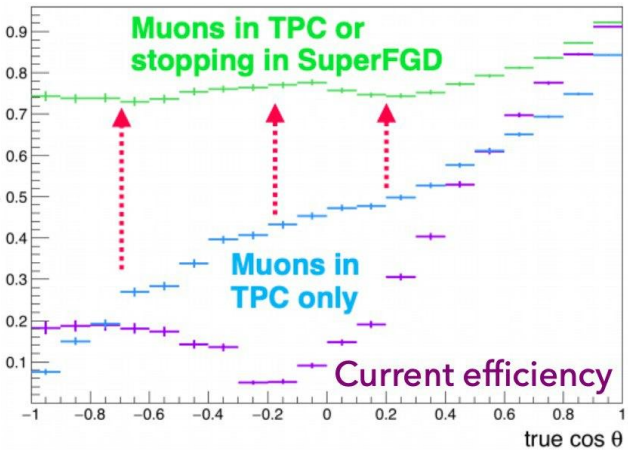

Figure 6.8: Efficiency of the muon detection upgraded ND280 versus the current one (in violet). The blue line represents muons that exit SuperFGD and are tracked with TPC, the green line take into account also muons contained in SuperFGD only.

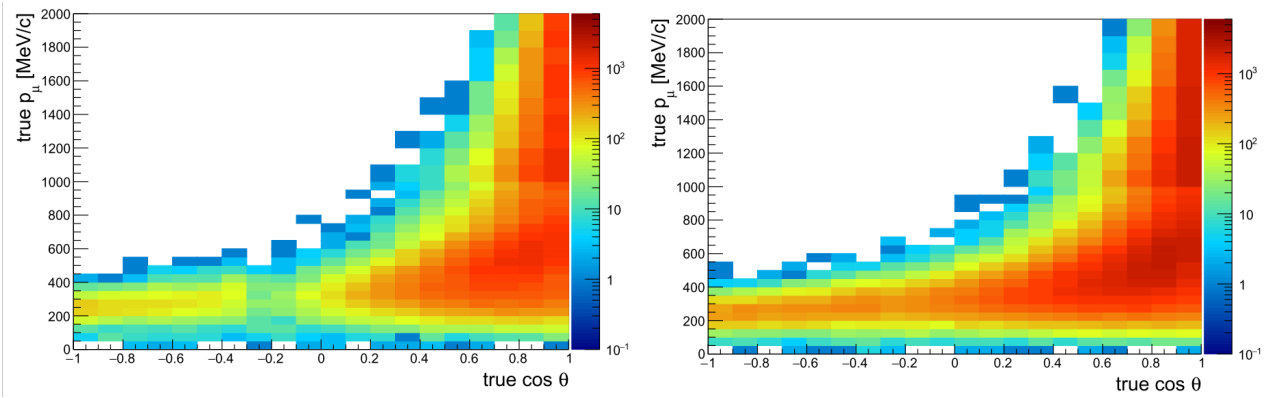

(a) (b)

Figure 6.9: Muon kinematics selected from ν_μCC interactions with current (a) and upgraded (b) configuration of the ND280.

CHAPTER 7

TIME PROJECTIONS CHAMBERS (TPC)

The combination of the TPCs and scintillator detectors in ND280 provides accurate physics measurements of the neutrino interactions. The precision of the oscillation analyses is greatly improved with the data collected with the near detector. The TPCs play a key role in the reconstruction of daughter particles from neutrino interactions. The momentum and charge are reconstructed with the track curvature, the particle type is estimated with the ionization energy loss (dE/dx). During the ND280 upgrade, two new TPC will be placed above and below the scintillator target and will aim at a high angle track detection (Figure 7.1). Therefore the new detectors are called High–Angle TPC (HA–TPC).

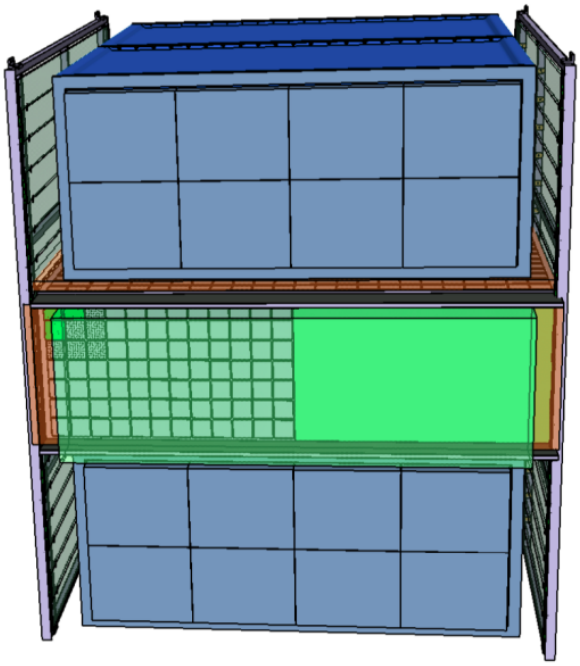

Figure 7.1: The upstream detectors of the upgraded ND280: HA–TPC (blue) and scintillator target (green). Beam is coming from the left. On the CAD the cathode dividing the drift volume and the Micromegas on the edge of the boxes can be seen.

1 HA–TPC design

1.1 Requirements

For the precise neutrino oscillation analysis, it is critical to meet the requirements of the existing TPCs and to study the possibilities of improvements. The momentum resolution of the current TPCs is 10% at the momentum around 1 GeV/c. It was driven by the accuracy of the neutrino energy reconstruction. The quasi–elastic reaction is assumed to compute the incoming neutrino energy from the outgoing lepton momentum and angle. In this assumption, an initial nucleon stays at rest and is free. We are studying neutrino interactions with the nuclei where nucleons don't satisfy these conditions. Thus the reconstructed neutrino energy will be smeared because of nuclear effects. Fermi motion will be the dominating smearing effect. In the Oxygen and Carbon nucleon movement is characterized by the Fermi momentum $p_F \approx 200$ MeV/c. It will give ≈10% uncertainty for the neutrino energy measurements. With the HA–TPCs, we are going to measure tracks with high angle w.r.t. the beam thus with lower momentum. Lower momentum will result in the larger track curvature and more precise reconstruction. Hence the same spatial resolution as in the current TPC is the minimum requirement for the new detectors. We are going to use the resistive Micromegas (MM) technology (subsection 1.4) that will allow making the pads larger, but keep the spatial resolution unchanged or even slightly improve it. The spatial resolution of the current TPCs is at the level of 800 μm.

The other critical point for the ND280 performance is the dead material between subdetectors. The TPCs provide excellent tracking for the charged particles so it's strongly desired to detect all the particles that exit the scintillator towards the TPCs with minimal distortions. In the case of a massive field cage or a high Z material, several particles will lose the energy and suffer from multiple scattering making the precise measurements impossible. In the new TPCs, we are going to use a field cage made of a solid insulator laminated on a composite material. Thus the dead material between the scintillator target and the HA-TPC will be minimized. It's an important improvement as high–angle tracks are low energetic and even a small amount of material can cause track distortions. Also, the new field cage will maximize the fiducial volume of the detector.

A good energy resolution is essential for the separation of electrons and muons. As we are going to measure ν_e cross–sections while the ν_e contamination in the neutrino beam is at the level of 1% the superior e/μ separation in the TPC is required. The current TPCs provide an 8% energy resolution that results in 4σ separation between electron and muon. The performance of the new detectors should be at least at the same level.

1.2 Conceptual design

The schematic view of the HA–TPC is presented in Figure 7.2 and the main parameters are listed in Table 7.1. The TPC will consist of a rectangular box divided into 2 parts by the high voltage cathode. The box serves as a gas vessel and a field cage (subsection 1.3). The maximum drift distance in each module is 90 cm. The same Ar:CF_4:iC_4H_4 gas mixture as in the existing TPC will be used. It will provide a drift velocity at the level of 7.8 cm/μs resulting in a maximum drift time 11.5 μs. The electronics will sample the measurements every 40 ns and store in total 511 samples (20μs window). Thus tracks from the whole drift distance will be stored. The time window will

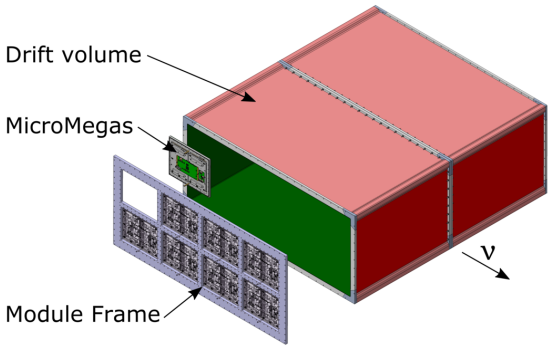

Figure 7.2: The schematic view of the new TPC

Parameter	Value
Overall x×y×z (m)	2.0×0.8×1.8
Drift distance (cm)	90
Magnetic Field (T)	0.2
Electric field (V/cm)	275
Gas Ar:CF_4:iC_4H_4 (%)	95-3-2
Drift Velocity cm/μs	7.8
Transverse diffusion (μm/$\sqrt{\text{cm}}$)	265
Micromegas gain	1000
Micromegas dim. z×y (mm)	340×410
Pad z×y (mm)	10×11
N pads	36864
el. noise (ENC)	800
S/N	100
Sampling frequency (MHz)	25
N time samples	511

Table 7.1: Main parameters of the new TPC

cover the whole accelerator bunch which is distributed by Gauss with σ = 19 ns. The field cage provides a uniform electric field with strength 275 V/cm inside the box. The high field uniformity is necessary for the uniform electron drift velocity. The latter is essential for the precise measurements of the track position along the drift distance. The signal from the drift electrons is amplified and read-out with the 16 Micromegas modules, 8 at each side. Each module has dimensions of 340×410 cm^2 and is paved with 32×36 pads 10×11 mm^2 each. The pads are covered with the resistive foil that provides a charge spreading, improves the detector spatial resolution, and prevents Micromegas discharges (subsection 1.4). The analog electrical signal from the pads is digitized with Front–End Cards (FEC), processed with Front–End Mezzanine cards (offset correction, zero-suppression, etc.), and then transferred to the ND280 global data acquisition system. The FEC and FEM cards are mounted on the TPC itself. The signal acquisition scheme is similar to the one we use in the existing TPCs.

1.3 Field cage

The requirements set for the field cage are to contain as little material as possible and use only low Z elements to minimize photon conversion and a charged particle scattering. At the same time, the box should be tight enough to hold the gas pressure without leakage, prevent atmospheric Oxygen and Nitrogen from entering the box, and contaminating the gas mixture. The walls of the field cage should be flat to prevent high voltage discharge. To meet the requirements mentioned above a composite material was chosen for the cage box. The composite materials are widely used in the industry. The TPC wall is going to consist of an Aramid honeycomb core and laminate skins on both sides of the core. In the inner part, the box will be covered with Kapton foil covered by Copper strips. It is the main field forming element of the structure.

The total thickness of the new field cage is 30 mm and its fraction to the radiation length is d/X_0 = 1.7%. This value is improved comparing to the existing TPC. The old setup consists of two nested boxes 14 and 12 mm thick separated with a 68 mm gap. Also, heavier materials were used. The new structure minimizes the dead space between the HA–TPCs and scintillator targets by three times and suppresses the particle track distortions.

1.4 Resistive Micromegas technology

The resistive bulk Micromegas technology is going to be used as a readout detector of the HA–TPCs. The TPC working principle is described in subsubsection 2.2.c of chapter 3. In short, the drift electrons are amplified with the high electric field between the micro–mesh and readout pads (Figure 7.3 left). The analog electrical signal is formed in the pads and further transported to the readout electronics. The bulk Micromegas [128] was proved to have excellent performance and long life–time in the existing experiments. The technique is laminating a woven mesh on a Printed Circuit Board (PCB) covered by a photoimageable film. This part is a sensitive detector. On top, the micromesh is put and fixed with an insulator above and below the mesh. The gap between the mesh and the PCB is the amplification region. The Micromegas technology minimizes the dead space on the detector plane and provides an excellent gain uniformity over the whole detector area. They have been operated in the experiments for a long period and the aging effect was found negligible.

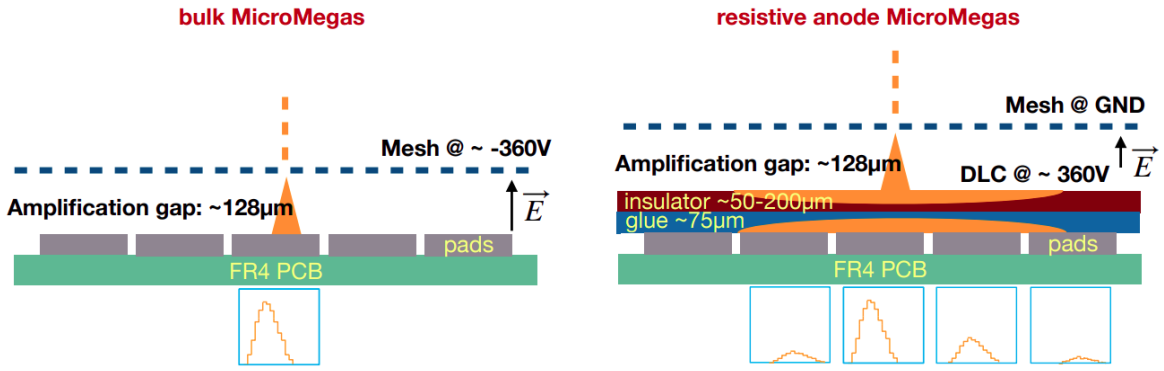

Figure 7.3: The schematic view of the bulk Micromegas operation without the resistive foil (left) and with resistive foil (right). The charge spreading due to the resistive foil is illustrated.

The resistive Micromegas is an upgrade for the existing technology. An insulator layer made from Kapton is glued to the pads. The Kapton layer is covered with a thin Diamond-Like-Carbon structure (DLC) (Figure 7.3 right). Such a design provides natural avalanche quenching. Thus the Micromegas discharge is prevented and there is no need for protection diodes in the front–end electronics. The resistive layer serves as a two dimensional RC network spreading the charge over the pads. For a point-like charge source the charge density versus the time t and radius r is described by the exponential law:

$$\rho(r,t) = \frac{RC}{2t} e^{-2r^2 RC/(4t)} \tag{7.1}$$

where R and C are resistivity and capacitance for unit area respectively. For example, giving the shaping time equal to 100 ns, resistivity equal to 400 kΩ/□, and glue thickness set to 75 μm (controlling the capacity) the standard deviation of the charge spreading is expected to be 2.6 mm. Thus the spreading can be controlled with both resistivity and capacity. For example, for the larger spreading, the resistivity can be decreased or/and the thicker glue layer can be used (smaller capacity).

The effect of the charge spreading can improve the spatial resolution of the setup. If the electron cloud is close to the pad center and is smaller than the pad size. In the absence of the resistive foil, only one pad will register the signal. In such a case the spatial resolution will be limited by the

pad size. However, with the charge spreading all the neighbor pads will register some signal. Even a simple barycenter measurement [129] can improve the spatial resolution comparing to the traditional Micromegas. This improvement is the most significant at small drift distances when the electron cloud is compact and not has yet expanded with the transverse diffusion. In the ND280 TPCs, we observed a dramatic degradation of the resolution for the drift distances smaller than 200 mm because of this effect. The spectacular spatial resolution improvement down to 70 μm with the resistive Micromegas was found for the International Linear Collider (ILC) TPC prototype [130]. For the case of the T2K, the resistive Micromegas allows using larger pads without any degradation of the detector performance.

1.5 Electronics

The architecture of the HA–TPC data acquisition system is schematically shown in Figure 7.4. The analog electric signal from the pads first goes to the Application Specific Integrated Circuit (ASIC) [131] called AFTER. They are used in the existing TPC and were proved to have low noise rate, high range of sampling frequency (up to 50 MHz), shaping time (100 ns ÷ 2 μs) and gain (120 fC ÷ 600 fC). Each ASIC collects information from 72 pads and provides only one analog output. The 511-cell deep circular buffer is used to store the signal from each pad. Together with sampling frequency, it sets the time window for signal acquisition. The nominal sampling time is 40 ns (25 MHz) that gives an acquisition window nearly twice larger than the maximum drift time. 8 ASICs are mounted on the Front End Card chip (FEC) that performs the signal digitizing. Two FECs are inserted directly at the Micromegas back and connected to the pads with pitch connectors. Front End Mezzanine Card (FEM) is mounted on top of each two FECs and synchronizes signal digitization with a master clock. At FEM all the data from AFTER chips are collected and zero suppression is applied. All the electronics mentioned above are located inside the magnet. From the FEM the signal is transferred outside the magnet with the optical fiber. The CADs of the electronics that are mounted on the Micromegas inside the basket is provided in Figure 7.5. The cards' temperature is maintained with the water cooling system.

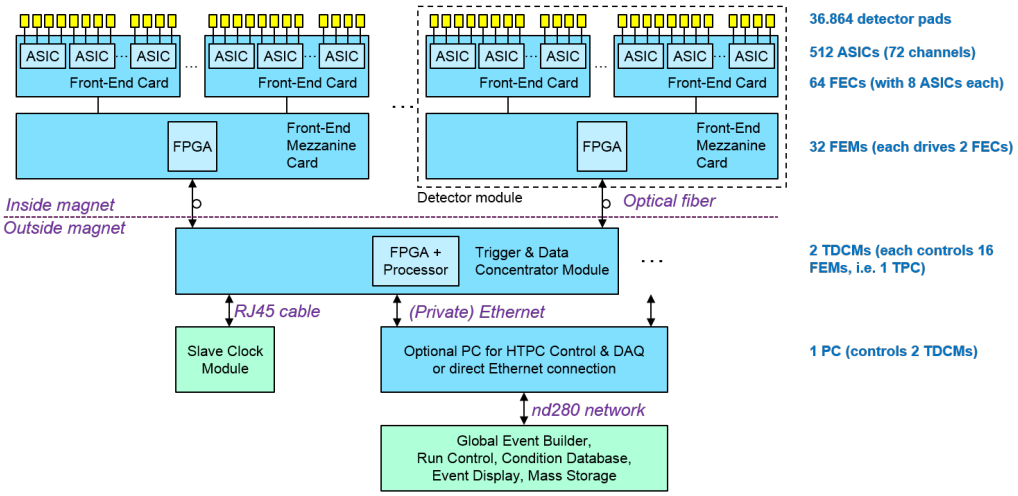

Figure 7.4: Scheme of the TPC electronics system.

The digitized and pre-processed data is transferred with the optical fiber to the Trigger and Data Concentrator Module (TDCM). Each unit reads data from 16 Micromegas and provide timing synchronization and trigger signals to the FEMs. The TDCMs communicate with the global ND280 data acquisition system with a standard Gigabit Ethernet link.

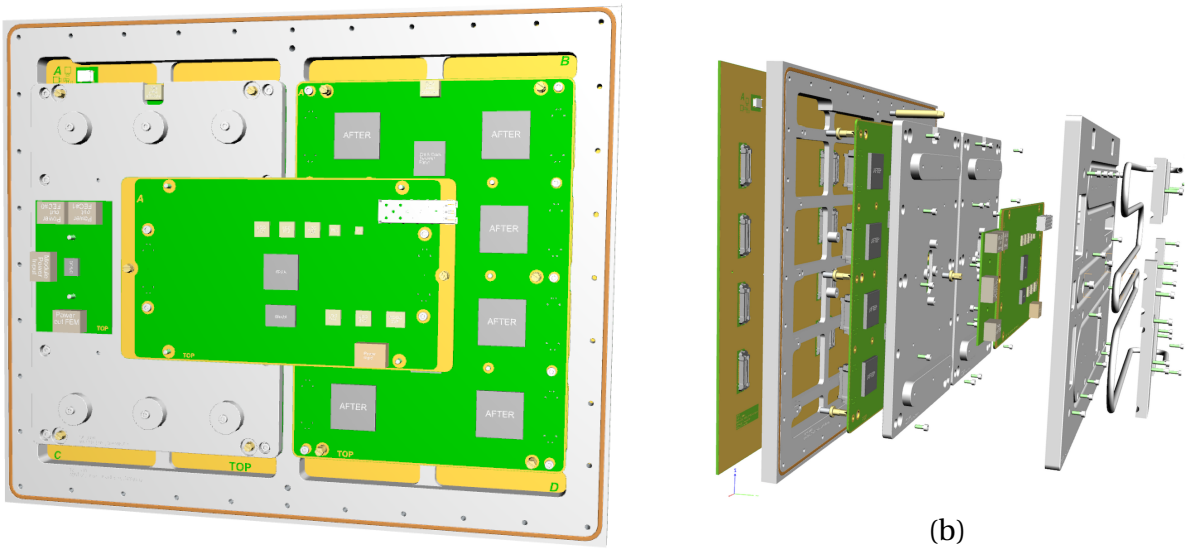

(a) (b)

Figure 7.5: The CAD of the HA–TPC electronics mounted on the Micromegas without the cooling system (a) and sectional view of the whole setup (b).

2 Prototype tests

An improved spatial resolution is going to be achieved with the new TPC with a resistive anode. At the same moment, the energy resolution should not decrease as it's critical for the T2K ν_e measurements. Few detector prototypes were built and tested. The main goals of the tests are to test the detector production technology, to find the optimal hardware parameters and to estimate the spatial and energy resolution of the future detector.

2.1 Cosmic test

The Micromegas prototype was produced for the test with the beam of charged particles at CERN beam test area. Before that, it was tested at the test bench in Saclay. The primary goal of the detector test was to figure out that the whole detector plane was operating as expected, the detector response is uniform and the Micromegas was not damaged.

The scheme and the photo of the setup are shown in Figure 7.6. The field cage with a 15 cm drift region was used for the test setup. It was filled with Argon (95%) and Isobutane(5%). The uniform electric field was maintained with the strips that you can see in Figure 7.6 (b). The drift field was set to 183 V/cm. The resistive Micromegas was mounted on the side of the field cage. The size of the module was 36×34 cm^2 and it was paved with 36×48 pads 0.98×0.70 cm^2 each. The same PCB as in the existing TPC was used.

The RC feature was implemented with a 200 μm insulator layer (capacitance) and a 50 μm Kapton with a thin Diamond-Like-Carbon layer (DLC) (resistivity). The resistivity value was set to 2.5 MΩ/□. The side pads are partly covered with a frame that is fixing the mesh and providing the grounding of the DLC. Thus the first and the last row/column are excluded from all the analysis as they are known to measure less charge than the other pads. The Micromegas voltage was varied for different samples during the data taking from 350 V up to 390 V. The front–end electronics were mounted on the outer side of the Micromegas and could be seen in Figure 7.6 (c).

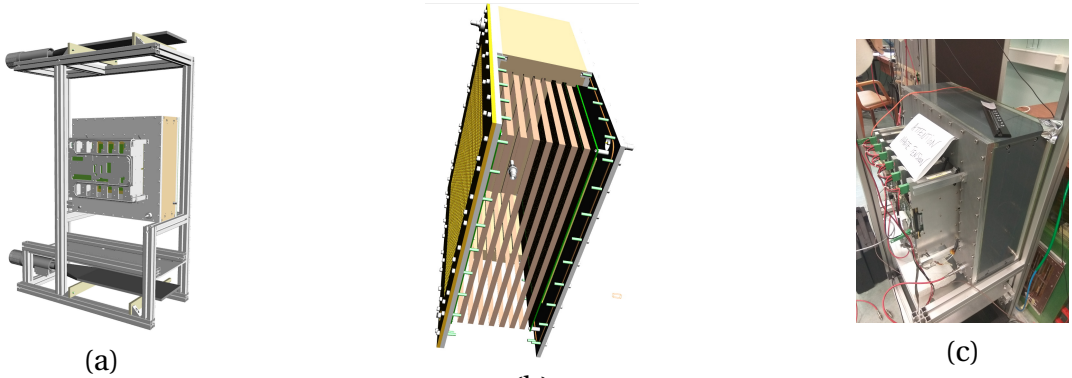

(a) (b) (c)

Figure 7.6: TPC test bench in Saclay. (a) a CAD model of the whole test bench with the scintillator bars above and behind the detector as a trigger. (b) the CAD model of the field cage. (c) a photo of the test bench during the data taking.

The data was taken with the cosmic rays and the X–ray radioactive source (^{55}Fe). The trigger system for the cosmic muons was built around the setup. On the Figure 7.6 (a) two scintillator planes above and below the detector are shown in dark gray. The planes are readout with photo-multipliers and the coincidence of signal in two planes serves as a trigger for the through-going cosmic ray. From the ^{55}Fe source, we expect continuous decays, so we can sample the data nearly at any time. The pulse generator was used as a trigger for this sample.

As at any other detector, we expected to see a certain level of noise in our measurements. The noise level was measured for each channel independently. The pulse generator was used to sample the data from each pad. As we expected no signal in the pad the measured value should be caused by the noise and suppressed in future measurements. As the noise is a subject of fluctuation its value was measured for a continuous period. The measured values were fit with the Gaussian distribution and the mean and sigma characteristics were extracted from the fit. The mean value was going to be subtracted from every measurement done with this particular pad. The sigma value was used to treat the measured amplitude as a signal or a noise. If the amplitude was different from the mean value by more then four sigmas the measurement would be recorded. The procedure described above is called “zero–suppression”. It is usually quantified with the value of standard deviations used to divide signal and noise, e.g. 4σ or 5σ zero–suppression.

The examples of the event displays are shown in Figure 7.7. As the gain supposed to be uniform over the whole Micromegas, we expect a uniform measured charge. I analyzed the hit map with merging the information from all the cosmic tracks together. The detector response was found uniform, thus the data from the prototype may be used for the further precise analysis.

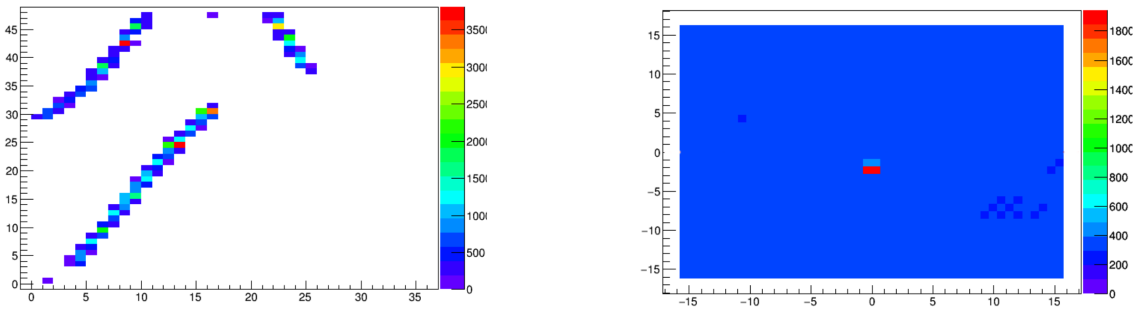

(a) (b)

Figure 7.7: Events observed in the TPC prototype during the test in Saclay. (a) cosmic ray and (b) an X–ray detection from ^{55}Fe source.

At the hit maps, a cluster of the missed pads was observed at the top left part of the Micromegas. It was found that the problem was in the electronic connection in the readout system, but not in the Micromegas itself.

With the collected data I estimated the energy resolution of the detector with both cosmic rays and ^{55}Fe source with a truncated mean technique (subsubsection 2.2.d). The distribution of the dE/dx for cosmic tracks is shown in Figure 7.9 and gives a 20% energy resolution. The resolution measurement with cosmic rays is not precise. The energy loss depends on the muon energy. The dE/dx measurements from tracks are made for all the cosmic tracks in a whole spectrum. The obtained value is an upper limit and more precise measurements will be done during the beamtest. The analyses of the ^{55}Fe events is more precise as the isotope is a monoenergetic source of 5.9 keV photons. The resolution for the 5.9 keV line was measured at a level of 7.3% that is comparable with the performance of the existing detectors [110].

The charge spreading in the Micromegas is the main feature in the prototype. The spreading needs to be measured and prove to be working. As we are working with the vertical cosmic tracks the number of triggered pads in a row is a good metric to quantify the charge sharing between the pads. We will call this metric “pad multiplicity”. Without the resistive foil, with a small drift distance, we expect to have one pad illuminated if the track goes over the pad center and two pads if the track goes over the pad border. The pad multiplicity for the vertical cosmic rays going through the TPC prototype is shown in Figure 7.8. Clusters with two pads are dominating. We also have some clusters with more than two pads in a row that is completely impossible in the absence of the resistive layer. Thus we have a clear indication that the RC network is working. Though there are many pads with only one pad in a row. It may be caused by the low ionization by the cosmic muon or by not sufficient charge spreading in the Micromegas. The beam test will provide more accurate result. The resistivity of the Micromegas can be tuned according to obtained results.

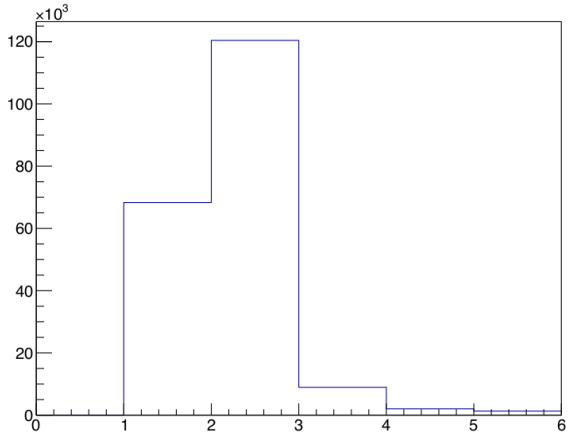

Figure 7.8: The number of pads in a row for the vertical cosmic track (pad multiplicity) in the TPC prototype at Saclay.

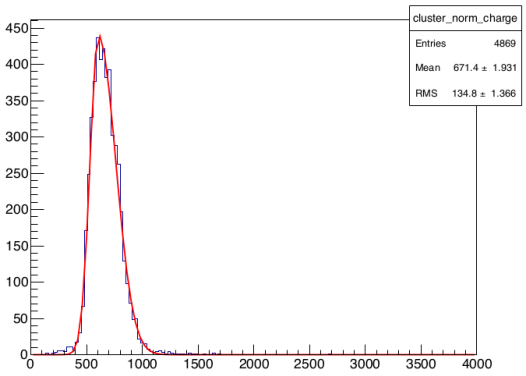

Figure 7.9: The distribution of the average charge per cluster after the truncation fit with Gaussian function.

To sum up, the detector was tested at the test bench with cosmic rays and ^{55}Fe source. The measured energy resolution for the isotope is similar to the performance of the existing TPCs. The charge spreading over pads was proved to be working. After these preliminary measurements detector will be tested at the beam of charged particles.

2.2 CERN beamtest

The Micromegas module tested with the cosmic rays in Saclay was further studied in CERN with the charged particle beam from the accelerator beamline.

a Setup

The detector was mounted in the former HARP TPC field cage [132]. The HARP experiment was conducted in the early 2000s and was aimed at precise measurements of the hadron production on various solid and liquid targets. The high tracking performance was obtained with the HARP field cage. It is a 2 m long and 0.8 m diameter cylindrical volume that provides 1.5 m drift region. In our test setup, the cathode and Micromegas were mounted on the opposite edges of the cylinder and cathode set at 25 kV providing a drift field of 167 V/cm. A ^{55}Fe source was mounted on the cathode plane for the MM gain measurements. The gas mixture of Ar:CF_4:iC_4H_{10} (95:3:2) was used to fill the gas volume. It is the same mixture that has been used in the ND280 TPCs. The electronics were the same that had been developed for the T2K TPCs. No magnetic field was used in this test. The photo of the setup is shown in Figure 7.10.

Figure 7.10: The photo of the TPC prototype installed at the CERN beamline. The Micromegas are installed in the closes end cap of the cylinder field cage. The scintillator planes for the cosmic trigger are put above and below the TPC.

CERN T9 beamline was used for the charged particle source. It is based on the proton synchrotron (PS) and was operated in the “hadron enriched mode” with a copper target. The beam polarity, momentum and focus point can be adjusted by tuning of the beamline magnets. At the energies below 1 GeV the beam is mostly electron/positron, while above this energy it is mostly pions. The proton contribution is roughly one third of all the particles. These particles are important for the TPC tests as all of them can be produced with the neutrino interactions in ND280. The type of particles in the particular data sample is determined with the trigger system configuration.

The scheme of the trigger system is shown in Figure 7.11. For example, the Cherenkov detectors signals (C1, C2) will explicitly indicate the electron or a positron, while for pion or a proton there should be no signal in these detectors. Pions and protons were separated with the time difference between the signal in the scintillator detectors (S1, S2, S3). Thus the beam data is divided into electron, proton and pion samples with the appropriate trigger consequence used. We expect the particles of certain type to dominate in each sample.

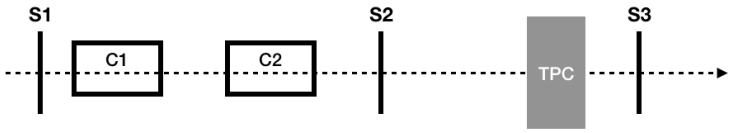

Figure 7.11: The scheme of the trigger system for the TPC prototype test at CERN beamline. The system consists of two Cherenkov detectors (C1, C2) and three scintillator detectors (S1, S2, S3).

The data were taken with three trigger activation schemes: electron, pion and proton and with three drift distances 10, 30, and 80 cm. During these scans, the Micromegas was operated with a voltage of 340 V, the electronics sampling and peaking time were set to 80 ns and 600 ns respectively. In addition, with the beamline and trigger set to 1 GeV/c pion selection, the MM voltage scan was performed. Samples with high voltage from 330 V up to 380 V with 10 V steps were taken. During the whole data taking, cosmic rays were also recorded. For this purpose, two scintillators panels were put above and below the field cage and served as a trigger. The signal readout from the panels was done with wavelength shifting fibers (WLS) and multi-pixel photon counters (MPPC). The cosmic trigger can be activated only outside of the beam window time. The signal from ^{55}Fe source was also collected. We expected a couple of source events for the drift time at a distance of 1.5 m (whole detector), so no additional trigger was set. We would be able to see enough source events in the samples with beam or cosmic tracks.

After the trigger arrives each pad is open for data recording with 511 time bins. Most of the time, the sampling of 80 ns was used. That gives us a time window 1.5 times larger than the expected drift time for the whole TPC length. The 4σ zero suppression was used with a similar technique that was described in the Saclay test. The signal in the particular pad is stored only if the maximum amplitude was higher than the mean noise by more than 4 standard deviations. The examples of the waveforms are shown in Figure 7.12. There are few options for the definition of the collected charge in the pad: maximum amplitude, integral over a time interval, etc. In our study, we found that the maximum amplitude gave us the best performance so here and further this definition of the "charge collected with a pad" would be used. The Figure 7.12 also illustrates the resistive charge spreading between the pads. The track went over the pad shown in black where the highest signal was observed. But because of the resistive foil, the charge was spread to the pad below and above (blue and red) with some delay in time.

b Track reconstruction

A simple algorithm was developed to reconstruct the cosmic and beam tracks. With the beamline intensities, several particles can cross the TPC within one event. I expect a through-going track to be a continuous chain of hits between the Micromegas edges. The track reconstruction starts with a selection of groups of pads at the beginning and at the end of the Micromegas. Relatively high threshold of 50 charge unit is set to suppress all the noisy pads. The pads that are illuminated with charge spreading are suppressed as well. At this step I'm interested only in the pads that are

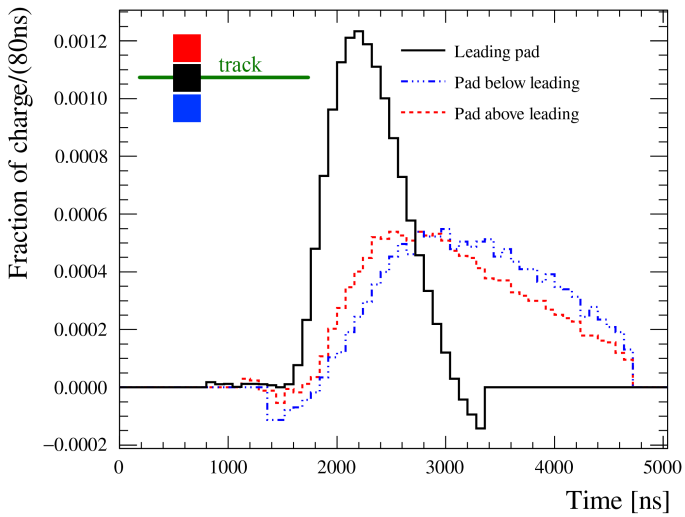

Figure 7.12: The waveform recorded in the three neighbor pads. The tracks went over the pad shown in black and the resistive foil spread the charge to the pad below and above (blue and red) with some delay in time.

crossed by the track. Then the algorithm looks for all the possible connections between these clusters. Again, a high threshold is applied to deal with primary pads only and do not take into account charge sharing. The sharing is essential for the precision track positioning, but not for the pattern recognition. Delayed pads can make a confusion and result in merging of two different tracks. If there is a chain of hits connecting these clusters in three dimensions such a chain will be recognized as a track. After that, the time window in space and time is defined “around” the track. I’m looking for hits on both sides and with possible time delay up to 2.5 μs. The pads of the side of the track that where triggered before the central one are not considered as a charge spreading should be delayed.

At our energies, most of the tracks are straight lines. There are very few events with complicated topologies like decays or scatterings and such events were omitted. I put a cut on the maximum number of clusters at the beginning and at the end of the track. If it’s more than four, the event seems to be too complicated to perform an accurate reconstruction and is omitted. If the tracks width is more then six pads, the track is omitted as well. I observed that normal tracks do not spread more then five pads and when the large spreading happens it clearly indicates that there was some kind of reaction, scattering or a delta—ray emission.

An example of a raw event with two tracks is presented in figure Figure 7.13 (a). With our algorithm, we extracted the bottom track and omitted the upper one as we suspect some interaction that causes the large charge deposition with a spreading up to 7 pads in width.

c Gas quality

The gas quality is an important characteristic of the TPC. We performed its checks with the drift velocity, attenuation length and gain measurements.

The drift velocity is a convenient metric of the gas mixture quality. The stability of the drift velocity is an essential characteristic of the mixture for the precise analyses. For the drift velocity measurements, we used cosmic tracks that were intersecting a cathode or Micromegas. It was possible since the scintillator bars used for the cosmic trigger system were wider than the detector

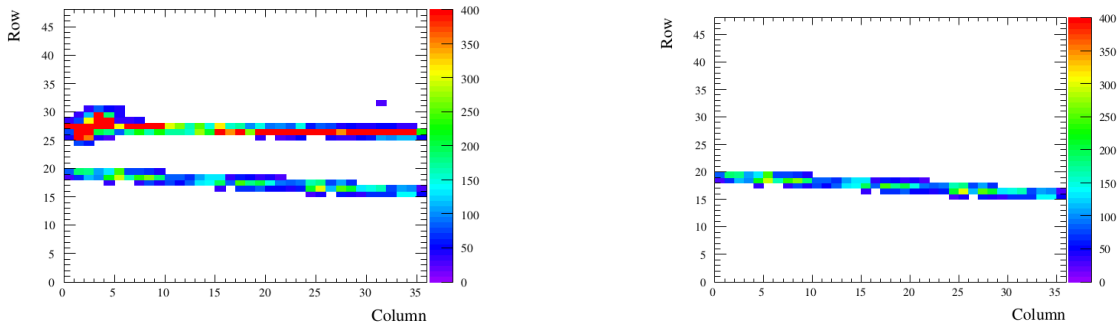

(a) (b)

Figure 7.13: The example of the raw event (a) and the extracted track of interest (b) in the TPC prototype.

drift region. Such tracks can be recognized with a start or endpoint in the middle of the detector plane. The timestamps of the anode/cathode crossings are presented in Figure 7.14 (a). The different amount of tracks at each end was caused by the significantly lower acceptance of the cosmic trigger for tracks close to the anode. The time difference between two peaks will give us an electron drift time for the given drift distance of the 150 cm. The evolution of the drift velocity is shown in Figure 7.14 (b).

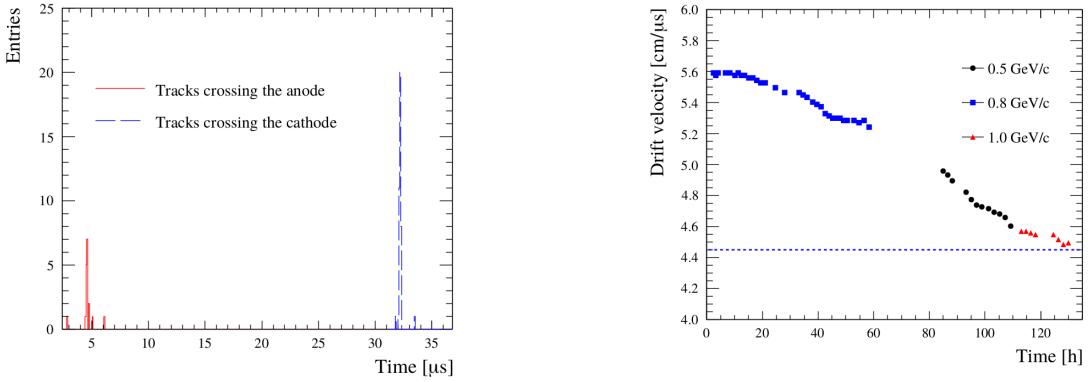

(a) (b)

Figure 7.14: The drift velocity measurements in the TPC prototype in CERN beamtest. (a) The timestamps of the cathode/Micromegas intersection and (b) the estimated values of the drift velocity.

The attenuation length is another characteristic of gas quality. It shows how many electrons were absorbed during the drift. Lower attenuation length will result in the lower measured charge and will affect more the tracks that are away from Micromegas. We used cosmic tracks for this measurement as they crossed the TPC at all the range of drift distances. The mean collected charge versus the drift distance was fit with the exponential law to extract the attenuation length. The illustration of the attenuation effect and the evolution of the attenuation length during the data taking are shown in Figure 7.15. A slight degradation was observed but it was always at least twice the TPC length and would not cause a degradation of the data quality.

The gain evolution during the data taking was measured using the ^{55}Fe source. The radioactive source was mounted at the center of the cathode. For each event triggered by either cosmic or a beam trigger the time window for data recording is more than the drift time for the whole TPC length. During that time we expect to detect about two ^{55}Fe decays with 5.9 keV X-ray emission.

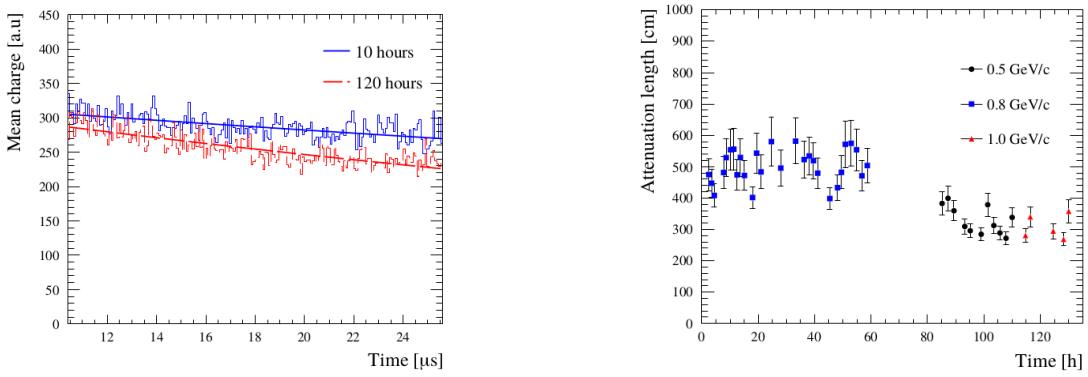

(a) (b)

Figure 7.15: The attenuation effect in the TPC prototype at the beamtest at CERN (a) and the attenuation length during the data taking (b). The measurements were done with the cosmic tracks, the momentum of the beam is illustrating what data sample were taken with the beam at that time.

Therefore no special trigger was needed and the clusters from the source decays can be found in the beam or cosmic data. The total charge collected from the cluster was used for the gain estimations. The gain itself is computed as a ratio of the measured electrons to initial electrons from X–ray interaction. From the 5.9 keV photon interaction with Argon, 230 initial electrons are expected. This value was measured in the various gaseous detectors' tests and used as an input in our analyses. The whole dynamic range of each pad is 4096 channels that correspond to the total charge of 120 fC. The measured spectrum for the radioactive source is shown in Figure 7.16 (a). A resolution was good enough to see also a 2.9 keV escape line in Argon. The gain was expected to depend on the Micromegas voltage with an exponential law. The expected dependence was observed during the MM high voltage scan (Figure 7.16 (b)). The gain evolution with a constant MM voltage during the data taking is shown in Figure 7.16 (c). The gain value depends on the gas quality (e.g. water contamination), atmospheric pressure and temperature. All these parameters were not precisely controlled during the data taking thus fluctuations were possible.

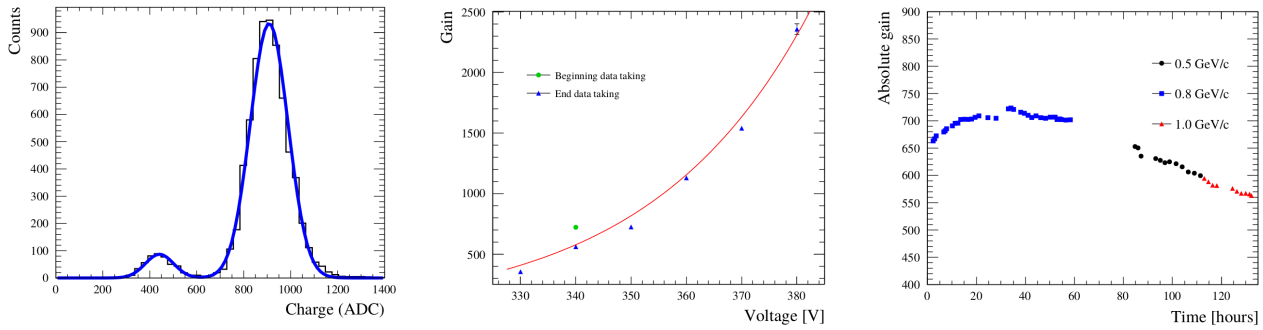

(a) (b) (c)

Figure 7.16: The spectrum of the ^{55}Fe source with measured 5.9 keV X–ray and 2.9 keV escape line in Argon (a). The evaluation of the gain versus the Micromegas voltage (b) and versus the data taking period (c)

For all the measurements of the gas parameters, we observed a slight improvements of the gas quality at the very beginning with further degradation with time. We assume that the degradation was due to increasing H_2O contamination in the mixture. Water is known to slow down the elec-

tron drift, increase the attenuation and reduce the gain. The HARP field cage was stored in the air for a long time and was not dried before the operation. During the test the TPC was operated in overpressure, thus we consider that the gas quality degradation was caused by the water releasing from the field cage. The evolution of the gas parameters during the beamtest was correlated with the change of the gas flow in the detector. At the beginning of the data taking the flow was set to 60 L/h and was further decreased to 25 L/h as the mixture was believed to be stable enough. During the data analyses, it was found that the gas flow reduction caused the degradation of the mixture parameters. However, this degradation is not critical for the measurements. For the data analyses, the corrections were applied to compensate for the gain and attenuation length drop.

d Ionization energy loss (dE/dx) resolution

The dE/dx resolution is critical for the T2K measurements. As mentioned in subsubsection 2.2.c of chapter 3, during the ionization process charged particles lose the energy with high fluctuations. The average value of several independent measurements is used for the particle type estimations. The resistive foil usage implements a correlation of the measured charge values in the neighbor pads. It can spoil the dE/dx resolution as each measurement is not independent anymore. I estimated the dE/dx resolution for the beam tracks with the CERN TPC prototype.

The dE/dx resolution was measured with the horizontal beam tracks. The track is considered as a group of "clusters". The "cluster" is defined as a group of pads perpendicular to the track direction. E.g. for the horizontal track the hits in a particular column of the Micromegas will form a "cluster". The charge collected in the cluster is summed up and considered as an energy loss per fixed length (0.9 mm — pad size). The distribution of the charge per cluster has a long tail towards the high energy. This is in agreement with the expected ionization energy spectrum as it is described with Landau distribution. To omit the clusters with large charge deposition the "truncation" method is used. All the clusters in the track are sorted by increasing charges. Some clusters from the beginning of the list (e.g. 70%) are used to estimate the average energy loss per cluster. The truncation fraction is varied to obtain the best dE/dx resolution. The 62.5% truncation was found to provide the best performance (Figure 7.17 (a)). The average energy loss per unit length before and after the truncation is shown in Figure 7.17 (b). As one can see the distribution becomes Gaussian. Therefore the mean and the standard deviation can be estimated and the resolution can be computed.

The dE/dx distributions for 0.8 GeV/c electrons, pions and protons samples are shown in Figure 7.18 (a). The particle type per each sample is defined based on the trigger combination that was used. However, the contamination of other particle types is possible. The pion sample has two peaks, and the second peak matches perfectly with the peak in the electron sample. As the electrons are dominating in the beam, we suspected that a small impurity in the pion trigger can cause the acceptance of the electrons. The resolution for each particle sample and drift distance is shown in Figure 7.18 (b). For the pion sample, only the first peak that indeed corresponds to the pion is used. The results are summarized in Table 7.2. The worse resolution in the pion sample is understood as they are less ionizing comparing to protons or electrons. Less deposited charge is more affected by the fluctuations. Scaling of the obtained results to the twice longer ND280 TPC will give us a performance similar to one at the existing detectors. That is a very important conclusion as we were afraid of the dE/dx resolution degradation with the resistive anode technology.

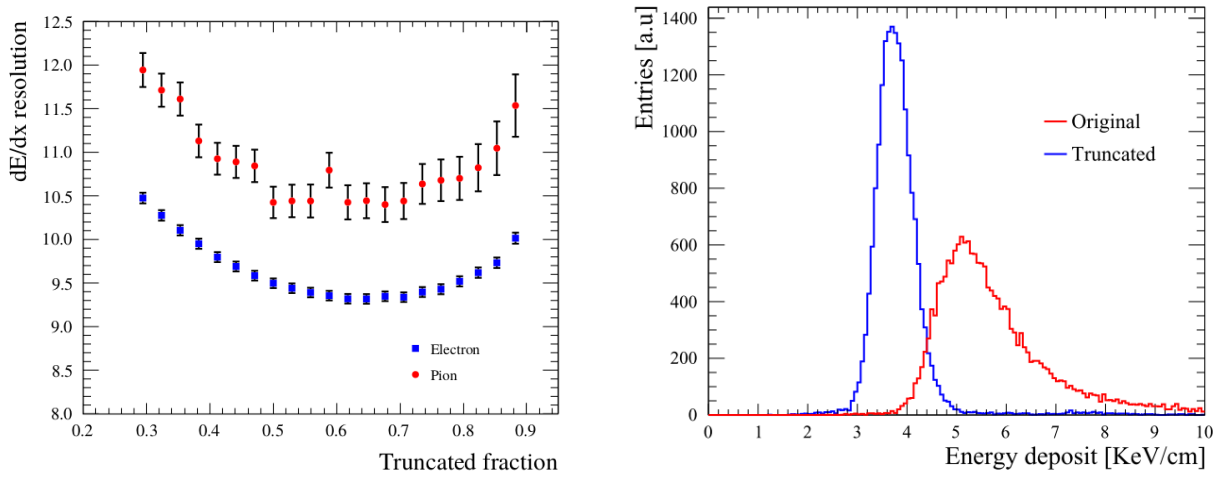

(a) (b)

Figure 7.17: Resolution on the energy deposit per unit of track length for different truncation values (a). Comparison on the energy deposited per unit length on the same beam sample of positrons at 0.8 GeV/c with and without applying the truncation mean method (b).

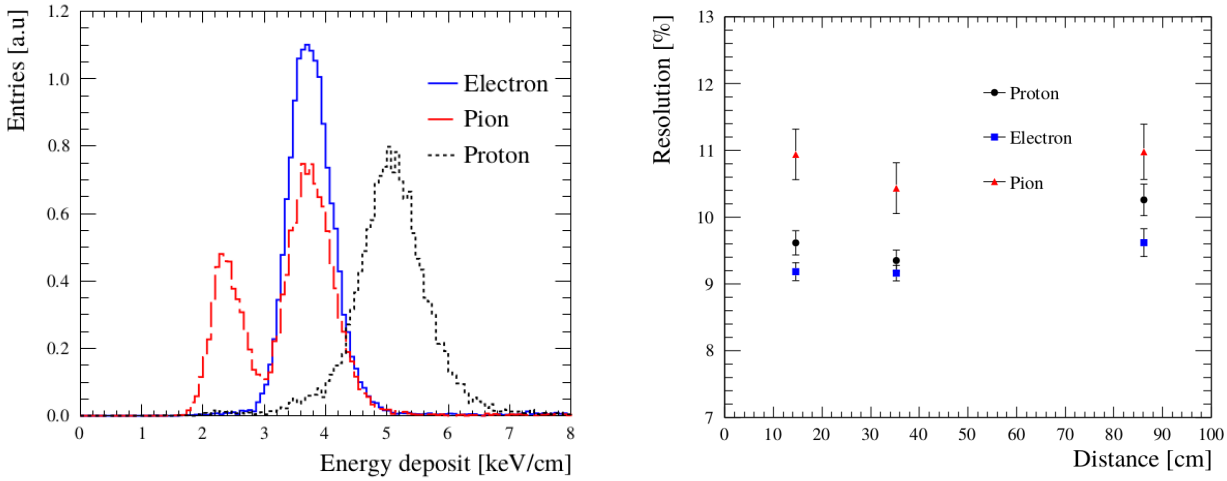

(a) (b)

Figure 7.18: The dE/dx resolution for different particles samples and drift distances (b) obtained from the dE/dx distributions for each sample (a) in the TPC prototype test at CERN.

Sample	Resolution, %
Electron	9.2 ± 0.1
Pion	10.9 ± 0.4
Proton	9.6 ± 0.2

Table 7.2: The dE/dx resolution for different particles samples at 10 cm drift distance.

e Spatial resolution

The spatial resolution analyses is extremely important as we expect a noticeable improvement comparing to the existing TPCs. With the resistive Micromegas the charge is shared between few

pads that allows more accurate position reconstruction (Figure 7.3). The easiest method to extract the position based on the signal in a few pads is a weighted mean. The description of the method is provided in Equation 7.2. The group of pads perpendicular to the track direction is referred to as a "cluster". In our beamtest particles provide horizontal track, therefore each column is a "cluster". In the cluster, all the pads are weighted with the measured charge and the weighted mean will give a track position in the particular cluster.

$$x_{track} = \frac{\sum(x_{pad} \cdot Q_{pad})}{\sum Q_{pad}} \tag{7.2}$$

The track position in all the clusters can be further fit with a straight line or with an arc in the presence of the magnetic field. It was proved that such a method demonstrates the resolution improvement comparing to the existing TPCs [129]. But there is room for further improvement. The charge spreading is described with the exponential law. With the weighted mean, we sample the exponential distribution in large bins. The pad size is a few times bigger than the standard deviation of the charge spreading. With the weighted mean the whole charge collected in the pad is assigned to the pad center while with the exponential distribution of the charge it behaves differently. The improved method of the spatial resolution estimation is based on a so–called "pad response function" (PRF) that is used to describe the spreading of the charge. It was implemented in the ILC prototype analyses and was proved to improve the result over the weighted mean [130].

By definition, the PRF function describes the fraction of the cluster charge deposited in the particular pad versus the distance between the track and pad center.

$$Q_{pad}/Q_{cluster} = PRF\left(x_{track} - x_{pad}\right) \tag{7.3}$$

Assuming the PRF is known, we can compare the measured $Q_{pad}/Q_{cluster}$ with the expectations for the given track position. And the best track position in the cluster can be chosen based on the χ^2 fit.

$$\chi^2 = \sum_{pads} \frac{Q_{pad}/Q_{cluster} - PRF\left(x_{track} - x_{pad}\right)}{\sigma} \tag{7.4}$$

where σ is an uncertainty of the $Q_{pad}/Q_{cluster}$. I assumed the charge deposition follows the Poisson distribution and therefore the uncertainties can be estimated with $\sigma = \sqrt{Q_{pad}}/Q_{cluster}$. To extract the track position the PRF shape should be known , but to estimate the PRF we need the information about the track position. To deal with it I used the weighted mean method as a prior guess about the track position. Based on the known information the PRF scattered plot is filled (Figure 7.19 (a)). Then the obtained 2D histogram is profiled. In the 1D slice along the Y axis (Figure 7.19 (b)) the maximum is interpreted as a PRF value and the width at the half maximum as an uncertainty. As a result, I obtained 1D graph that can be fit with the analytical function (Figure 7.19 (c)). For the analytical function, the 4-th order polynomial was chosen.

$$PRF(x, \Gamma, \Delta, a, b) = \frac{1 + a_2 x^2 + a_4 x^4}{1 + b_2 x^2 + b_4 x^4} \tag{7.5}$$

The coefficients a_2 and a_4, and b_2 and b_4 can be expressed in terms of the full width half maximum Γ, the base width Δ of the PRF, and two scale parameters a and b.

The spatial resolution analyses flow looks as following:

1. Start with the weighted mean as a prior:

    a) track position in each cluster is evaluated with weighted mean

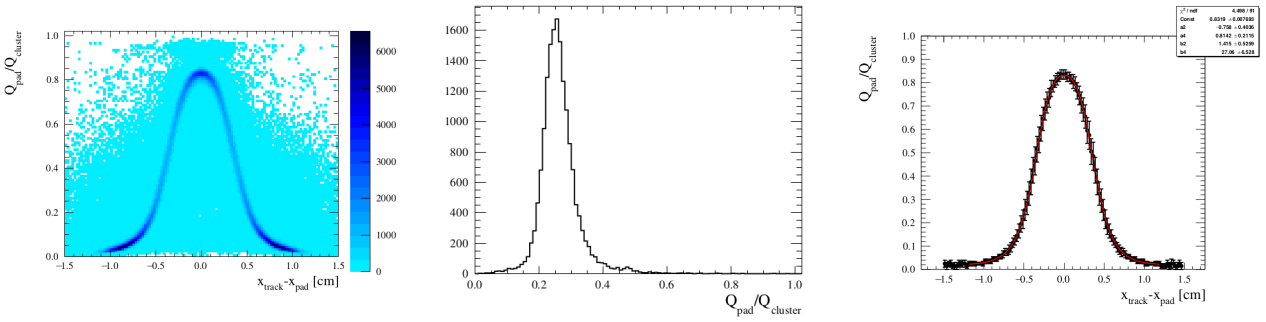

(a) (b) (c)

Figure 7.19: The PRF estimations steps: 2D scatter plot filled with each track cluster (a), the 1D slice for particular value of $x = -0.5$ (b) and a 1D graph that can be fit with the analytical function.

   b) positions in the cluster are fit together to form a track
   c) the PRF scatter plot is filled for each pad with $X_{track} - X_{pad}$ and $Q_{pad}/Q_{cluster}$

2. PRF scatter plot is profiled to the graph and fit with the analytical function

3. PRF method:

   a) track position in each cluster is evaluated with χ^2 fit (Equation 7.4)
   b) positions in the cluster are fit together to form a track
   c) the PRF scatter plot is filled for each pad with $X_{track} - X_{pad}$ and $Q_{pad}/Q_{cluster}$

To estimate the spatial resolution the residuals are defined as a difference between the global track fit and position reconstructed in the particular cluster. The residuals are fit with the Gaussian function. The spatial resolution and bias are defined as sigma and mean of the fit respectively. Steps 2 and 3 are repeated while the spatial resolution is improving. The spatial resolution and the bias obtained with weighted mean and PRF are shown in Figure 7.20. The PRF method provides a much more accurate result over the weighted mean. Also, it is more uniform over the detector. The resolution across all particle types and drift distances is presented in Figure 7.21. As was expected protons have a better resolution as they deposit more charge and the position can be estimated more precisely. Also, I observed the expected degradation of the spatial resolution with the increase of the drift distance. Because of the transversal diffusion the electron cloud becomes wider during the drift and the position reconstruction accuracy decreases. Finally, I observed the accuracy at the level of 250 μm for the 10 cm drift distance. In the existing T2K TPC the resolution is at the level of 750 μm at the same distance. The resistive foil was confirmed to improve the precision without changing the pad size.

The dependence of the spatial resolution on the drift distance is an important characteristic of the resistive TPC. Without a resistive layer, the resolution becomes worse with decreasing the drift distance. That happens because the transverse diffusion is not sufficient to spread the charge to more then one pad. All the charge is collected by one pad, thus the uncertainty of the measurement is limited by its size. The analytical study of the spatial resolution dependence on the drift distance is provided in [133]. The advantage of the resistive Micromegas is a charge spreading in the resistive foil, therefore more than one pad receive the signal even for a track close to the readout plane. The spatial resolution for such a detector is expected to follow the square root dependence with respect to the drift distance (z). The dependence of the resolution is given by Equation 7.6 [134].

$$\sigma(z) = \sqrt{\sigma_0^2 + \frac{D_{Tr}^2 z}{N_{eff}}} \tag{7.6}$$

where σ_0 is the resolution at zero drift distance, D_{Tr} is the transverse diffusion constant, and N_{eff} is the effective number of electrons over the length of pad. N_{eff} is computed based on the number of initial ionization electrons N with $N_{eff} = 1/\langle\sqrt{1/N}\rangle^2$.

Thus, improving the spatial resolution with the reduction of the drift distance is a clear effect of the resistive foil.

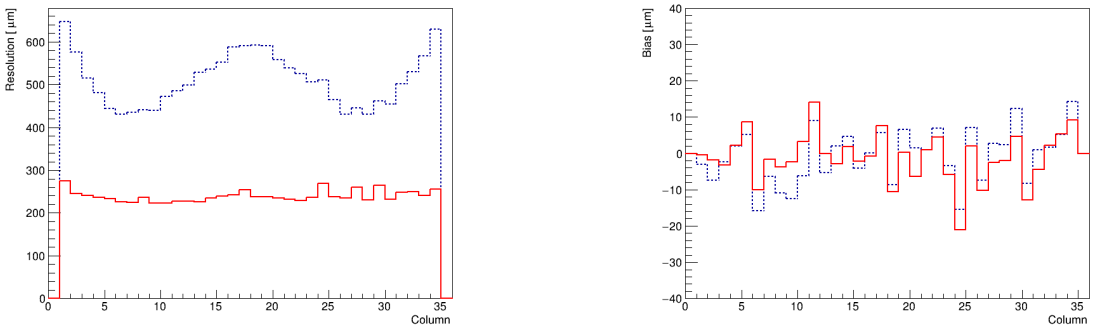

(a) (b)

Figure 7.20: The spatial resolution (a) and a bias (b) obtained in the TPC prototype test at CERN with 10 cm drift distance with electron sample. The results of the weighted mean method are shown in dashed blue and the results from PRF method is solid red.

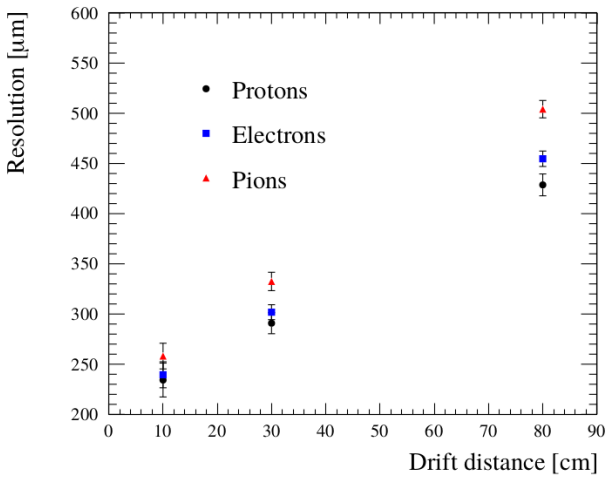

Figure 7.21: The spatial resolution for all the particles types and drift distances in the CERN beam test.

The beamtest at CERN shows good performance of the resistive TPC prototype. Different samples with different particles types and at various drift distances were tested. The dE/dx resolution was estimated at the same level as in existing TPCs but the spatial resolution was proved to be significantly improved. The paper describing the analyses and the results I obtained was published [3].

2.3 DESY beamtest

The CERN beamtest confirms the good performance of the new detector. The tested detector was based on the same circuit board (PCB) as we are using in the ND280 TPCs at the moment. The planned HA–TPCs will have different dimensions and pad sizes. The new micromegas was produced for the next beamtest. The same dimensions as in HA–TPC were used. The module size is 34×42 cm^2 and is paved with 32×36 pads 1.1×1.0 cm^2 each. The thin 75 μm insulator layer is covered with 50 μm Kapton with the DLC on top of it. Compared to the first prototype ($200 + 50$ μm) the capacitance was increased. The resistivity was decreased from 2.5 $M\Omega/\square$ down to 0.4 $M\Omega/\square$. The side pads were partly covered for mesh fixation as before and these pads were excluded from the analyses.

The DESY beamtest facility provides a beam of electrons. The momentum can be adjusted from 1 to 5 GeV/c. The scheme of the beamtest facility is provided in Figure 7.22. A magnetic field was used in this test. Most of the samples were taken with 0.2 T field strength, while some data were collected in the absence of the field.

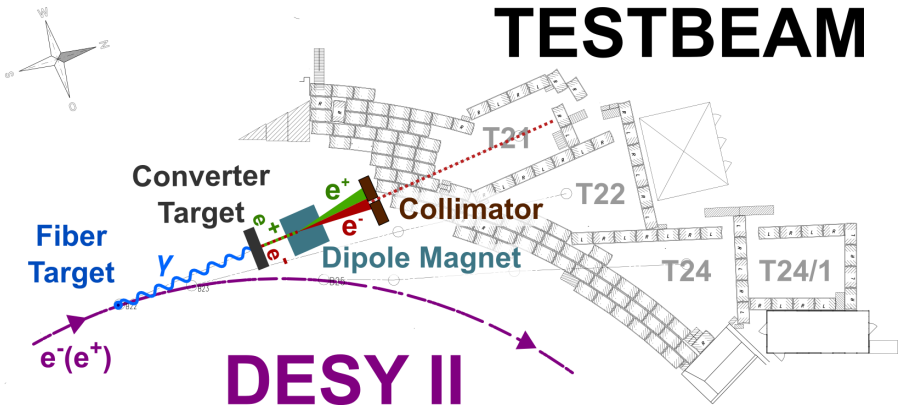

Figure 7.22: The scheme of the DESY beamtest facility

a Track reconstruction

In addition to the track reconstruction method described in the CERN test section, we also tried the DBSCAN (Density-Based Algorithm for Discovering Clusters) algorithm [135]. As it is aimed at matching the hits into clusters based on the hit "weight", it looks like a good framework for our case. In the CERN beamtest it was found excessive and was not used for the final result, but in the DESY analyses it demonstrated better performance and was chosen as the main algorithm. The examples of the reconstructed tracks are shown in Figure 7.23.

b Ionization energy loss resolution

The dE/dx resolution was tested with the same method as was used for CERN and Saclay analyses. The truncated mean of the charge collected from the track distribution was fit to estimate the resolution. In the CERN beam test analyses I observed mostly two pads per cluster. We suspect that not sufficient charge spreading may limit the spatial resolution. In the DESY test the nominal MM voltage was increased to 360 V. The effect of the high voltage on the multiplicity can be seen

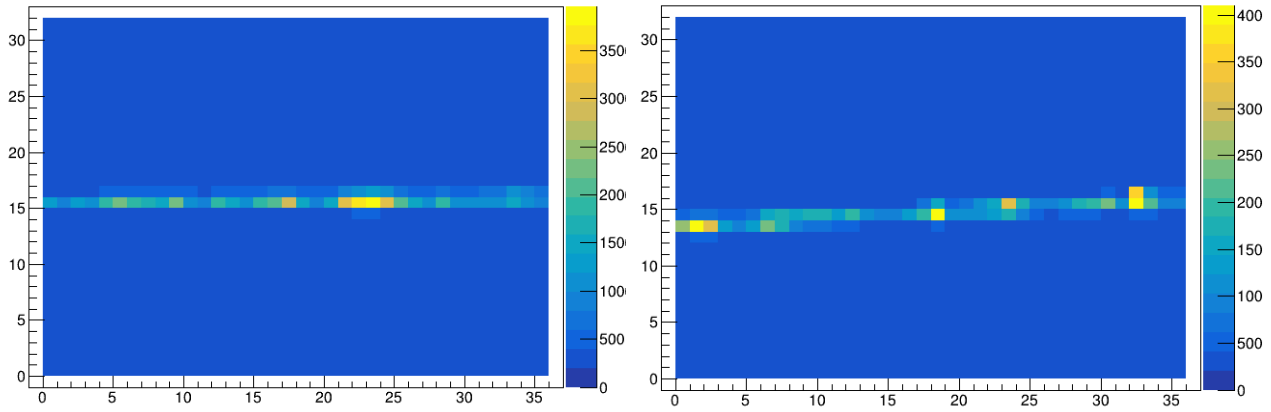

Figure 7.23: Two examples of the reconstructed tracks from the DESY beamtest.

in Figure 7.24. Thus with the nominal voltage I observed 3 pads per cluster in most of the cases. With this I expected to improve the spatial resolution.

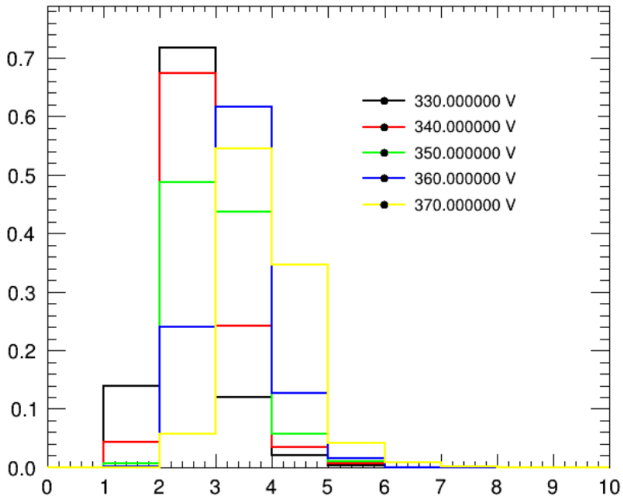

Figure 7.24: The number of pads in the cluster in the DESY test versus the MM voltage.

The dE/dx resolution and the collected charge for the different detector parameter scans are presented in Figure 7.25—7.28.

From these plots, we can see that the resolution remains stable over the different parameters of the setup. Though I found some expected dependencies. The presence of the magnetic field improves the charge collection and also improves the energy resolution (Figure 7.25). The dependence of the resolution and the collected charge over the drift distance is not completely understood. The larger collected charge in the sample at 530 mm position is not expected as there is nothing specific in it. We suspect the electric field uniformity as a possible reason for such an effect.

Overall, the energy resolution was estimated below 10% for nearly all the samples with the magnetic field. In the absence of the field the dE/dx resolution is below 12%. As before, we are using one module so for the proper comparison with the existing TPCs performance, the result should be scaled with $1/\sqrt{2}$. It will give us 7% resolution that is the same as what we observed in the existing ND280 TPCs.

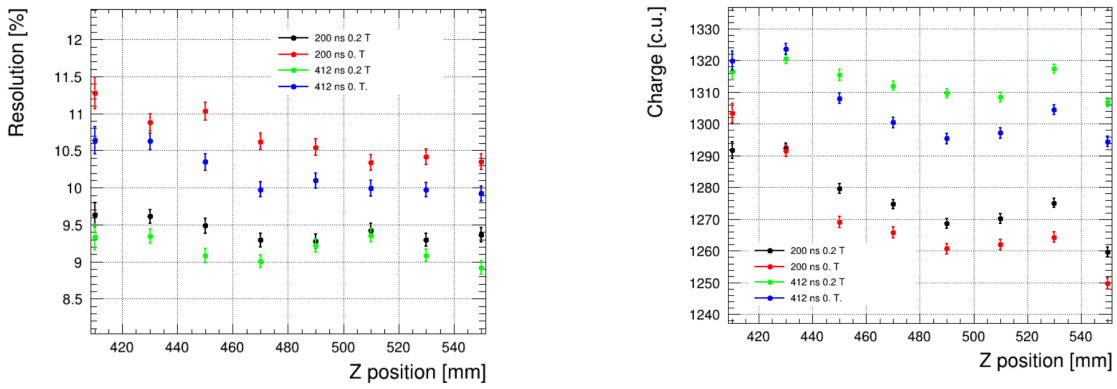

(a) (b)

Figure 7.25: The dE/dx resolution (a) and average charge per cluster (b) for the 4 GeV/c electron tracks in the DESY beamtest versus the drift distance (a.u.) for different peaking time and magnetic field setup.

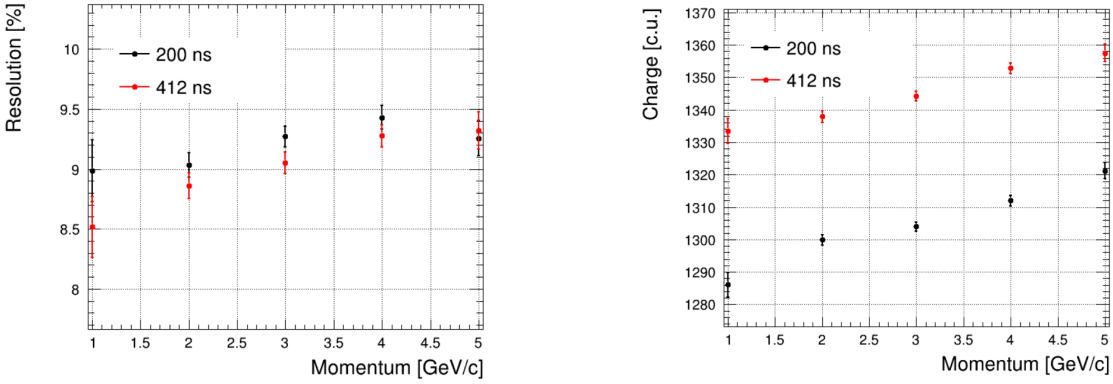

(a) (b)

Figure 7.26: The energy resolution (a) and average charge per cluster (b) for the electron tracks in the DESY beamtest versus the track momentum for different peaking time. The magnetic field is set to 0.2T, the track position is set to 430 mm along Z axis.

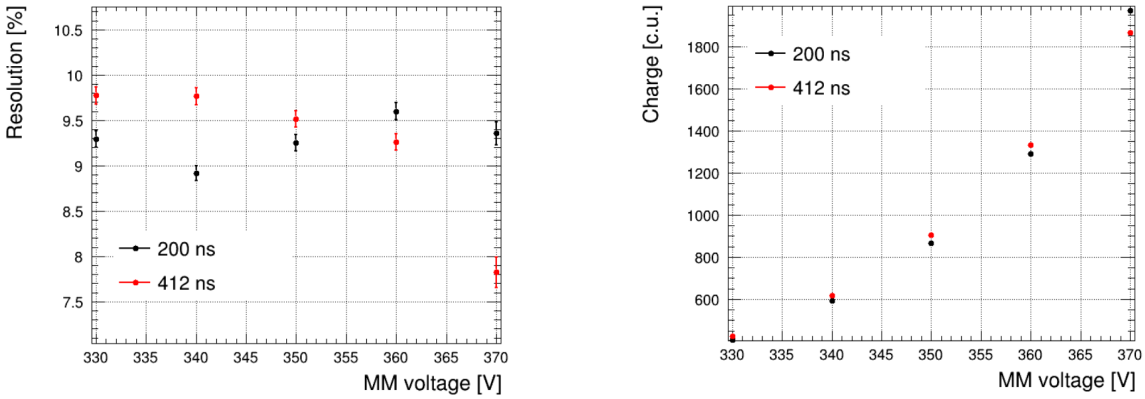

(a) (b)

Figure 7.27: The energy resolution (a) and average charge per cluster (b) for the 4 GeV/c electron tracks in the DESY beamtest versus the Micromegas voltage for different peaking time. The magnetic field is set to 0.2T, the track position is set to 430 mm along Z axis.

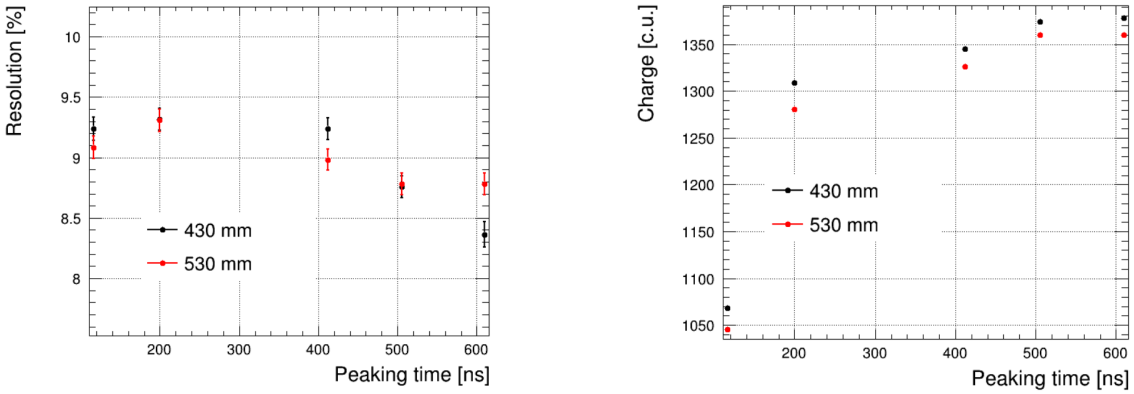

(a) (b)

Figure 7.28: The energy resolution (a) and average charge per cluster (b) for the 4 GeV/c electron tracks in the DESY beamtest versus the peaking time for different drift distances (a.u.). The magnetic field is set to 0.2T.

c Spatial resolution

The PRF technique described in the CERN test section was used to estimate the spatial resolution of the new setup. The various scans with horizontal tracks were used to evaluate the dependence of the resolution over the detector parameters. The result is shown in Figure 7.29 and Figure 7.30. The spatial resolution below 220 μm was observed over all drift distance region. It was found that the higher voltage provides remarkable improvements in the detector performance decreasing the resolution from 300 μm down to 150 μm. The higher voltage cause the larger amplification. Therefore more pads detect the signal with the charge spreading. With more pads the more robust position extraction is possible. It was also found that the peaking time has no strong influence of the resolution that allows to choose any value of this parameter.

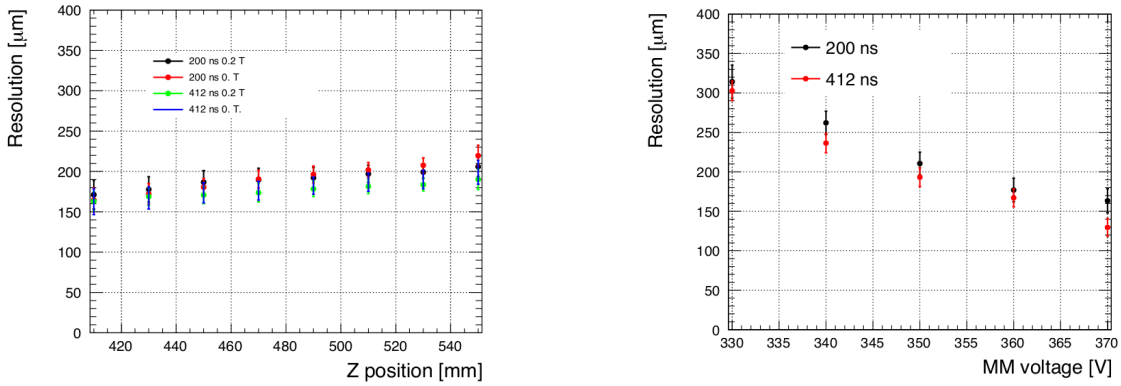

(a) (b)

Figure 7.29: The spatial resolution of the DESY test versus the drift distances (a.u.) (a) and the Micromegas voltage (b)

The electron beam in the facility is spread in space. The beam profile can be described with a Gaussian shape with a sigma around 1 cm. This allows us to study the dependence of the spatial resolution from the track position in the pad. The detector is kept at the same position but because of the natural beam spread tracks cross pads in the different positions. The obtained spatial resolu-

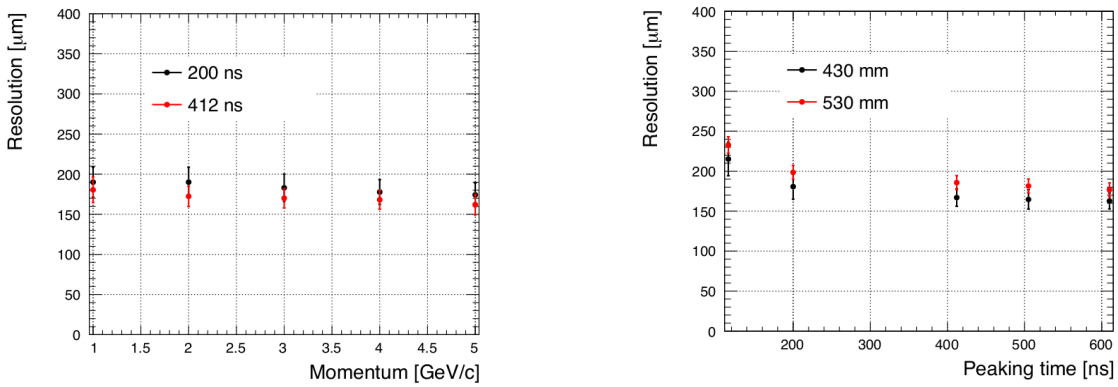

(a) (b)

Figure 7.30: The spatial resolution of the DESY test versus the track momentum (a) and the peaking time (b)

tion versus the position in the pad is shown in Figure 7.31. I observed a significant variation of the resolution. It changes from 100 μm at the pad border up to 200 μm in the pad center. The behavior is mostly understood. When a track crosses a pad center the pad multiplicity in the perpendicular direction is lower compared to the case when the track goes over the border of two pads. More pads detect the signal more accurate position reconstruction in the cluster we expect. The effect can be reduced with implementation of larger charge spreading. But the tracking in case of events with many particles will be more difficult. The investigation of the possible analyses algorithm improvements is ongoing. The Mont–Carlo simulation can help with testing the different detector configurations and obtaining the best one. The MC algorithm is under development, we are looking for the best analytical description of the charge sharing effect. Since the simulation toolkit is established, we can test various detector configuration with different reconstruction algorithms to find the best combination.

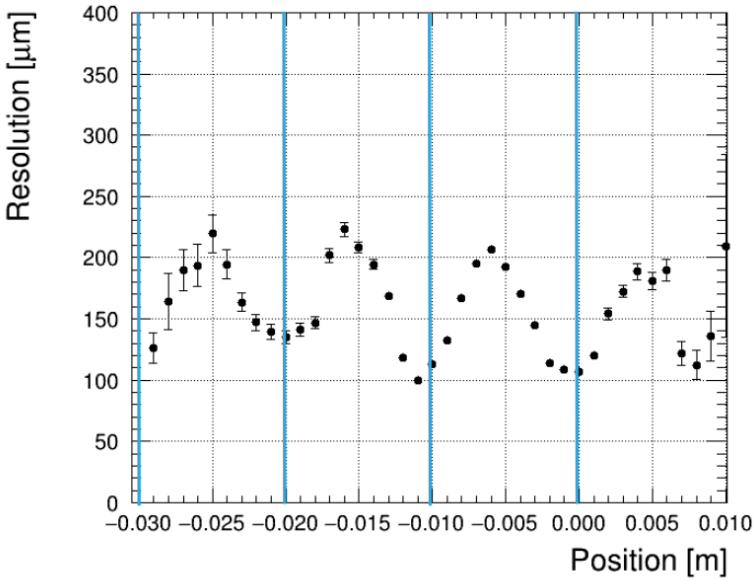

Figure 7.31: The spatial resolution versus the track position in the pad in the particular column. The pad borders are represented with the vertical lines.

d DESY test results

The DESY test analyses has already demonstrated the large improvement of the spatial resolution. Values below 200 μm were reached. The energy resolution was observed at the level of the existing ND280 TPCs.

The analyses of the beamtest data is still ongoing. Many improvements can be made. For example, we are working on a better understanding of the waveforms that will allow us to get rid of taking the maximum amplitude but use the information from the whole distribution. For this a good understanding of the electronics is required. The possible benefit is a more precise treatment of the charge in a pad resulting in better spatial resolution. A precise description of the detector response will also help a lot with the future Monte–Carlo simulations. In the T2K the MC simulation is an integral part of the analyses. A good detector model is required for future HA–TPC.

The other major improvement that can be made is the development of a different algorithm for track reconstruction. The PRF method demonstrated good performance for the horizontal tracks, but it looses the precision for the inclined tracks. Better analyses techniques are under investigation.

3 Conclusion

The high angle TPCs will play an important role in the upgraded near detector of the T2K experiment. The new field cage and the new MicroMegas detector with the resistive foil were designed. The prototypes of the TPC with the resistive anodes were tested in the different regimes. I found that the energy resolution will not be worse compared to the existing TPCs, which is critical for the ν_e measurements in T2K. The spatial resolution will be improved that will provide more precise momentum reconstruction.

As was mentioned in the introduction the improved spatial resolution will not gain the neutrino energy reconstruction accuracy under the CCQE reaction assumption. The smearing effect of the Fermi motion is larger than the uncertainty on the lepton momentum. But some analyses can improve the accuracy with more precise momentum reconstruction. T2K spent a lot of effort on studying nuclear effects such as Fermi motion, FSI, nucleon correlation effects. It is already the dominant systematic on current T2K measurements of oscillation parameters and will soon become the principal precision limitation. There are plenty of models describing the effects, but the precision of the measurements does not allow us to select the most appropriate one. In our experiment, to study the nuclear effects, we use the kinematic imbalance between the final state lepton and hadrons in the plane transverse to the neutrino direction [136]. The presence of such an imbalance explicitly indicates the nuclear effects. This particular approach allows studying the effects of interest with minimal dependence from the incoming neutrino energy. Also, it provides the natural separation between Fermi motion effects and nucleon correlation. This is very helpful in the determination of the appropriate model. As we can study the kinematic region where Fermi motion is severely suppressed this effect will not provide the domination smearing anymore. Thus the improvements in the momentum resolution will gain the physics analyses performance. One more analyses technique that will be able to improve its performance with the new TPCs is an analysis of the pion production in a neutrino interaction. The double transversal momentum imbalance is a technique [137] that can distinguish the neutrino interactions with Hydrogen and Carbon in our scintillator target. Such an analysis will also gain performance with more precise momentum measurements. This list of possible improvements is not limited to the studies mentioned above.

Any analysis that requires the momentum precision better than 10% will gain accuracy with the new detectors.

The production of the HA–TPC is ongoing and the installation is planned for 2022.

CHAPTER 8

SUPER FGD

In the ND280, the Fine-Grained Detectors (FGD) [109] serve as neutrino targets. They are made from scintillator bars oriented in the perpendicular directions w.r.t the neutrino beam. Such a structure provides excellent performance in the reconstruction of the forward-going tracks. But the acceptance for tracks at a high angle is limited. The whole track may be contained in one scintillator bar and the accurate measurement will not be possible. One of the main goals of the ND280 upgrade is to study tracks at a high angle, thus a target with a new concept is required. A new target is going to be built with optically isolated scintillator cubes [2]. The scheme of the new detector is shown in Figure 8.1. Each $1\times1\times1$ cm^3 cube will have three holes in x, y, and z directions. The signal readout is organized with wavelength shifting fibers (WLS) that will transfer light to the Multi–Pixel Photo Counters (MPPC). With such a concept, the events will be reconstructed in three projections that can be further merged into a 3D image.

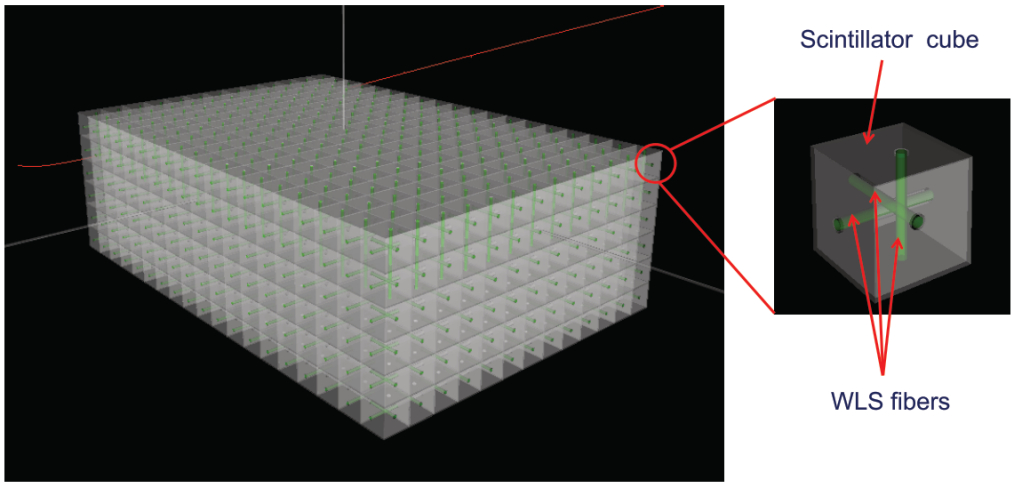

Figure 8.1: The schematic concept of the SuperFGD detector made with scintillator cubes. Wavelength shifting fibers are used for the signal readout. The size of each cube is $1\times1\times1$ cm^3.

High granularity is a strong advantage of the new detector. Hadron detection is critical for the accurate measurements of neutrino interactions. In T2K spectrum of protons from neutrino interactions starts from 200 MeV/c. With the current FGDs one can detect protons with $p_p > 400 \div 500$ MeV/c, the acceptance is limited mainly by the sandwich structure of the detector. The 200 MeV/c

proton will travel in average 5 cm in Carbon and what can be reconstructed with SuperFGD as five cubes will be illuminated (subsection 3.3). At this travel distance, we can identify the particles with dE/dx (section 3) and separate short muon and proton tracks. In the current ND280, a TPC is required to do an accurate particle identification. To conclude, with reconstruction and identification of short low energy tracks a new detector will provide very precise measurements of neutrino interactions as we will detect all the produced particles.

1 Conceptual design

The detector dimensions are 192×184×56 cubes 1×1×1 cm^3 each. The total number of cubes and channels will be 1 885 632 and 54 224 respectively. The fiducial mass of the ND280 will be nearly doubled with SuperFGD. The details about the cube's characteristics are provided in subsection 1.1. The MPPCs will be placed on the upstream, top, left and right side of the detector. The front–end electronics, including the digitizers, is going to be installed on site. The digitized signal will be transported through the optical fiber outside the magnet to the ND280 data acquisition system. More details about the electronics can be found in section 2.

The described detector can be used in other experiments. The expected characteristics are most suitable with neutrino experiments, where we expect low track multiplicity comparing to hadron experiments. There are proposals about the installation of a similar setup in the DUNE near detector complex [138].

1.1 Scintillator cubes

The scintillator cubes are made from polystyrene doped with 1.5% of paraterphenyl (PTP) and 0.01% of POPOP. The cubes production is done with injection molding with a press-form. Ten cubes could be produced at one molding that speeds up the mass production of the detector. The molding technology also increases the cube size accuracy comparing to the extrusion technology that is usually used for the scintillator detectors production. Cube dimensions accuracy is critical as we are going to assemble the detector from nearly 2 million cubes. Size fluctuations are required to be minimal to prevent cube's holes misalignment because of the position fluctuations.

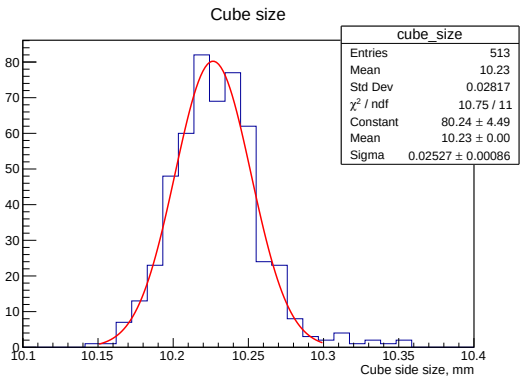

Figure 8.2: The accuracy of the cube dimensions after the etching with a reflector. The results of 513 measurements are fit and demonstrates 25 μm accuracy.

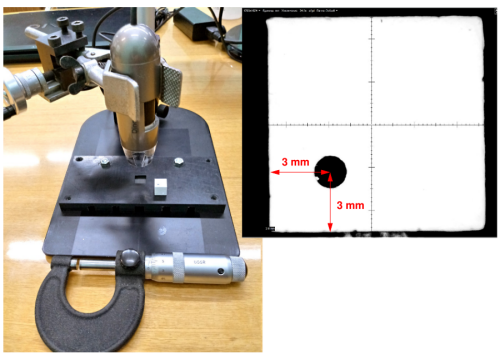

Figure 8.3: The digital microscope used for the measurements of the hole position

After the molding, the cubes are covered by a chemical diffuse reflector by etching the scintillator surface in a chemical agent. The fluctuations of the cube size were measured after the etching procedure. The results are shown in Figure 8.2 and demonstrate a Gaussian behavior with 25 μm accuracy. Afterward, three holes with a 1.5 mm diameter are drilled. The positions of the holes are also precisely controlled with the digital microscope (Figure 8.3). Variations at the level of 80 μm were observed. Since the fiber diameter is 1 mm while the hole size is 1.5 mm, this is not supposed to bring a problem during the assembly. The cube size fluctuations remain the main challenge for the detector construction.

1.2 Assembly

The assembly of the detector needs to be designed carefully. The setup requires aligning all the cubes at their position in three dimensions and easy insertion of the WLS fibers. With the given number of 2 million cubes and with measured uncertainties on cube size and hole positions, this is a challenging task.

a Loose structure

We considered creating a loose structure of cubes self–aligned with fishing lines. The key idea is to fully assemble the detector with 1.2 mm fishing lines instead of the 1 mm WLS fibers. Cubes positions are fixed only with these lines without precise control over the position of each cube. Then the fishing line will be replaced one by one with the fibers. As WLS fiber diameter is smaller compared to the fishing line it should be easy to perform such a replacement. During the whole replacement procedure, cubes are aligned with lines and fibers. Such a technique will also protect the fibers that are quite expensive and fragile. They are going to be inserted only at the final stage of detector construction.

Detector assembly starts from the string construction (Figure 8.4 (a)). A line of 192 cubes is assembled on the fishing line. The set of 184 strings is joint line by line to the plane 192×184 (Figure 8.4 (b)). Planes are put on top of each other to form a full detector (Figure 8.4 (c)). The planes will be aligned so that the fishing lines will be inserted in the vertical holes as well. The alignment along the 3rd axis is the most difficult part of the assembly. The loose structure allows us to solve this problem with the small cube displacements during the insertion of the fishing line in the 3rd axis.

Several tests of the assembly were performed. The first one includes a 2 m long prototype with the transverse dimensions 6×6 cubes. This prototype was aimed to test the robustness of the assembly strategy, the possibility of the lines replacement with WLS, the length fluctuations of the 2 m long setup. The photos of the prototype are presented in Figure 8.5. With such a test it was proven that we can construct the detector with the proposed method. The tests were performed with and without a 50 kg payload on the top cover of the detector. In both cases, the fishing lines can be easily replaced by fibers. The friction of the fishing line with the 200 cubes is small and the line can be easily removed. There is no strong friction during fiber insertion as well. The length of the prototype was in agreement with the expectations.

Two prototypes were built for the detector tests with the beam of charged particles. These prototypes served also as an assembly technology tests. The first one was quite small 5×5×5 cubes. The second one was slightly larger and contained 48×24×8 cubes. Details about prototypes construction and beamtest results will be overviewed in section 4. I participated in the construction of all the prototypes and of the detector as well.

(a) (b) (c)

Figure 8.4: The assembly technology of the SFGD detector with the fishing lines. The technology starts from the string assembly (a) that are further merged into the planes (b). Finally, the planes are put on top of the each other and the vertical holes are aligned with steel needles(c).

(a) (b)

Figure 8.5: Photos of the detector prototype built with 200×6×6 cubes. Cubes assembled with the fishing line (a) and after the replacement of several lines with WLS fibers (b).

After the successful beamtests, a tall "tower" was built with 15×56×192 cubes. The main purpose of this prototype was to test the possibility of the fishing lines replacement with the WLS fibers in a tall and long structure of cubes. It was confirmed that such a detector can be built with fishing lines and they can be replaced with the fibers afterward. The photo of the prototype is shown in Figure 8.6. In addition, the test of the SuperFGD box strength and deformations was performed with this prototype. The details about the detector box will be provided in the next section.

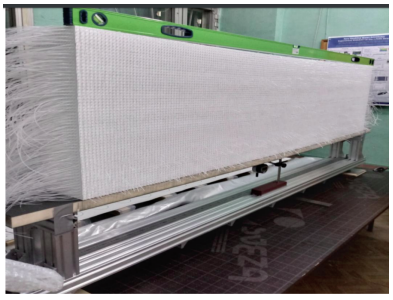

Figure 8.6: The tall prototype of the SuperFGD detector made with 15×56×192 cubes.

b SuperFGD mechanics

The mechanical structure of the scintillator target should provide a robust detector fixation to minimize the detector deformation due to load. The loose structure of cubes is subject of deformation, while the WLS fibers are fragile and can be broken with the cube offset. At the same time, the dead space between the target and HA–TPC is desired to be as small as possible to gain the precision of charged particle tracking. The mechanical structure should provide the optical interface to readout all the channels and host the calibration system.

To meet these requirements, the walls of the box are made from 16 mm AIREX core laminated with 2 mm carbon fiber skins and are screwed together. The box is drilled with 3 mm holes providing the exit for every WLS fiber. Three of the six walls carry the signal readout system. The MPPCs are soldered on printed circuit boards (PCB) that are screwed on the carbon fiber box. On the readout sides, the fibers are equipped with optical connectors to provide reliable light transfer to MPPC. The drawing of the optical interface and readout system is shown in Figure 8.7. The other fibers endings are covered with the plastic coverage screwed to the box. This coverage protects the fibers from external light and also hosts the calibration system.

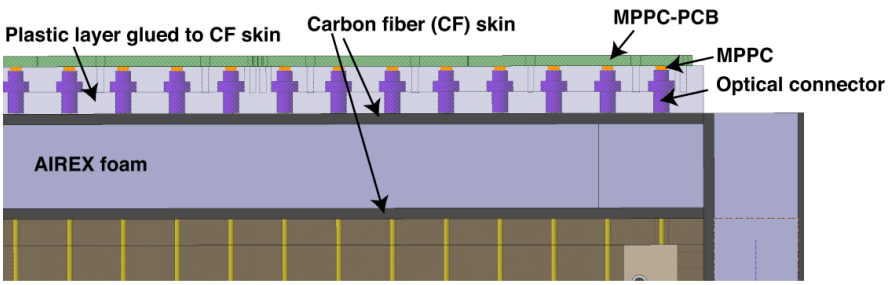

Figure 8.7: The optical interface of the SuperFGD detector

The deformation of the mechanical support structure was tested with the long and tall SuperFGD prototype (15×56×192 cubes). The measured sagitta was at the level of 20 mm. This value is close to the distance between the detectors but still meets the requirements and makes possible the detector assembly.

The calibration system is required to measure the MPPC gain, i.e. associate the output MPPC channel with the number of detected photoelectrons. In the current FGD, we use MPPC with a high noise rate that allows us to perform a calibration with the noise only. In the SuperFGD new low-noise MPPC will be used. It will make the signal cleaner, but will require the external light injection system for calibration. The Light Guide Plane (LGP) is used for this purpose. On the non-readout side of the fibers, a plastic plate is glued to the SuperFGD box. The light will be injected with LEDs at the plate border. The notches in the plate are made opposite to the fibers ends to scatter some light into the fibers (Figure 8.8). With such a system the gain of each channel can be monitored continuously. It is especially important at the assembly stage to check all the MPPCs and fibers operate normally.

2 Electronics

SuperFGD electronics should measure the signal amplitude for every channel for every bunch of the neutrino beam. In T2K 8 bunches are separated with 600 ns and forms a spill that comes ev-

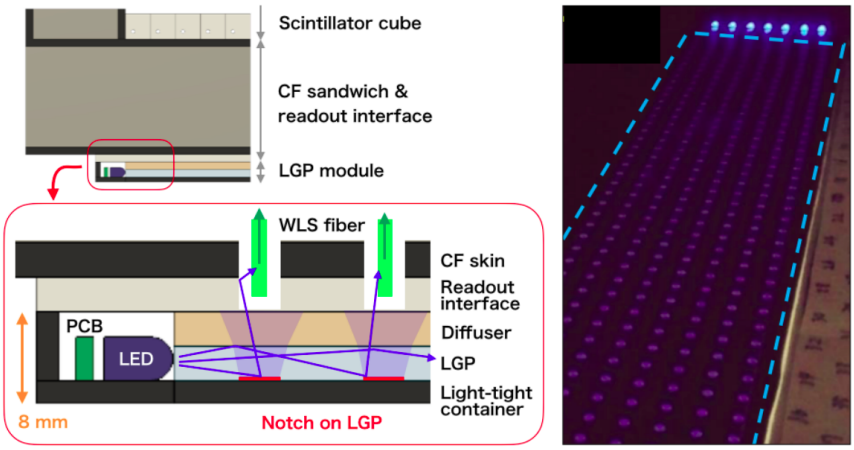

Figure 8.8: SuperFGD calibration system with Light Guide Plane (left) and a LGP prototype (right).

ery 2 seconds. The readout system should be compatible with this regime. High dynamic range and precise timing are required for the precise physics measurement. Nucleons produced in the neutrino interactions are mostly low-energetic and stops shortly with large energy deposition. Since accurate energy measurements of the nucleons are required for the neutrino interactions measurements, a high dynamic range is essential. Time measurement is important for dividing particles directed to/from the target. The time-of-flight (ToF) system around the SFGD and HA–TPCs measures time with 100 ps accuracy. At our energies, the SFGD time resolution at the level of 1 ns is sufficient for the reliable estimation of the track direction.

The electronics system based on the CITIROC chips (Cherenkov Imaging Telescope Integrated Read Out Chip) was chosen as a baseline option. These chips are used in BabyMIND [139] experiment in the T2K near detector complex. Thus these chips were designed to operate with scintillator detector at the same neutrino beam and therefore are compatible with the beam timing. CITIROC electronics suits the requirements of the dynamic range and time resolution. It stores the signal in both low–gain and high–gain regime simultaneously and thus provides accurate amplitude measurements for both low and high light yield. At the moment, the bottle–neck of the dynamic range is a number of pixels in the MPPC. But our S13360-1325PE MPPCs carry 2668 pixels and this is more than enough for the precise measurements. The highest signal is expected to come from the stopping proton. The expected amplitude in the cube where proton stops is estimated at the level of 600 photo electrons (section 3). The sampling rate of the CITIROC chip is 400 MHz (2.5 ns). That brings us below 1 ns time resolution per channel.

Front–End Boards (FEB) are mounted in towers on both sides of SGFD inside the magnet. PCBs are connected with the FEB with the coaxial cables. Such a scheme minimizes the dead material between the SFGD and HA–TPC. FEB provides signal amplification, digitization, and zero–suppression. An optical cable transmits the data outside the magnet to the ND280 global DAQ system. This connection serves for the time synchronization as well.

3 Simulations

To estimate the behavior and main physical characteristics of the future detector we performed several simulations. The framework based on Geant4 [123] toolkit was created to perform a Monte–Carlo simulation of the proposed detector [140]. The detector response was estimated based on the well-known behavior of the scintillator detector FGD. Further corrections based on the test beam

data are considered. The geometry of the cubes with holes, instrumented with WLS fibers was fully implemented in the framework. The visualization of the simulated geometry is shown in Figure 8.1. The propagation and interactions of the particles in the detector are carried out by Geant4 toolkit. As an output, we know the energy spent on the ionization in the scintillator material.

Based on the known energy loss in the scintillator we estimated the amount of light measured by the MPPC. The first step is evaluating the amount of ionization energy that went to light emission. The empirical Birks law was used for this purpose [141]. The energy emitted with a scintillator light (dS) tends to be saturated with high ionization energy loss (dE/dx).

$$\frac{dS}{dx} = \frac{dE/dx}{1 + k_B \times dE/dx} \tag{8.1}$$

where $k_B = 0.0208$cm/MeV is a Birks constant that was precisely measured for the plastic scintillators. Based on the total energy spent on light emission we estimate the number of photons produced and captured with the WLS fibers. Based on our experience with FGD we started with the value of 156.42 γ/MeV. This value will be tuned later with the beamtest data. The attenuation of the light in the fiber is estimated with the exponential law (Equation 8.2).

$$L\times = a \cdot e^{-x/L_{long}} + (1-a) \cdot e^{-x/L_{short}} \tag{8.2}$$

where L_{long} and L_{short} are 2 attenuation lengths and a is their relative strength. As before, we have some knowledge about the attenuation length from the FGD operation. In addition, the measurements of the attenuation length in our fiber type were performed with LED. Attenuation parameters were set to $a = 0.77$, $L_{long} = 4634$ mm, $L_{short} = 332$ mm. The MMPC photodetection efficiency is specified by its manufacturer at 25%. Thus the energy deposited by a charged particle is transformed into the number of detected photo electrons. A similar approach is used in the simulation of the FGD in the ND280.

3.1 Expected light yield and PID

a Simulation cross–check

One of the goals of the simulations is to estimate the light yield of the detector with different particle types. We want to be sure that the dynamic range of the MPPC is suitable for the amount of light that is going to be measured. First of all, we compared the results of the simulation with the results of the first beam test (subsection 4.1). I found that with our simulation we expect to observe 41 photo electrons per channel in the first small SuperFGD prototype with the beam at the CERN T10 area (mostly Minimum Ionizing particles (MIP)). In the data, we observed a very similar result — 42 p.e. per channel. Thus we decided that the simulation parameters are reliable enough.

b Beamtest simulations

After the validation of the simulation parameters with the first beamtest, I simulate the signal from the second prototype (subsection 4.2). The main goal is to estimate the detector response for through-going MIP particles and stopping protons. As I expect a large energy deposition in the second case, our detector should be able to measure high signal amplitude. Simulated event displays are shown in Figure 8.9.

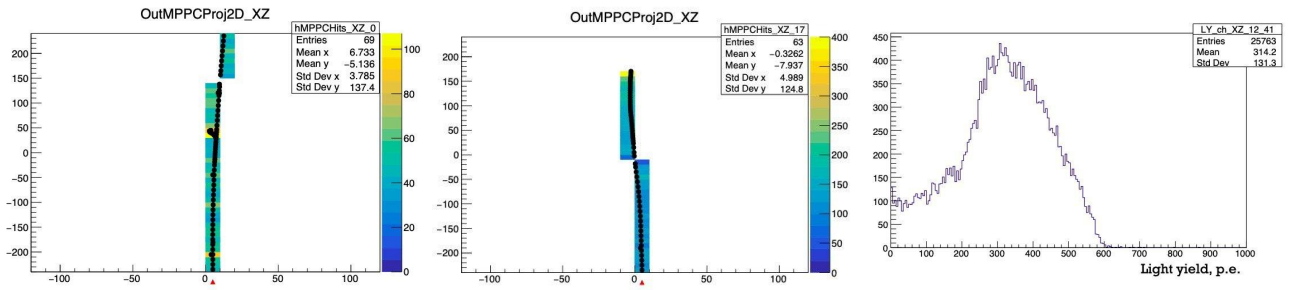

(a) (b) (c)

Figure 8.9: The simulations of the second prototype of the SFGD detector. Event displays of the through-going 1 GeV/c pion track (a) and a stopping proton track (b). The light yield distribution in the stopping proton last cube (c).

I estimated the light yield from the through-going MIP track at a value of 50 p.e.. The value is similar to the measurements done with the first prototype and is sufficient for the tracking and time resolution measurements. The signal from the stopping proton is much higher and reaches 600 p.e.. The majority of the prototype's channels are equipped with MPPC with a dynamic range of 2668 pixels that is more than enough for successful energy measurements.

c PID studies

As mentioned before, with SuperFGD we can determine the type of self-contained particle by the energy loss. I performed a simulation to study the accuracy of such a determination. The effect of light attenuation should also be studied. As we are using 2 m long fibers, the attenuation may be quite severe and affect particle identification. I performed simulations of the propagation of different particles through the detector. The samples with the different initial locations of the particles were considered: close to the MPPC, excluding the attenuation effect and at the far corner of the detector where the attenuation is the strongest. The ionization energy loss estimated for muon and proton in both positions is shown in Figure 8.10. The particle momenta are taken from the neutrino interactions simulated with GENIE generator. The cut was put at the value where muon and proton PDF intersects. Thus the efficiency and purity of the muon selection can be estimated. As one can see the quality of the selection depends very weakly on the initial particle position. The light attenuation reduces the total amount of light but doesn't spoil the particle identification. These plots also demonstrate a good PID power of the detector even with a simple comparison of dE/dx. More sophisticated selection using momentum by range can further improve the accuracy of particles separation.

3.2 Pileups

Neutrino interactions happen not only in the fiducial material but also in the concrete of the pit, in the magnet coil of the ND280 and in the other detectors. SuperFGD will suffer from the pile ups as the particles from such interactions could enter the detector and overlap with the signal from the neutrino interactions inside the fiducial volume. I estimated the rate of pile ups for different beam intensities. Simulation of the neutrino interactions outside of the basket was already done and widely used in the experiment. I used this sample and selected tracks that entered the basket and point towards SuperFGD. Such tracks are used as an input for the SuperFGD simulation framework to estimate detector response. The results are overlapped with the simulation

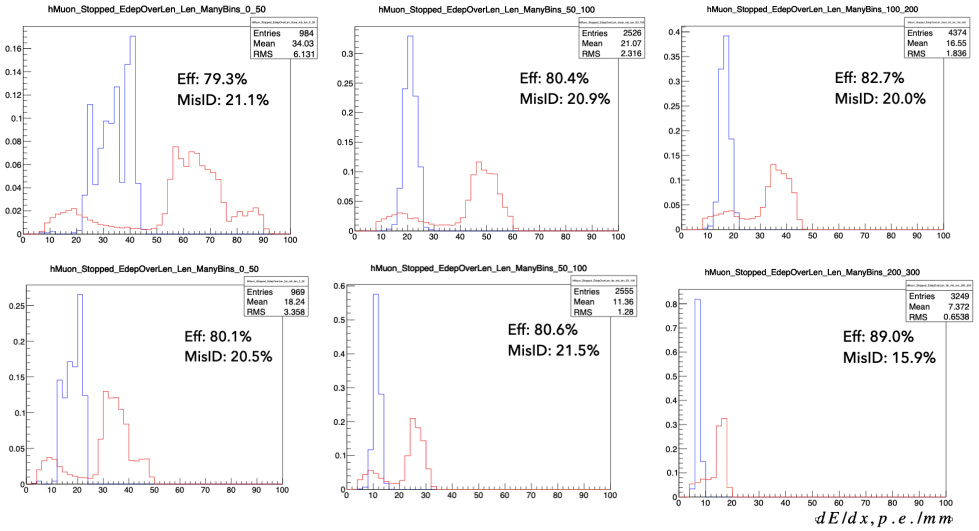

$L < 50$ mm $\quad$ $50 < L < 100$ mm $\quad$ $100 < L < 200$ mm

Figure 8.10: The energy loss per unit length PDFs for muon (blue) and proton(red) for different track length and at different distances from MPPCs. Top row corresponds to the particle position close to MPPC and bottom row corresponds to position far away from MPPC so the light attenuation in fiber is the strongest. The efficiencies of the muon identification as well as a rate of the misidentified protons is shown.

of the neutrino interactions inside SuperFGD. Finally, I got the fraction of pileuped events in the whole detector and a number of pileuped channels in 2D projections. The results are summarized in Table 8.1. Two beam powers are considered 500 and 1000 kW. These numbers represent a total number of events when at least one pileup is observed. I normalized the generated sample to 10^{21} POT statistics. For this dataset we expect to observe 234 546 ν interactions. With 1 MW beam in 22 147 events SuperFGD will detect also tracks from the outside of the target. Only in 1.28 events I observed the track from outside and inside the target to go through exactly the same cube. The overlaps in 2D projections are more often as we degeneralize one dimension.

For 10^{21} POT total number of ν events in neutrino mode in SFGD: 234 546

Beam	Pile ups in:				
power, kW	whole detector	certain cube	XY projection	YZ projection	XZ projection
500	11 520	0.64	14.09	9.95	55.58
1000	22 147	1.28	28.12	19.91	111.17

For 10^{21} POT total number of $\overline{\nu}$ events in anti-neutrino mode in SFGD: 60 837

Beam	Pile ups in:				
power, kW	whole detector	certain cube	XY projection	YZ projection	XZ projection
500	1 382	1.01	2.43	2.17	10.90
1000	2 659	1.93	4.68	4.17	21.00

Table 8.1: The number of pileuped events in the SuperFGD. The events are divided into cases when tracks from neutrino interaction in the target and from outside enter the detector, when they go through the same cube and when the overlap in particular projection was found.

The YZ plane has a lower number of pileuped events as it has the largest number of channels and coincidence is less probable. XY plane contains the least number of channels, but the pile up rate is lower comparing to XZ plane. Most of the out of fiducial volume particles are going

downstream that's why their tracks are extended along the Z axis and the coincidence of channel in XZ projection is more probable. In total, the number of events pileuped with the out of fiducial volume tracks is low and will not affect the data quality.

3.3 Proton threshold

As was mentioned above, an expected low threshold for proton detection is one of the main advantages of the SuperFGD detector and will provide precise measurement of the neutrino interactions. I participated in the simulation to determine the exact value of this threshold. We use the simulation framework that we developed for the SuperFGD studies, so all the materials are simulated as well as detector response. The proton spectrum from the neutrino interaction generated with NEUT is used. You can see the spectrum together with the current efficiency of the FGD detectors in Figure 8.11 (a). I recognize the proton track as reconstructed in the SuperFGD if I observed a light in 5 different cubes. The value was driven by the fact that the vertex activity around the neutrino interaction point is usually smaller and a proton track of such a length can be extracted. The cut can be further reduced with a more accurate study of the vertex activity. The obtained efficiency for the proton detection is shown in Figure 8.11 (b). As expected we are able to reconstruct the proton tracks with momentum starting from 200 MeV/c and efficiency goes above 60% for protons with $p > 300$ MeV/c. The performance of the detector made with scintillator bars, like existing FGD, but with different bars orientation was also tested with the simulation. The bars were aligned along and perpendicular to the beam (ZX axis). It was proven that the SuperFGD provides lower threshold for proton detection.

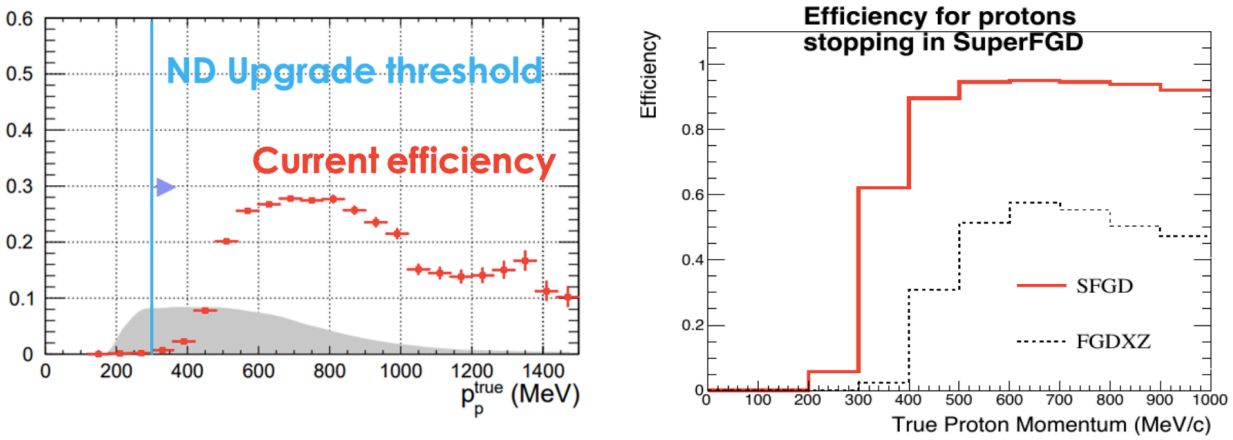

(a) (b)

Figure 8.11: The spectrum of the protons produced in neutrino interactions in ND280 overlapped with the current efficiency for its detection (a) and an efficiency of their detection in SuperFGD or FGD with a different bars orientation(b).

4 Beamtest

Several beamtests were performed to evaluate the detector performance and characteristics.

4.1 First CERN beamtest

The first ever test was done with the small 5×5×5 cubes prototype. The main goals of the test were the first measurement of the light yield and time resolution with the beam of charged particles. A photo of the first prototype is shown in Figure 8.12.

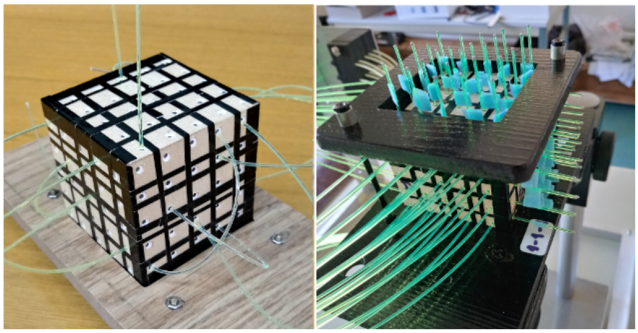

Figure 8.12: The first 5×5×5 cubes prototype of the SuperFGS detector. The assembly stage (left) and a complete prototype with inserted WLS readout fibers (right).

The beamtest was performed at the T10 area of the CERN Proton Synchrotron (PS). The 6 GeV/c beam consisted mostly of positron and protons, thus the energy losses in the prototype are similar to what we expect from MIPs. Two scintillator bars were installed 26 cm before and after the prototype and used as a trigger and reference measurements for the time resolution studies.

The light was readout with two fibers perpendicular to the beam direction, fibers along the beam were not inserted. The distribution of the sum of the light yield from two channels is shown in Figure 8.13 (a). So we observed on average 80 photo electrons from one cube that is enough for the particle tracking and accurate time measurements. The time resolution was measured with respect to both trigger bars. A 5 GHz digitizer was used for sampling the data from the detector. Combing the measurements from two fibers in the same cube we reached a time resolution at the level of 650 ps (Figure 8.13 b) and the resolution of the single channel is 0.95 ns. This result is beyond the minimal requirements and opens a way towards precise ToF measurements inside the SFGD that may be used for the neutron energy measurements (see chapter 9).

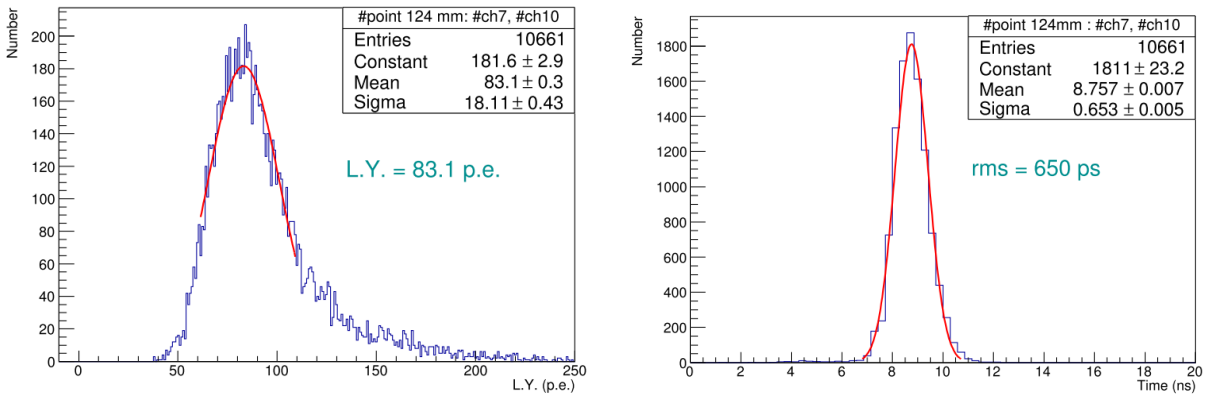

(a) (b)

Figure 8.13: The light yield from two channels (a) and a time resolution (b) of the first prototype of the SuperFGD detector.

The results of the beam test that contain the results of the study presented above were published in [142].

4.2 Second CERN beamtest

The first small prototype was used to test the concept and measure basic detector characteristic. More sophisticated tests are required to study setup performance with different particle types at various energies. The second prototype was made of 48×24×8 cubes. The size was driven by the size of the magnet in which it would be placed. In this larger version all the channels were instrumented with fibers and MPPCs. The readout was organized with CITIROC electronics that is going to be used in the full scale detector. The photos of the setup are shown in Figure 8.14 (b).

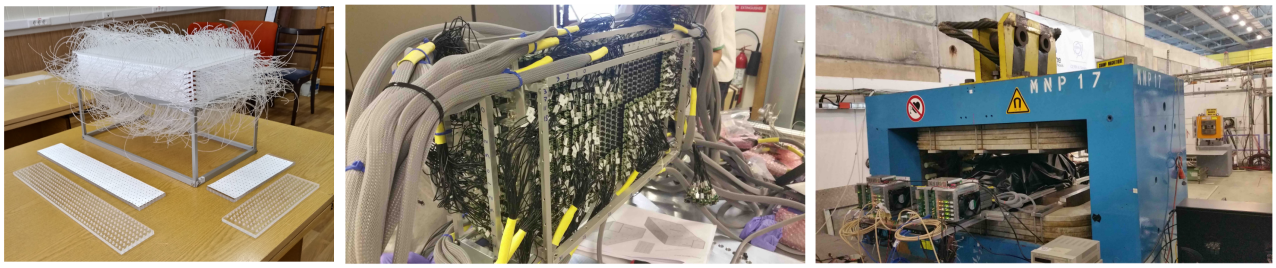

(a) (b) (c)

Figure 8.14: The second SuperFGD prototype made of 48×24×8 cubes. During the assembly with fishing lines (a), fully instrumented with WLS fibers, MPPCs and cabled (b), installed in the magnet at the beamline (c).

The test was performed at the T9 area at Proton Synchrotron (PS) beamline at CERN. The beam parameters are similar to what was described in the TPC beamtest chapter (subsection 2.2 of chapter 7). The beam is composed of electrons, pions, and protons with a momentum that varies from 800 MeV/c up to 6 GeV/c. Thus we can observe a through going MIP tracks as well as more complicated topologies like single photon production and conversion, electromagnetic shower, stopping proton. All these events are likely to happen in the ND280 detector and it is interesting to study them with the prototype. Some event displays are shown in Figure 8.15.

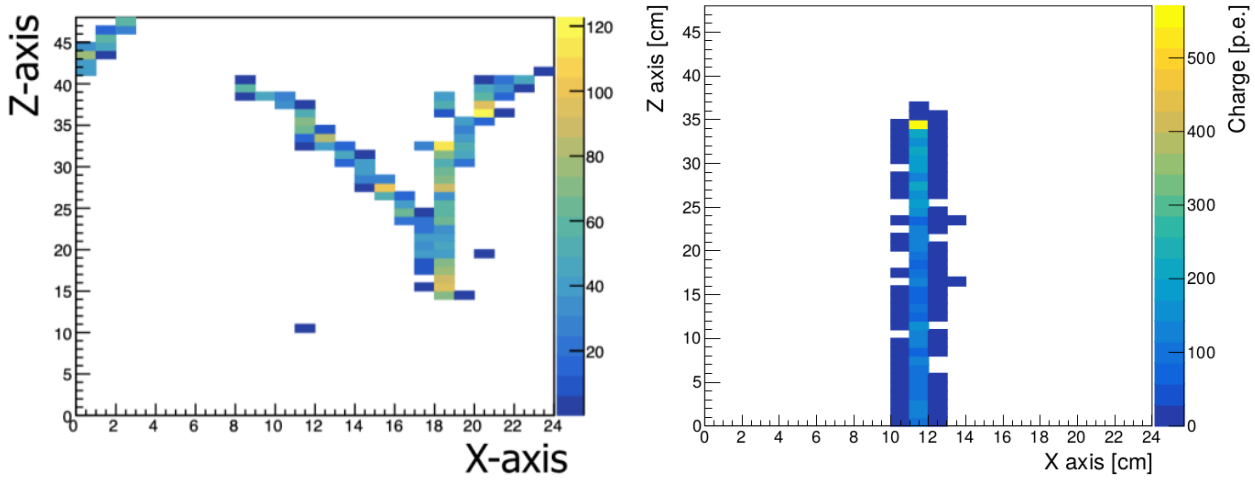

(a) (b)

Figure 8.15: Event displays from the second prototype of the SuperFGD detector. A photon production and conversion into electron–positron pair (a) and a stopping proton track (b)

The analysis started with estimating the basic detector characteristics like the light yield and time resolution. The light yield was studied with the 0.8 GeV/c MIP sample. The light attenuation in the fibers is not negligible in our detector. Hence we first measured the attenuation effect and then apply the correction to each measurement based on the distance between an illuminated cube and a MPPC. Therefore, the obtained value that characterizes the light production and collection in the cube does not depend on cube position inside the detector. The attenuation was measured for fibers perpendicular to the beam directions. The observed light follows the exponential law with respect to the distance from the cube to the MPPC. The parameters of the exponential law are extracted from the fit and further used for correction of the measured light. The attenuation with respect to the travel distance of the light in the fiber is shown in Figure 8.16 (a). The corrected values of the light yield per cube are shown in Figure 8.16.

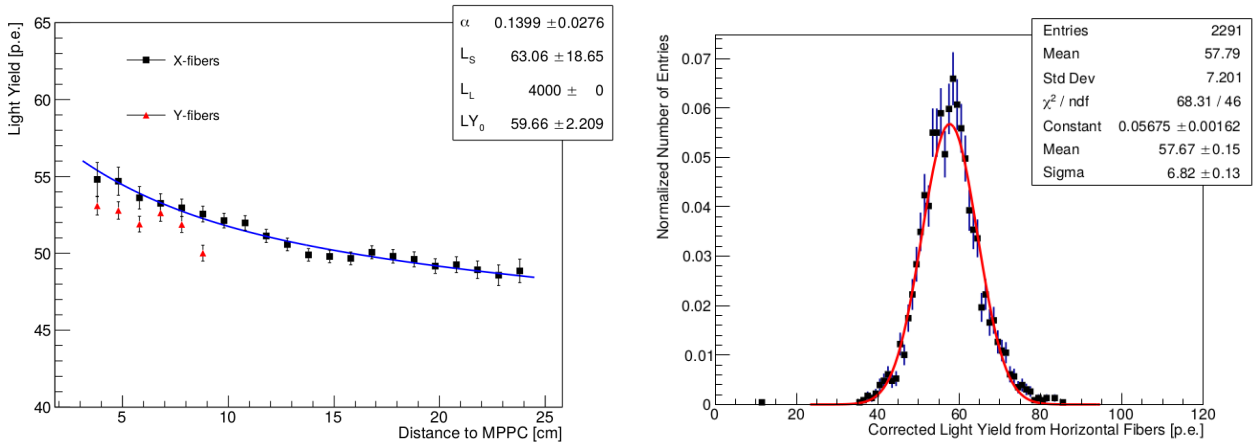

(a) (b)

Figure 8.16: The attenuation of the light in the fibers (a) is used to estimate the light yield of the cube (b).

The measurements of the time resolution were done separately for short and long fibers (8 and 24 cm respectively). The trigger used during the test was not precise. It has an uncertainty much more than 1 ns, thus can not be used as a reference. Instead, the measurements in the particular cube were compared to the cube in the middle of the prototype (in the 24 layers of 48). The uncertainty is supposed to be the same for both and the final time resolution is $\sqrt{2}$ times smaller than the smearing of the $\Delta T = T_{cube} - T_{reference}$. The distribution of the time resolution across different channels and different fiber lengths is shown in Figure 8.17. The obtained result is a bit worse than 1 ns. Some channels tend to have worse resolution forming a distribution with a long tail. This result is slightly worse compared to the resolution obtained with the first prototype (0.95 ns). In the second test, the CITIROC electronics with 400 MHz sampling was used, while in the first test we used 5 GHz digitizer and that may be the main reason for the different results.

Several physics measurements were performed with the prototype. As we have a composition of different particles, we can plot the energy loss per unit length (dE/dx) and study how well the samples are separated. This will demonstrate the possibility of the detector to distinguish types of self-contained particles. The information from the trigger was used to distinguish muon/pion, electron, and proton samples. The energy losses per each sample are shown in Figure 8.18.

The other interesting sample is stopping protons. The energy deposition rises at the end of the proton track (Bragg peak) and results in a large light deposition. Since we are going to measure low energy protons from neutrino interactions it is interesting to see the detector response for such a sample. We used 0.8 GeV/c protons as the minimal momentum that could be selected with the beamline. The energy deposition of the proton, positron, and muon/pion along their track is

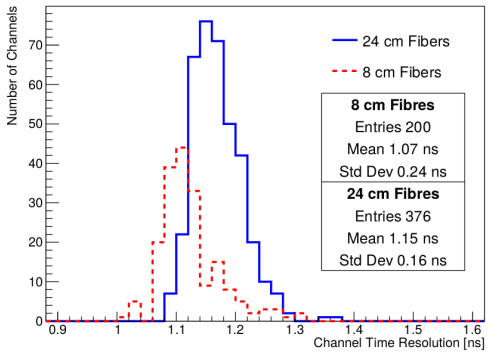

Figure 8.17: The time resolution of the second prototype of the SuperFGD detector measured independently for every channel and fiber length.

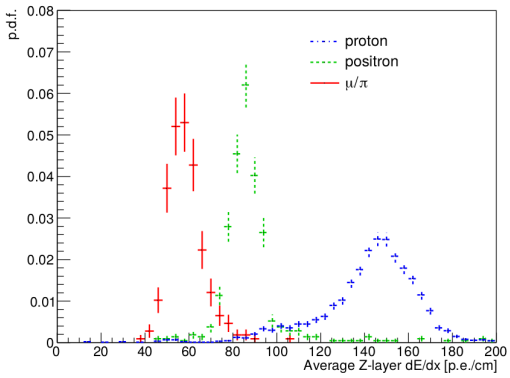

Figure 8.18: The energy loss per unit length (dE/dx) for different particles samples distinguished by the trigger type. 0.8 GeV/c muon/pion and proton samples and 1 GeV/c positron sample were used.

shown in Figure 8.19. On this plot, the Bragg peak is clearly seen. The dynamic range of MPPCs used in the test is enough to measure light deposition.

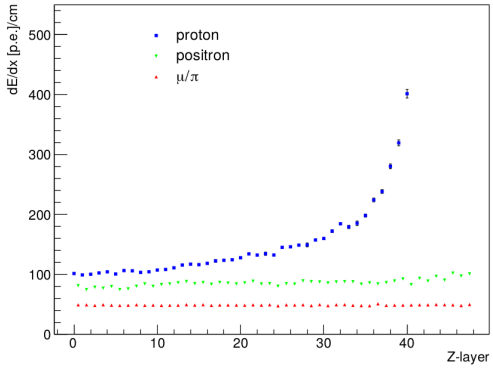

Figure 8.19: The energy deposition along the track for different particle samples. The Bragg peak for protons is clearly seen and can be measured with our MPPCs.

In the SuperFGD we expect an optical cross–talk — a migration of the scintillation light to the neighbour cube with no initial scintillation. It happens because the cube reflector is not completely opaque. In addition, photons can go through the cube holes or WLS fibers. The effect was studied in the beamtest with the stopping proton sample. The large light deposition allows precise measurement of the small fraction of the migrated photons. An attempt to suppress such an effect

was performed by putting the Tyvek sheets between Y layers of the prototype. Additional material with a high reflection coefficient prevents photons from going to a neighbour cube. The scheme of the cross–talk effect in the track transverse plane is shown in Figure 8.20 (a). As an effect characteristic, we are using the ratio of the light detected in the neighbour cube to the sum of the light in the central and side cubes.

$$\kappa = \frac{M_{xtalk}}{M_{main} + 2M_{xtalk}} \tag{8.3}$$

The observed light migration is shown in Figure 8.20 (b) and (c). We found that the cross–talk probability is less than 3%. The effect is not expected to be significant for MIP particles where we expect 40 photo electrons per channel. But the cross–talk may be used for the measurements when the channel is saturated with a high signal. Though our MPPCs have a high dynamic range, the stopping proton going along the fiber may saturate this channel. In this case, the information from the neighbour cubes may be used to measure an amplitude that is above the saturation limit of one MPPC. Also, the position reconstruction precision may be improved with the usage of the cross talk. This is similar to the charge spreading effect in the TPC (subsection 1.4 of chapter 7) that was proven to improve spatial resolution.

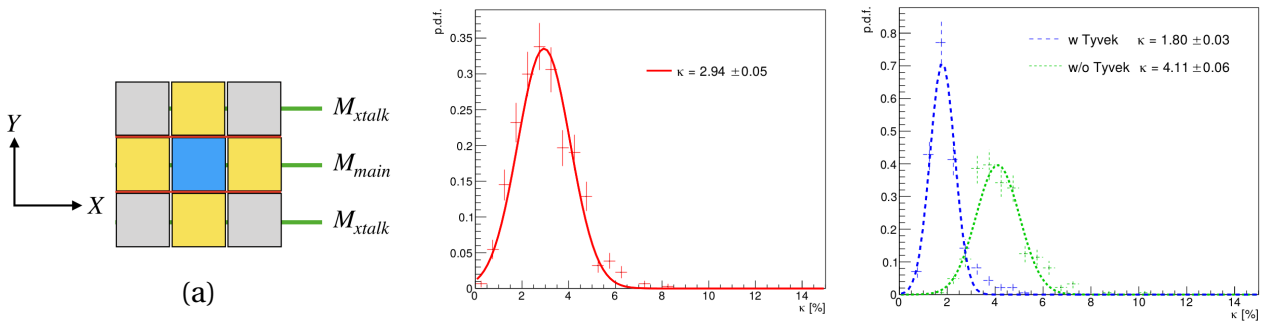

(a) (b) (c)

Figure 8.20: The cross–talk scheme (a) and the measured probability (Equation 8.3) of the light migration to the neighbor cube (b) divided into the vertical and horizontal direction(c). The migration in vertical direction is suppressed with the Tyvek sheets.

I implemented the measured cross–talk probability in the SuperFGD simulation framework. Based on the observed light in the cube containing a track, a signal in the neighbour is randomly thrown with a known cross–talk probability. Such a simulation is useful for the development of the reconstruction tool for the SuperFGD.

5 Conclusion

The new scintillator target is going to be built for the upgrade of the near detector. It will be placed between two HA–TPCs. The detector is highly granular. The readout is organized from 3 surfaces making possible the 3D reconstruction of the events.

The performed beamtests demonstrate good detector performance for the processes of interest. High light yield and small time resolution were observed with the beam of charged particles with momentum O(1 GeV/c).

The setup opens a road towards sophisticated measurements of the neutrino interactions. First of all, the total fiducial mass in ND280 will be doubled providing many more statistics for the analysis. A high granularity allows the detection of the short nucleon tracks. Lower threshold for proton detection will allow us to reconstruct nearly all the protons produced in the neutrino interactions

in ND280. With such a measurement, the resolution of the neutrino energy measurements will be improved. The new detector can distinguish a type of self-contained particle, thus it can measure neutrino interactions producing low momentum lepton and/or pion. In the current detector, TPCs are obligatory for particle type definition. A small time uncertainty and usage of the time-of-flight detectors provide a robust separation between particles going inside and outside the target. High granularity is useful for the separation between gamma conversion and electron production in neutrino interactions. Constraints on the electron neutrino cross-section with the near detector can improve the precision of the oscillation analysis. Conversion of the gamma rays produced in neutrino interaction outside of the fiducial volume is the main background for the process of interest and it can be severely suppressed in the new target.

With the SuperFGD, new analysis techniques should be developed to use all the benefits of the setup for neutrino studies. An example of an improved method of anti-neutrino energy reconstruction is presented in the next chapter.

CHAPTER 9

NEUTRON TAGGING IN SUPERFGD

The SuperFGD detector opens a possibility for the new method of physics measurements. In this chapter I will discuss a method for an improved anti-neutrino energy reconstruction in the CCQE interactions $\overline{\nu}_\mu + p \rightarrow \mu^+ + n$. With the large mass of the SuperFGD detector (2 tons), neutrons are likely to scatter off the nucleon, producing charged particles. If the detector has good enough time resolution, neutron energy can be measured precisely with the time of flight. The time difference between muon production and neutron rescattering will indicate its energy. Knowledge about the hadron kinematics will allow a precise anti-neutrino energy reconstruction. With the imbalance in the transverse kinematics of the muon and hadron, we can probe the nuclear effects. Such an analysis was performed for neutrino but was impossible for anti-neutrino as neutron detection efficiency was small.

We tested the possibility of neutron detection in a SuperFGD-like setup with different options considering detector time resolution. A possibility to measure neutron energy with reasonable uncertainty was demonstrated. The improvement of the anti-neutrino energy reconstruction was obtained. Overall, the method allows an interesting reduction of the strong correlations between the flux and the interaction models that arise in the measure of the neutrino oscillation probability and δ_{CP} phase.

1 Motivation

As was overviewed in chapter 3 the accurate measurements of the neutrino energy are essential for the precise oscillation analysis. Future experiments (DUNE, Hyper–Kamiokande) are very sensitive to the neutrino energy spectrum in their measurements of the CP violating phase δ_{CP}. At the moment, T2K uses charged current quasi–elastic (CCQE) interactions to reconstruct neutrino energy. With the measured lepton momentum and direction and assuming known incoming neutrino direction and fixed liberation energy, the neutrino energy calculation is straight-forward. But such a measurement can be biased. The bias is due to the initial movement of the target nucleons (Fermi motion) and liberation energy spread. Also, mesonless neutrino interactions with multiple nucleons (mostly 2) will have different kinematics compared to CCQE. Another source of bias is unreconstructed meson or a meson that was absorbed in the nucleus medium. These secondary interactions and multi-nucleons reactions are studied very poorly and the predictions of different models varies widely. Even using the same detector at near and far sites can not solve the problem

because the oscillated flux is different from the initial one. A precise model of neutrino interactions is essential to estimate the number of events at the far detector based on the measurements in the near detector.

To avoid the effects mentioned above, one can select a sample that is free from nuclear effects. The usage of the so–called "transverse kinematic variables" was theoretically motivated [136] and successfully implemented in the experiment [143]. The key idea is to study momentum imbalance in the plane perpendicular to the neutrino direction. Presence of such an imbalance is a clear probe of nuclear effects. For example, in neutrino interactions with free proton at rest ($\nu_\mu + n \rightarrow \mu^- + p$), projections of proton and muon momentum to this plane are fully compensated. While in neutrino interactions with Carbon, an initial nucleon is moving (Fermi motion) and will induce some imbalance in the momentum in the transverse plane.

The implementation of the method is straight forward for neutrino interactions, where we expect to detect a muon and a proton in the final state. But it can not be directly applied for the anti-neutrino, where the charge–less neutron is produced. The SuperFGD–like detector makes possible effective neutron detection and energy measurements. Thus the transverse variables become measurable for the anti-neutrino interactions as well.

In the hydrocarbon scintillator, we have neutrino interactions on Hydrogen and Carbon only. Moreover, interactions on Hydrogen are free from nuclear effects and allow to measure neutrino energy precisely. The transverse momentum for the interactions over these two nuclei in the SuperFGD with T2K anti-neutrino flux is shown in Figure 9.1. The interactions over Hydrogen are clearly separated from the Carbon ones. If we manage to measure δp_T we will be able to extract a Hydrogen sample that is free from the nuclear effects and measure anti-neutrino energy precisely.

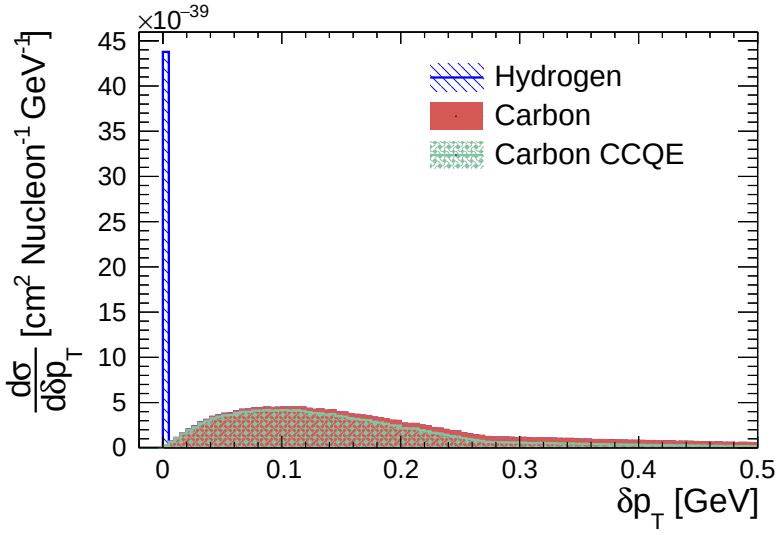

Figure 9.1: The differential cross section for $CC0\pi$ interactions on a hydrocarbon target as a function of δp_T for anti-neutrino interactions from the T2K experiments anti-neutrino flux simulated with the NEUT generator. The samples are divided into the target nucleon and reaction type (for Carbon only).

To measure the transverse momentum we need to estimate the neutron energy precisely with the time of flight. The time of the neutron production can be measured accurately with the timing of a muon track. In a massive detector, a neutron is likely to scatter over the nuclei producing charged particles. The most common daughters are low energy protons and alpha-particles. Thus we expect a large light deposition from the stopping hadron that will allow accurate time measurement of the neutron scattering. With the end and start time references neutron velocity and thus energy can be easily reconstructed. The scheme of the process of interest is shown in Figure 9.2.

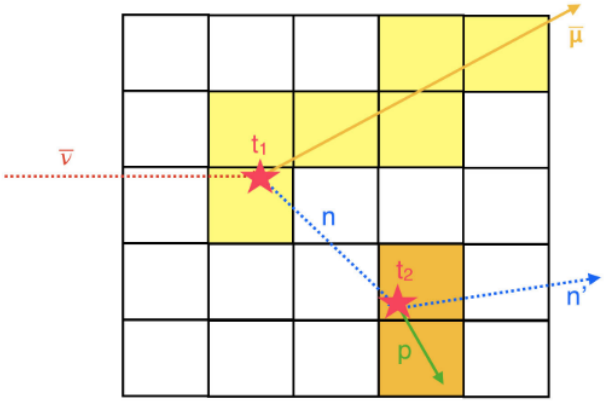

Figure 9.2: The process of interest that is going to be used for the measurement of the neutron energy produced in neutrino interaction with the time of flight.

2 Geant4 simulation

I developed a simulation toolkit to study secondary interactions of the neutron produced in the anti-neutrino interactions. The simulation procedures discussed in section 3 of chapter 8 are used. For simplicity, I started with the particle gun samples with the neutron energy distributed uniformly from 0 up to 800 MeV. The starting position in the geometrical center of the detector is set. The neutron direction is distributed uniformly in 4π angle. Neutron interactions as well as interactions of secondary particles are carried by the Geant4 toolkit with "QGSP BERT HP" physics list that is widely used in HEP (e.g. ATLAS experiment). It uses quark gluon string model for the high energy events ($\geqslant$ 20 GeV) and Bertini cascade model for lower energies ($\leqslant$ 10 GeV). All the standard EM processes and decays are included. It also uses precise simulations of the low energy neutrons (E<20 MeV) cross-sections. The full chain of readout simulation including ionization energy loss by charged particles, Birks saturation, light attenuation in the fibers, MPPC efficiency is applied.

2.1 Efficiency and energy resolution

The first analysis output is the fraction of neutrons producing particles that are further detected. I obtained the efficiency that is presented in Figure 9.3. The angular dependence comes from the detector shape. X and Z dimensions are similar with 192 and 184 cubes but Y dimension is much smaller with 56 cubes, thus fewer neutrons interact along this direction. Z axis is assumed parallel to the incoming neutrino beam.

Neutron energy is measured with a time of flight method. Velocity is estimated based on the distance between two clusters in Figure 9.2 and measured time difference. Detector time resolution is expected to be the main source of the reconstructed energy smearing. The accuracy of the time measurements at the neutrino interaction vertex is assumed to be excellent as we will have large light deposition from the vertex activity and a long outgoing muon track that will provide many time measurements by illuminating many channels. Thus the time smearing in the neutron cluster is assumed to be the dominating uncertainty on the neutron energy reconstruction. In the study, I assume several options on the detector time resolution. Both estimations are based on the fact that the observed time resolution per MIP is 0.95 ns per channel. Then I apply corrections to estimate the precision of the time measurements of the stopping hadrons. The first method is

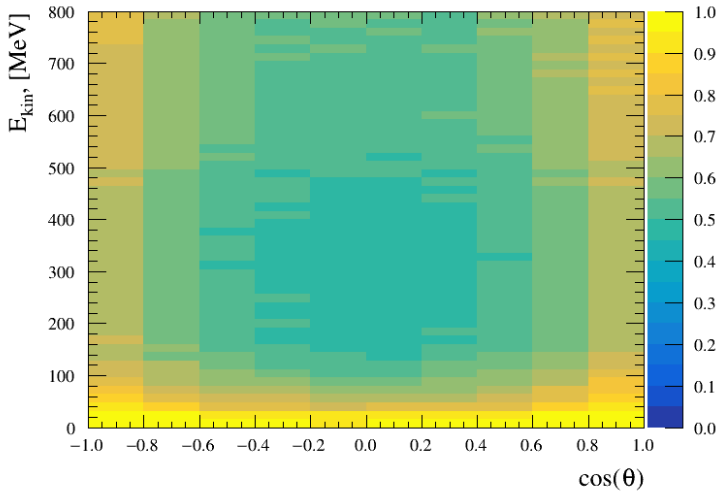

Figure 9.3: The efficiency of the neutron detection in the SuperFGD detector. Neutron particle gun was fired from the detector center isotropically. The angular dependence comes from the detector shape. θ angle is measured with respect to the neutrino beam (Z axis).

based on the measured light yield from the neutron cluster. With higher light yield, a waveform grows faster and a deviation of the time delay between a signal and its registration is smaller. The measurements with precise digitizer observed a square root dependence of the time resolution on the light yield [144]. As we measured 0.95 ns uncertainty per muon track that gives 40 p.e., I can extrapolate the uncertainty with the known dependence.

$$\sigma_t^{ly} = 0.95 \text{ ns}/\sqrt{3} \cdot \sqrt{40 \text{ PE/LY}}, \qquad \sigma_t^{ly} > 200 \text{ ps} \tag{9.1}$$

The factor of $\sqrt{3}$ shows the improvements in the measurement with 3 channels over the one channel. The bottom limit of 200 ps is set as further improvements are limited by the smearing in scintillator and fibers. Light emission by scintillator and light rescattering in fibers are not instant and provide some uncertainty.

This method is quite optimistic but the prototypes were not tested with the detection of large light emission. Thus to prevent an exaggeration of the energy resolution I considered a conservative estimation. If the measurements for each channel are independent their uncertainties can be summed up in quadrature. Thus the average uncertainty of N measurements will be $\sqrt{N}$ times more accurate than the single one.

$$\sigma_t^{ch} = 0.95 \text{ ns}/\sqrt{\#\text{channels}}, \qquad \sigma_t^{ch} > 200 \text{ ps} \tag{9.2}$$

With the known model of the time resolution, I estimated the smearing of the reconstructed neutron energy. The results are presented in Figure 9.4 (a).

The observed smearing is large. There are two main sources of such a large resolution. The first one is neutrons with a short travel distance. The time resolution is similar for all neutron interactions, but at a small distance it affects the energy estimation more significantly. A cut on the travel distance can improve the resolution. The distribution of the neutron travel distance with respect to its energy is shown in Figure 9.5. I am also accepting all the neutron clusters whatever the light yield. Events with a very low level of signal provide large smearing and should be also excluded. The time resolution estimated based on the light yield is shown in Figure 9.6. The discrete peaks come from the events with a small number of photoelectrons (1 p.e - 3.29 ns, 2 p.e - 2.45 ns, etc.)

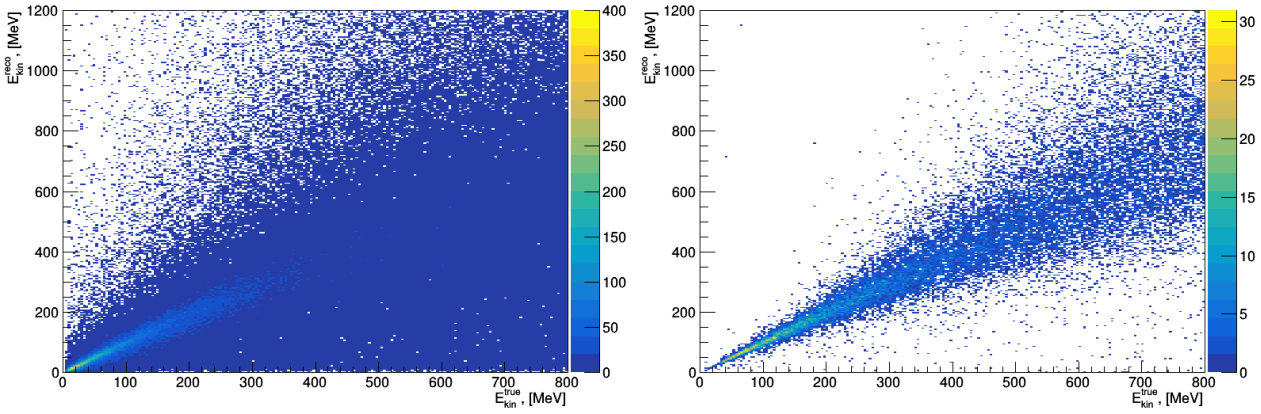

(a) (b)

Figure 9.4: The neutron energy smearing for all neutrons (a) and for neutrons with travel distance more then 70 cm (b). The time resolution is estimated with Equation 9.1. The efficiency and energy resolution are summarized in Table 9.1.

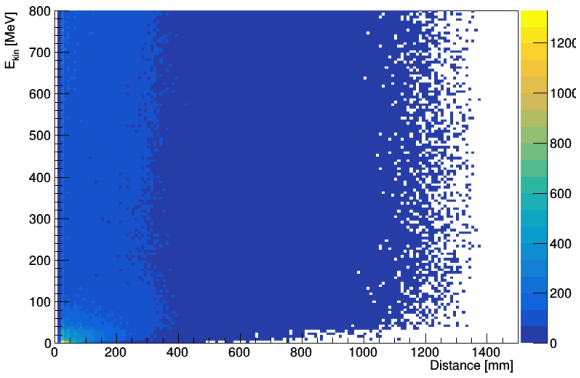

Figure 9.5: The neutron travel distance until the scattering with respect to its initial energy.

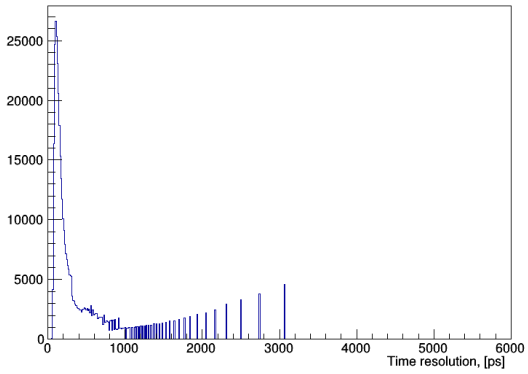

Figure 9.6: The estimations on the time resolution for the neutron clusters.

A cut on the light yield at the level of 40 p.e. was set to provide a time resolution not worse than for a MIP particle. I also studied the dependence of the energy resolution and detection efficiency with different lever arm cuts. The effect of the resolution improvement with the larger travel distance cut is shown in Figure 9.8. The efficiencies for 20 cm and 70 cm lever arm cuts are shown in Figure 9.7.

The balance between efficiency of the neutron detection and energy resolution should be found. The average efficiency and resolution for the 50 MeV neutron are provided in Table 9.1. The effect of the lever arm cut is demonstrated. The optimal cut value is going to be set based on both efficiency and purity of the separation between Hydrogen and Carbon samples. The cut optimization is described in section 4.

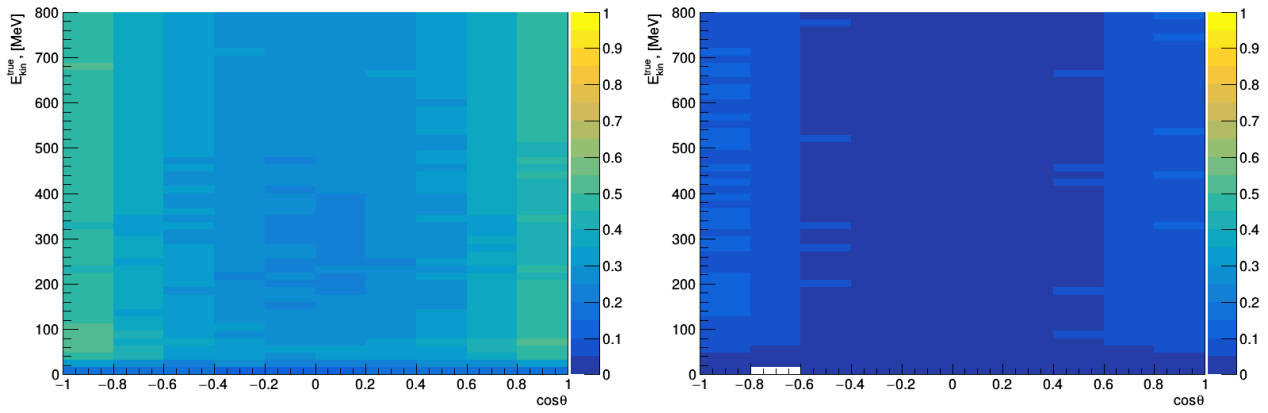

(a) (b)

Figure 9.7: The efficiency of the neutron detection with the cut on the travel distance at 20 cm (a) and 70 cm (b).

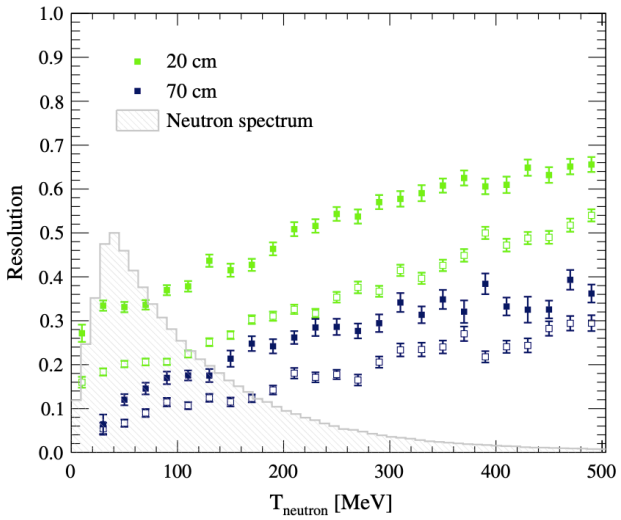

Figure 9.8: The neutron kinetic energy resolution as a function of the its kinetic energy, assuming different lever-arm cuts (20 cm and 70 cm, denoted by differing colors) and timing resolutions. The hollow markers correspond to a timing resolution using Equation 9.1, while the filled markers correspond to Equation 9.2. The resolution is taken as the ratio of the largest of the two standard deviations to the mean of a double-sided Gaussian fitted to the reconstructed neutron kinetic energy in a bin of true neutron kinematic energy. The gray band shows NEUT 5.4.0s predicted distribution of neutron kinematic energies for CC0π neutrino interactions using the T2K anti-neutrino flux.

$L > x$, cm	Eff, %	σ_E with eq. 9.2, %	σ_E with eq. 9.1, %
20	50	33	20
70	6.5	12	7

Table 9.1: The efficiency of the 50 MeV neutron selection in SuperFGD and the energy resolution with the time of flight with different values of the lever arm cut

3 Pileup estimations

In the method described above, I assumed the isolated cluster was originated by the neutron from the neutrino interaction. This analysis may be affected by the out of fiducial volume back-

grounds when a photon or neutron produced outside SuperFGD interacts inside the detector. Such a cluster can not be separated from the interaction of the neutron produced by the anti-neutrino interaction inside SuperFGD. I estimated the rate of such a pileup with 1 MW beam power and compared the signal and the background. A similar technique to what was described in subsection 3.2 is used to generate the out of fiducial volume sample. I studied the time delay between the anti-neutrino interaction in SuperFGD and the neutron cluster detection versus the lever arm for both signal and background samples. The resulting distribution is presented in Figure 9.9. One can see the large difference in the distributions of both samples. The rate of background events is small.

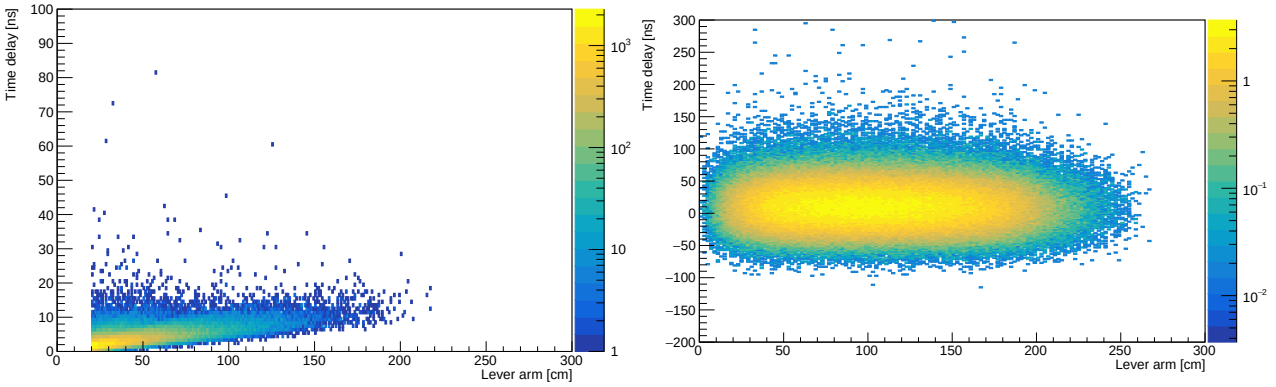

(a) (b)

Figure 9.9: The distribution of the time delay between the anti-neutrino interaction in SuperFGD and neutron cluster detection versus the distance between them for the signal events (a) and out of fiducial volume interactions (b) normalized to the number of signal events.

I merged these samples event by event to study the purity of the neutron detection. The time structure of the neutrino interactions was taken to be the same for both samples. I assumed the bunches are Gaussian with σ = 19 ns. The first isolated cluster that was found after the anti-neutrino interactions is considered as a neutron detection. If it is caused by the OOFV interaction it will be marked as a background otherwise it is a signal. Based on this classification the purity was estimated. I found that with such a method it is very unlikely to misinterpret the background as a signal. The main reason is the overall low background rate. The other one is usually a large difference in time between neutrino interaction and a cluster from a background neutron. A signal neutron interacts faster in time. The obtained purity is presented in Figure 9.10. The average purity over all lever arms and time window is 87%. It can be further improved with narrow time window.

4 Prospects for physics

The main goal of the current study is a more sophisticated measurement of neutrino interactions. We performed a simulation to evaluate how neutron detection may improve accuracy. The kinematic spectra of the CC0π events was generated using NEUT 5.4.0. Only events with muon momentum higher than 100 MeV/c are considered as it is an expected threshold of the muon detection in the SuperFGD. Lepton detection is essential for the proper identification of neutrino type and flavor. Smearings were applied to the simulation to estimate the detector output. Muon momentum was smeared by 4% with a Gaussian distribution. The value comes from the typical resolution of the TPC in the ND280. The angle of the outgoing muon is smeared with 1° driven

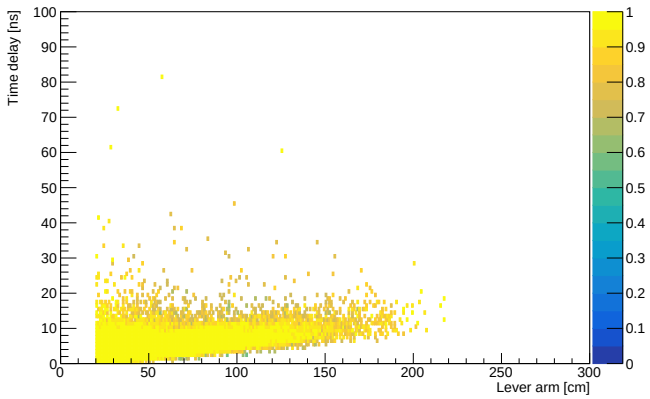

Figure 9.10: The purity of the neutron cluster selection. The contamination of the neutral particles produced OOFV is proved to be small.

by the granularity of the scintillator detector. The neutron kinematics is smeared according to the resolution obtained with the GEANT4 simulations described in the previous sections.

After incorporation of all the smearing effects, we can estimate the output of the measurements with SuperFGD. The distribution of the transverse momentum δp_T is shown in Figure 9.11. Comparing this figure to Figure 9.1 we can see the effect of the detector smearing. However, the hydrogen sample is largely distinct from the Carbon one.

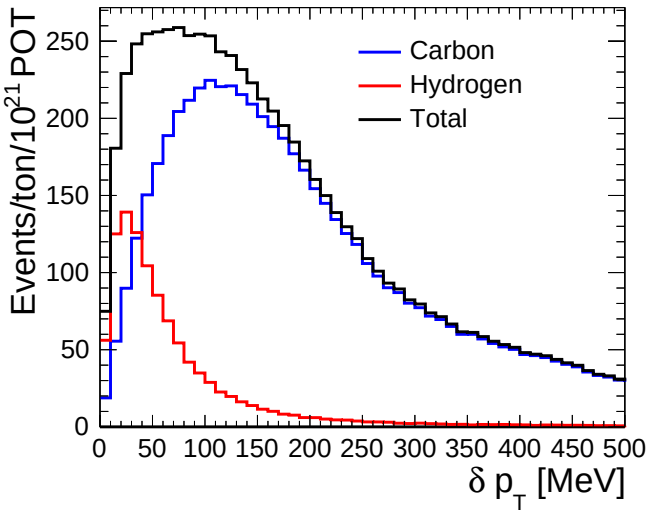

Figure 9.11: The NEUT 5.4.0 predicted event rate of CC0π interactions from the T2K anti-neutrino flux as a function of δp_T obtained after applying the detector smearing effects. The detector time resolution is estimated with Equation 9.1.

In our analysis, we are trying to find the best value of the cuts on the lever arm and δp_T to maximize the improvement of neutrino energy reconstruction precision. All the events with δp_T below the cut value are supposed to be interactions on Hydrogen. The efficiency and purity of such a selection for different lever arms and cut values are shown in Figure 9.12. For this particular figure, the detector resolution was estimated with Equation 9.1. If I use Equation 9.2 instead, the shape will be the same but the purity will be approximately 10% smaller. A good compromise was found with cuts $\delta p_T < 40$ MeV/c and $L < 10$ cm. The resulting Hydrogen purity and efficiency are 61% and 22% respectively. With the full T2K-II data set of 7×10^{21} POT we expect around 26 000 anti–neutrino interactions in SuperFGD on both Hydrogen and Carbon. The interactions over Carbon are dominating. In average we expect one of seven anti–interaction interactions to happen on Hydrogen.

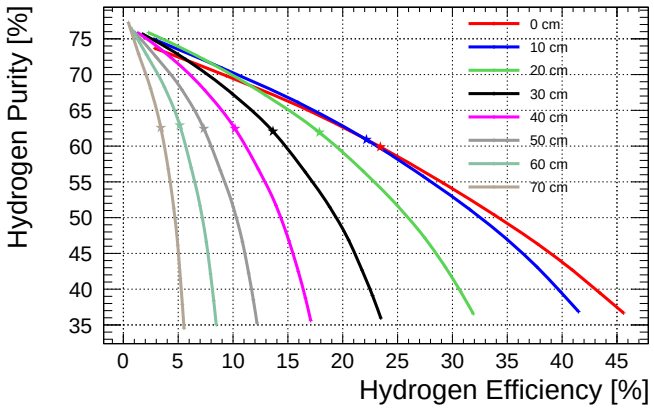

Figure 9.12: The anti-neutrino hydrogen purity vs efficiency for different δp_T and lever-arm cuts. The top left lines' endings correspond to a 10 MeV cut and then the star corresponds to the chosen δp_T cut of 40 MeV. Each line corresponds to a different lever-arm cut and is made using Equation 9.1 to determine the time resolution.

From Figure 9.12 one can see that a stronger lever arm cut sharply reduces the efficiency, but not improving the purity. This happens because of the correlation between the neutron energy and travel distance. Most of the neutrons produced in ND280 in anti-neutrino interactions are below 100 MeV (Figure 9.8). In this region the travel distance increase with the growing energy (Figure 9.5). Therefore, a longer lever arm cut accepts more energetic thus faster neutrons and the energy resolution is not improving. The best performance is expected with the lever arm cut set to 10 cm and δp_T cut set to 50 MeV. The events passing the cuts are further used to reconstruct anti-neutrino energy under the assumption of CCQE interaction.

$$E_\nu = \frac{m_n^2 - m_p^2 - m_\mu^2 + 2m_p E_\mu}{2\left(m_p - E_\nu + p_\mu \cos\theta_\mu\right)} \tag{9.3}$$

The smearing of the reconstructed energy with and without δp_T cut is shown in Figure 9.13. It was observed that the additional information from the neutron ToF improves the anti-neutrino energy reconstruction precision from 15% to around 7%.

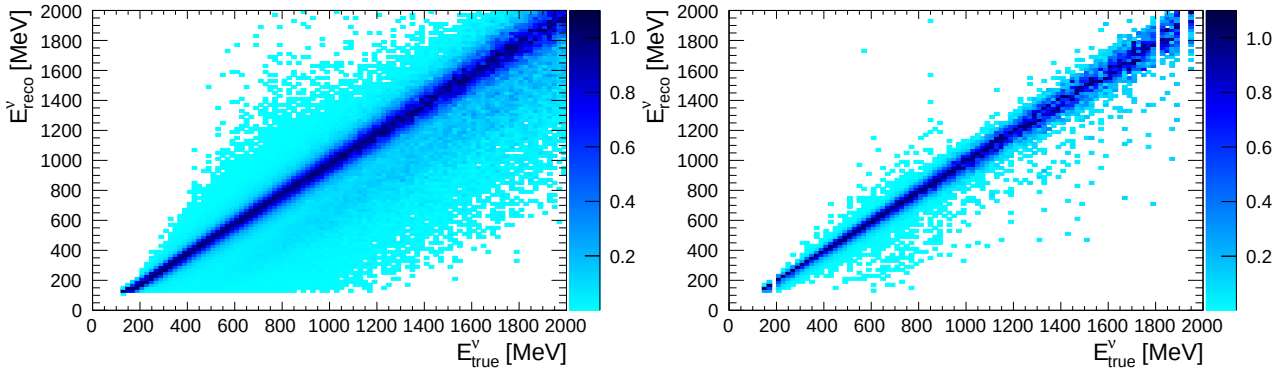

(a) (b)

Figure 9.13: The reconstructed energy of anti-neutrino under the CCQE assumption with Equation 9.3 before applying lever arm and δp_T cut (a) and after (b). The Z-axis is normalized such that the highest value in each plot is one.

The key feature of the transverse variables is the measurements that are independent of the poorly understood nuclear effects. To prove that the selected sample depends weakly on the theoretical models we estimated anti-neutrino energy resolution with various 2p2h normalization and

with different models of the initial nucleon momentum. The results of these cross-check is shown in Figure 9.14. One can see that solid lines that are obtained after applying the cuts demonstrate much weaker dependence on the input parameters. Relatively large changes in the normalization of the interactions with two particles don't degrade the neutrino energy resolution at all. Thus the proposed method provides precise measurement of the neutrino energy and is largely unaffected by nuclear effects.

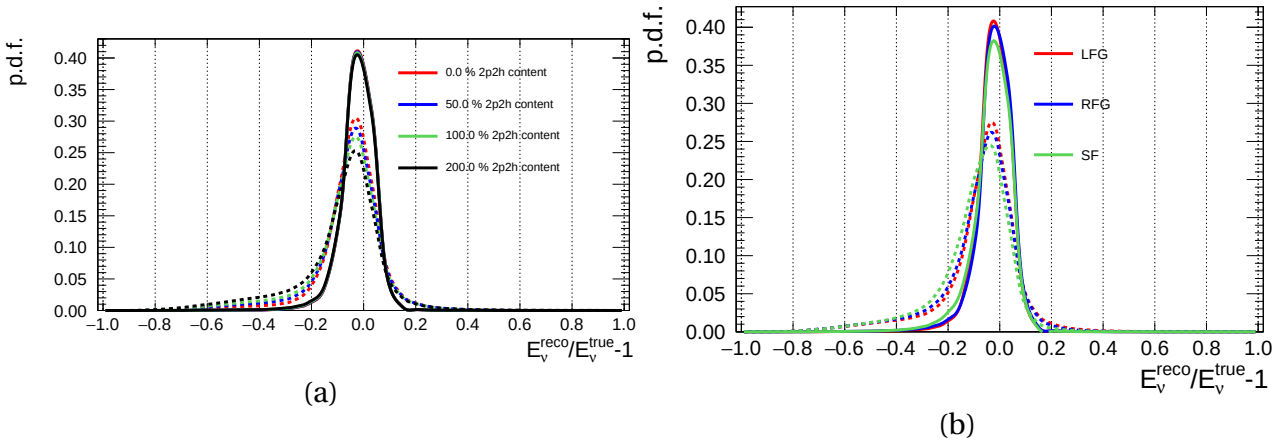

(a) (b)

Figure 9.14: Accuracy of the reconstructed anti-neutrino energy after applying the lever arm and δp_T cuts. The dependence on the 2p2h normalization (a) and initial nucleon momentum model (b) is shown. The solid lines correspond to the measurement after the cuts $L > 10$ cm $\delta p_T < 50$ MeV/c, the dashed lines are obtained before the cuts.

The main problem of the neutrino flux measurements are poorly studied nuclear effects. Since we found a sample that is affected by these effects very weekly, the precise measurements of the neutrino flux can be performed. The advantage of our method is that the shape of the flux can be measured accurately together with the global normalization. As the neutrino oscillations change the flux shape, its precise measurements can improve the accuracy of the oscillation analysis, especially searches for the CP–violation in the lepton sector.

In this particular study, proton kinematics is not used. We do not expect a proton to be produced in the anti–neutrino CCQE interaction but it can be born due to nuclear effects. The measurements of the stopping hadrons can be performed precisely with a highly granular SuperFGD detector. Thus, further precision improvement is possible with additional information.

We concentrated on the CC0π topology in the analysis, while CC1π topology can be also very promising. A double transverse momentum should be used for this ($\delta p_T T$), taking into account all the particles in the final state. A plane is defined to contain neutrino and lepton momentum. Then the momentum imbalance between a proton/neutron and a pion can be studied. This technique is similar to the single transverse variable and allows probing nuclear effects in CC1π typologies.

5 Conclusion

The proposed method demonstrates the ability of the new scintillator detector SuperFGD to measure neutrons produced in the anti-neutrino interactions. Neutron energy can be measured with a relatively small uncertainty with the time of flight method. This information can be further used to compute the transverse kinematic imbalance of the neutrino interaction. The sample that is nearly free from nuclear effects can be selected with the requirement of low δp_T value. This method has a strong advantage as it is sensitive to both the shape and normalization of the

neutrino energy spectrum. Other flux–constraining methods are mainly sensitive to the normalization only. The constraints on the flux shape for both neutrino and anti–neutrino are essential for precise measurements of the δ_{CP} phase.

The performed analysis was published in [4]. A prototype beam test with a neutron beam was performed at Los Alamos laboratory. The analysis of the data is ongoing at the moment. The main goal of the beamtest is to prove the ability of the SuperFGD to detect neutrons and try to estimate its efficiency.

CONCLUSION

Neutrino physics is a very promising field of particle physics. The discovery of neutrino oscillations was an important milestone as a non-zero neutrino mass was proven. To explain the nature of the neutrino mass, physics beyond the Standard Model is essential. This thesis is concentrated on the search for the new physics and the upgrade of the near detector of the long-baseline accelerator neutrino experiment T2K (Tokai-to-Kamioka) hosted in Japan.

Modern accelerator neutrino experiments are performing precise measurements of the neutrino oscillation parameters. The most interesting problem is the search for CP–violation in the neutrino oscillations as this phenomena may be a hint for the explanation of the baryon asymmetry of the Universe. The main limitation of the current experiments is the systematic uncertainties of the flux predictions and neutrino interaction models.

1 T2K near detector upgrade

The near detector of the T2K experiment ND280 provides a remarkable reduction of uncertainties from 14% down to 7% with flux and neutrino cross–section constraints. But its performance may be further improved. The current setup has a limited acceptance for high-angle tracks. The energy threshold of hadron detection is high, thus not all the secondary particles from neutrino interactions are detected and reconstructed neutrino energy is smeared. To gain accuracy of the neutrino interaction measurements an upgrade of the ND280 is being performed. A combination of the fine–grained scintillator detector (FGD) and vertical Time Projection Chambers (TPC) has been shown to provide good performance in particle tracking, charge and particle identification, momentum measurements.

A new fully active fine–grained scintillator detector SuperFGD will be installed as an additional neutrino target. It is made from 1 cm^3 cubes and performs tracking in 3D. The dimensions of the new detector are $192 \times 184 \times 56$ cm^3 and a fiducial mass is 2 tons. Fine granularity reduces the threshold for hadron and muon detection. Nearly all the charged secondary particles from neutrino interactions are going to be detected. Thus the accuracy of neutrino interaction measurements is increased.

The production and assembly of the new detector are complicated. A method for the SuperFGD assembly has been developed and tested. It was demonstrated that the whole detector may be assembled in this way. The loose structure of cubes will provide their self-alignment during the fishing line insertion in three dimensions. Fragile fibers are inserted only at the last step of the detector contraction.

A simulation toolkit for the SuperFGD detector was developed. Detector response simulation was calibrated with the data taken during the beamtest. The light yield for different event topologies was estimated. The simulation of the optical cross-talk between the cubes was done. With such a simulation it was demonstrated that the detector can separate different particles with the

measurements of the deposited energy. The dynamic range of the MPPCs is large enough (2668 pixels) to measure the stopping protons that will provide at most 600 photoelectrons.

New detectors will provide more detailed information about neutrino interactions, thus new analysis methods have to be developed. A new method of anti-neutrino energy reconstruction using the neutron time of flight energy measurements in SuperFGD was proposed. With the simulation toolkit of the SuperFGD, it was demonstrated that with this additional information, the interaction over Hydrogen can be separated from the interactions over Carbon. Hence we can select a sample of neutrino interactions free from nuclear effects and reconstruct neutrino energy in a more precise way. This method will allow us to constrain both flux normalization and shape that is critical for precise measurements of the δ_{CP} phase.

Two new TPCs will be installed above and below the SuperFGD. They will provide precise tracking, identification of the charge and particle type, accurate momentum measurements. Resistive Micromegas will be used as a sensitive detector. A resistive foil over the usual Micromegas detector is responsible for the charge sharing between sensitive pads and improving the spatial resolution. Therefore the momentum resolution becomes better.

The prototypes of the new detectors were constructed and tested with beams of charged particles. The performance of the TPC detector was found to exceed the expectations. Spatial resolution for tracks that are parallel to pad borders was measured at the level of 200 μm. That will make possible very precise measurements of the momentum, thus accurate probe of neutrino interaction models. The energy resolution was estimated at the same level as we observed in the existing TPC (10% for one module). With the new detectors we are going to decrease the systematic uncertainty in the oscillation analysis from 7% to 4%.

2 Search for Heavy Neutral Lepton

Accelerator neutrino experiments are capable not only to measure the oscillation parameters, but to perform a search of the physics beyond the Standard Model (SM). A hypothesis proposing Heavy Neutral Leptons (HNL) is an extension of the SM that can explain the nature of the neutrino mass, existence of the Dark Matter and baryon asymmetry of the Universe. A search of the HNL decays was performed with the near detector of the T2K experiment. Heavy neutrinos are expected to be produced in the meson decay. With T2K beamline, intense beam of kaons is produced. Thus the search of the HNL with masses $M_N < 500$ MeV/c^2 is possible. We concentrated on the search of the two body decays $N \to \mu\pi$, $N \to e\pi$ and dimuon mode $N \to \mu\mu\nu$. The fiducial volume of the three TPCs was used in this analysis. Few neutrino interactions are expected in the gas with atmospheric pressure, comparing to the scintillator detectors. Thus the background is naturally suppressed. The ND280 tracker already demonstrated good performance and ability to identify particle's charge and type. That is very helpful in the searches for neutral particle decay.

Expected signal events were simulated in the detector. Kinematic spectra of the daughter particles were studied in order to separate them from the neutrino interactions in gas. A cut sequence was developed to suppress the background from the neutrino interactions. The final efficiency for the signal detection was observed at the level of 20% and nearly no background was expected. The systematic uncertainties from the flux predictions and detector efficiency were estimated.

After data unblinding only one event in the $N \to \mu\mu\nu$ mode was observed. A strong upper limit on the existence of the heavy neutrino with masses $M_N < 500$ MeV/c^2 was set. The best result was achieved at the high mass. Mixing elements were constrained with $|U_e|^2 < 2 \times 10^{-9}$ for $M_N > 420$ MeV/c^2 and $|U_e|^2 < 3 \times 10^{-9}$ for $M_N > 350$ MeV/c^2. This result improved the previous analysis done by the PS191 experiment.

BIBLIOGRAPHY

[1] K. Abe et al. "T2K ND280 Upgrade - Technical Design Report". In: (Jan. 2019). arXiv: 1901.03750.

[2] A. Blondel et al. *A fully-active fine-grained detector with three readout views*. July 2018. DOI: 10.1088/1748-0221/13/02/P02006.

[3] D. Attié et al. "Performances of a resistive Micromegas module for the Time Projection Chambers of the T2K Near Detector upgrade". In: *Nuclear Instruments and Methods in Physics Research, Section A: Accelerators, Spectrometers, Detectors and Associated Equipment* 957 (Mar. 2020), p. 163286. DOI: 10.1016/j.nima.2019.163286.

[4] L. Munteanu et al. "New method for an improved antineutrino energy reconstruction with charged-current interactions in next-generation detectors". In: *Physical Review D* 101.9 (May 2020), p. 092003. DOI: 10.1103/PhysRevD.101.092003.

[5] K. Abe et al. "Search for heavy neutrinos with the T2K near detector ND280". In: *Physical Review D* 100.5 (Sept. 2019), p. 052006. DOI: 10.1103/PhysRevD.100.052006.

[6] J Chadwick. "Intensitätsverteilung im magnetischen Spectrum der β-Strahlen von radium B + C". In: *Verhandl. Dtsc. Phys. Ges.* 16 (1914), p. 383.

[7] W. Pauli. *Letter to L. Meinter and other participants of the conference in Tubingen in 1930, a copy of the letter can be found in W. Pauli, Neutrino Physics ed. by K. Winter, Cambridge Univ. Press, Cambridge 1991, p.4, the first publication was given in W. Pauli.* 1930.

[8] E. Fermi. "Versuch einer Theorie der β-Strahlen. I". In: *Zeitschrift für Physik* 88.3-4 (Mar. 1934), pp. 161–177. DOI: 10.1007/BF01351864.

[9] C. L. Cowan et al. "Detection of the free neutrino: A confirmation". In: *Science* 124.3212 (1956), pp. 103–104. DOI: 10.1126/science.124.3212.103.

[10] G. Danby et al. "Observation of high-energy neutrino reactions and the existence of two kinds of neutrinos". In: *Physical Review Letters* 9.1 (1962), pp. 36–44. DOI: 10.1103/PhysRevLett.9.36.

[11] C. N. Yang and R. L. Mills. "Conservation of isotopic spin and isotopic gauge invariance". In: *Physical Review* 96.1 (1954), pp. 191–195. DOI: 10.1103/PhysRev.96.191.

[12] Sheldon L. Glashow. "Partial-symmetries of weak interactions". In: *Nuclear Physics* 22.4 (Feb. 1961), pp. 579–588. DOI: 10.1016/0029-5582(61)90469-2.

[13] Steven Weinberg. "A model of leptons". In: *Physical Review Letters* 19.21 (1967), pp. 1264–1266. DOI: 10.1103/PhysRevLett.19.1264.

[14] Donald C Cundy. "Neutrino Physics - CERN". In: *17th International Conference on High-energy Physics*. London, 1974. URL: http://cds.cern.ch/record/417920/.

[15] G. Arnison et al. "Experimental observation of isolated large transverse energy electrons with associated missing energy at s=540 GeV". In: *Physics Letters B* 122.1 (Feb. 1983), pp. 103–116. DOI: 10.1016/0370-2693(83)91177-2.

[16] G. Aad et al. “Observation of a new particle in the search for the Standard Model Higgs boson with the ATLAS detector at the LHC”. In: *Physics Letters, Section B: Nuclear, Elementary Particle and High-Energy Physics* 716.1 (Sept. 2012), pp. 1–29. DOI: 10.1016/j.physletb.2012.08.020.

[17] M. Goldhaber, L. Grodzins, and A. W. Sunyar. *Helicity of neutrinos*. 1958. DOI: 10.1103/PhysRev.109.1015.

[18] J. A. Bagger et al. *Precision electroweak measurements on the Z resonance*. May 2006. DOI: 10.1016/j.physrep.2005.12.006.

[19] L. B. Auerbach et al. “Measurement of electron-neutrino electron elastic scattering”. In: *Physical Review D* 63.11 (May 2001), p. 112001. DOI: 10.1103/PhysRevD.63.112001.

[20] J. A. Formaggio and G. P. Zeller. “From eV to EeV: Neutrino cross sections across energy scales”. In: *Reviews of Modern Physics* 84.3 (Sept. 2012), pp. 1307–1341. DOI: 10.1103/RevModPhys.84.1307.

[21] B. Pontecorvo. “Inverse beta processes and nonconservation of lepton charge”. In: *Zh.Eksp.Teor.Fiz.* 7 (1957), p. 247.

[22] Z Maki, M Nakagawa, and S Sakata. *REMARKS ON THE UNIFIED MODEL OF ELEMENTARY PARTICLES*. Tech. rep. 1962, p. 221.

[23] D. Sakharov. “Violation of cp in variance, C asymmetry, and baryon asymmetry of the universe”. In: *Soviet Physics - Uspekhi* 34.5 (1991), pp. 392–393. DOI: 10.1070/PU1991v034n05ABEH002497

[24] M. Tanabashi et al. *Review of Particle Physics*. Aug. 2018. DOI: 10.1103/PhysRevD.98.030001.

[25] Sacha Davidson, Enrico Nardi, and Yosef Nir. *Leptogenesis*. Sept. 2008. DOI: 10.1016/j.physrep.2008.06.002.

[26] T. D. Lee and C. N. Yang. “Question of Parity Conservation in Weak Interactions”. In: *Physical Review* 104.1 (Oct. 1956), pp. 254–258. DOI: 10.1103/PhysRev.104.254.

[27] C. S. Wu et al. “Experimental Test of Parity Conservation in Beta Decay”. In: *Physical Review* 105.4 (Feb. 1957), pp. 1413–1415. DOI: 10.1103/PhysRev.105.1413.

[28] M. Gormley et al. “Experimental test of C Invariance in $\eta \to \pi+\pi-\pi 0$”. In: *Physical Review Letters* 21.6 (1968), pp. 402–406. DOI: 10.1103/PhysRevLett.21.402.

[29] J. H. Christenson et al. “Evidence for the 2π decay of the K20 meson”. In: *Physical Review Letters* 13.4 (July 1964), pp. 138–140. DOI: 10.1103/PhysRevLett.13.138.

[30] A. Alavi-Harati et al. “Observation of Direct CP Violation in K S , L → π π Decays”. In: *Physical Review Letters* 83.1 (July 1999), pp. 22–27. DOI: 10.1103/PhysRevLett.83.22.

[31] V. Fanti et al. “A new measurement of direct CP violation in two pion decays of the neutral kaon”. In: *Physics Letters B* 465.1-4 (Oct. 1999), pp. 335–348. DOI: 10.1016/S0370-2693(99)01030-8.

[32] B. Aubert et al. “Measurement of CP -Violating Asymmetries in B0 Decays to CP Eigenstates”. In: *Physical Review Letters* 86.12 (Mar. 2001), pp. 2515–2522. DOI: 10.1103/PhysRevLett.86.2515.

[33] K. Abe et al. “Observation of Large CP Violation in the Neutral B Meson System”. In: *Physical Review Letters* 87.9 (Aug. 2001), p. 091802. DOI: 10.1103/PhysRevLett.87.091802.

[34] R. Aaij et al. “Observation of CP Violation in Charm Decays”. In: *Physical Review Letters* 122.21 (May 2019). DOI: 10.1103/PhysRevLett.122.211803.

[35] L. Wolfenstein. "Neutrino oscillations in matter". In: *Physical Review D* 17.9 (May 1978), pp. 2369–2374. DOI: 10.1103/PhysRevD.17.2369.

[36] S. P. Mikheyev and A. Yu. Smirnov. "Resonance enhancement of oscillations in matter and solar neutrino spectroscopy". In: *Yadernaya Fizika* 42 (1985), p. 1441.

[37] Raymond Davis, Don S. Harmer, and Kenneth C. Hoffman. "Search for neutrinos from the sun". In: *Physical Review Letters* 20.21 (May 1968), pp. 1205–1209. DOI: 10.1103/PhysRevLett.20.1205.

[38] T. A. Kirsten et al. "GALLEX solar neutrino results and status of GNO". In: *Nuclear Physics B - Proceedings Supplements* 77.1-3 (May 1999), pp. 26–34. DOI: 10.1016/S0920-5632(99)00389-8.

[39] J. N. Abdurashitov et al. "Measurement of the solar neutrino capture rate with gallium metal". In: *Physical Review C - Nuclear Physics* 60.5 (Oct. 1999), p. 32. DOI: 10.1103/PhysRevC.60.055801.

[40] Y. Oyama et al. "Experimental study of upward-going muons in Kamiokande". In: *Physical Review D* 39.6 (Mar. 1989), pp. 1481–1491. DOI: 10.1103/PhysRevD.39.1481.

[41] Q. R. Ahmad et al. "Direct Evidence for Neutrino Flavor Transformation from Neutral-Current Interactions in the Sudbury Neutrino Observatory". In: *Physical Review Letters* 89.1 (June 2002), p. 011301. DOI: 10.1103/PhysRevLett.89.011301.

[42] Y. Fukuda et al. "Measurement of the flux and zenith-angle distribution of upward through-going muons by super-kamiokande". In: *Physical Review Letters* 82.13 (Mar. 1999), pp. 2644–2648. DOI: 10.1103/PhysRevLett.82.2644.

[43] K. Eguchi et al. "First Results from KamLAND: Evidence for Reactor Antineutrino Disappearance". In: *Physical Review Letters* 90.2 (Jan. 2003), p. 6. DOI: 10.1103/PhysRevLett.90.021802.

[44] J. K. Ahn et al. "Observation of reactor electron antineutrinos disappearance in the RENO experiment". In: *Physical Review Letters* 108.19 (May 2012), p. 191802. DOI: 10.1103/PhysRevLett.108.191802.

[45] Y. Abe et al. "Improved measurements of the neutrino mixing angle θ_{13} with the double chooz detector". In: *Journal of High Energy Physics* 2014.10 (Oct. 2014), pp. 1–44. DOI: 10.1007/JHEP10(2014)086.

[46] F. P. An et al. "Independent measurement of the neutrino mixing angle θ_{13} via neutron capture on hydrogen at Daya Bay". In: *Physical Review D - Particles, Fields, Gravitation and Cosmology* 90.7 (Oct. 2014), p. 071101. DOI: 10.1103/PhysRevD.90.071101.

[47] M. H. Ahn et al. "Measurement of neutrino oscillation by the K2K experiment". In: *Physical Review D - Particles, Fields, Gravitation and Cosmology* 74.7 (Oct. 2006), p. 072003. DOI: 10.1103/PhysRevD.74.072003.

[48] P. Adamson et al. "Combined analysis of $\nu\mu$ disappearance and $\nu\mu \rightarrow \nu$e appearance in MINOS using accelerator and atmospheric neutrinos". In: *Physical Review Letters* 112.19 (May 2014), p. 191801. DOI: 10.1103/PhysRevLett.112.191801.

[49] K. Abe et al. "First combined measurement of the muon neutrino and antineutrino charged-current cross section without pions in the final state at T2K". In: *Physical Review D* 101.11 (Feb. 2020). DOI: 10.1103/physrevd.101.112001.

[50] M. A. Acero et al. "First measurement of neutrino oscillation parameters using neutrinos and antineutrinos by NOvA". In: *Physical Review Letters* 123.15 (Oct. 2019), p. 151803. DOI: 10.1103/PhysRevLett.123.151803.

[51] N. Agafonova et al. “Observation of tau neutrino appearance in the CNGS beam with the OPERA experiment”. In: *Progress of Theoretical and Experimental Physics* 2014.10 (July 2014). DOI: 10.1093/ptep/ptu132.

[52] M Jiang et al. “Atmospheric neutrino oscillation analysis with improved event reconstruction in Super-Kamiokande IV”. In: *Progress of Theoretical and Experimental Physics* 2019.5 (May 2019). DOI: 10.1093/PTEP/PTZ015.

[53] IceCube Collaboration and T. DEYOUNG. “Status of the icecube neutrino telescope”. In: *International Journal of Modern Physics A*. Vol. 20. 14. World Scientific Publishing Company, June 2005, pp. 3160–3162. DOI: 10.1142/S0217751X05026029.

[54] Ivan Esteban et al. “Global analysis of three-flavour neutrino oscillations: synergies and tensions in the determination of θ 23 , δ CP , and the mass ordering”. In: *Journal of High Energy Physics* 2019.1 (Jan. 2019). DOI: 10.1007/JHEP01(2019)106.

[55] K. Abe et al. “Constraint on the matterantimatter symmetry-violating phase in neutrino oscillations”. In: *Nature* 580.7803 (Apr. 2020), pp. 339–344. DOI: 10.1038/s41586-020-2177-0.

[56] Peter W. Higgs. “Broken Symmetries and the Masses of Gauge Bosons”. In: *Physical Review Letters* 13.16 (Oct. 1964), pp. 508–509. DOI: 10.1103/PhysRevLett.13.508.

[57] M. Aker et al. “Improved Upper Limit on the Neutrino Mass from a Direct Kinematic Method by KATRIN”. In: *Physical Review Letters* 123.22 (Sept. 2019). DOI: 10.1103/PhysRevLett.123.221802.

[58] C. Athanassopoulos et al. “The liquid scintillator neutrino detector and LAMPF neutrino source”. In: *Nuclear Instruments and Methods in Physics Research, Section A: Accelerators, Spectrometers, Detectors and Associated Equipment* 388.1-2 (Mar. 1997), pp. 149–172. DOI: 10.1016/S0168-9002(96)01155-2.

[59] A. A. Aguilar-Arevalo et al. “Event excess in the MiniBooNE search for $\nu\mu\rightarrow\nu$e oscillations”. In: *Physical Review Letters* 105.18 (Oct. 2010), p. 181801. DOI: 10.1103/PhysRevLett.105.181801.

[60] Y. J. Ko et al. “Sterile Neutrino Search at the NEOS Experiment”. In: *Physical Review Letters* 118.12 (Mar. 2017), p. 121802. DOI: 10.1103/PhysRevLett.118.121802.

[61] I. Alekseev et al. “Search for sterile neutrinos at the DANSS experiment”. In: *Physics Letters, Section B: Nuclear, Elementary Particle and High-Energy Physics* 787 (Dec. 2018), pp. 56–63. DOI: 10.1016/j.physletb.2018.10.038.

[62] H. Almazán et al. “Sterile Neutrino Constraints from the STEREO Experiment with 66 Days of Reactor-On Data”. In: *Physical Review Letters* 121.16 (Oct. 2018), p. 161801. DOI: 10.1103/PhysRevLett.121.161801.

[63] J. Ashenfelter et al. “First Search for Short-Baseline Neutrino Oscillations at HFIR with PROSPECT”. In: *Physical Review Letters* 121.25 (Dec. 2018), p. 251802. DOI: 10.1103/PhysRevLett.121.251802.

[64] A. P. Serebrov et al. “Neutrino-4 experiment on the search for a sterile neutrino at the SM-3 reactor”. In: *Journal of Experimental and Theoretical Physics* 121.4 (Oct. 2015), pp. 578–586. DOI: 10.1134/S1063776115100209.

[65] K. N. Abazajian et al. “Light Sterile Neutrinos: A White Paper”. In: (Apr. 2012). arXiv: 1204.5379.

[66] Takehiko Asaka, Steve Blanchet, and Mikhail Shaposhnikov. "The νMSM, Dark Matter and Neutrino Masses". In: *Physics Letters B* 631.4 (Mar. 2005), pp. 151–156. DOI: 10.1016/j.physletb.2005.09.070.

[67] Takehiko Asaka and Mikhail Shaposhnikov. "The νMSM, Dark Matter and Baryon Asymmetry of the Universe". In: *Journal of Physics: Conference Series* 39.1 (May 2005), pp. 9–11. DOI: 10.1016/j.physletb.2005.06.020.

[68] Ch Kraus et al. "Final results from phase II of the Mainz neutrino mass searchin tritium β decay". In: *European Physical Journal C* 40.4 (Apr. 2005), pp. 447–468. DOI: 10.1140/epjc/s2005-02139-7.

[69] V. N. Aseev et al. "Upper limit on the electron antineutrino mass from the Troitsk experiment". In: *Physical Review D - Particles, Fields, Gravitation and Cosmology* 84.11 (Dec. 2011). DOI: 10.1103/PhysRevD.84.112003.

[70] A. Gando et al. "Search for Majorana Neutrinos Near the Inverted Mass Hierarchy Region with KamLAND-Zen". In: *Physical Review Letters* 117.8 (Aug. 2016). DOI: 10.1103/PhysRevLett.117.082503.

[71] Nathalie Palanque-Delabrouille et al. "Neutrino masses and cosmology with Lyman-alpha forest power spectrum". In: *Journal of Cosmology and Astroparticle Physics* 2015.11 (Nov. 2015). DOI: 10.1088/1475-7516/2015/11/011.

[72] Kenny C.Y. Ng et al. "New constraints on sterile neutrino dark matter from NuSTAR M31 observations". In: *Physical Review D* 99.8 (Apr. 2019), p. 083005. DOI: 10.1103/PhysRevD.99.083005.

[73] Kerstin Perez et al. "Almost closing the νmSM sterile neutrino dark matter window with NuSTAR". In: *Physical Review D* 95.12 (June 2017), p. 123002. DOI: 10.1103/PhysRevD.95.123002.

[74] Andrea Caputo, Marco Regis, and Marco Taoso. "Searching for sterile neutrino with X-ray intensity mapping". In: *Journal of Cosmology and Astroparticle Physics* 2020.3 (2020). DOI: 10.1088/1475-7516/2020/03/001.

[75] Dmitry Gorbunov and Mikhail Shaposhnikov. "How to find neutral leptons of the νMSM?" In: *Journal of High Energy Physics* 2007.10 (Oct. 2007), pp. 015–015. DOI: 10.1088/1126-6708/2007/10/015.

[76] V. Khachatryan et al. "Search for heavy Majorana neutrinos in $\mu\acute{s}\mu\acute{s}$ + jets events in proton-proton collisions at s=8 TeV". In: *Physics Letters, Section B: Nuclear, Elementary Particle and High-Energy Physics* 748 (July 2015), pp. 144–166. DOI: 10.1016/j.physletb.2015.06.070.

[77] P. Abreu et al. "Search for neutral heavy leptons produced in Z decays". In: *Zeitschrift fur Physik C-Particles and Fields* 74.1 (Mar. 1997), pp. 57–71. DOI: 10.1007/s002880050370.

[78] O. Adriani et al. "Search for isosinglet neutral heavy leptons in Z0 decays". In: *Physics Letters B* 295.3-4 (Dec. 1992), pp. 371–382. DOI: 10.1016/0370-2693(92)91579-X.

[79] R. Aaij et al. "Search for Majorana neutrinos in $B \to \pi^+\mu^-\mu^-$ decays". In: *Physical Review Letters* 112.13 (Apr. 2014), online. DOI: 10.1103/PhysRevLett.112.131802.

[80] D. Liventsev et al. "Search for heavy neutrinos at Belle". In: *Physical Review D - Particles, Fields, Gravitation and Cosmology* 87.7 (Apr. 2013), p. 071102. DOI: 10.1103/PhysRevD.87.071102.

[81] A. M. Cooper-Sarkar et al. “Search for heavy neutrino decays in the BEBC beam dump experiment”. In: *Physics Letters B* 160.1-3 (Oct. 1985), pp. 207–211. DOI: 10.1016/0370-2693(85)91493-5.

[82] E. Gallas et al. “Search for neutral weakly interacting massive particles in the Fermilab Tevatron wideband neutrino beam”. In: *Physical Review D* 52.1 (July 1995), pp. 6–14. DOI: 10.1103/PhysRevD.52.6.

[83] A. V. Artamonov et al. “Search for heavy neutrinos in $K^+ \to \mu\nu_H$ decays”. In: *Physical Review D - Particles, Fields, Gravitation and Cosmology* 91.5 (Mar. 2015), p. 052001. DOI: 10.1103/PhysRevD.91.052001.

[84] M. Aoki et al. “Search for massive neutrinos in the decay $\pi \to e\nu$”. In: *Physical Review D - Particles, Fields, Gravitation and Cosmology* 84.5 (Sept. 2011), p. 052002. DOI: 10.1103/PhysRevD.84.052002.

[85] D. I. Britton et al. “Improved search for massive neutrinos in $\pi+\to$ e+ ν decay”. In: *Physical Review D* 46.3 (Aug. 1992), R885. DOI: 10.1103/PhysRevD.46.R885.

[86] G. Bernardi et al. “Further limits on heavy neutrino couplings”. In: *Physics Letters B* 203.3 (Mar. 1988), pp. 332–334. DOI: 10.1016/0370-2693(88)90563-1.

[87] P. Vilain et al. “Search for heavy isosinglet neutrinos”. In: *Physics Letters B* 343.1-4 (Jan. 1995), pp. 453–458. DOI: 10.1016/0370-2693(94)01422-9.

[88] A. Vaitaitis et al. “Search for neutral heavy leptons in a high-energy neutrino beam”. In: *Physical Review Letters* 83.24 (Jan. 1999), pp. 4943–4946. DOI: 10.1103/PhysRevLett.83.4943.

[89] J. Badier et al. “Direct photon production from pions and protons at 200 GeV/c”. In: *Zeitschrift für Physik C Particles and Fields* 31.3 (Sept. 1986), pp. 341–347. DOI: 10.1007/BF01588030.

[90] R. S. Hayano et al. “Heavy-neutrino search using Kμ2 decay”. In: *Physical Review Letters* 49.18 (Nov. 1982), pp. 1305–1309. DOI: 10.1103/PhysRevLett.49.1305.

[91] Marco Drewes and Björn Garbrecht. “Combining Experimental and Cosmological Constraints on Heavy Neutrinos”. In: *Nuclear Physics B* 921 (Feb. 2015), pp. 250–315. DOI: 10.1016/j.nuclphysb.2017.05.001.

[92] J. Dorenbosch et al. “A search for decays of heavy neutrinos in the mass range 0.5-2.8 GeV”. In: *Physics Letters B* 166.4 (Jan. 1986), pp. 473–478. DOI: 10.1016/0370-2693(86)91601-1.

[93] S. Baranov et al. “Search for heavy neutrinos at the IHEP-JINR Neutrino Detector”. In: *Physics Letters B* 302.2-3 (Mar. 1993), pp. 336–340. DOI: 10.1016/0370-2693(93)90405-7.

[94] J. Orloff, A. Rozanov, and C. Santoni. “Limits on the mixing of tau neutrino to heavy neutrinos”. In: *Physics Letters, Section B: Nuclear, Elementary Particle and High-Energy Physics* 550.1-2 (Dec. 2002), pp. 8–15. DOI: 10.1016/S0370-2693(02)02769-7.

[95] P. Astier et al. “Search for heavy neutrinos mixing with tau neutrinos”. In: *Physics Letters, Section B: Nuclear, Elementary Particle and High-Energy Physics* 506.1-2 (May 2001), pp. 27–38. DOI: 10.1016/S0370-2693(01)00362-8.

[96] K. Abe et al. “Proposal for an Extended Run of T2K to 20×10^{21} POT”. In: (Sept. 2016). arXiv: 1609.04111.

[97] Hyper-Kamiokande Proto-Collaboration et al. “Hyper-Kamiokande Design Report”. In: (May 2018). arXiv: 1805.04163.

[98] R. Acciarri et al. “Long-Baseline Neutrino Facility (LBNF) and Deep Underground Neutrino Experiment (DUNE) Conceptual Design Report Volume 1: The LBNF and DUNE Projects”. In: (Jan. 2016). arXiv: 1601.05471.

[99] Cedric Cerna. “The Jiangmen Underground Neutrino Observatory (JUNO)”. In: *Nuclear Instruments and Methods in Physics Research, Section A: Accelerators, Spectrometers, Detectors and Associated Equipment* 958 (Apr. 2020), p. 162183. DOI: 10.1016/j.nima.2019.05.024.

[100] N. Di Marco. “Searching for neutrinoless double-beta decay with GERDA”. In: *Nuclear Instruments and Methods in Physics Research, Section A: Accelerators, Spectrometers, Detectors and Associated Equipment* 958 (Apr. 2020), p. 162112. DOI: 10.1016/j.nima.2019.04.066.

[101] L. Cardani. “Final Results of the CUPID-0 Phase I Experiment”. In: *Journal of Low Temperature Physics* 199.1-2 (Feb. 2020), pp. 425–432. DOI: 10.1007/s10909-020-02382-w.

[102] M.G. Aartsen et al. “The IceCube Neutrino Observatory: instrumentation and online systems”. In: *Journal of Instrumentation* 12.03 (Mar. 2017), P03012–P03012. DOI: 10.1088/1748-0221/12/03/P03012.

[103] Rémy Le Breton. *KM3NeT: Next-generation neutrino telescope in the Mediterranean Sea*. Aug. 2019. DOI: 10.1016/j.nima.2018.10.103.

[104] the FCC Collaboration. “FCC-ee: The Lepton Collider: Future Circular Collider Conceptual Design Report Volume 2”. In: *European Physical Journal: Special Topics* 228.2 (June 2019), pp. 261–623. DOI: 10.1140/EPJST/E2019-900045-4.

[105] C. Ahdida et al. “The experimental facility for the Search for Hidden Particles at the CERN SPS”. In: *Journal of Instrumentation* 14.3 (Oct. 2019). DOI: 10.1088/1748-0221/14/03/P03025.

[106] K. Abe et al. “Observation of electron neutrino appearance in a muon neutrino beam”. In: *Physical Review Letters* 112.6 (Feb. 2014), p. 061802. DOI: 10.1103/PhysRevLett.112.061802.

[107] F. P. An et al. “Observation of electron-antineutrino disappearance at Daya Bay”. In: *Physical Review Letters* 108.17 (Apr. 2012). DOI: 10.1103/PhysRevLett.108.171803.

[108] K. Abe et al. *T2K neutrino flux prediction*. Tech. rep. 1. 2013, p. 37. DOI: 10.1103/PhysRevD.87.012001.

[109] P. A. Amaudruz et al. “The T2K fine-grained detectors”. In: *Nuclear Instruments and Methods in Physics Research, Section A: Accelerators, Spectrometers, Detectors and Associated Equipment* 696 (2012), pp. 1–31. DOI: 10.1016/j.nima.2012.08.020.

[110] N Abgrall et al. “Time projection chambers for the T2K near detectors”. In: *Nuclear Instruments and Methods in Physics Research, Section A: Accelerators, Spectrometers, Detectors and Associated Equipment* 637.1 (Dec. 2010), pp. 25–46. DOI: 10.1016/j.nima.2011.02.036.

[111] H. Bethe. “Zur Theorie des Durchgangs schneller Korpuskularstrahlen durch Materie”. In: *Annalen der Physik* 397.3 (Jan. 1930), pp. 325–400. DOI: 10.1002/andp.19303970303.

[112] L. Landau. “On the energy loss of fast particles by ionization”. In: *J.Phys.(USSR)* 8 (1944), pp. 201–205.

[113] S. Fukuda et al. “The Super-Kamiokande detector”. In: *Nuclear Instruments and Methods in Physics Research, Section A: Accelerators, Spectrometers, Detectors and Associated Equipment* 501.2-3 (Apr. 2003), pp. 418–462. DOI: 10.1016/S0168-9002(03)00425-X.

[114] K. Abe et al. “Measurement of neutrino and antineutrino oscillations by the T2K experiment including a new additional sample of veinteractions at the far detector”. In: *Physical Review D* 96.9 (July 2017), p. 092006. DOI: 10.1103/PhysRevD.96.092006.

[115] Robert D. Cousins and Virgil L. Highland. “Incorporating systematic uncertainties into an upper limit”. In: *Nuclear Inst. and Methods in Physics Research, A* 320.1-2 (Aug. 1992), pp. 331–335. DOI: 10.1016/0168-9002(92)90794-5.

[116] K. Abe et al. “Measurement of the charged-current electron (anti-)neutrino inclusive cross-sections at the T2K off-axis near detector ND280”. In: (Feb. 2020). arXiv: 2002.11986.

[117] Robert D. Cousins. “Unified approach to the classical statistical analysis of small signals”. In: *Physical Review D - Particles, Fields, Gravitation and Cosmology* 57.7 (Apr. 1998), pp. 3873–3889. DOI: 10.1103/PhysRevD.57.3873.

[118] Takehiko Asaka, Shintaro Eijima, and Atsushi Watanabe. “Heavy neutrino search in accelerator-based experiments”. In: *Journal of High Energy Physics* 2013.3 (Dec. 2012), p. 125. DOI: 10.1007/JHEP03(2013)125.

[119] N Abgrall et al. “NA61/SHINE facility at the CERN SPS: beams and detector system”. In: *Journal of Instrumentation* 9.06 (June 2014), P06005–P06005. DOI: 10.1088/1748-0221/9/06/P06005.

[120] Lev Davidovich Landau. *The classical theory of fields*. Vol. 5. 5. Elsevier, 2013, p. 25. ISBN: 0-08-025072-6. DOI: 10.1063/1.3067575.

[121] Frederick E James. *Monte Carlo phase space - CERN Document Server*. Tech. rep. 1968, 41 p. DOI: 10.5170/CERN-1968-015.

[122] Jean-Michel Levy. “Rates and differential distributions in heavy neutral leptons production and decays”. In: (May 2018). arXiv: 1805.06419.

[123] S Agostinelli et al. “Geant4 – a simulation toolkit”. In: *Nuclear Instruments and Methods in Physics Research Section A: Accelerators, Spectrometers, Detectors and Associated Equipment* 506.3 (2003), pp. 250–303. DOI: 10.1016/S0168-9002(03)01368-8.

[124] Y. Hayato. “Neut”. In: *Nuclear Physics B - Proceedings Supplements* 112.1-3 (Nov. 2002), pp. 171–176. DOI: 10.1016/S0920-5632(02)01759-0.

[125] C. Andreopoulos et al. “The GENIE neutrino Monte Carlo generator”. In: *Nuclear Instruments and Methods in Physics Research Section A: Accelerators, Spectrometers, Detectors and Associated Equipment* 614.1 (Feb. 2010), pp. 87–104. DOI: 10.1016/j.nima.2009.12.009.

[126] Jakub Zmuda et al. “NuWro monte carlo generator of neutrino interactions-first electron scattering results”. In: *Acta Physica Polonica B*. Vol. 46. 11. Jagellonian University, Nov. 2015, pp. 2329–2334. DOI: 10.5506/APhysPolB.46.2329.

[127] K. Abe et al. “J-PARC Neutrino Beamline Upgrade Technical Design Report”. In: (Aug. 2019). arXiv: 1908.05141.

[128] I. Giomataris et al. “Micromegas in a Bulk”. In: *Nuclear Instruments and Methods in Physics Research, Section A: Accelerators, Spectrometers, Detectors and Associated Equipment* 560.2 (Jan. 2005), pp. 405–408. DOI: 10.1016/j.nima.2005.12.222.

[129] M.S. S. Dixit et al. “Position sensing from charge dispersion in micro-pattern gas detectors with a resistive anode”. In: *Nuclear Instruments and Methods in Physics Research, Section A: Accelerators, Spectrometers, Detectors and Associated Equipment* 518.3 (Feb. 2004), pp. 721–727. DOI: 10.1016/j.nima.2003.09.051.

[130] D Attié. “Beam tests of Micromegas LC-TPC large prototype”. In: *Journal of Instrumentation*. Vol. 6. 1. IOP Publishing, Jan. 2011, pp. C01007–C01007. DOI: 10.1088/1748-0221/6/01/C01007.

[131] P. Baron et al. “AFTER, an ASIC for the readout of the large T2K Time Projection Chambers”. In: *IEEE Nuclear Science Symposium Conference Record*. Vol. 3. 2007, pp. 1865–1872. ISBN: 1424409233. DOI: 10.1109/NSSMIC.2007.4436521.

[132] G. Prior. “The HARP time projection chamber”. In: *Nuclear Physics B - Proceedings Supplements* 125 (Sept. 2003), pp. 37–42. DOI: 10.1016/S0920-5632(03)90963-7.

[133] D. C. Arogancia et al. “Study in a beam test of the resolution of a Micromegas TPC with standard readout pads”. In: *Nuclear Instruments and Methods in Physics Research, Section A: Accelerators, Spectrometers, Detectors and Associated Equipment* 602.2 (Apr. 2009), pp. 403–414. DOI: 10.1016/j.nima.2009.01.014.

[134] M. Dixit et al. “Micromegas TPC studies at high magnetic fields using the charge dispersion signal”. In: *Nuclear Instruments and Methods in Physics Research, Section A: Accelerators, Spectrometers, Detectors and Associated Equipment* 581.1-2 SPEC. ISS. (Oct. 2007), pp. 254–257. DOI: 10.1016/j.nima.2007.07.099.

[135] Martin Ester et al. “A Density-Based Algorithm for Discovering Clusters in Large Spatial Databases with Noise”. In: *Proceedings of the 2nd International Conference on Knowledge Discovery and Data Mining*. 1996, pp. 226–231. URL: www.aaai.org.

[136] X. G. Lu et al. “Measurement of nuclear effects in neutrino interactions with minimal dependence on neutrino energy”. In: *Physical Review C* 94.1 (July 2016), p. 015503. DOI: 10.1103/PhysRevC.94.015503.

[137] X. G. Lu et al. “Reconstruction of energy spectra of neutrino beams independent of nuclear effects”. In: *Physical Review D - Particles, Fields, Gravitation and Cosmology* 92.5 (Sept. 2015), p. 051302. DOI: 10.1103/PhysRevD.92.051302.

[138] Guang Yang. “3D Projection Scintillator Tracker in the DUNE Near Detector”. In: *PoS*. Vol. ICHEP2018. Sissa Medialab, Aug. 2019, p. 868. DOI: 10.22323/1.340.0868.

[139] A. Blondel et al. “Readout scheme for the Baby-MIND detector”. In: *Proceedings of Science*. Vol. 6-9-July-2. Proceedings of Science (PoS), Jan. 2015, p. 031. DOI: 10.22323/1.252.0031.

[140] *T2K upgrade software*. URL: https://github.com/t2k-nd280-upgrade/t2k-nd280-upgrade (visited on 06/30/2020).

[141] J B Birks. “Scintillations from organic crystals: Specific fluorescence and relative response to different radiations”. In: *Proceedings of the Physical Society. Section A* 64.10 (Oct. 1951), pp. 874–877. DOI: 10.1088/0370-1298/64/10/303.

[142] O. Mineev et al. “Beam test results of 3D fine-grained scintillator detector prototype for a T2K ND280 neutrino active target”. In: *Nuclear Instruments and Methods in Physics Research Section A: Accelerators, Spectrometers, Detectors and Associated Equipment* 923 (Apr. 2019), pp. 134–138. DOI: 10.1016/j.nima.2019.01.080.

[143] K. Abe et al. “Characterization of nuclear effects in muon-neutrino scattering on hydrocarbon with a measurement of final-state kinematics and correlations in charged-current pionless interactions at T2K”. In: *Physical Review D* 98.3 (Aug. 2018), p. 24. DOI: 10.1103/PhysRevD.98.032003.

[144] W. Baldini et al. “Measurement of parameters of scintillating bars with wavelength-shifting fibres and silicon photomultiplier readout for the SHiP Muon Detector”. In: *Journal of Instrumentation* 12.03 (Mar. 2017), p. 3005. DOI: 10.1088/1748-0221.

université PARIS-SACLAY
ÉCOLE DOCTORALE
Particules, hadrons, énergie et noyau: instrumentation, imagerie, cosmos et simulation (PHENIICS)

Titre: Recherche de neutrinos massifs avec l'experience T2K et mise à niveau du détecteur proche ND280

Mots clés: T2K, physique des neutrinos, neutrino détecteur

Résumé: Les expériences sur les neutrinos de l'accélérateur se concentrent sur la mesure précise des paramètres d'oscillation des neutrinos et recherchent la violation de la CP dans le secteur des leptons. L'incertitude systématique des modèles de flux et d'interaction des neutrinos sont les principales limites de la sensibilité. L'expérience T2K améliore le complexe de détecteurs proches (ND280) pour réduire ces incertitudes. Une nouvelle cible à scintillateur à grain fin et Chambres Projections Temporelles avec anode résistive fournirent une sonde précise des modèles d'interaction des neutrinos. Les prototypes de détecteurs ont été testés avec des faisceaux de particules chargées et ont démontré une bonne performance. Les incertitudes systématiques dans l'analyse des oscillations seront réduites de 7% à 4%.

La découverte des oscillations du neutrino indique une masse non nulle du neutrino. L'existence de neutrino lourds est une hypothèse prometteuse qui fournit une explication naturelle minimale de la masse du neutrino, de l'existence de la matière noire et de l'asymétrie baryonique de l'Univers. Une recherche des désintégrations HNL a été effectuée avec le détecteur proche de l'expérience T2K. Le volume actif des TPC gazeux a été utilisé car le bruit de fond attendu des interactions des neutrinos devrait être faible par rapport aux détecteurs à scintillation. Une recherche des désintégrations des HNL a été effectuée avec l'ensemble des données T2K. Aucun signe significatif des particules exotiques n'a été observé et une limite supérieure importante a été fixée à leur existence.

Title: Search for heavy neutrinos in the T2K experiment and upgrade of the near detector ND280

Keywords: Neutrino physics, T2K, neutrino detectors

Abstract: Accelerator neutrino experiments are focusing on the precise measurements of the neutrino oscillation parameters and search for the CP–violation in the lepton sector. The systematic uncertainty of the flux and neutrino interaction models are the main limitations of the sensitivity. The T2K experiment is upgrading near detector complex (ND280) to reduce these uncertainties. A new 3D fine-grained scintillator target and Time Projections Chambers with resistive anode will provide a precise probe of neutrino interaction models. Detectors' prototypes were tested with charged particles beams and demonstrated a good performance. The systematic uncertainties in the oscillation analysis will be reduced from 7% down to 4%.

The discovery of the neutrino oscillations indicates a non-zero mass of the neutrino. The existence of Heavy Neutral Leptons (HNL) is a promising hypothesis that provides a minimal natural explanation of the neutrino mass, the existence of Dark Matter, and baryon asymmetry of the Universe. A search of the HNL decays was performed with the near detector of the T2K experiment. The active volume of the gaseous TPCs was used since the background from the neutrino interactions is expected to be small compared to scintillator detectors. A search for HNL decays was performed with T2K data set (2010-2017). No significant signs of the exotic particles existence were observed and a strong upper limit on the corresponding mixing matrix elements were set.

Université Paris-Saclay
Espace Technologique / Immeuble Discovery
Route de lOrme aux Merisiers RD 128 / 91190 Saint-Aubin, France